الجمهورية الجزائرية الديمقراطية الشعبية

Democratic and Popular Republic of Algeria

وزارة التعليم العالي والبحث العلمي

Ministry of Higher Education and Scientific Research

Serial N° .....

Order N° .....

KASDI MERBAH OUARGLA UNIVERSITY
FACULTY OF APPLIED SCIENCES
DEPARTMENT OF ELECTRICAL ENGINEERING
THESIS

Submitted for the award of the Doctoral Degree (3rd cycle)

Sector: Electrotechnics

Specialty: Electrotechnics

Presented by:

BOURAMDANE ABDERRAOUF

Thesis Title

Comparative Study of Four Mini Photovoltaic Power Plants of different Technologies and Inclinations for Grid Injection

1. جعفور أحمد	، الرتبة: أستاذ	، جامعة: قاصدي مرباح ورقلة	رئيسًا
2. الوازن محمد الأخضر	، الرتبة: أستاذ	، جامعة: قاصدي مرباح ورقلة	مشرفًا و مقررًا
3. بن مير عبد القادر	، الرتبة: أستاذ محاضر أ	، جامعة: قاصدي مرباح ورقلة	مساعد مشرف (مدعو)
4. ختاش العيد	، الرتبة: أستاذ محاضر أ	، جامعة: قاصدي مرباح ورقلة	مناقشًا
5. بوحفص علي	، الرتبة: أستاذ محاضر أ	، جامعة: قاصدي مرباح ورقلة	مناقشًا
6. خليفة موسى	، الرتبة: أستاذ محاضر أ	، جامعة: قاصدي مرباح ورقلة	مناقشًا
7. عمير توفيق	، الرتبة: أستاذ	، جامعة: جامعة العربي التبسي تبسة	مناقشًا

Academic year 2025/2026

DEDICATIONS

I would like to dedicate this work to sincerely:

My father, Bouramdane Mohammed, and my **mother, Badaui MA**. Their sacrifices, love, and unwavering support have been the foundation of my journey. Their strength and encouragement have provided me with the determination to reach this point.

My brothers and sisters Abdelkhader, Massouda, Yassin ,Nadjoua, Nadia, Nardjies, Abdelwahab, Abdelwadoud, and my youngest brothers **Anfal , Farah, Lujain, and Waile** — for always believing in me and standing by my side.

My dear friends, for their presence and encouragement throughout this process.

The entire **Bouramdane and Badaui families,** whose support has always meant so much to me.

And to all those who use science for the benefit, happiness, and prosperity of humanity.

ACKNOWLEDGMENTS

Above all, I would like to express my deepest gratitude to Allah for granting me the strength, patience, and determination to complete this doctoral thesis. I pray for His continued guidance and support as I strive to advance further in research and to contribute meaningfully to science and academia as a future professor, researcher, and scientist in my field.

I extend my sincere thanks to **Professor LOUAZENE Med Lakhdar and Professor Benmir Abdelkhader**, my advisor and reviewer, for their invaluable guidance, continuous encouragement, and substantial efforts throughout my research journey. Their insights, advice, and unwavering support were instrumental in the development of this work. I am especially grateful for their help with my publications and for giving me the opportunity to explore the world of research and its diverse dimensions.

I am also deeply grateful to **Mr. Ilyase Souid,** a dear friend, for his exceptional support during the experimental investigations at the Oued Nechou station. His valuable insights, scientific guidance, and consistent presence were a great source of motivation throughout this journey. His generosity in sharing knowledge and offering assistance had a significant impact on the successful progress of this work.

My heartfelt thanks go to **Mr. BENSAHA Kaddour**, Central **Director, Mr. Fathie Charmat, Mr. Moussa BENSAHA, Mr.**

Ahmed Dahmana and the entire team at **Oued Nechou** and the Ghardaïa Photovoltaic Station for their scientific, technical, and logistical support.

I would also like to sincerely thank all the professors, each by name, who kindly accepted to serve as examiners for this work. I am truly honored by the presence of the jury members at my defense and am especially grateful to the President of the Jury for accepting this role and honoring my work.

Special thanks go to **Mr. Danoune Bilal** and **Mr. Gougui A. Abdelmoumen,** researcher at the University of Ouargla, for their scientific expertise, valuable advice, availability, and outstanding human qualities. I would also like to warmly thank my friends each by name for being present and for honoring me with their support on this important day. Their presence meant a great deal to me and brought joy to this special moment.

Finally, I extend my sincere appreciation to all the professors and administrative staff of the Department of Electrical Engineering my second professional family for their continuous support throughout my academic path.

TITLES LIST

SYMBOL LIST

TABLE LIST

FIGURE LIST

FIGURE LIST

GENERAL INTRODUCTION

• GENERAL INTRODUCTION

The global energy sector is experiencing a swift transition driven by rising electricity demand, depletion of fossil fuel reserves, and growing environmental concerns about greenhouse gas emissions and climate change **[1].** In light of this, sustainable energy sources are now considered vital for developing secure, low-carbon, and environmentally friendly energy systems.

Among renewable energy sources, solar energy is one of the most abundant and promising. Global photovoltaic (PV) capacity exceeded 2.2 TW in 2024, with more than 600 GW added in a single year, reflecting rapid technological and economic progress in solar power worldwide **[2-3].** This growth underscores the increasing role of PV technologies in achieving decarbonized energy systems.

Algeria is particularly well positioned to benefit from solar deployment due to its exceptional irradiation levels, ranging from 5 to 7 kWh/m²/day and reaching up to 3,900 sunshine hours annually in the Sahara region **[4].** These conditions make PV systems highly suitable for national energy transition strategies and large-scale grid integration.

PV technologies differ in structure and performance, including monocrystalline silicon (mc-Si), polycrystalline silicon (pc-Si), amorphous silicon (a-Si), and cadmium telluride (CdTe). Their electrical output is strongly influenced by environmental factors such as solar irradiance, temperature, humidity, and wind speed. Additionally, single-axis solar tracking systems can enhance annual energy yield compared to fixed-tilt installations, particularly in high-irradiation regions **[4-5].**

Despite Algeria's abundant solar resources, the real-world performance of these PV technologies under desert climatic conditions remains insufficiently documented, and the influence of meteorological parameters on PV output across seasons has not been thoroughly analyzed. This raises the central research problem of the study: Which photovoltaic technologies and mounting configurations-fixed or single-axis tracking-provide the best performance in terms of peak power, daily energy productivity, and seasonal stability for 100 kW grid-connected PV subfields in southern Algeria **[1]-[5].**

To address this problem, the OUED-NECHOU Solar Research Center in Ghardaïa provides an ideal platform for evaluating PV performance, hosting multiple fixed and

tracking subfields at a 30° tilt connected to the national grid. This thesis compares four fixed 100 kW PV technologies (mc-Si, pc-Si, a-Si, CdTe) in terms of peak power, daily energy productivity, and seasonal behavior. Additionally, mc-Si and pc-Si modules with single-axis tracking are evaluated against their fixed counterparts to determine performance gains and reliability under desert climatic conditions.

The findings aim to optimize PV deployment in Algeria and similar regions by identifying the most efficient and reliable configurations. The OUED-NECHOU Solar Research Center contributes 1.1 MW of PV capacity directly fed into SONELGAZ's grid, supporting national renewable energy and energy transition goals.

This research thesis is presented in three structured chapters as follows:

✓ **The First chapter** presents an analysis using empirical mathematical models to predict total hourly solar radiation on a surface tilted at 30°. The three selected models-Perrin de Brichambaut, Liu & Jordan, and Capderou-are implemented in MATLAB and evaluated against real-time experimental data collected using a pyranometer installed on the rooftop of the OUED-NECHOU pilot PV plant. Data were recorded on four representative days, each corresponding to a different season, and the models' accuracy was assessed using statistical indicators.

✓ **The Second Chapter** provides an in-depth overview of photovoltaic (PV) technologies, detailing the four generations of solar cells, their operating principles, key performance metrics, advantages, and limitations. It includes a historical perspective, technological milestones, and a comparative analysis highlighting the strengths and weaknesses of each generation.

The Third Chapter evaluates the performance of various PV subfields at the OUED-NECHOU power plant, focusing on four fixed subfields (mc-Si, pc-Si, a-Si, CdTe) each rated at 100 kWp. It also compares fixed and single-axis tracking systems using mc-Si and pc-Si modules. Performance is analyzed based on peak power, average daily output, and energy yield using four-minute interval data collected across seasonal experimental days. The influence of key meteorological parameters, such as solar irradiation, temperature, wind speed, and humidity, is examined. A two-stage augmentation percentage analysis quantifies power gains, first identifying the most efficient fixed system, then comparing it to its tracking counterpart. The results demonstrate the performance benefits of single-axis tracking systems over fixed installations under real Saharan climatic conditions.

CHAPTER I
SOLAR IRRADIANCE ESTIMATION USING EMPIRICAL MODELS

I. Introduction

Solar radiation data are essential for climatology, agrometeorology, hydrology, and solar energy system design, yet many regions lack measurement stations. To address this, numerous empirical models have been developed to estimate solar radiation.

This chapter evaluates three empirical models- PERRIN DE BRICHAMBAUT, LIU & JORDAN , and CAPDEROU - for predicting total solar flux on a 30° inclined surface. The models are implemented in MATLAB and validated using pyranometer measurements taken at the same tilt at the OUED-NECHOU photovoltaic power plant (Ghardaïa).

Data were collected from 06:00 to 20:00 on four seasonal days: January 1st, May 1st , July 1st , and October 1st . Correlation coefficients were used to assess model accuracy, and comparisons between measured and estimated values identified the model best suited to the Algerian Sahara.

The chapter begins with the importance of solar energy in Algeria, then presents the three model equations and compares their performance**.**

II. Solar Energy Around the World and in Algeria

II.1. Solar Energy in The World

The Sun radiates approximately 3.846×10^{26} W in total, and at the distance of Earth, this corresponds to a solar irradiance - known as the Solar constant - of about 1,361 W/m² outside the atmosphere **[6].** As solar radiation traverses the atmosphere, it is scattered, absorbed, and reflected, reducing the irradiance. On a clear day at ground level, the maximum direct normal irradiance rarely exceeds about 1,000 W/m² (clear-sky, direct-normal-irradiance upper bound) **[6].**

Global solar photovoltaic (PV) capacity has grown dramatically in recent decades, reaching approximately 1.6 terawatts (TW) by the end of 2023 **[7].** Accelerated deployment continued in 2024, with global PV capacity reportedly surpassing 2.2 TW by year-end **[8].**

Africa- and in particular its northern and Saharan regions - benefits from exceptionally high solar resource. According to recent assessments, the continent receives, on average, about 2,119 kWh/m²/year of global horizontal irradiation (GHI), with many areas in North, West, and Southern Africa exceeding 2,100 kWh/m²/year. Regions classified as “sun-belt zones” (e.g., parts of the Sahara) often experience > 2,300 kWh/m²/year **[9].** Given these solar resource levels, large-scale PV (or concentrated solar power) deployment in sun-belt regions is technically very promising.

Fig I.1 presents the long-term average global horizontal irradiation (GHI) received across the Earth's surface, measured in kWh/m² per year. The northern regions of Africa, particularly the Sahara Desert, receive some of the highest levels of irradiation, exceeding 2,200 kWh/m² per year. This illustrates their significant potential for solar energy generation **[10].**

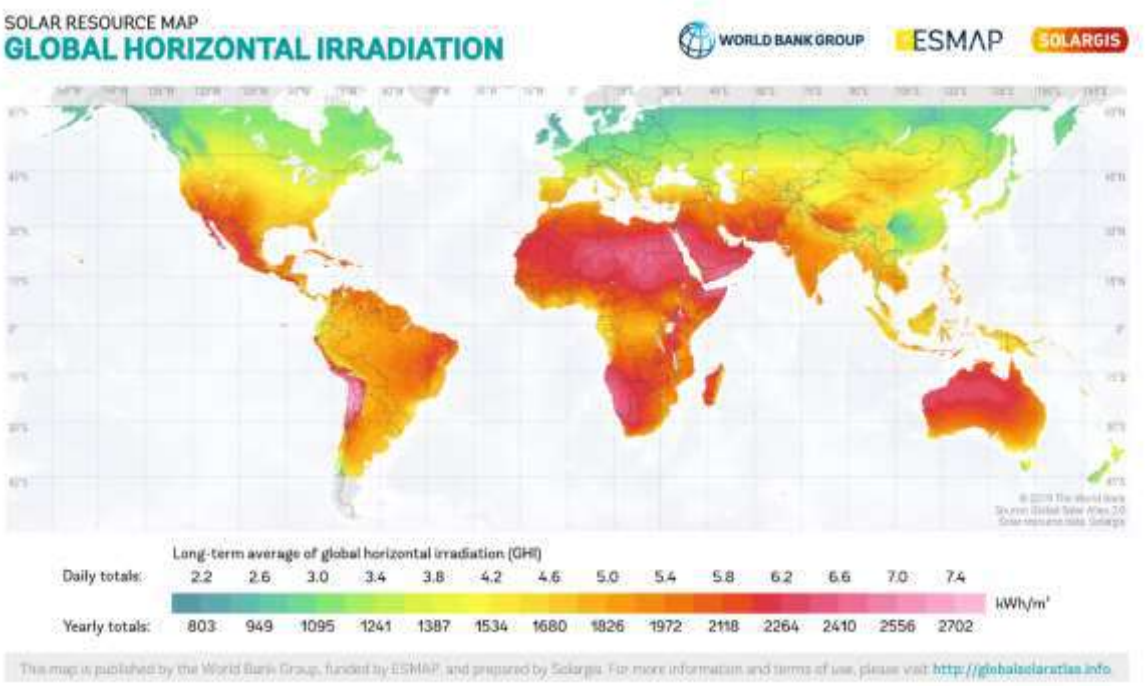

Fig I.1: Global map of average annual GHI (kWh/m²/year) **[10].**

II.2. Solar Energy Potential in Algeria

Due to its geographical location, Algeria has one of the highest solar deposits in the world. The sun remains to date the most important source of energy despite the considerable distance that separates it from the earth (150×10^6 km). The power emitted by the sun in the form of radiation is estimated at 90×10^{15} GW, while the earth's layer can only receive 180×10^6 GW. Before reaching the earth, solar radiation undergoes considerable changes, mainly due to absorption and diffusion phenomena. Also, we introduce the notion of illumination which is the power density received by a surface subjected to a luminous flux, in optimal atmospheric conditions. This power density reaches 1 kW / m^2 for a site located at sea level **[11]**, this energy is available in abundance on the entire earth's surface, despite significant attenuation during crossing the atmosphere; the quantity that remains is still quite significant, when it reaches the ground. It can thus reach 1000 W/m² peak in temperate zones when the atmosphere is slightly polluted. Algeria has approximately 3200 hours of

sunshine per year, for this reason, it can be said that Algeria benefits from a climatic situation favorable to the application of solar techniques **Fig I.2 [12-13].**

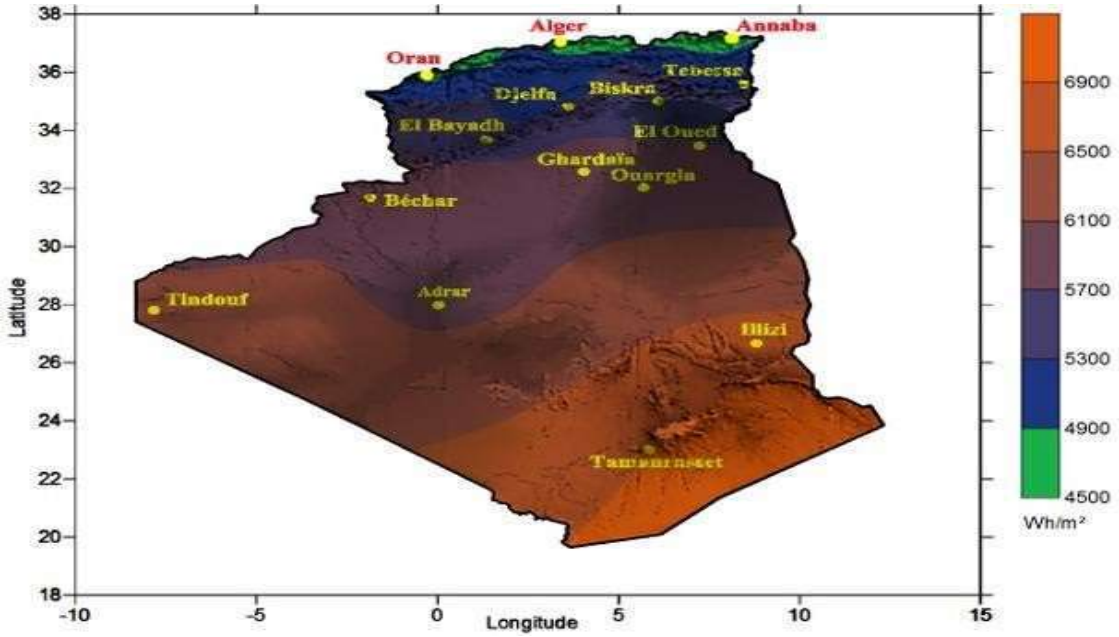

Fig. I.2 : Annual Solar Radiation Map of Algeria

III. Geographical representation of the OUED-NECHOU, photovoltaic plant, Ghardaïa .

The Ghardaïa photovoltaic solar power plant, located in southern Algeria, is part of the renewable energy development program initiated by the supervisory ministry. It is situated near the village of OUED - NECHOU, 15 km north of Ghardaïa along National Road No. 01, with a nominal power capacity of approximately 1100 kW. The site is bordered by National Road No. 01 to the north and west and vacant land to the east and south. The plant's precise location is 32°34′43.79″ N, 3°41′55.36″ E. longitude, at an altitude ranging from 450 to 566 meters. The closest wilayas are Laghouat and Ouargla. The topography of the site is relatively flat, with a gentle east-west slope. Solar irradiation during the summer months can reach 900-1000 W/m², it may also exceed this value.

IV. Coordinates including geographical and astronomic

It refers to angular coordinates that make it possible to locate any point situated on Earth, which has a specific latitude and longitude **[14-16].**

Latitude (φ)

Latitude φ indicates the angular distance of any point from the equator. It is counted positively from 0 to 90° towards the north and negatively from 0 to -90° towards the south.

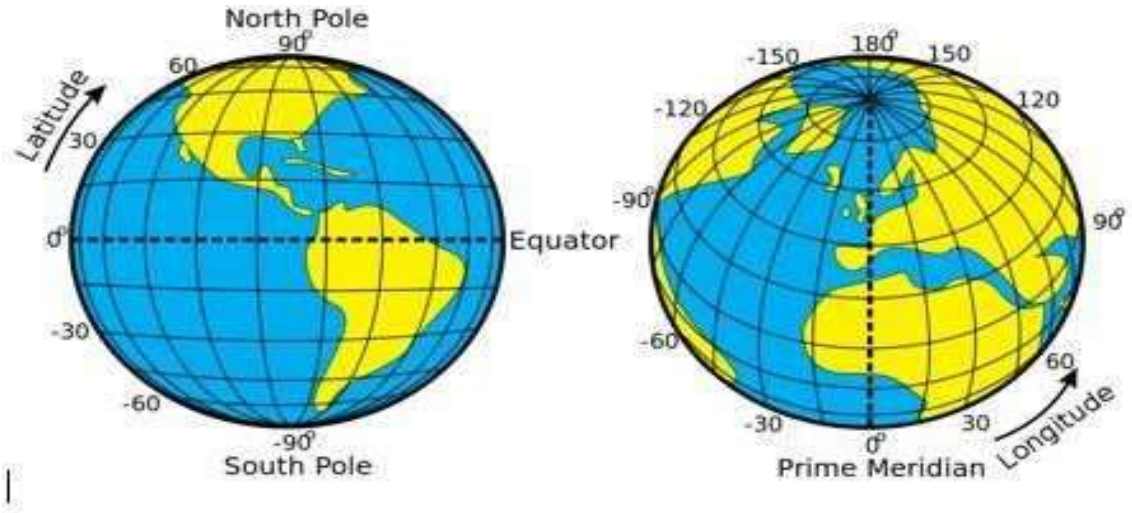

Fig I. 3: Geographic coordinates **[17].**

- **Longitude (L)**

The longitude **L** is used to locate a point to the East or West of a North-South reference line called the Greenwich meridian, the longitude **L** varies between -180° to +180° , is counted positively towards the East and negatively towards the West, starting from the Greenwich meridian. **Fig I.3.** Shows the geographical coordinates of any place .

IV.1. Sun Parameters and Position (Hour Angle Coordinates (δ, ω))

IV.1.1- Solar Declination (δ , ω)

It is the angle of the direction of the sun with the equatorial plane and varies between two extreme values, this variation in a sinusoidal way during the year. It is maximum (23.27') on June 22, at the summer solstice; minimum (-23.27'), on December 21, at the winter solstice. At the solstice periods, the variations of the declination are: The declination is zero on March 21 and September 23 which correspond to the spring and autumn equinoxes, outside these periods, the variation becomes rapid and weak from one day to another. To calculate the value of the declination, da, there are several formulas that have been reported in the literature, the most cited is equation (I.1), which was derived by Spencer (1971), some other simpler equations that are used in solar applications equation (I.2) by Perrin DE BRICHAMBAUT(1975) and equation (I.3) by Cooper (1969) **[17-18].**

$$\delta = 0.006918 - 0.399912\cos(T) + 0.070257\sin(T) - 0.0066758\cos(2T) + 0.00090\sin(2T) - 0.002697\cos(3T) + 0.00148\sin(3T) \quad \textbf{(I.1)}$$

With :

$$T = 2\pi \frac{(n-1)}{365}$$

$$\delta = 23.45.\sin\left(\frac{360}{365}(n + 284)\right) \quad \textbf{(I.2)}$$

Or

$$\delta = \sin^{-1}\left(0.4.\sin\left(\frac{360}{365}(n - 80)\right)\right) \quad \textbf{(I.3)}$$

n : is the day number of the year (first of January n=1 and last day is 365), means , it ranges from 1 to 365 in a calendar year. **See Fig I.4.**

J = 365 days. For the Leap year: **J = 366 days**

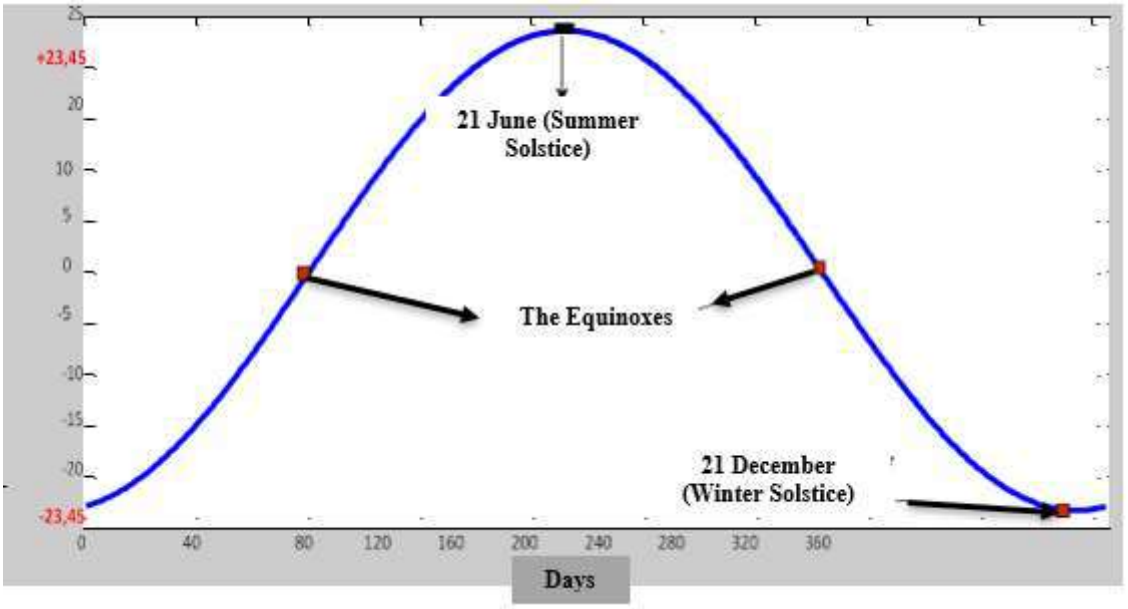

Fig I.4 : Variation of the declination according to the number of the day in the year **[17].**

Hour angle (ω)

It is defined as 15° multiplied by the number of hours of difference from solar noon, assigned a positive sign for the hours after solar noon and a negative sign for the hours before solar noon. It is expressed by the relation (**II.11**):

$$\omega = (TSV - 12) \times 15 \quad \textbf{(I.4)}$$

- **ω = 0** Involves **TSV = 12:00 h**
- **ω <** The morning
- **ω >** The afternoon.

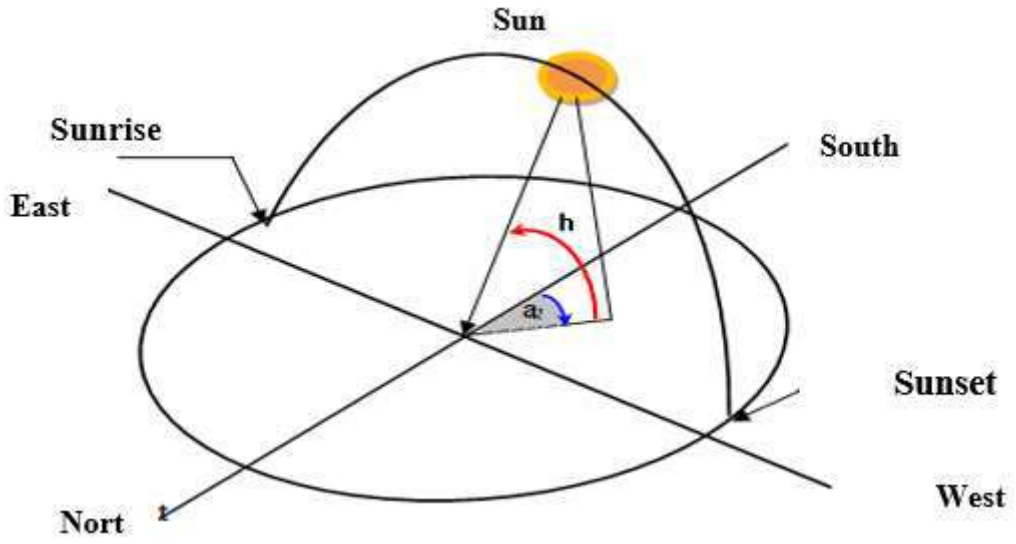

Fig I.5: Time coordinates **[17].**

- **Sunrise and sunset (ω_s)**

- From the height of the sun h we can deduce the times of sunrise and sunset

$$\omega_s = cos^{-1}(-\tan \Phi \times \tan \delta) \quad \textbf{(I.5)}$$

IV.2- Horizontal coordinates

The positioning of the sun is determined through two angles: azimuth **(a)** and height (h), as illustrated in the **Fig I.6** below:

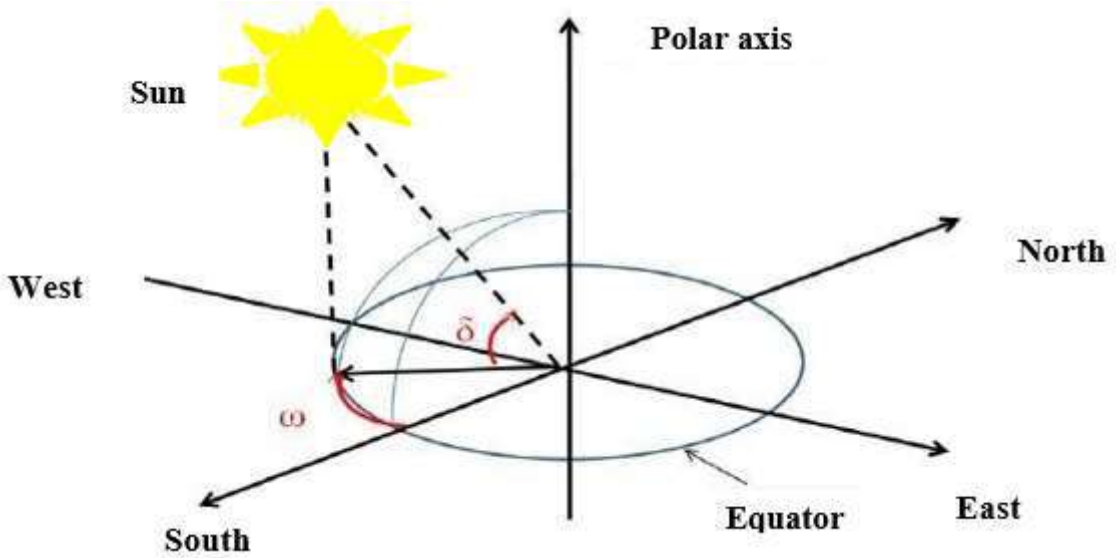

Fig I.6: Horizontal coordinates **[12].**

The azimuth (α)

The angle that the projection of the direction of the sun makes with the direction of the south is counted from 0° to 360° from the west. This angle (a) is noted with the same conventions as the azimuth of the plane **α [15],** and it is expressed with the equation **(I.6).**

$$\sin(\alpha) = \frac{\cos(\delta) \times \sin(\omega)}{\cos(h)} \qquad (\mathbf{I.6})$$

Generally, the surface of the study plane is oriented towards the south that's to say (a = 0). The solar azimuth is negative in the morning (East direction), zero or equal to 180° at noon, and positive in the afternoon (West direction) over the entire globe.

The height (h)

The height of the sun (elevation of the sun) is an angle between the apparent direction of the sun and its projection on the horizontal plane of the plane considered. Its value becomes zero in the Coche and the sunrise but takes a maximum value at solar noon

The height **(h)** is given by the following equation **(I.7):**

$$\mathbf{Sin\ (h) = Sin\ (\delta).Cos\ (\varphi) + Cos\ (\varphi).Cos\ (\delta).Cos\ (\omega)} \qquad \mathbf{(I.7)}$$

With :

h : The height of the sun

α : Sun azimuth

δ : The declination of the sun

ω : The hour angle

φ : The altitude of the study location.

IV. 3 -Time

The Earth undergoes two types of movement; one is the rotation of the Earth around the axis of the poles and its revolution around the Sun. The movement of the Earth on itself defines the concept of a solar day. A complete rotation takes 24 hours. This thus provides the definition of time, as each hour corresponds to an angular difference of 15° .

Solar Times

For solar energy applications, true solar time TSV must be used, which is calculated by taking into account the difference between mean solar time **TSM** and local time **TL**.

True Solar Time (TST)

True solar time is defined from the rotation of the Earth on itself. It is therefore directly linked to the hour angle. The Earth makes a complete rotation in 24 hours. It is noon (12H) when the sun is at its zenith **[20]:**

It is given by the relation **(I.8):**

$$TST = TL - DE\ (Et + 4\lambda) \qquad \textbf{(I.8)}$$

$$TST\ \text{« l »} = 12 + w/15$$

$$TST\ \text{« c »} = 12 + w/15$$

Where : **TST= 12h if w = 0 °**

LT : Legal time (given by a watch) , is defined in Equation (**I. 14**).

DE : Time offset relative to the Greenwich meridian (equal to 1 for Algeria).

ET: This is the correction to the equation of time, defined in Equation (**I. 10**). This correction varies over the year from −14.3 (min) to 16.4 (min).

Mean Solar Time (MST)

The Earth's speed on its orbit varies throughout the year, and to have time that flows at a constant rate, as measured by clocks, a Mean Solar Time (MST) is defined. This is based on a hypothetical mean sun that moves at a constant speed throughout the year.

It is the time that separates on average two successive passages of the sun at the meridian of the place, the mean solar day has a duration of 1 day = 24h 00m 00s.

The duration of a mean solar day is 24 hours, regardless of the day of the year **[21].** The mean solar time is slightly from the actual solar time, this difference defines the equation of time.

$$ET = TST - MST \quad \textbf{(I.9)}$$

Et is the correction of **TST** relative to **MST**; this correction varies from 14 minutes. In the 11th of February to -16 minutes in the 3rd of November, Et can be expressed with the formula **I.10.**

$$ET = 9.87.\sin(2N) - 7.52.\cos(N) - 1.5\cos(N) \quad \textbf{(I.10)}$$

With :

$$N = \frac{360}{365}(n - 81) \quad \textbf{(I.11)}$$

ET: Calculate in minutes and in decimal fractions of a minute.
λ **:** Longitude of the location, in degrees.
TSV "l": sunrise in true solar time.
TSV "c": sunset in true solar time .

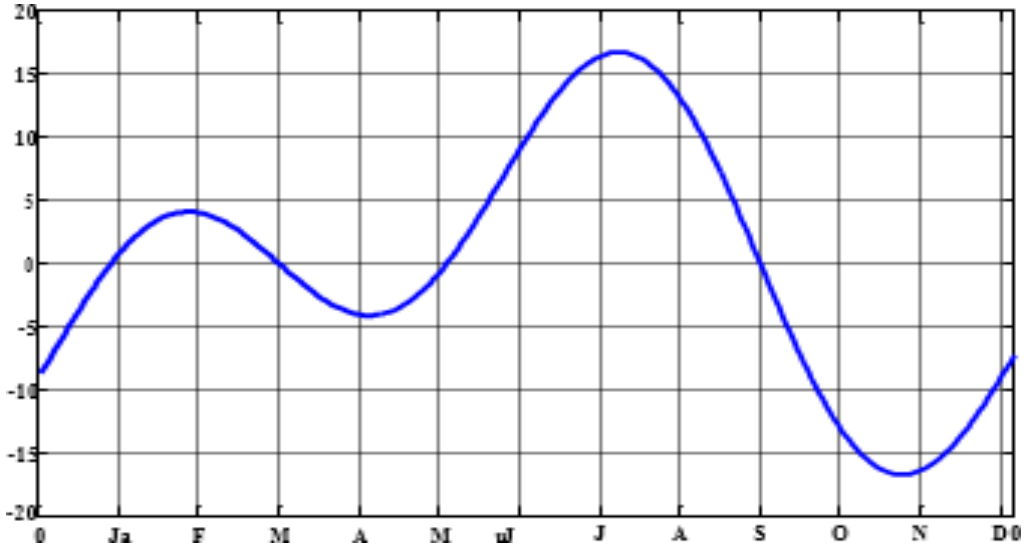

Fig I.7: Graphical representation of the equation of time as a function of months.

Universal Time (UT)

At a location with a given longitude, Universal Time (UT) is linked to the local Mean Solar Time, formerly known as TMG or GMT (Greenwich Mean Time). For a location with longitude L, UT can be expressed by the following equation **(I.12):**

$$UT = MST + \frac{L}{15} \quad \textbf{(I.12)}$$

When we replace equation **(I.9)** in equation **(I.12)** we obtain the UT with the following equation **(I.13):**

$$UT = TST + ET + \frac{L}{15} \quad \textbf{(I.13)}$$

- **Legal Time (LT)**

This is the official time of the state or the time of the time zone. The Earth is divided into 24 beams of 150 wide centered on the meridians whose longitude is a multiple of 15, this time linked to the UT by a fixed difference, expressed in an integer number of hours that depends on the longitude and customs of each country, the UT is expressed with the following relation . See the following equation (**I.14**):

$$LT = UT + DH \quad \textbf{(I.14)}$$

DH: represents the time difference between the Greenwich meridian and the considered state (DH = 1 hour for Algeria).

$$LT = SDT + 4\,(\lambda_{STD} - \lambda_{local}) + E_t \quad \textbf{(I.15)}$$

SDT: The standard time of the location.

λ_{STD}: The standard meridian longitude of the region.

λ_{local} **:** The local longitude of the region.

V. Solar Radiation in The Presence of The Atmosphere

Before reaching the ground, solar radiation is diffused and absorbed by gas molecules, aerosols, droplets, and various suspended dust particles. The absorbed radiation is transformed into heat and disappears from the usable balance on the ground.

V. 1-Models for Calculating Daily Global Irradiation on a Horizontal Surface

The solar radiation received on a horizontal surface consists of two main components: direct and diffuse radiation. The diffuse component can be further divided into:

- **Sky diffuse radiation:** Scattered sunlight reaching the surface from the atmosphere.
- **Ground-reflected radiation (Albedo):** Radiation reflected from the ground surface back to the receiver.

V.1.1-The Total Global horizontal solar irradiance (GHI)

Is the sum of direct and diffuse solar radiation when the surface has no tilt **(β = 0°)[13]** . It is mathematically expressed in equation **(I.15)** and illustrated in **(I. 8)** :

$$GHI = H_B + H_D \quad \textbf{(I.16)}$$

- **GHI** = Global Horizontal Irradiance (W/m²)
- H_B = Direct normal irradiance (DNI) (W/m²)
- I_D = Diffuse horizontal irradiance (DHI) (W/m²)

Fig I. 8 : Distribution of Global Solar Radiation on a Horizontal Surface **(β = 0°).**

V.1.2- Models for Estimating Daily Global Solar Irradiation on an Inclined Surface

The tilt angle of a surface significantly influences the amount of solar radiation it receives. Adjusting this angle optimizes the distribution of direct, diffuse, and ground-reflected radiation, thereby improving energy absorption. The total global solar radiation on an inclined surface **(H_T)** consists of three components: direct radiation **(H_B),** diffuse radiation **(H_D),** and ground-reflected radiation **(H_R),** assuming isotropic reflection (**Fig 2.3**).

As a result, the global solar radiation on an inclined surface (H_T) can be calculated using the equation proposed by Duffie and Beckman (1991) **[21-22].**

$$H_T = H_B + H_D + H_R \quad \textbf{(I.17)}$$

The components of global solar irradiance on an inclined surface are shown in **Fig. I.9**

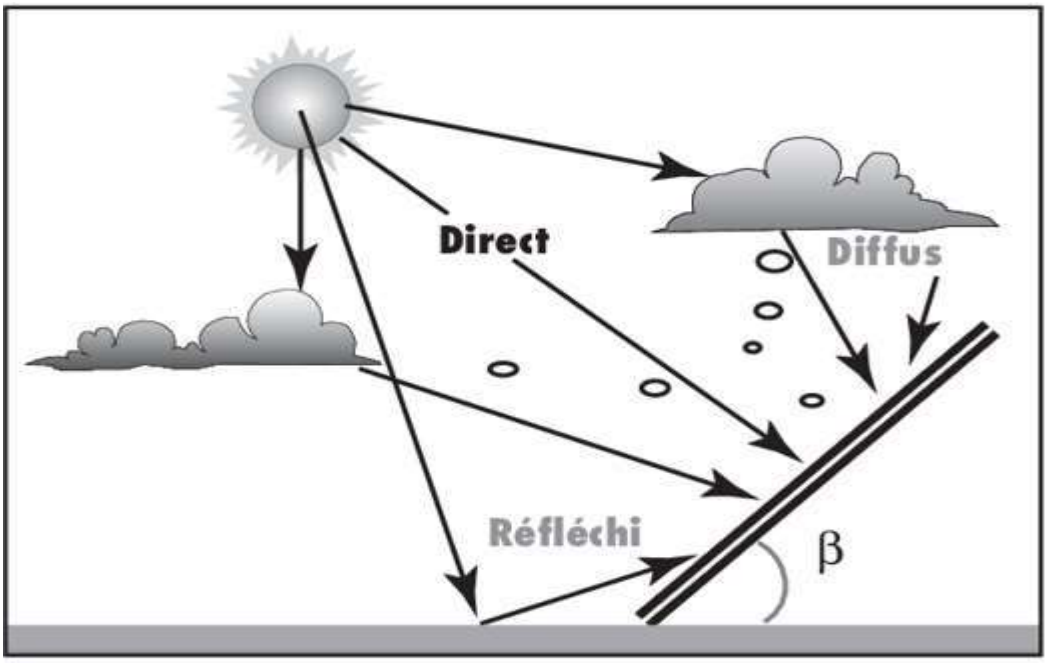

Fig I.9 : Components and Distribution of Global Solar Radiation on an Inclined Surface **β=30 [23] .**

- H_B = Direct Solar Irradiance
- H_D = Diffuse Solar Irradiance
- H_R = Reflected Solar Irradiance

VI. Instruments for measuring solar radiation

Sunshine (G) corresponds to the intensity of solar radiation received on a surface at a given moment. It is usually expressed in Watts per square meter (W/m²), BTU, or LUX; sunshine varies from zero at sunrise to its maximum value, typically at solar noon **[24].** The classic principle of measuring illumination is the thermoelectric effect: a black body absorbs solar radiation, and a series of thermoelectric couples measure the increase in its temperature. An electromotive force is generated, and obtaining precise measurements can be challenging, especially when the device is placed outdoors. Solar radiation measuring devices provide data on climatic conditions and measure solar radiation at ground level. These devices are essential components of weather stations, for example.

VI.1- The Pyranometer

It is an instrument that can measure direct and diffuse radiation , with temperature sensors used in these devices. The response of the temperature sensor is proportional to the light intensity falling on the sensor, the signals from the sensors are then correctly converted into the response.

The thermopile is generally used as a light sensor. One end of the thermopile is attached under a black plate, which gets heated when light falls on it. Due to the design, both direct and diffuse rays fall on the black plate. The black plate is covered with two hemispherical glass covers which are evacuated so that convection and radiation heat losses can be minimized. The other end of the thermopile is placed in such a way that it does not receive solar radiation, due to this temperature difference, a voltage is generated. The voltage generated is proportional to the amount of radiation falling on the black plate **[25].**

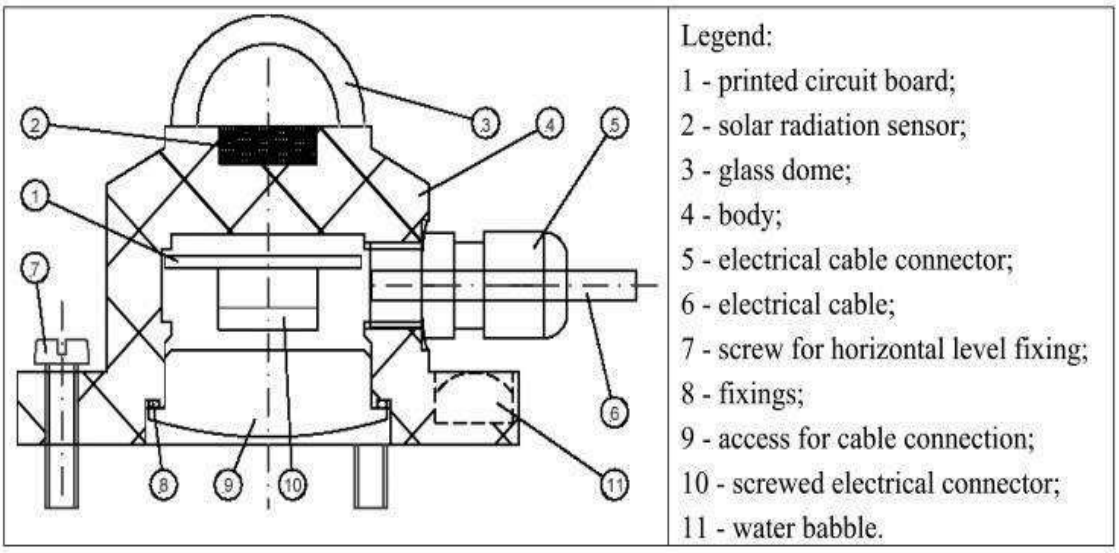

Fig. I.10: Technical Specifications of the Pyranometer.

The technical parameters of the pyranometer instruments (used to measure inclined radiation) are presented in **Table I.1** below. These instruments are connected to and installed at the meteorological station located on the rooftop of the control room of the photovoltaic power plant in OUED- NEACHOU, Ghardaïa.

Table I.1 :Technical Analysis of Pyranometers at Photovoltaic Power Plants in OUED- NEACHOU ,Ghardaia .

Technical Instrument	**Pyranometer sensor (Global Inclined solar radiation)**
Brand	LSI LASTEM
Model	DPA 053
County of Origin	Italy
Measurements	Solar Direction radiation
Measurement range	0-1300W/m^2
Precision	5 W/m^2
Resolution	10 /m^{-2}

VI.2- The Pyrheliometer

A direct radiation measurement instrument. The device is oriented so that its receiving surface is expected to solar rays. It measures solar radiation from the solid angle limited to the solar disk, reaching a unit surface perpendicular to the axis of this solid angle **[21]** .

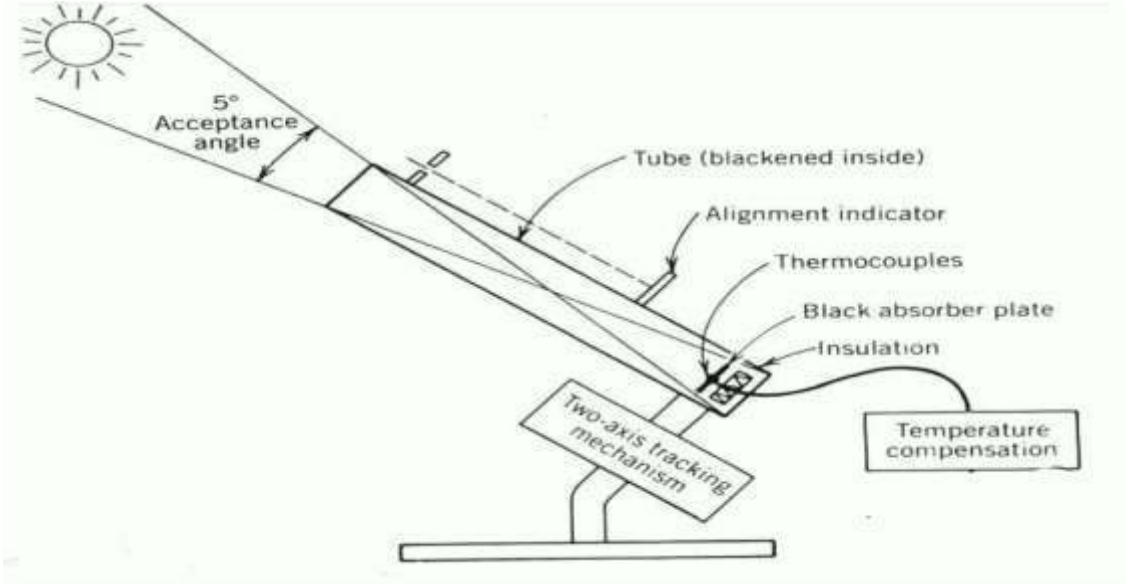

Fig. I.11: The pyrheliometer elements.

VI. 3- Radiometer

The radiometer is a device used to demonstrate the energy carried by radiation. It consists of a glass bulb containing low-pressure air and a small four-pane rotor, with one side of each pane black and the other white. This setup creates an asymmetry in the absorption of the incident radiation, causing the rotor to spin.

VI.4- Albedometer

The albedometer is a device designed to measure albedo, defined as the ratio of reflected radiation to the received global radiation. It consists of two pyranometers positioned opposite each other horizontally.

VI.5- Héliographe

The heliograph is a measurement device used to record the periods of the day during which the intensity of direct radiation exceeds a certain threshold. As long as shadows can

be observed on the ground, meteorologists refer to this as direct radiation, to which the heliograph is sensitive. The sum of these periods represents the duration of daily insolation, enabling the determination of the fraction of insolation recorded by the heliograph.

In the Campbell-Stokes heliograph, a glass sphere focuses direct radiation onto a burn point on a special paper. As the burn point moves, it traces the apparent movement of the sun, drawing a curve whose length is proportional to the duration of sunshine.

VII. Meteorological station installed at the photovoltaic plant in OUED-NECHOU, Ghardaïa.

The photovoltaic power plant in OUED-NECHOU, Ghardaïa, includes a meteorological station installed at the top of the control room, as shown in **Fig. I.12**. This station is used to collect meteorological data and mainly consists of :

Fig. I.12: Metrology station of solar PV panels center OUED-NECHOU, Ghardaïa.

a) - Barometer to measure atmospheric pressure.

b) - Rain gauge to measure the amount of rain.

c) - Humidity measurement.

d) - Wind speed measurement.

e) - Wind direction measurement.

f) - Pyranometers to measure direct, diffuse and inclined radiation.

g) - Ambient temperature sensor.

h) - Instrument for measuring the duration of sunshine.

VIII. Empirical estimation of hourly solar radiation

Due to the limited availability of weather stations and measurement centers across the national territory, theoretical models are often used to estimate solar irradiation. These models rely on correlations to make them applicable to various sites, especially where meteorological stations are unavailable.

To determine the amount of solar radiation received on a surface at a specific location, it is necessary to measure or estimate direct and diffuse radiation. This estimation is typically done using empirical equations derived from theoretical models. Consequently, numerous models have been developed to estimate direct, diffuse, and global solar radiation, including those by Michel Capderou, Perrin de Brichambaut, R. Sun, Liu & Jordan, Atwater & Ball, and Bird & Hulstrom…). In this study, we utilize two highly regarded empirical models the LIU & JORDEN model and the CAPDEROU model, both incorporating the Linke turbidity factor along with the PERRIN DE BRICHAMBAUT model. These models are applied to estimate global inclined solar radiation and are compared with experimental data collected from the meteorological station at the SKTM Center (now part of Sonelgaz Renewable Energy) in the OUED-NECHOU region, reflecting the center's current organizational structure. The data were collected on four experimental days, each representing one of the four seasons: January 1st (Winter), May 1st (Spring), July 1st (Summer), and October 1st (Fall) in 2016.

The analysis is conducted at a 30° tilt angle, which approximates the region's optimal angle. Statistical tests evaluate the accuracy of the models, identifying the one that most closely matches actual measurements. The selected model will be recommended for studying solar radiation in the region, particularly in areas lacking meteorological station

a. Linke Turbidity Factor

The knowledge of the atmospheric turbidity factor is necessary to determine irradiance under clear sky conditions. This factor represents the number of ideal atmospheres that, if stacked, would cause the same attenuation as the actual atmosphere. The advantage of the Linke factor is that it expresses various parameters, such as atmospheric water vapor and aerosols. In this model, the Linke atmospheric turbidity factor under clear sky conditions is given by **[26 -27].**

$$T = T0 + T1 + T2 \quad \text{(I.18)}$$

T0 : Is the disorder due to gaseous absorption by both fixed constituents of the atmosphere , including ozone and especially water vapor. A modeling of this factor based on geo-astronomical parameters , allowed CAPDEROU to propose the following expression **[28-29].**

$$T0 = 2.4 - 0.9 \times \sin(\Phi) + 0.1 \times (2 + \sin(\Phi)) \times Ahe - 0.2 \times Z - (1.22 + 0.14 \times Ahe) \times (1 - \sin(h)) \quad \text{(I.19)}$$

Or

$$Ahe = \sin\left[\left(\frac{360}{365}\right) \times (n - 121)\right]$$

Z: site altitude [Km].

T1: Is the turbidity corresponding to the absorption by atmospheric gases (O2, CO2 and O3) and the molecular Rayleigh scattering , as given by the approach **[26].**

$$T1 = 0.89^{Z} \quad \text{(I.20)}$$

T2: Is the turbidity related to scattering by aerosols coupled with slight absorption (it depends on both the nature and the quantity of aerosols **[26],[29].**

$$T2 = (0.9 + 0.4 \times Ahe) \times (0.63)^{Z} \quad \text{(I.21)}$$

VIII.2. LUI & JORDAN Model

VIII.2.1. Solar radiation formulas on an inclined plane

The global radiation on an inclined plan composed of three components: direct component, isotropic diffuse and diffuse coming from the sky given by the following equation: **[26],[30] .**

$$G_T = S_H \times R_b + D_H \times \left(\frac{1+\cos(\beta)}{2}\right) + (S_H + D_H) \times \left(\frac{1-\cos(\beta)}{2}\right) \times \rho \quad \text{(I.22)}$$

Where:

$$G_T = S_i + D_i + D_{ref} \quad \text{(I.23)}$$

S_i: Direct radiation on an inclined plane [W/m^2] is given by the following relation .

$$S_i = S_h \times R_b \quad \textbf{(I.24)}$$

$$S_h = S_H \quad \textbf{(I.25)}$$

R_b: is the inclination factor given in the equations **(I.27)** and **(I.28).**

D_i: Diffuse radiation on an inclined plane [W/m^2] , is given by the following relation **[26],[31].**

$$D_i = D_H \times \left(\frac{1+cos(\beta)}{2}\right) \quad \textbf{(I.26)}$$

D_{ref}: Ground reflection radiation on an inclined plane [W/m^2] , is given by the following relation **[26],[31].**

$$D_{ref} = (S_H + D_H) \times \left(\frac{1+\cos(\beta)}{2}\right) \times \rho \quad \textbf{(I.27)}$$

S_H, D_H : The direct radiation and diffuse radiation on a horizontal plane respectively, the ratio Rb of direct radiation on the inclined surface to that on a horizontal plane is called geometric factor (or sometimes inclination ratio) **[14].**

- In the northern hemisphere

$$R_b = \frac{\cos(\delta)\times\cos(\omega)\times\cos(\Phi-\beta)+\sin(\delta)\times\sin(\Phi-\beta)}{\cos(\delta)\times\cos(\omega)\times\cos(\Phi)+\sin(\delta)\times\sin(\Phi)} \quad \textbf{(I.28)}$$

- In the southern hemisphere

$$R_b = \frac{\cos(\delta)\times\cos(\omega)\times\cos(\Phi-\beta)+\sin(\delta)\times\sin(\Phi-\beta)}{\cos(\delta)\times\cos(\omega)\times\cos(\Phi)+\sin(\delta)\times\sin(\Phi)} \quad \textbf{(I.30)}$$

β : The inclination angle of the area .

ρ : Ground albedo .

Table I.2 provides some ground soil albedo ρ values.

Table I.2: Ground albedo values ρ **[32].**

Ground cover	Average reflectivity (albedo)
Snowy ground	0.7
Ground covered with dead leaves	0.3
Green grass	0.26
Golden fields	0.26
Pebbles white stones	0.20
dry grass	0.20

VIII.2.2 Solar radiation formulas on a horizontal plane S_H and D_H

- Direct radiation SH for a clear sky on a horizontal plane given by **[33]:**

$$S_H = Gne \times \sin(h) \times \exp\left(-\frac{T}{0.9+\frac{9.4}{T1}\times \sin(h)}\right) \quad \textbf{(I.31)}$$

Or Gne is the extraterrestrial radiation on the normal incident plane.

$$\textbf{Gne} = \textbf{Gsc} \times \textbf{C} \quad \textbf{(I.32)}$$

- **C:** Distance correction due to the elliptical trajectory of the earth
- **C:** $(1 + 0.0334 \times \cos(\frac{360}{365} \times (n - 2)))$ **(I.33)**
- **Gsc=** Solar constant **1367 [W/m^2].**

Diffuse radiation on a horizontal plane given by:

$$D_H = \text{Gne} \times \exp[-1 + 1.06 \times \log(\sin(h))] + a - \sqrt{a^2 + b^2} \quad \textbf{(I.34)}$$

$$a = 1.1 ; \qquad b=\log(T1+T2) - 2.8 + 1.02 \times (1 - \sin(h))^2$$

- The Global Horizontal Solar Radiation Formula:

$$G_H = S_H + D_H \quad \textbf{(I.35)}$$

VIII.3 PERRIN DE BRICHAMBAUT Model

The empirical model of PERRIN DE BRICHAMBAUT was established based on a series of experimental measurements conducted in the Trappes center (Paris region) and in Carpentras (southern France). This model is applicable to several parts of the world, except for regions characterized by an atmosphere heavily laden with dust, such as the Sahel regions, including Mali and Niger, during certain periods of the year. For Algeria, experiments conducted have demonstrated the validity of the PERRIN DE BRICHAMBAUT formulas in both the northern and southern regions of the country **[32].**

VIII.3.1 . Solar radiation on a horizontal plane in the Perrin model

The global radiation on a horizontal plane is the sum of direct radiation and diffuse radiation, estimated by the following expression **[34],[32].**

$$G_H = S_H + D_H \quad \textbf{(I.36)}$$

S_H**:** Direct radiation on a horizontal plane [W/m^2] **[26].**

D_H**:** Diffuse radiation on a horizontal plane [W/m^2] **[26].**

$$S_H = A \times \sin(h) \times exp\left[\frac{-1}{C \times \sin(h+2)}\right] \quad \textbf{(I.37)}$$

Where h is the height of the sun **A, B** and **C** are constants given in the table as a function of the nature of the sky**[26],[32].**

$$D_H = B \times (\sin(h))^{0.4} \quad \textbf{(I.38)}$$

According to another approximation, the global radiation on a horizontal plane can also be estimated by the global formula of PERRIN DE BRICHAMBAUT expressed by:

$$G'_H = A' \times (\sin(h))^{D} \quad \textbf{(I.39)}$$

Table I.3 : Depending On The Type of Sky The Values of The Variables **A, A', B, C,** and **D [35].**

The nature of the sky	A	A'	B	C	D
Very pure sky	1300	1150	87	6	1.15
Clear medium sky	1230	1080	125	4	1.22
Polluted sky	1200	990	187	2.5	1.25

VIII.3.1 .Solar radiation on an inclined plane in the Perrin model

$$G_T = S + D_{ciel} + D_{sol} \quad \textbf{(I.40)}$$

G_T **:** Global Inclined Solar radiation **[26].**

S : Direct radiation on an inclined plan [W/m^2] .

D_{ciel}**:** The diffuse radiation on an inclined plane [W/m^2] .

D_{sol}**:** The ground reflection radiation on an inclined plane [W/m^2] .

$$S = S_H \times R_b \quad \textbf{(I.41)}$$

Where R_b is the geometric factor given in the equations **(I.27)** and **(I.28).**

$$D_{ciel} = D_H \times \left(\frac{1+\cos(\beta)}{2}\right) \times \rho \quad \textbf{(I.42)}$$

VIII.4.CAPDEROU Model

The CAPDEROU model **[36-37]** is based on the atmospheric turbidity factor. Turbidity factors express the absorption and scattering caused by atmospheric constituents. Using these factors, direct and diffuse irradiance under clear sky conditions can be expressed horizontally and on an inclined plane. Knowledge of the atmospheric turbidity factor is essential to determining global irradiance under clear sky conditions.

VIII.4.1 . Global illumination received on a horizontal surface according to the CAPDEROU model.

VIII.4.1.1- Direct radiation estimated by the CAPDEROU model.

The direct illumination under clear skies obtained on a horizontal plane is given by **[34],[28] :**

$$I=I_0 \times C_{ts} \times exp\left(-T_L \times \left(\left(0.9+\frac{9.4\times \sin(h)}{T_1}\right)^{-1}\right)\right) \times sin(h) \quad \textbf{(I.43)}$$

$$C_{ts} = (1 + 0.0334 \times cos\,(\frac{360}{365})\,(J-2)) \quad \textbf{(I.44)}$$

Where :

I_0**= 1533** , Solar Constant

C_{ts}**=** Correction factor for the average Earth-Sun distance (dimensionless).

h = The height of the sun (degrees).

δ **:** Solar declination (degrees).

φ: Longitude of the studied location (degrees).

T_L**:** Turbidity factor (dimensionless) .

VIII.4.1.2- Diffuse radiation on a horizontal plane by CAPDEROU model

$$D = I_0 \times C_t \times \exp(-1 + 1.06\log(\sin(h))) + a - \sqrt{a^2 + b^2}) \times \sin(h) \quad \textbf{(I.45)}$$

$$a = 1.1 \quad \text{and} \quad b = \log(T_L - T_0) - 2.8 + 1.02 \times (1 - sin(h))^2 \quad \textbf{(I.46)}$$

The total amount of light received on a horizontal surface is expressed by the following equation **[28]:**

$$G = I + D \quad \textbf{(I.47)}$$

G: Global radiation on horizontal surface (W/m²).

VIII.4.2- Global illumination received on an inclined surface according to the CAPDEROU model .

$$I = I_0 \times C_{ts} \times exp\left[-T_L \left(0.9 + \frac{9.4}{0.89^Z} \times \sin(h)\right)^{-1}\right] \times cos(i) \quad \textbf{(I.48)}$$

Direct illumination is the projection of the standard component onto an inclined plane.

***i* :** It is the angle of incidence formed by the direction of the incident solar rays, which is expected to the plane of the receiving surface. The following relation gives it:

$$\cos i = \cos \delta \times cos\ \omega \times \cos\ (L - \beta) + \sin\delta \times \sin(L - \beta) \quad \textbf{(I.49)}$$

Given that :

***ω* :** The hour angle

***β*:** The inclination of the plan

The diffuse illumination of the sky is composed of three parts:

VIII.4.2.1-Direct radiation:

It comes from the vicinity of the sun in a cone with a half-angle or apex between 3° and 15°, and it can also be considered as originating directly from the sun **[38],[17] .**

The following equation represents the direct component of the diffuse illumination.

$$S_d = I_0 \times C_{ts} \times \exp(-2.8 + \sin(h) + a - \sqrt{a^2 + 4b^2}) \quad \textbf{(I.50)}$$

In this case, the parameters **a** and **b** are given by the following equation (**I.49**):

$$b = \log(T_L - T_0) - 2.28 - 0.51 \times log(\sin(h)) \text{ and } a = 3.1 - 0.4b \quad \textbf{(I.51)}$$

VIII.4.2.2- Isotropic component : which corresponds to a sky of uniform luminance

$$S_i = D - S_d \times \sin(h) \quad \textbf{(I.52)}$$

D: is the diffuse illumination on a horizontal plane.

VIII.4.2.3 - Component of the horizon circle that comes from a horizon jump at a height of 60°, it is associated with an accumulation of aerosols in the lower atmospheric layers. In this case, the parameters a and b are given by:

$$\begin{cases} b = \exp(0.2 + 1.75\log(\sin(h))) \\ a = \log(T_L - T_0) - 3.1 - \log(\sin(h)) \end{cases} \quad \textbf{(I.53)}$$

$$\delta_h = I_0 \times C_{ts} \times \frac{-0.02a}{a^2+ab+1.8}\exp(\sin(h)) \quad \textbf{(I.54)}$$

$$d_{CIEL} = S_d \times \cos(i) + S_i \frac{1+\sin(\gamma)}{2} + \delta_h \cos(\gamma) \quad \textbf{(I.55)}$$

The sky diffuse is the diffuse illumination incident in the presence of the sky.

- The diffuse illumination of the ground is characterized by the albedo of the ground, which indicates the reflection of incident light for any given plan .

$$d_{SOL} = S_d \times \frac{1+\sin(\gamma)}{2} \quad \textbf{(I.56)}$$

$$S_d = \sigma G \quad \textbf{(I.57)}$$

With:

G: is the horizontal global illuminance.

σ **:** Soil albedo

- The retro-diffused diffuse lighting is the light that is diffusely re-emitted by the sky towards the ground. According to CAPDEROU'S reasoning, this component is calculated using the following formula **[38]:**

$$\delta_i = 0.9(\sigma - 0.2)G \times exp\left(-\frac{4}{\sqrt{T_L - T_0}}\right) \quad \textbf{(I.58)}$$

- The diffuse illumination incident on an inclined plan is given by:

$$D = d_{Ciel} + d_{Sol} + \delta_i \frac{1+\sin(\gamma)}{2} \quad \textbf{(I.59)}$$

- The global illumination incident, at a given moment, on a plan (α,γ) is :

$$G = I + D \quad \textbf{(I.60)}$$

VIII.5. Choosing the optimal inclination

The optimal angle for a solar energy capture system has been the subject of several proposals in the literature, which have been studied and implemented. Some of these proposals are presented in the references **[17],[39-44]** . In our study, the position of the meteorological station and the pyranometer device used to obtain accurate solar radiance data is close to the optimal angle for the region.

VIII.6. Simulation Flowchart of the empirical models(The three Empirical models).

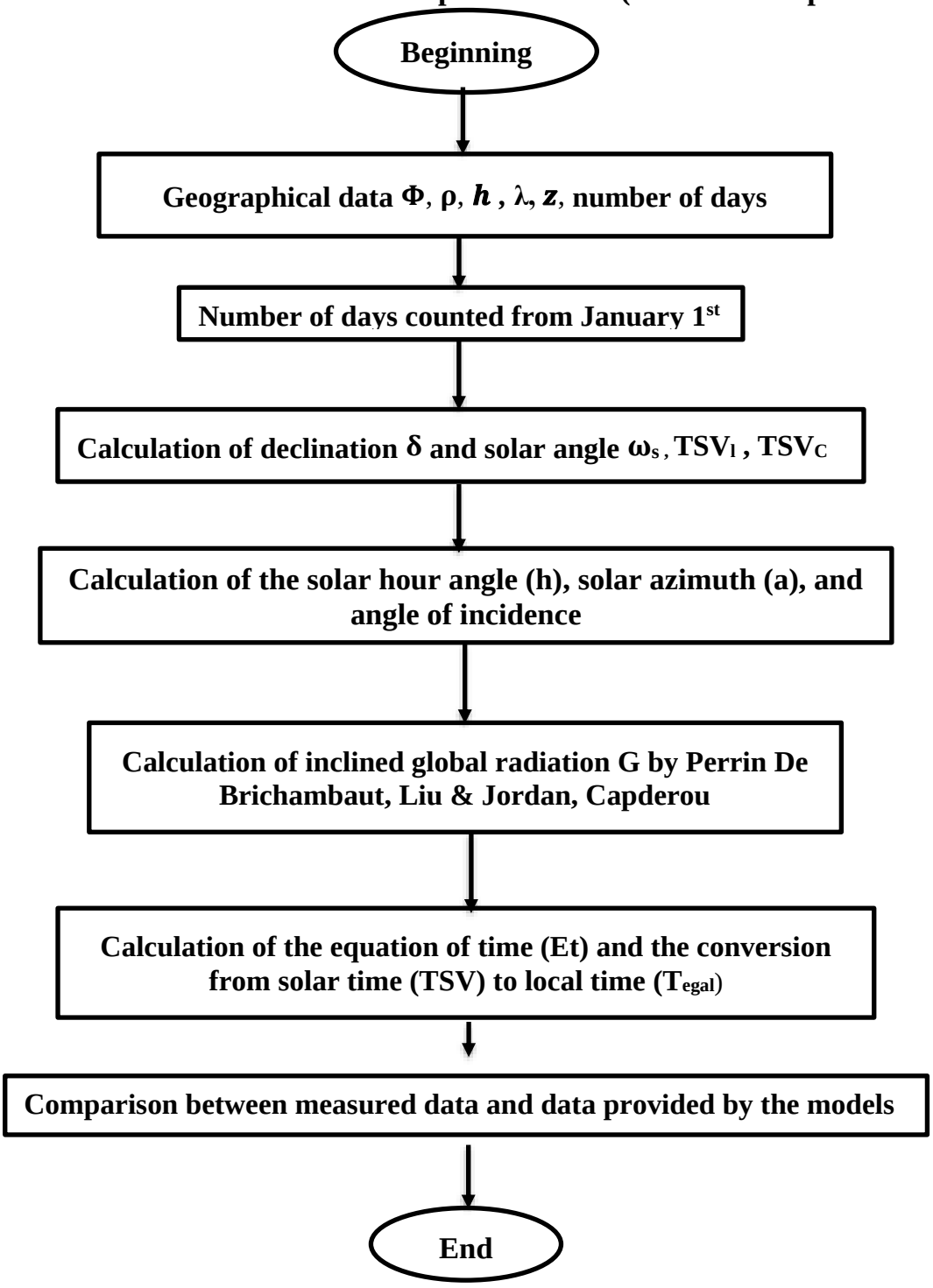

Fig. I.13. Flowchart of solar radiation estimation by three empirical methods.

IX. Software designed for the study of solar potential (estimated solar radiation).

There are many software programs designed for the study of solar deposit and the dimensioning of solar systems . Among these software programs, we mention a few in **Table I.4 [13].**

Table I.4: Common Software Tools for Solar Resource Assessment and System Design **[13].**

Software	Description
MATLAB	MATLAB is a powerful tool for studying solar radiance, as it provides a comprehensive environment for data analysis, modeling, and simulation. In the context of solar energy, MATLAB can be used to: Calculate Solar Irradiance: also calculate the amount of solar radiation (irradiance) received on different surfaces (inclined, tilted, or horizontal) by using empirical models that account for factors like the sun's position (solar zenith, azimuth angles) and atmospheric conditions.
SoDa (F)	Web service (from the Paris Mines School) for solar energy professionals. Climate database and solar irradiation on the planet with different applications.
METEONORM 5.0 (CH)	Software (from Meteotest) climatic data and solar irradiation calculated according to orientation and inclination. Downloadable software operating in demonstration mode for 10 days.
PVSOL (GE)	Software of Valentin, simulation program for photovoltaic installations. Possibility to download a demonstration version as well as the user manual
PVGIS	The free online application PVGIS is an excellent simulation tool that allows for the free calculation of the production of grid-connected photovoltaic systems in Europe and Africa (and also for off-grid sites in Africa only). With its integrated Google Maps interface, it is very easy to obtain the production data of a PV system based on the site's precise sunlight data (including distant shading related to the terrain, hills, and mountains).
RETScreen (CAN)	Free downloadable software on solar data, simulation of photovoltaic, thermal, passive systems and on GES emission

X. Estimation of Solar Radiation in the Study Region: Results and Analysis

We developed three MATLAB 8.1 programs to estimate incident radiation on a horizontal surface. For simplicity, we assume that the studied day reflects the meteorological conditions of the OUED-NECHOU region, located in Ghardaïa. The site is characterized by precise coordinates: 32°34'43.79" N latitude and 3°41'55.36" E longitude, at an elevation ranging from 450 to 566 meters**.**

X.1- Description of the Program and Calculation Methodology

To better understand the sequence of calculation steps followed in this work, a program was developed to first simulate the different solar angles by introducing all the geographic data (month, number of days, location, sky type, ground albedo or reflectivity, tilt angle, etc.). Then, a subprogram was created to calculate global radiation based on the empirical equations of the proposed estimation models. In this case, the program reads the geographic location data and calculates the inclined global solar radiation. Next, it converts the true solar time to real time using the equation of time to compare the experimental measurements with those obtained by the program. The calculation model allows for the visualization of global radiation evolution curves as a function of real time.

The estimation of these models is done in the **MATLAB 8.1** environment. We declare the number of days in the year, then we determine the astronomical data and the geographical data of the study location in order to calculate the hour angle and the height of the sun. Finally, to compare the simulation results with the experimental results, we need the conversion of the measurement time (local time) to the true solar time (TSV) using the equation of time.

X.2- Models Evaluation

To validate the solar radiation model, we compared solar radiation measurements obtained from the weather station's pyranometer, installed on the rooftop of the control room at the photovoltaic power plant with estimated values. Measurements were taken on four representative days, each corresponding to a different season. Data were recorded in real-time from sunrise (06:00 AM) to sunset (20:00 PM).

The following figures present comparative graphs of inclined global solar radiation predictions from the LIU & JORDAN, PERRIN DE BRICHAMBAUT , and CAPDEROU models alongside experimental data collected at the site.

To assess the models' accuracy, we propose using absolute and relative error curves, supported by four statistical indicators: mean absolute error (MAE) (W/m2), root mean square error (RMSE) (W/m^2), mean absolute percentage error (MAPE), and the coefficient of determination (R^2). These metrics quantify the deviation between measured and estimated values, enabling us to identify the model that most closely matches the actual solar radiation data. The ultimate objective is to validate the proposed models and determine the most accurate one for predicting solar irradiance **[45-52],[14].**

X.2.1-Absolute Error (AE)

Absolute error is a metric used to compare the accuracy of different models. It measures the difference between an observed or measured value and the actual value **[51-52].**

$$\textbf{Absolute error (AE) = Eabs= } | E_{measured} - E_{estimated} | \quad \textbf{(I.61)}$$

$E_{measured}$, $E_{estimated}$: are the instantaneous values of the measured and estimated radiation, respectively.

Plotting the absolute error curve allows us to visualize discrepancies and assess model performance effectively. By calculating absolute error, we can identify potential sources of error and improve estimation methods. It serves as a valuable tool for evaluating the quality of approximations and determining the level of confidence in the estimates.

X.2.2-Relative error or relative uncertainty (RE) or (RU).

The relative error represents the magnitude of the error relative to the measured quantity. The latter is generally expressed in %; the equation for the relative error is shown below **[14],[17].**

$$\textbf{Err} = \left(\frac{\Delta G}{G_{mes}}\right) \times 100\% = \left(\frac{G_{calculated} - G_{measured}}{G_{measured}}\right)) \times 100\% \quad \textbf{(I.62)}$$

Where:

ΔG : The difference between measured values and calculated values

G_{mes}: The measured value

X.2.3 - Mean absolute error (MAE)

MAE measures the average absolute difference between the predicted and actual values in a dataset. It provides an indication of the magnitude of errors made by a model, with a lower MAE value indicating better accuracy, and a higher value suggesting poorer accuracy.

$$\textbf{Absolute means of error (MAE)} = \frac{1}{N}\sum_{i=1}^{N} \boldsymbol{Eabs}(\boldsymbol{i})\ \% \qquad \textbf{(I.63)}$$

Where : N is the calculated **N-th** value

X.2.4- Root Mean Square Error (RMSE)

Is a commonly used metric to assess the performance of a regression model. It measures the average difference between the predicted and actual values of the target variable. A lower RMSE indicates a more accurate model, as it reflects more minor discrepancies between predicted and actual values. RMSE is always positive and provides insights into the short-term accuracy of a model **[45-52],[14].**

$$\textbf{RMSE} = \sqrt{\frac{\sum_{i=1}^{n}(G_e^i - G_m^i)}{n}} \qquad \textbf{(I.64)}$$

X.2.5 - Mean Absolute Percentage Error (MAPE)

MAPE (Mean absolute percentage error) measures the percentage difference between predicted and actual values. It serves as a general indicator of forecast accuracy, with lower values indicating better model performance. Typically, an MAPE value of less than 10% is considered acceptable, though this threshold may vary depending on the specific context and application **[45-52],[14].**

$$\textbf{MAPE} = \frac{1}{N}\sum_{i=1}^{n}\left|\frac{G_m^i - G_e^i}{G_m^i}\right| \qquad \textbf{(I.65)}$$

X.2.6 - Correlation Coefficient R^2 (CC)

The correlation coefficient **(CC)** is a statistical measure that indicates the degree of the linear relationship between two variables (**e.g.,** predicted and measured values). A correlation coefficient value closer to 1 indicates a stronger positive linear relationship meaning a better estimate. Conversely, values closer to -1 or 0 suggest weaker relationships or less reliable predictions **[45-52],[14].**

$$CC = 1 - \frac{\sum_{i=1}^{n}(G_m^i - G_e^i)}{\sum_{i=1}^{n}(G_m^i - \overline{G_m^i})} \quad \textbf{(I.66)}$$

- Where **n** indicates the number of observations

- G_m^i **:** The measured inclined global radiation values (W/m^2)

- G_e^i **:** The predicted or estimated inclined global radiation values (W/m^2).

- $\overline{G_m^i}$**:** The mean measured inclined global radiation (W/m^2).

XI. Resultats et interpretation

The irradiation measurement is performed and recorded using a pyranometer. This device generates a voltage proportional to the irradiation in W/m², allowing us to quantify the illumination on the inclined surface of the solar panels in our application. To validate the most accurate model, we compare three models with measurements obtained from the pyranometer installed on the rooftop of the OUED-NECHOU photovoltaic power plant, located in the center of Ghardaïa.

In the MATLAB environment, measurements are conducted on four specific days, each representing one of the four seasons: January 1st , May 1st , July 1st , and October 1st of the year 2016. Data is recorded in real-time at 4-minute intervals from sunrise at 06:00 AM to sunset at 20:00 PM. The following figures present comparative graphs of global inclined radiation at a 30° tilt angle, simulated using the PERRIN DE BRICHAMBAUT model, the empirical method of LIU & JORDAN, and the CAPDEROU model, compared with experimental data from the OUED-NECHOU site in Ghardaïa. The results are as follow

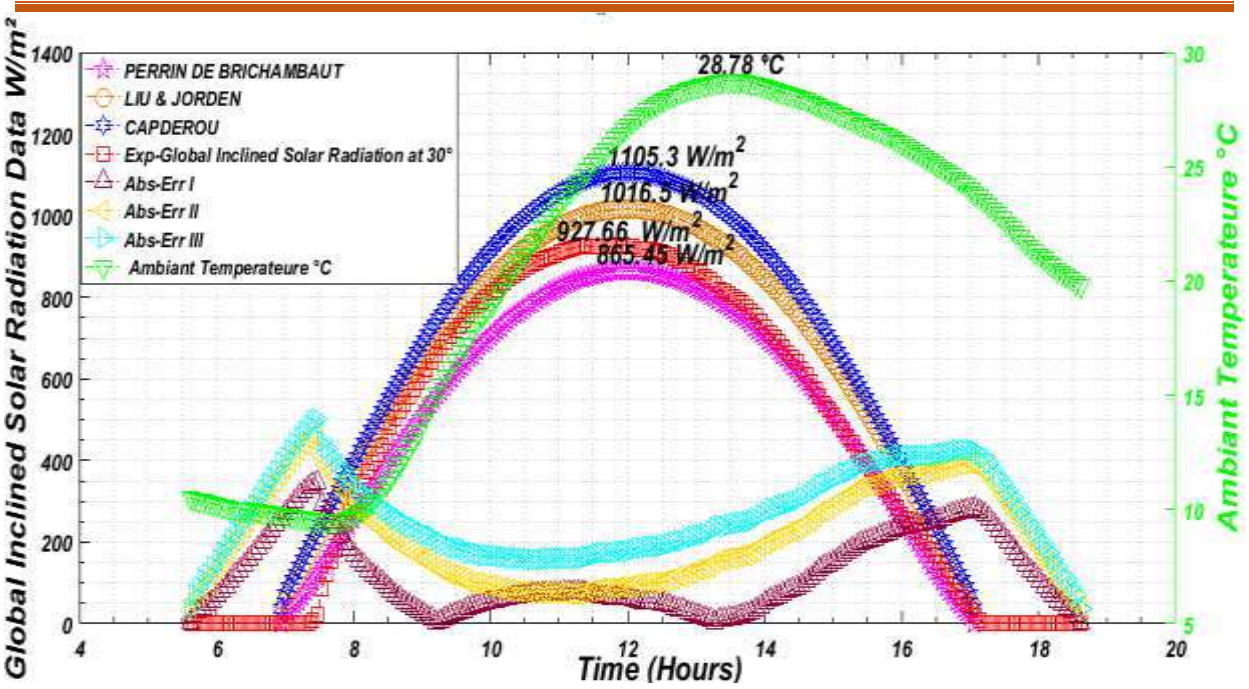

Fig I.14 : Comparison of Inclined Solar Radiation Estimates from Three Models with Experimental Data on January 1st , 2016 – A Winter Day.

Fig I.14. Compares three empirical models PERRIN DE BRICHAMBAUT, LIU & JORDAN , and CAPDEROU with experimental data for global inclined solar radiation. The analysis was conducted on January 1st , a winter day, covering the period from sunrise to sunset. The figure also illustrates the absolute error between the estimated values from each model and the measured data, providing a detailed evaluation of their accuracy.

The evaluation, conducted on January 1st from sunrise to sunset, indicates that the experimental curve reaches a peak of 865.45 W/m². Among the estimated models, the maximum values recorded are PERRIN DE BRICHAMBAUT at 927.66 W/m², LIU & JORDAN at 1016.5 W/m², and CAPDEROU at 1105.3 W/m². From this comparison, the PERRIN DE BRICHAMBAUT model provides the closest approximation, followed by LIU & JORDAN, while CAPDEROU exhibits the highest deviation. This trend suggests that PERRIN DE BRICHAMBAUT effectively captures the overall solar radiation variation throughout the day, particularly in the early morning and late afternoon. In contrast, LIU & JORDAN , and CAPDEROU underestimated the measured values, with CAPDEROU being the least accurate.

The absolute error curves provide further insight into the accuracy of each model. The absolute error of PERRIN DE BRICHAMBAUT**(Abs - Err I)** remains minimal in the morning and late afternoon but slightly increases around noon, reflecting a minor underestimation of peak values.

The absolute error of LIU & JORDAN **(Abs-Err II)** starts relatively low but increases significantly as solar radiation intensifies, indicating a consistent deviation throughout the day. The absolute error of CAPDEROU **(Abs-Err III)** exhibits the highest deviation, particularly during peak radiation hours, highlighting its lower accuracy compared to the other models.

The ambient temperature curve follows a smooth trend, peaking at 28.78°C, and there is a clear correlation between temperature increase and radiation intensity.

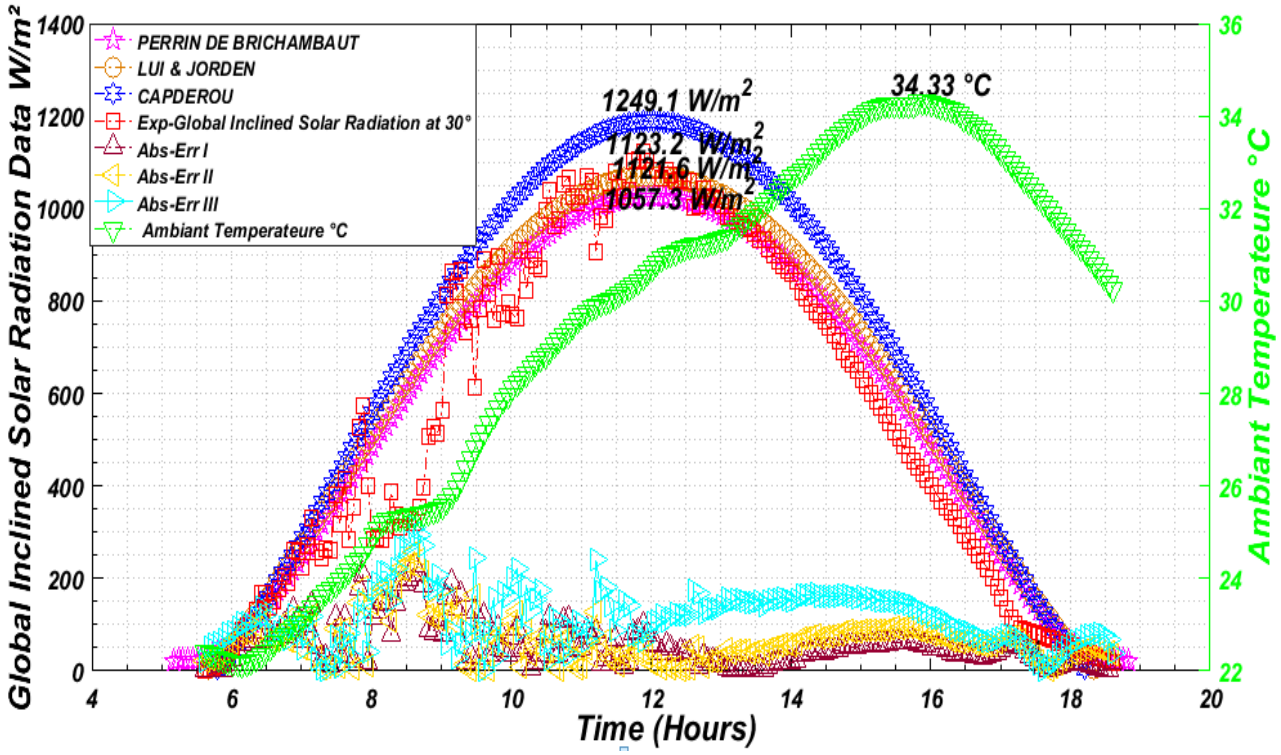

Fig I.15 : Comparison of Inclined Solar Radiation Estimates from Three Models with Experimental Data on May 1st , 2016 – A Spring Day.

A comparative assessment of three empirical models PERRIN DE BRICHAMBAUT**,** LIU & JORDEN, and CAPDEROU against experimental data for global inclined solar radiation at 30° is illustrated in **Fig I.15.** The study, conducted on May 1st (Spring season), examines solar radiation trends from sunrise to sunset, with a recorded peak ambient temperature of 34.33°C.

The experimental curve shows a smooth increase in solar radiation, peaking at 1121.6 W/m² around midday. Among the models, CAPDEROU provides the highest estimation, reaching 1249.1 W/m², which overestimates the experimental peak. LIU & JORDAN follows with a peak value of 1123.2 W/m², making it the closest to the experimental data, with a minimal deviation of 1.6 W/m².

PERRIN DE BRICHAMBAUT, on the other hand, exhibits the lowest estimation among the three, with a maximum of 1057.3 W/m², indicating a more conservative prediction of solar radiation. The ambient temperature curve in the experiment shows a steady rise throughout the day, reaching its peak at 34.33°C around midday. This temperature increase corresponds to the solar radiation peak, highlighting the strong relationship between solar energy and ambient temperature, particularly during midday hours.

While all models generally follow the experimental trend, their deviations are most pronounced during peak radiation hours. The absolute error analysis further supports this observation, as LIU & JORDAN 'S model demonstrates the smallest peak deviation, confirming its higher accuracy in estimating maximum radiation values. CAPDEROU 's model, despite following the experimental curve closely, significantly overestimates peak irradiance. PERRIN DE BRICHAMBAUT 'S model , although consistently underestimating radiation values, maintains a more stable error distribution throughout the day.

Consequently, LIU & JORDAN emerges as the most reliable model for this dataset, given its closest match to the experimental peak and overall better agreement with measured values ..

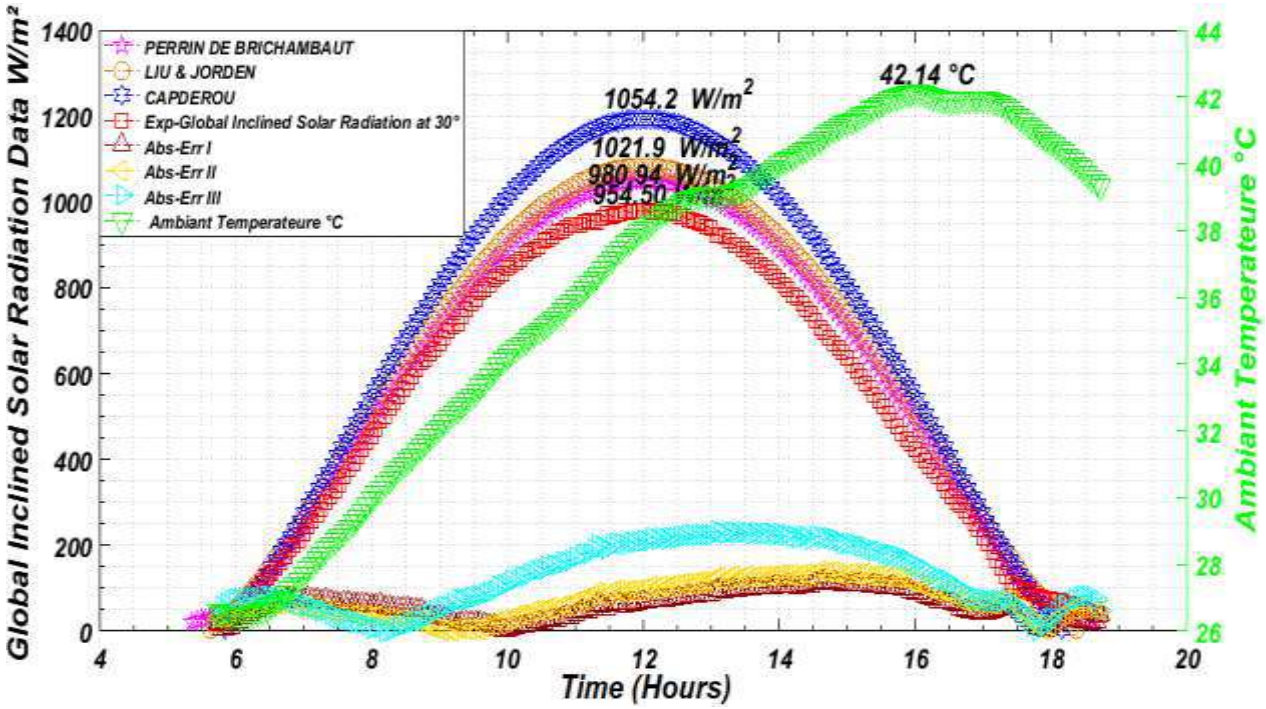

Fig. I.16 : Comparison of Inclined Solar Radiation Estimates from Three Models with Experimental Data on July 1st , 2016 – A Summer Day.

Fig I.16. Illustrates a comparative assessment of three empirical models PERRIN DE BRICHAMBAUT**,** LIU & JORDAN, and CAPDEROU evaluated against experimental measurements of global inclined solar radiation at 30° on July 1st . This Summer day study examines how well each model aligns with real-world data over the entire diurnal cycle, during which ambient temperature peaked at 42.14 °C.

The experimental data indicates a maximum solar radiation value of 954.50 W/m² around midday. Among the models, PERRIN DE BRICHAMBAUT provides the closest estimate, reaching 980.94 W/m², making it the most accurate model in this case. Its slight overestimation remains within an acceptable range, reinforcing its reliability. CAPDEROU follows with a peak value of 1021.9 W/m², slightly overpredicting radiation levels, while LIU & JORDAN records the highest estimate at 1054.2 W/m²,showing the greatest deviation from the experimental data.

The absolute error curves further highlight these deviations by quantifying the difference between the modeled and experimental values. The errors tend to be higher around midday, corresponding to the peak solar radiation period, where the empirical models generally overestimate the actual measured values. However, PERRIN DE BRICHAMBAUT maintains the lowest absolute error throughout most of the day, reinforcing its reliability in this case.

The ambient temperature curve shows a steady increase throughout the morning, reaching a maximum of 42.14°C in the early afternoon before gradually declining. This temperature trend is significant, as higher ambient temperatures influence photovoltaic performance by increasing thermal losses, which can reduce overall energy conversion efficiency. Understanding these variations is crucial for optimizing PV system performance under varying climatic conditions.

PERRIN DE BRICHAMBAUT stands out as the most accurate model, closely aligning with experimental data. LIU & JORDAN show better correspondence with measured values during sunrise and sunset, whereas CAPDEROU consistently overestimates solar radiation, especially around midday. Despite these differences, all three models effectively represent the daily solar radiation trend, offering valuable insights for estimating solar energy.

.

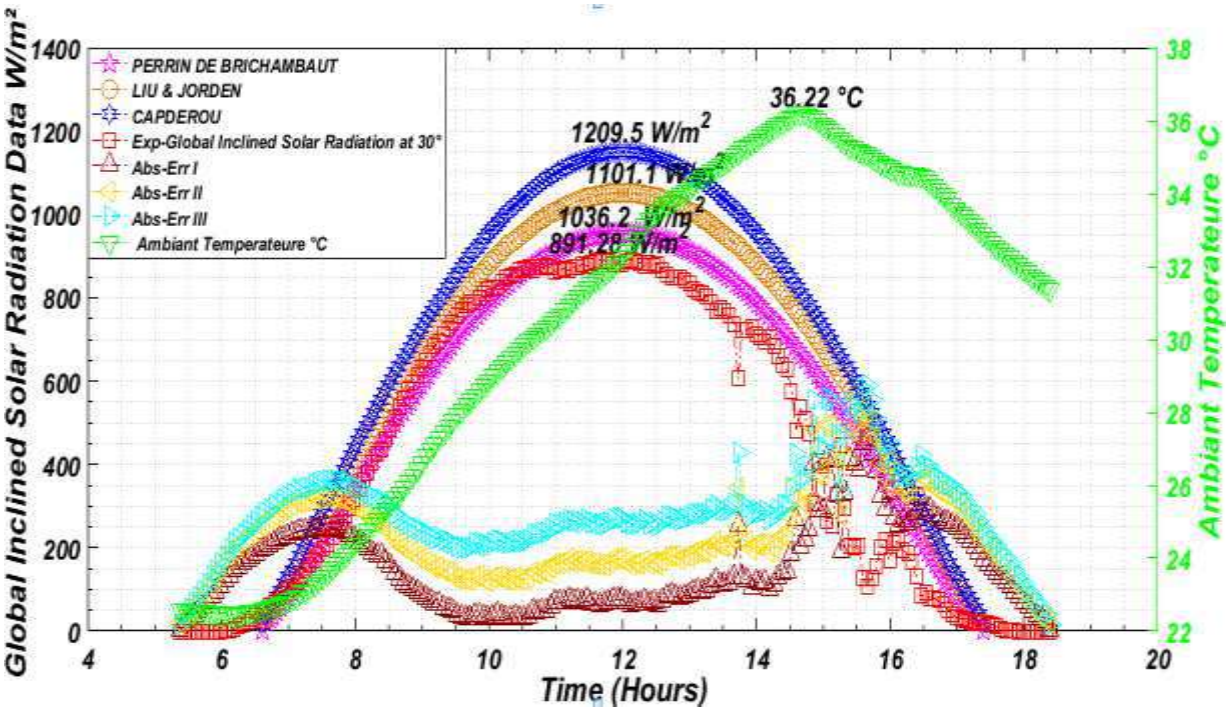

Fig I.17 : Comparison of Inclined Solar Radiation Estimates from Three Models with Experimental Data on October 1st , 2016 A Fall Day.

Fig I.17, presents a comparative analysis of three empirical models: PERRIN DE BRICHAMBAUT , LIU & JORDAN, and CAPDEROU, against experimental data for global inclined solar radiation at a 30° tilt on July 1st , which is a Full day. The data covers the entire diurnal cycle from sunrise to sunset, illustrating the variations in solar radiation and ambient temperature throughout the day **.**

The experimental solar radiation curve follows a steady increase in the morning, reaching a peak of 891.4 W/m² around midday before gradually declining toward sunset. Among the empirical models, CAPDEROU provides the highest estimation, with a peak of 1209.5 W/m², significantly overestimating the experimental peak. LIU & JORDAN follows with a peak of 1101.1 W/m², still overestimating the measured values. PERRIN DE BRICHAMBAUT , however, is the closest to the experimental data, peaking at 1036.2 W/m², making it the most reliable model in this case. Although it slightly overestimates the experimental values, its deviation is much smaller compared to the other two models, particularly during peak radiation hours .

The absolute error analysis confirms that PERRIN DE BRICHAMBAUT exhibits the lowest overall deviation, making it the best-performing model for this dataset.

LIU & JORDAN, while providing reasonable estimates, still shows noticeable overestimation, whereas CAPDEROU consistently predicts the highest radiation levels, leading to larger discrepancies with experimental data.

The ambient temperature curve shows a steady increase throughout the morning, reaching a maximum of 36.22°C in the early afternoon before gradually declining. This temperature trend is significant as higher ambient temperatures influence photovoltaic performance by increasing thermal losses, which can reduce overall energy conversion efficiency.

Overall, PERRIN DE BRICHAMBAUT demonstrates the highest accuracy in this case, closely aligning with the experimental data. At the same time, LIU & JORDAN , and CAPDEROU exhibit more significant deviations, especially during peak radiation hours.

In this section, we present the instantaneous relative error (RE %) curve to evaluate the accuracy of the empirical models used for solar irradiance estimation, as shown in the figures below. This study is based on precise data collected over four experimental days, where we compare estimated irradiance values with measured ones to identify deviations over time. By analyzing these variations, we assess the reliability of different models under real-world conditions, offering insights into their applicability for evaluating photovoltaic performance. Photovoltaic performance. This validation is essential for selecting the most reliable empirical models for the region, particularly in the absence of a local meteorological station. This ensures accurate solar resource estimation for photovoltaic applications.

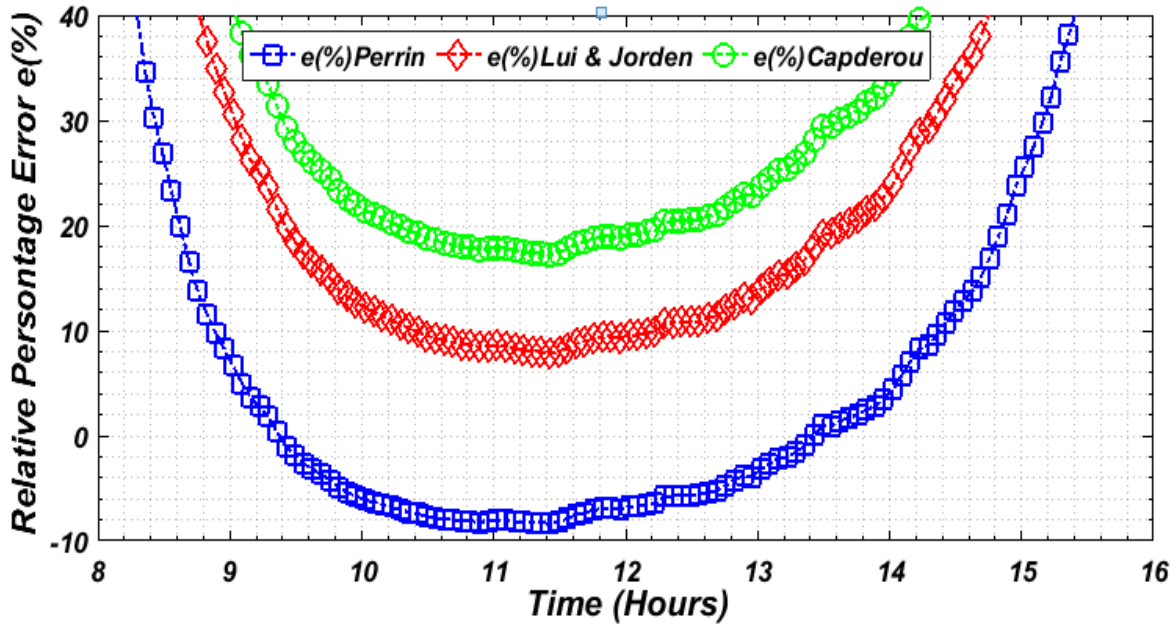

Fig. I.18: Instantaneous Relative Error Curve for January 1st , 2016.

The instantaneous relative percentage error **(**e%**)** curves illustrate the accuracy of three empirical models (PERRIN DE BRICHAMBAUT , LIU & JORDEN , and CAPDEROU) in estimating solar irradiance compared to experimental data on the measured day (January 1st,2016) **.** The Perrin model (blue curve**)** demonstrates the highest accuracy, with an error dropping to approximately -8% at 12:00 PM**,** though it exceeds 35% in the early morning and late afternoon**.** The LIU & JORDEN model (red curve) has a minimum error of around 8% at noon**,** while its deviations increase to 30% at lower solar angles**.** The CAPDEROU model (green curve) shows the largest discrepancies, with an error of about 18% at noon**,** rising above 35% in the morning and afternoon**.** All models exhibit their lowest error around solar noon**,** with increasing deviations during periods of low solar angles. Among them, the Perrin model proves to be the most reliable**,** showing the smallest deviations from the experimental data on the measured day**.**

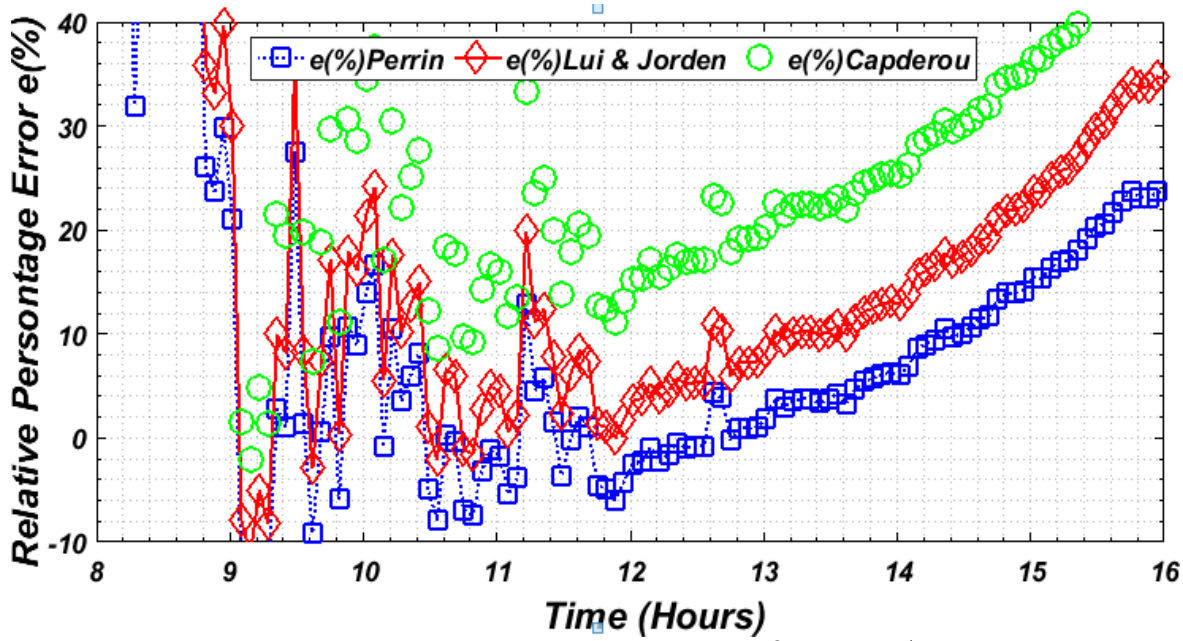

Fig I. 19 : Instantaneous Relative Error Curve for May 1st , 2016.

On May 1st , 2016, the PERRIN DE BRAICHAMBAUT model demonstrates a relative error ranging from approximately -8% at noon to over 30% during early morning and late afternoon. The model provides a relatively good estimation at noon, but its accuracy decreases significantly during periods of lower solar radiation. The LIU & JORDEN model maintains errors between 0% and 30%, showing a more stable trend but still presenting notable discrepancies, particularly in the afternoon. The CAPDEROU model shows relative errors from -1% to 35%, occasionally aligning closely with the experimental data but generally overestimating solar radiation, especially after midday. Overall, while all models tend to overestimate solar radiation, PERRIN DE BRAICHAMBAUT offers the closest approximation at noon.

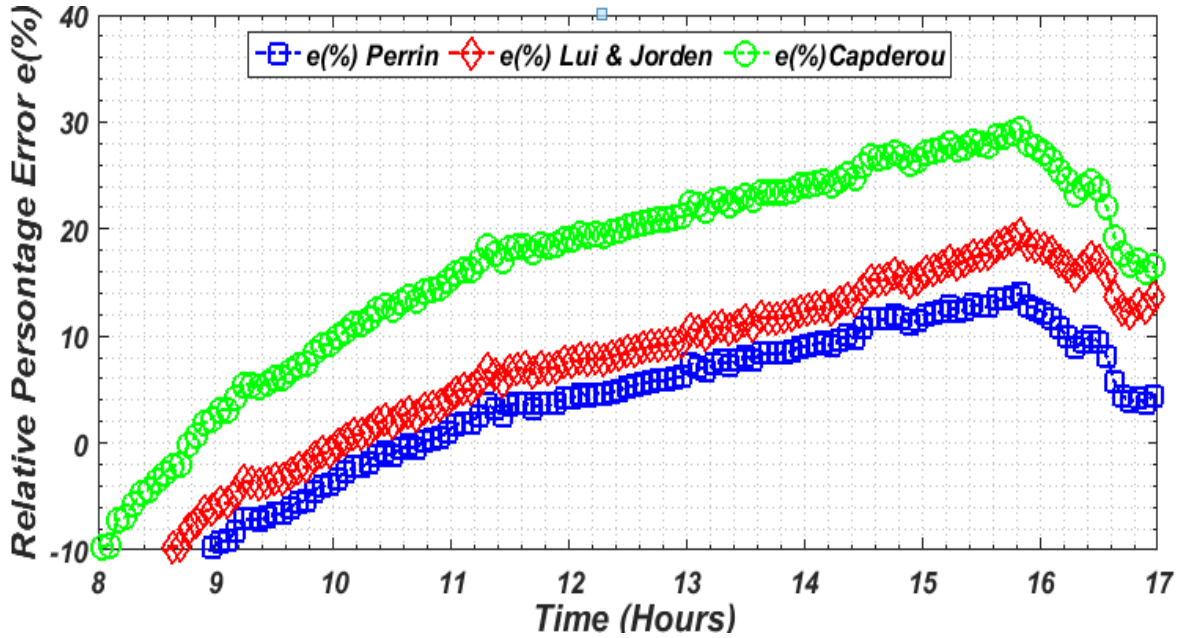

Fig.I.20 : Instantaneous Relative Error Curve for July 1st , 2016.

On July 1st , 2016**,** all three empirical models PERRIN DE BRICHAMBAUT, LIU & JORDEN, and CAPDEROU, started with a relative error of -10% at 8:00 AM, indicating an initial underestimation of solar radiation. As solar radiation intensifies, the errors increase for all models. The Perrin model exhibits the least deviation, stabilizing near 0% at noon and peaking at 10% in the late afternoon, demonstrating a balanced estimation. The LIU & JORDEN model follows a similar trend but shows slightly higher errors, exceeding 20% in the afternoon, indicating a moderate overestimation. Meanwhile, the CAPDEROU model consistently exhibits the highest errors, rising from -10% in the morning to over 20% by midday and peaking above 35% in the late afternoon, particularly during peak irradiance. Overall, while all models follow a similar trend, the PERRIN DE BRICHAMBAUT model provides the most accurate and stable estimation, making it the most reliable for this dataset.

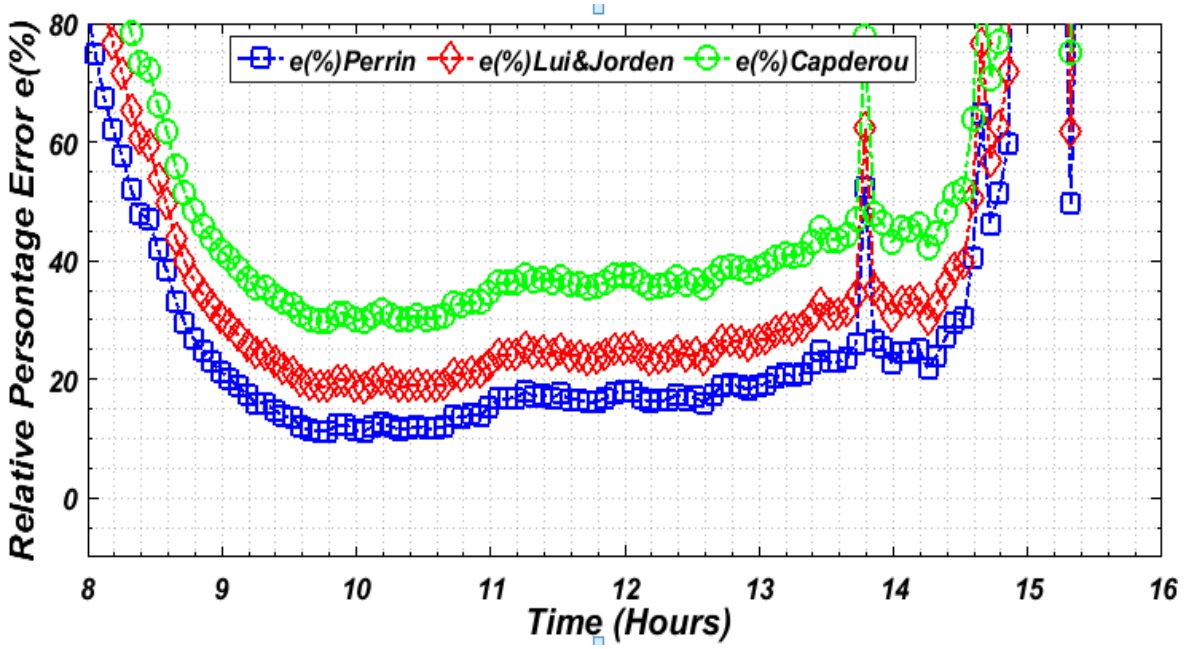

Fig. I.21 : Instantaneous Relative Error Curve for October 1st , 2016.

On October 1st , 2016, the PERRIN DE BRCIHAMBAUT, LIU & JORDEN, and CAPDEROU models exhibited significant relative errors in estimating solar radiation throughout the day. All three models start with high initial errors exceeding 60% at 8:00 AM, indicating a substantial overestimation during early morning hours. As the day progresses, the errors decrease, reaching their lowest values around midday, where the PERRIN model stabilizes around 10**%,** while LIU & JORDEN remains near 20% and CAPDEROU exceeds 30%. After noon, the errors gradually increase again, particularly in the afternoon, where fluctuations become more pronounced. Notably, a sharp rise in relative errors occurs after 2:00 PM, suggesting more significant deviations in model estimations during lower solar radiation periods.

Among the three models, PERRIN consistently shows the lowest error values, followed by LIU & JORDEN, while CAPDEROU exhibits the highest deviations**,** indicating that Perrin provides the most reliable estimation for this dataset.

The primary objective of this study is to evaluate the accuracy of three empirical models in the OUED-NECHO region. To accomplish this, we utilize various statistical tests over four designated test days. These tests include the absolute error (AE) curve, mean absolute error (MAE), root mean square error (RMSE), mean absolute percent error (MAPE), and the coefficient of determination (R^2), as shown in **Table I.5** .

The AE curve, which visually depicts the difference between the estimated and observed data, proves to be particularly useful. To demonstrate its significance, we present the AE curve alongside the estimated and experimental data for inclined solar radiation measured on January 1st , May 1st , July 1st , and October 1st , 2016.

Table I.5: Statistical Test Results of the Three Empirical Models on January 1st , 2016.

Day	Empirical models	MAE (W/m^2)	RMSE (W/m2)	MAPE (%)	CC
January 1st,2016	Perrin De Brichambaut	97.0995	7.3320	1.1240	0.9963
	Lui & Jorden	103.5828	10.7183	2.1323	0.9332
	Capderou	153.2530	17.6439	4.325	0.95213

Table I.6: Statistical Test Results of the Three Empirical Models on May 1st , 2016.

Day	Empirical models	MAE (W/m^2)	RMSE (W/m2)	MAPE (%)	CC
May 1st ,2016	Perrin De Brichambaut	55.5830	4.2737	0.8925	0.9112
	Lui & Jorden	66.2512	5.0293	1.2256	0.9366
	Capderou	89.3325	11.2523	1.7855	0.9255

Table I.7: Statistical Test Results of the Three Empirical Models on July 1st , 2016.

Day	Empirical models	MAE (W/m^2)	RMSE (W/m2)	MAPE (%)	CC
July 1st ,2016	Perrin De Brichambaut	76.2552	3.2261	3.3321	0.9965
	Lui & Jorden	77.3393	6.4132	11.251	0.9888
	Capderou	88.6321	10.225	21.225	0.9443

Table I.8: Statistical Test Results of the Three Empirical Models on October 1st , 2016.

Day	Empirical models	MAE (W/m²)	RMSE (W/m2)	MAPE (%)	CC
Octobre 1st ,2016	Perrin De Brichambaut	101.2542	6.3258	2.6544	0.9885
	Lui & Jorden	152.336	8.2236	5.1248	0.8993
	Capderou	155.25	10.2547	7.2143	0.9012

➢ **Table I.5** presents statistical indicators as of January 1st , 2016. The mean absolute error was lowest for PERRIN DE BRICHAMBAUT at 97.0995 W/m². In comparison, LIU & JORDEN recorded a mean absolute error of 103.5828 W/m², while CAPDEROU showed a higher deviation at 153.2530 W/m². Additionally, the mean root mean square error (RMSE) values were notably higher for CAPDEROU, which reached 17.6439 W/m². LIU & JORDEN reported an RMSE of 10.7183 W/m², while PERRIN DE BRICHAMBAUT achieved the lowest RMSE value of 7.3320 W/m², indicating the highest accuracy among the three. In terms of Mean Absolute Percentage Error (MAPE), PERRIN DE BRICHAMBAUT achieved the best result with an error rate of 1.1240%. This was followed by LIU & JORDEN at 2.1323%, while CAPDEROU exhibited the highest percentage error at 4.325%. PERRIN DE BRICHAMBAUT provides the most reliable estimation, as it has the lowest MAPE, indicating minimal deviation from observed values. When examining the Correlation Coefficient (CC), all three models demonstrated strong performance. PERRIN DE BRICHAMBAUT had the highest correlation at 0.9963, followed by CAPDEROU, which had a value of 0.95213, and LIU & JORDEN at 0.9332. This confirms their strong relationships with the observed values.

On May 1st , 2016, in the table I.6 , an evaluation was conducted on three empirical models PERRIN DE BRICHAMBAUT, LIU & JORDEN, and CAPDEROU-using various statistical metrics, including Mean Absolute Error (MAE), Root Mean Square Error (RMSE), Mean Absolute Percentage Error (MAPE), and Correlation Coefficient (CC). Among these models, PERRIN DE BRICHAMBAUT demonstrated the best performance with the lowest Mean Absolute Error (MAE) of 55.5830 W/m², indicating the least deviation from observed values. LIU & JORDEN followed with an MAE of 66.2512 W/m², while CAPDEROU had the highest MAE at 89.3325 W/m², reflecting greater discrepancies between the predicted and observed values.

For the Root Mean Square Error (RMSE), which emphasizes greater errors more significantly, PERRIN DE BRICHAMBAUT demonstrated the best performance with the lowest RMSE of 4.2737 W/m². LIU & JORDEN recorded an RMSE of 5.0293 W/m², while CAPDEROU had the highest RMSE at 11.2523 W/m², indicating greater deviations in its predictions. In terms of the Mean Absolute Percentage Error (MAPE), PERRIN DE BRICHAMBAUT achieved the most accurate result with an error rate of 0.8925%. LIU & JORDEN followed with a MAPE of 1.2256%. In contrast, CAPDEROU reported the highest MAPE at 1.7855%, suggesting lower accuracy in its predictions. Regarding the Correlation Coefficient (CC), which measures the strength of the relationship between predicted and observed values, LIU & JORDEN exhibited the highest correlation at 0.9366, followed closely by CAPDEROU at 0.9255. PERRIN DE BRICHAMBAUT recorded a slightly lower CC of 0.9112. Nevertheless, all three models demonstrated strong correlations with the observed data.

- The statistical evaluation of the three empirical models conducted on July 1st , 2016, in **Table I.7**, shows significant differences in their predictive accuracy. Among these models, PERRIN DE BRICHAMBAUT demonstrated the best overall performance, achieving the lowest Mean Absolute Error (MAE) of 76.2552 W/m², a Root Mean Square Error (RMSE) of 3.2261 W/m², and a Mean Absolute Percentage Error (MAPE) of 3.3321%. These results indicate a high level of accuracy in its estimations. Additionally, this model recorded the highest Correlation Coefficient (CC) of 0.9965, suggesting a strong agreement between the predicted and observed values.

- LIU & JORDEN exhibited slightly higher error values, with a Mean Absolute Error (MAE) of 77.3393 W/m², a Root Mean Square Error (RMSE) of 6.4132 W/m², and a Mean Absolute Percentage Error (MAPE) of 11.251%. These figures indicate moderate predictive accuracy. The correlation coefficient (CC) of 0.9888 confirms a strong correlation, although it is slightly lower than that of Perrin De Brichambaut. In contrast, CAPDEROU demonstrated the weakest performance among the three models, with the highest error values: an MAE of 88.6321 W/m², an RMSE of 10.225 W/m², and a MAPE of 21.225%. This suggests larger deviations in its predictions. Additionally, the lowest CC of 0.9443 indicates a weaker correlation between the predicted and observed values compared to the other models.

➢ On October 1st , 2016, in the **table I.8**, PERRIN DE BRICHAMBAUT demonstrated the highest predictive accuracy, exhibiting the lowest error values (MAE = 101.2542 W/m², RMSE = 6.3258 W/m², and MAPE = 2.6544%). Its correlation coefficient (CC = 0.9885) confirms a strong relationship between predicted and observed values, reinforcing its reliability. In contrast, LIU & JORDEN showed higher error values (MAE = 152.336 W/m², RMSE = 8.2236 W/m², and MAPE = 5.1248%), indicating moderate predictive accuracy. The CC of 0.8993 suggests a weaker correlation than Perrin De Brichambaut, reflecting greater deviations in its predictions.

➢ Among the three models, CAPDEROU exhibited the weakest performance, recording the highest error values (MAE = 155.25 W/m², RMSE = 10.2547 W/m², and MAPE = 7.2143%). Additionally, the lowest CC of 0.9012 indicates a weaker correlation between predicted and observed values compared to the other models .

XII. Conclusion

This study evaluates the accuracy of three empirical models-PERRIN DE BRICHAMBAUT, LIU & JORDEN, and CAPDEROU-for estimating global solar irradiance on a 30° inclined surface in the OUED-NECHOU region of Ghardaïa. Experimental measurements were collected from a rooftop pyranometer on four representative days corresponding to winter, spring, summer, and fall (January 1st , May 1st , July 1st , and October 1st , 2016).

Statistical analysis using Mean Absolute Error (MAE), Root Mean Square Error (RMSE), Correlation Coefficient (CC), Mean Absolute Percentage Error (MAPE), as well as Absolute Error (AE) and Relative Error (RE) curves, confirmed the reliability of the models under clear sky conditions. The PERRIN DE BRICHAMBAUT model exhibited the highest accuracy, particularly during peak irradiance hours, while LIU & JORDEN better captured sunrise and sunset variations. The CAPDEROU model generally underestimated solar irradiance, showing a more conservative prediction.

Overall, the findings demonstrate that the PERRIN DE BRICHAMBAUT model is the most suitable for estimating inclined solar irradiance in the OUED-NECHOU region and similar hot, arid climates. These models provide reliable solar radiation estimates even in the absence of pyranometer measurements, enabling effective solar resource assessment where radiometric stations are limited.

CHAPTER II

PHOTOVOLTAIC CELLS

I. Introduction

Future energy production poses a significant challenge due to continued reliance on carbon-based fuels, which result in higher greenhouse gas emissions and progressive resource depletion. These environmental and economic concerns have accelerated the development of sustainable solutions and the adoption of renewable energy technologies.

Solar energy is a rapidly growing and reliable power source. The Sun delivers approximately 1367 W/m^2 at the top of Earth's atmosphere, with nearly 1.8×10^{11} MW absorbed globally - far exceeding current electricity demand. Solar photovoltaic (PV) technologies provide an effective, scalable, and reliable method for converting this abundant resource into clean electricity.

This chapter provides an analytical overview of current solar cell technologies, emphasizing their efficiency, lifetime, advantages, and limitations**.** It further reviews the historical development of solar cells and concludes with a comparative assessment highlighting the suitability of each technology for different applications.

II. A Brief History and Development of Solar Cells

Since the beginning of time, people have considered the sun as a divine entity and a representation of the force that sustains all life on earth. Later, as the industrial and learning eras developed, people came to understand that the sun was a source of energy. When it has been established that the exploitation of fossil fuels for energy generation influences global temperatures, the significance of such a finding has peaked. On an energy day, the sun provides 10,000 times the amount of energy required on Earth. Ancient human civilizations relied on water, wind and bioenergy as energy sources all of which ultimately originated from solar energy in some form **[53] .**

In 1839, Alexandre Edmund Becquerel created the first solar power cell by coating platinum electrodes with silver chloride or silver bromide (Fonash, 2010) **[54].** Decades later, in 1882, Charles Fritts developed the first workable photovoltaic (PV) cell using selenium as a photosensitive material. Although it was expensive, it had only a 1% efficiency (Czochralski, 1918) **[55].** In 1916, polish chemist Jan Czochralski created a method, now known as the Czochralski technique, to cultivate single-crystal semiconductor materials (Chapin et al., 1954) **[56].** In 1954, a group of researchers at Bell Laboratories in the United States used the Czochralski process to create the first usable crystalline silicon solar cell, which had an efficiency of about 6% (Loff, 2023) **[57].** Solar cells became increasingly important in 1958 when they were incorporated into Vanguard-1, the first satellite powered by solar energy (Yamaguchi et al., 2021) **[58],** Launched by the United States Space Agency (NASA). Initially, NASA was hesitant about the advantages and necessity of solar power systems for its extraterrestrial products **[59].** Although this novel method of power generation resulted in multiple successful missions, it also provided solar panels with an opportunity to demonstrate their effectiveness. After two months, the Russian space program launched Sputnik-3, a satellite powered by photovoltaic solar energy. Since then, photovoltaic power sources have become crucial for space projects **[60-62].** This progression is elaborated further in Table 1, which outlines essential dates related to the development of photovoltaic (PV) solar energy technology.

Table II.1 : Key Dates in Photovoltaic Solar Energy Conversion .

Year	Scientists and innovation
1839	Becquerel discovers the photovoltaic effect
1876	Adams and Day notice photovoltaic effect in selenium
1900	Planck claims the quantum nature of light
1930	Wilson proposes Quantum theory of solids
1940	Mott and Schottky develop the theory of solid-state rectifier (diode)
1949	Bardeen, Brattain and Shockley invent the transistor
1954	Charpin, Fuller and Pearson announce 6% efficient silicon solar cell
1954	Reynolds et al. highlight solar cell based on cadmium sulphide
1958	First use of solar cells on an orbiting satellite Vanguard 1

As the power conversion component of a PV system with real-world applications, the creation of the first silicon solar cell marked a turning point in the development of solar technologies. These silicon cells are put together into modules rather than being utilized separately. Even though there are many different kinds of solar cells on the market today, research and development activities are still being conducted to improve and expand these energy gatherers.

The competition to explore space was unquestionably a significant factor in the advancement of photovoltaic technology **[60-62].** Achieving public applications was always a goal. However, the lack of optimized manufacturing processes and, consequently, the high cost of commercialization were the main barriers to this progress. Joseph Lindmeyer, a Communications Satellite Corporation (Comsat) employee, created a method in the 1970s that boosts silicon solar cells' efficiency by 50%. Lindmeyer departed from the company in 1973 and, along with Peter Varadi, co-founded Solarex, aiming to develop solar cells for public applications. Although Comsat owned the patent for this process and not Lindmeyer or Solarex, by 1980, Solarex held approximately 50% of the photovoltaic industry market. Although a modest market, it has been expanding due to the oil crisis since 1973, a few months after Solarex was founded **[60-61].**

The scientific community became more interested in photovoltaic technology as a result of this issue. In an effort to lower production costs, new technologies emerged that used novel and varied materials intended to lower the cost of manufacturing. A monocrystalline silicon, was utilized until 1973. After that, poly-Si and a-Si, took the market by storm because their techniques were less expensive and more straightforward **[60-61], [63].** Since then, photovoltaic technology has been enhanced through various techniques. New solar

cells have emerged, leading to the classification of these cells into two and later into three different generations **[63-66].** Currently, some researchers and manufacturers are advocating a new division, leading to the creation of a fourth. These research papers **[65 – 68]** also evidently show that the materials and production methods are the source of these generational classifications.

Additionally, advancements in areas like electronics, photonics, and quantum mechanics have enhanced photovoltaic cells. Flexible solar cells and even painted solar cells are now possible **[67],[69–71].**

The NREL (National Renewable Energy Laboratory) highlights advancements in the efficiency of various solar cell technologies **[63].** This chart is frequently presented and referenced in various research works, and it is organized and updated by the NREL. NREL maintains a chart showcasing the highest confirmed conversion efficiencies for various research cells, covering a range of photovoltaic technologies from 1976 to the present **[63].** This chart will be examined and discussed in the following sections. A comparison of various technologies and generations will follow. However, it is already clear that the field of photovoltaic technology research has been particularly noteworthy over the decades, especially in the past ten years, as indicated by the increasing milestones on the NREL chart.

The evolution of materials and structures will determine how far this technology may advance, but maintaining maximum power at the lowest possible cost will always be the aim. Moreover, the perception of a photovoltaic system has evolved to encompass not only the photovoltaic cells themselves but also key components such as inverters, batteries, and the cables used to connect these elements **[72–75].** Improvements in any of these devices contributed to enhanced system efficiency, which in turn improves the overall benefits of photovoltaic technology.

III. Operating Principles of Solar Cells

In Photovoltaic (PV) technology is pivotal in harnessing solar energy to meet the global demand for sustainable and clean energy. At its core lies the PV cell, the fundamental unit responsible for converting sunlight into electrical energy through the photovoltaic effect a phenomenon combining physical and chemical principles. When sunlight strikes a solar cell, photons are absorbed by silicon layers, exciting electrons to higher energy states.

The energy dissipated as heat during this process allows electrons to return to their ground state, enabling current generation. This mechanism relies on the chemical bonds within the silicon matrix. A typical solar cell comprises two silicon layers: one doped with boron to create a p-type region and another doped with phosphorus to establish an n-type region (**Fig II.1**) **[76].**

The photovoltaic effect drives the generation of direct current (DC) electricity by forming electron-hole pairs in the semiconductor material. The depletion region, enriched with minority carriers, facilitates the movement of these carriers toward quasi-neutral regions. This movement generates a photo-generated current **[77].**

To utilize the generated energy, a load is connected across the p-n junction electrodes, allowing current flow. As the current flows, the potential difference across the load decreases, which leads to an increase in the recombination current and a corresponding reduction in the electrostatic potential of the depletion region **[76].**

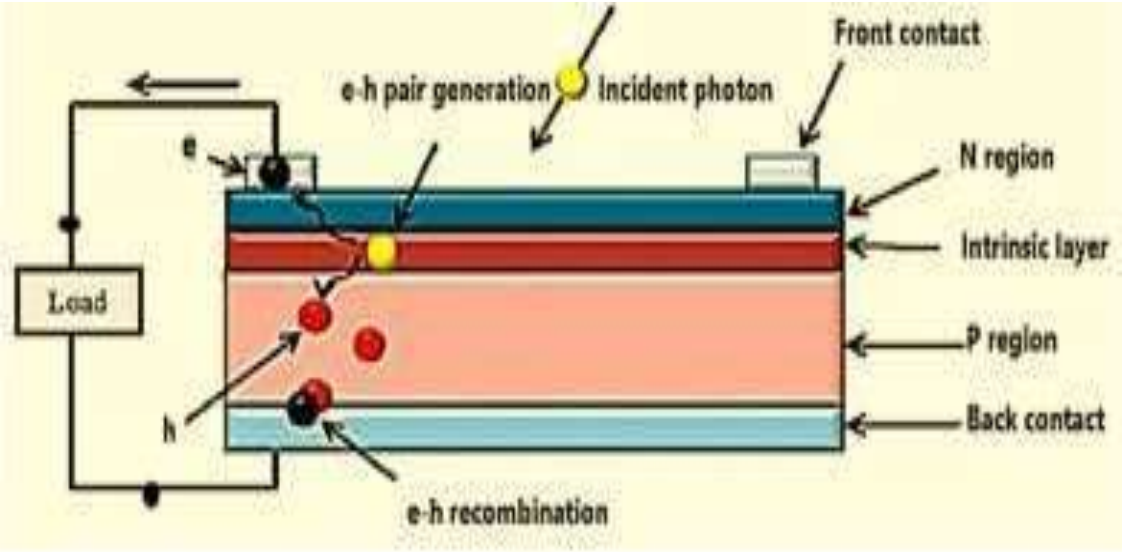

Fig II .1. Fundamentals of Solar Cells: The p-n Junction PV Cell **[78].**

Commonly referred to as photoelectric cells, solar cells are characterized by their electrical properties, such as power, voltage, and current. To enhance energy output and meet practical power demands, multiple solar cells are interconnected to form a solar module, also known as a solar panel. Typically, a single solar cell generates a maximum open-circuit voltage of 0.6 V and a short-circuit current of 7.34 A.

To enhance energy output and meet practical power demands, multiple solar cells are interconnected to form a solar module, also known as a solar panel. Solar panels consist of

cells connected in series and parallel configurations to achieve the desired power output. For example, connecting six cells in series results in an ideal voltage of 3 V (6 × 0.5 V), while maintaining the same current as a single cell. Additionally, series cells can be connected in parallel to increase current capacity. For instance, a series-parallel structure of twelve cells (two sets of six cells in parallel) can produce 4 A and 3 V, effectively doubling the current output compared to a single series string.

The process of solar cell operation involves several key stages. It begins with the absorption of sunlight by the semiconductor material and concludes with the recombination of some charge carriers. During this process, sunlight is primarily converted into electrical energy, although some energy is also lost as heat or light. These fundamental stages, as illustrated in **Fig II. 2**, form the basis of how solar cells work and how they are integrated into solar panels for energy generation.

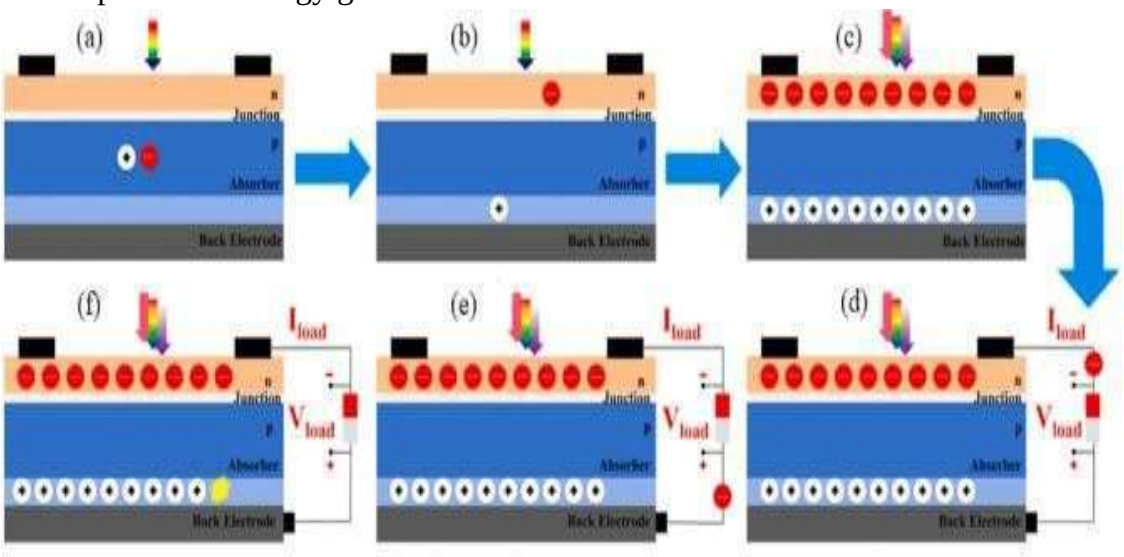

Fig II .2. Photovoltaic Energy Conversion Process (a) Absorption, (b) separation of charge carriers, (c) continuous generation and separation, (d) connection of external load, (e) the transfer of a charge carrier from high to low potential, (f) recombination of carriers **[79] .**

IV. Photovoltaic Cells Generation

Solar cells are classified into Four generations based on their materials and production techniques. The first generation consists of wafer-based silicon cells, which dominate the market and accounted for 95% of global solar power generation in 2020 **[80].** These cells are efficient and commonly used in traditional applications. The second generation utilizes thin-film technologies, which offer flexibility and cost reduction. While these cells initially had lower efficiencies, improvements have been made over time. The third generation of

solar cells builds on thin-film principles by incorporating novel materials such as perovskites and organic compounds. These advancements enable adjustable band gaps and multi-junction designs, which contribute to higher efficiency and open new possibilities for solar energy applications **[81].** However, these technologies are still under development. **[81].** The fourth generation of photovoltaic (PV) technology integrates low-cost, flexible thin-film polymers with durable nanostructures, including inorganic materials like metal oxides and organic materials such as graphene, carbon nanotubes, and their derivatives. This hybrid approach improves efficiency, stability, and scalability, making it suitable for a variety of solar energy applications **[82] .**

The classification of solar cell generations provides a clear framework for understanding advancements in photovoltaic technology, as shown in the figures below. A detailed discussion of each generation will follow in the next section.

IV .1- First generation Wafer-based Solar Technology

The first generation of solar cells is based on wafers, , meaning their manufacturing techniques were adapted from those used in integrated circuit production. This allowed them to leverage existing expertise in silicon wafer production **[83].**These cells typically consist of a single layer of light-absorbing material (single-junction) or use numerous physical configurations (multi-junctions) to apply various methods for charge separation and absorption **[84].**The first generation of solar cells consists of crystalline silicon cells, such as polysilicon and monocrystalline silicon.

The upper surface of the solar cell consists of a thin layer of p-type material, which facilitates efficient light absorption (see **Fig II. 3**). Metal rings are positioned around the p-type and n-type materials, serving as the positive and negative output terminals, respectively. Together, these semiconductor materials create a single unit of the photovoltaic (PV) cell **[85].**

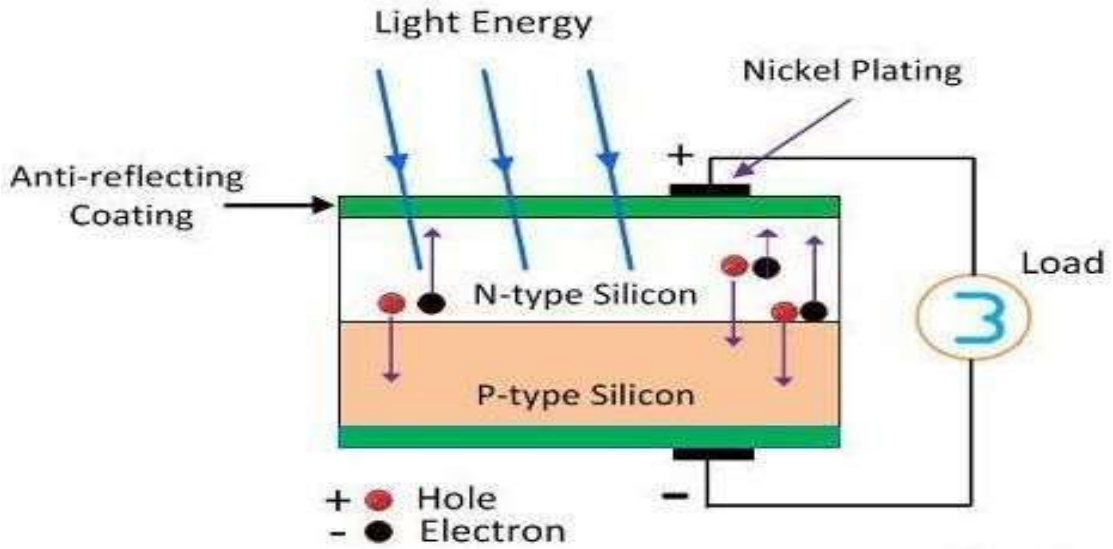

Fig II . 3. Wafer-based Solar Technology (Circuit Globe (n.d.)) **[86].**

The collaboration with the integrated circuit industry not only provided access to essential materials but also greatly advanced the development of first-generation photovoltaic technology, utilizing existing silicon wafer manufacturing expertise.

IV .1.1- Monocrystalline Solar Cell

Monocrystalline solar PV modules, a first-generation photovoltaic technology, have been in use for decades, demonstrating their reliability, durability, and longevity. Many of the early installations from the 1970s are still producing electricity today. These modules are the most widely used solar technology and constitute about 80% of the global photovoltaic market. They are expected to maintain their dominance until more efficient and cost-effective alternatives become available. These cells utilize crystalline silicon p-n junctions to convert solar energy into electricity. Their established performance and widespread use demonstrate their enduring viability in the industry.

Monocrystalline solar cells (**Fig II.4**) are produced using a single crystal of silicon (Si), which is typically grown through the Czochralski process **[87].** This method ensures high precision, starting with large ingots that are refined to create high-quality material. Historically, monocrystalline cells have achieved an efficiency of around 16%, but advancements in technology have led to efficiencies of up to 24.4% in laboratory conditions **[88].** Multicrystalline silicon cells have also seen improvements in efficiency, reaching 19.8% due to enhancements such as thermally formed oxide coatings and isotropic etching.

These techniques create a hexagonally symmetric 'honeycomb' surface texture, which helps reduce unfavorable electronic processes.

Dobrzanski et al. **[89]** described the traditional screen-printing process used in the manufacturing of monocrystalline silicon solar cells. These cells were equipped with Schottky and Zener diodes for protection and were integrated into photovoltaic (PV) modules to generate electricity **[90].** One practical application of these modules is in traffic lighting for pedestrian crossings, showcasing their versatility and effectiveness.

Fig II .4. Monocrystalline Solar Panel (Sendy 2017) **[91].**

IV . 1.2- Polycrystalline Solar Cell (Poly-Si or Multicrystalline)

Polycrystalline silicon, also called multi-crystalline silicon, is a high-purity material extensively used in the solar photovoltaic industry. It is primarily produced through the Siemens process, which involves the distillation of volatile silicon compounds followed by decomposition at high temperatures. Alternatively, upgraded metallurgical-grade silicon purification methods can be used. Poly-Si comprises small crystals, or crystallites, that give it a distinctive metallic flake appearance. Multi-crystalline solar cells, commonly referred to as polycrystalline cells, dominate the expanding photovoltaic (PV) market due to their lower production costs compared to monocrystalline cells. Despite their slightly lower efficiencies, which can reach up to 19.8%, as noted by Zhao et al. (1998) **[92],** their cost-effectiveness makes them widely preferred. The production process involves melting silicon and solidifying it to form rectangular ingots, which are subsequently sliced into thin wafers or shaped into wafer-thin ribbons using methods like those developed by Evergreen Solar.

Transitioning from mono-silicon to multi-silicon manufacturing reduces metal contamination defects and enhances crystal structure, making it a preferred option for large-scale PV module production. Producing 1 MW of conventional solar modules requires approximately 5 tons of poly-Si, underlining its critical importance in the solar industry see **Fig II.5.**

Fig II.5. Polycrystalline Solar Panel (Indiamart (n.d.)) **[93].**

IV. 1.3- Emitter wrap-though cells

Emitter wrap-through cells (Fig. 6) improve efficiency by focusing on enhanced cell design rather than material advancements. Small laser-drilled holes connect the rear n-type contact to the emitter on the opposite side, enabling optimized performance .

By removing the front contacts, the metal lines' masking is eliminated, allowing the entire surface area of the cell to absorb more solar radiation. Several tests **[94]** have shown that placing the contacts on the backs of solar cells offers manufacturing benefits. Companies like Advent Solar **[95]** and SunPower Corp **[96].** These are examples of those utilizing EWT technology in the US. Utilizing EWT has resulted in a 15–20% increase in efficiency. One significant drawback of this technology is apparent in large-area EWT cells, where it suffers from high series resistance that limits the fill factor. See **Fig II.6.**

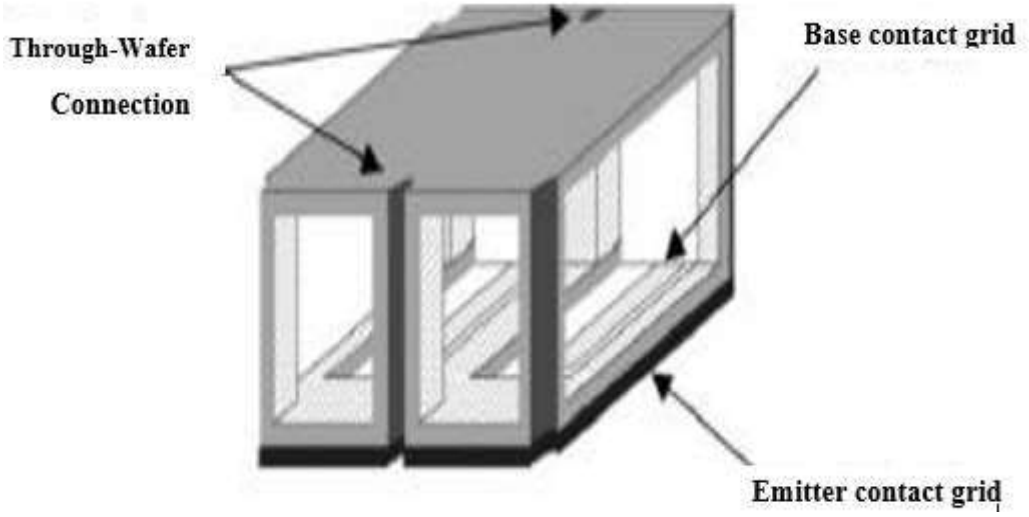

Fig II .6. Schematic illustration of an emitter wrap-through solar cell **[94].**

IV. 1.4- Silicon crystalline investment

Photovoltaic systems require a considerable initial capital investment, though they provide low ongoing operation and maintenance costs. The cost of delivered energy decreases as the lifespan of the system increases, with silicon-based technology modules typically lasting between 20 and 30 years. However, most photovoltaic (PV) systems experience lengthy payback periods unless they receive strong government incentives. To tackle this issue, research is concentrating on reducing initial capital costs, shortening payback periods, and improving the feasibility of photovoltaics as a self-sustaining energy source that does not heavily rely on subsidies.

First-generation silicon-based PV cells have maintained their dominance in the market, contributing to an impressive 95% of the power output from 2020 to the present. Concurrently, the advancement of second-generation thin-film solar cells focuses on minimizing manufacturing expenses, lowering module costs, boosting efficiency, and enhancing durability. This shift aims to achieve 'grid parity,' a point where the cost of electricity generated by photovoltaic systems equals that of traditional energy sources. Although this goal is still challenging, advances in technology have greatly reduced the cost per watt, making it more achievable .Adopting these innovations accelerates progress toward grid parity and creates a more sustainable energy future.

IV. 2 The Second-generation Thin film technology

Second-generation solar photovoltaic technologies are single-junction devices that use less material while maintaining the efficiency levels of first-generation photovoltaic cells. These include amorphous silicon (a-Si), cadmium telluride (CdTe), and copper indium gallium diselenide (CIGS) cells. Commonly used in large photovoltaic power stations, they provide excellent performance even in cloudy conditions. See **Fig II.7.**

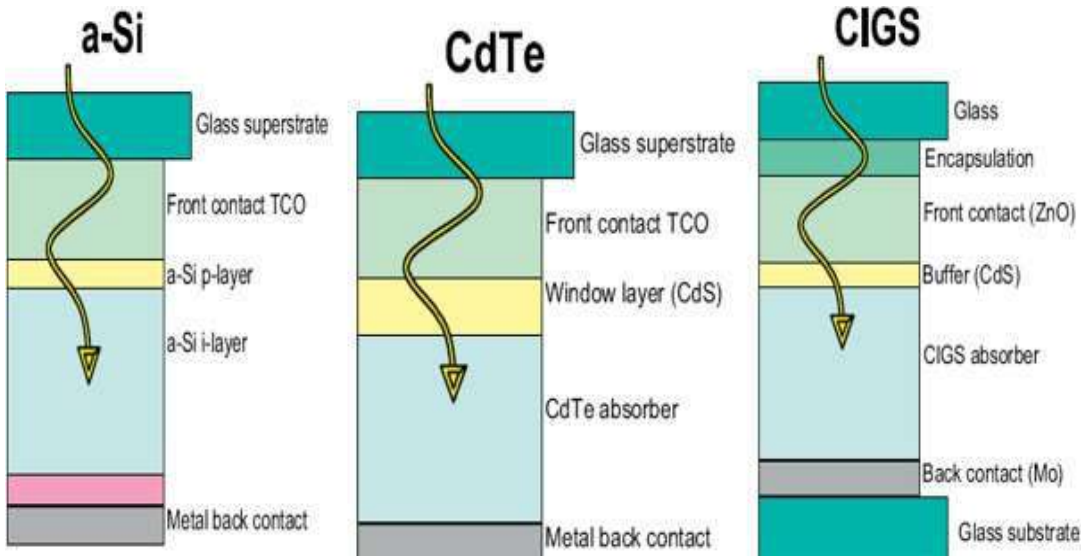

Fig II.7. Schematic Diagrams of a-Si, CdTe, and CIGS Thin-Film PV Technologies .

IV .2 .1- Amorphous Silicon Solar Cell (a-Si)

This type of solar cell is widely recognized as the most prevalent among thin films and has been commercially available for over 15 years. It has been widely used in pocket and desktop calculators, as well as in solar panels, for both domestic and utility-scale electricity generation. They are readily available owing to their low cost. These materials can be manufactured at very low temperatures, leading to numerous low-cost polymers and substrates with highly flexible applications.

Amorphous silicon is the most commonly and developed non-crystalline form of silicon. It is particularly popular in thin-film technology, although it is prone to degradation. Due to its random structure, amorphous silicon (a-Si) has a high band gap of 1.7 eV (Boutchich et al., 2012) **[97],** which results in a light absorptivity rate that is 40 times higher than that of monocrystalline silicon (Mah, 1998). Also it holds the top position in the market among all thin film materials. Carlson and Wronski (1976) reported the first amorphous thin-film solar cell of 1 mm thick with an efficiency of 2.4%. In addition, Rech and Wagner (1999)

detailed further improvements and potential of thin-film solar cells. A table presented by Mehreen Gul et al. **[98]** shows a list of 49 companies involved in the manufacturing and trading a-Si modules . According to this list, Stion Corporation (US13) in the USA manufactures a-Si modules with the highest efficiency of 13.8%. In contrast to monocrystalline and multi-crystalline modules, over half of the companies are based in China and Germany . The table shows that there is over a 10% difference between the lowest and highest efficiencies of commercially available modules.

Additionally, it is notable that most companies produce modules with efficiencies ranging from 5% to 9.9% efficiency. When comparing a-Si modules see Table 4 in **[98]** to monocrystalline and Table 2 in **[98]** and multi-crystalline modules presented in Table 3 **[98],** it is evident that the maximum efficiency of a-Si modules is 13.8%. This value is among the lowest efficiency ranges for monocrystalline and multi-crystalline modules. While, as compared to the highest efficiency of monocrystalline and multi-crystalline modules, a-Si modules are still behind by 6.6% and 3.1% see Tables 2 to 4 in **[98].** By examining the range of commercially available a-Si modules and comparing them with monocrystalline and multi-crystalline options, it is clear that they require significant research and development to enhance their performance. See **Fig II.8.**

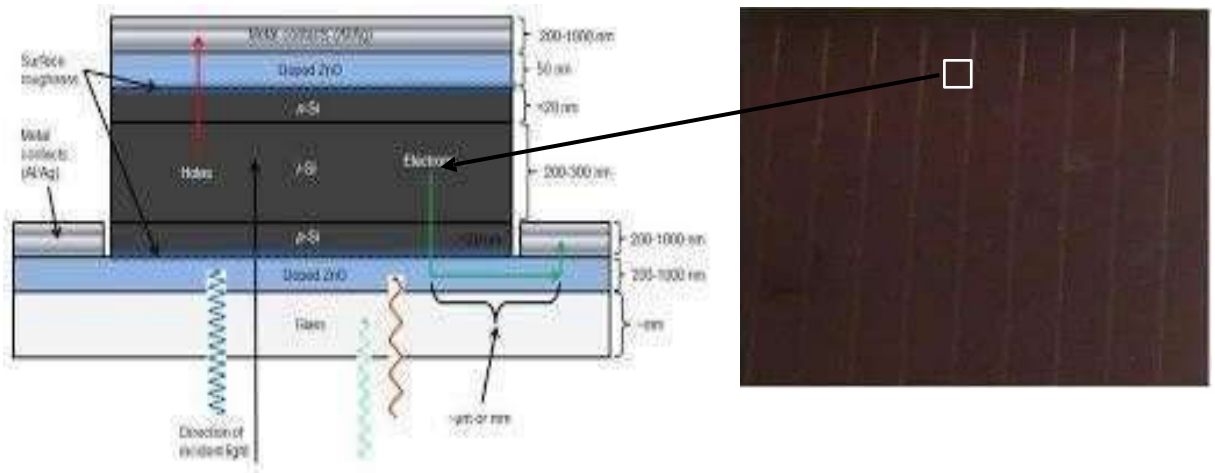

Fig II . 8. Amorphous Silicon Solar Cell Composition (Yang T.C. (2016) **[99]** .

IV .2.2- Cadmium telluride/cadmium sulphide (CdTe / CdS) solar cell .

Cadmium telluride (CdTe) solar cells are a promising category within second-generation photovoltaic technologies. CdTe is an ideal material for polycrystalline solar cells due to its excellent optoelectronic and chemical properties, combined with low production costs. As

a direct band gap material with a band gap of 1.45 eV and an absorption coefficient of approximately 10^5/cm in the visible spectrum, CdTe effectively absorbs around 90% of incident light with a thickness of just a few millimeters. This makes it a highly efficient light absorber for photovoltaic applications. High temperature deposition techniques typically result in films with lower cadmium content, imparting p-type conductivity. Furthermore, the high ion density in CdTe crystals (about 70%) contributes to enhanced passivation, robust chemical bonds, and significant chemical and thermal stability, with an energy reference of approximately 5.75 eV. These properties ensure that CdTe solar cells maintain stability under various conditions and exhibit strong resistance to degradation during deposition processes.

CdTe photovoltaic solar cells are considered the second most widely used solar photovoltaic technology globally after c-Si, representing 7% of the market in 2014. The highest recorded laboratory efficiency for a CdTe solar cell is 22.1% , achieved by First Solar, while its theoretically predicted efficiency is approximately 33%. Over the past 25 years, efficiency has improved from 15.8% **[100]** to 22.1% **[101-102]**. This slow progress in efficiency is largely attributed to a lack of research and development focused on CdTe, partly due to environmental concerns and the toxicity associated with its materials. See **Fig II.9.**

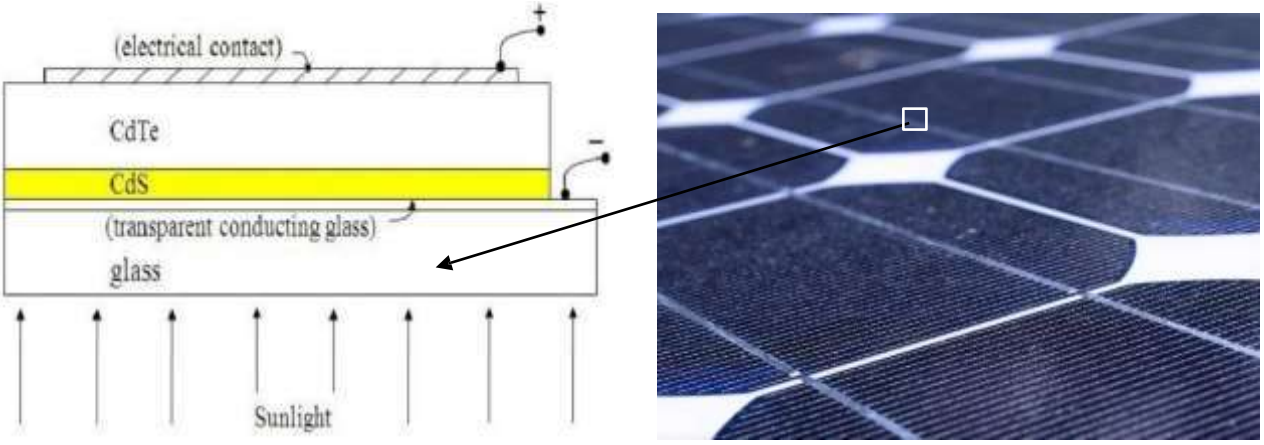

Fig II .9. CdTe Thin Film Solar Cell Layers. (Dharmada et al. (2014)) **[103].**

IV.2. 3- Copper Indium Gallium Di-Selenide (CIGS)

CIGS solar cells, which stand for Copper-Indium-Gallium-Selenide, are thin-film photovoltaic devices designed to convert sunlight into electricity. These cells are created by depositing a thin layer of copper, indium, gallium, and selenium onto a glass or flexible

plastic substrate, with electrodes on both the front and back to collect the current (**Fig 6**) **[104].** The right side of Figure 6 presents a transverse section of a real device obtained using a scanning electron microscope. Due to their high absorption coefficient, only a very thin film is needed, reducing material usage compared to other semiconductor technologies. Copper indium gallium diselenide (CIGS) photovoltaic solar cells exhibit the highest energy production among thin-film photovoltaic technologies. Their power conversion efficiency on glass substrates is now nearing 20%, with some achieving an efficiency of 22.8%. This level of performance competes favorably with crystalline silicon (c-Si) wafer-based solar cells **[105].** Additionally, CIGS solar cells generally outperform CdTe solar cells in terms of efficiency, making them a preferred option for high-performance applications. Recent advancements in the field of CIGS have shifted towards flexible

photovoltaic devices using polyamide or metal foil substrates. The flexible nature, resistance to solar radiation, and high specific power of CIGS solar cells have led to their increasing use in space applications. Additionally, CIGS solar cells exhibit a high absorption coefficient at a band gap of 1.5 electron volts, , enabling effective absorption of the solar light spectrum **[106-107].** See **Fig II.10.**

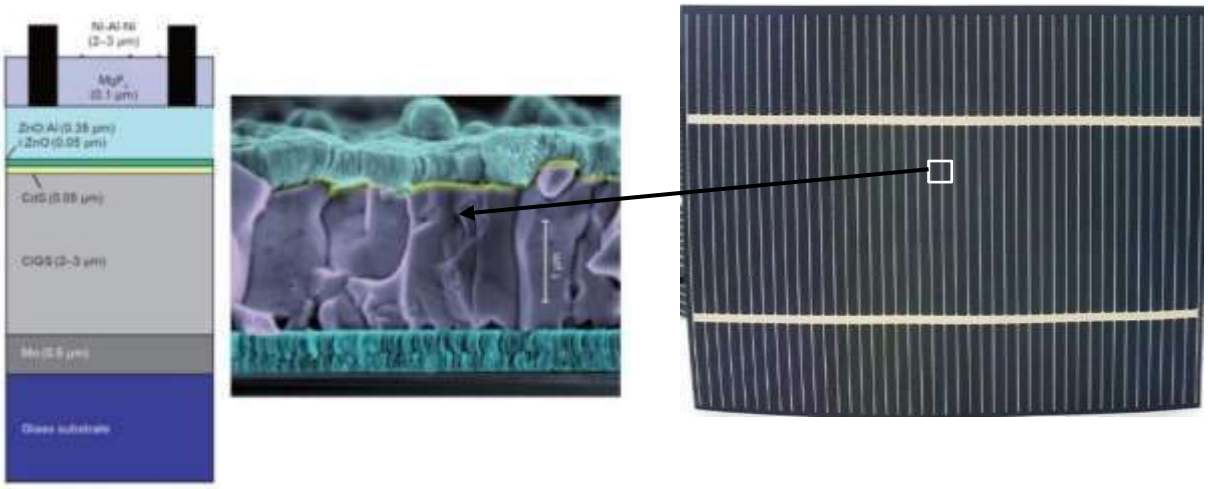

Fig II . 10. Copper Indium Gallium Di-Selenide (CIGS) Solar Cell Composition (Powalla et al. (2017)) **[106]**

IV.3- The Third Generation of photovoltaic Technologies (PV Solar Cells)

Third-generation photovoltaic (PV) technologies represent a significant leap in solar energy innovation, leveraging novel chemical compounds and advanced materials to overcome the limitations of traditional silicon-based and second-generation thin-film

technologies. These systems incorporate cutting-edge materials such as nanocrystalline films, quantum dots, and perovskite structures, which offer unique advantages like tunable bandgaps, enhanced light absorption, and the potential for exceeding traditional efficiency limits. Research and development efforts aim to optimize these materials for improved efficiency, cost-effectiveness, and scalability. Despite their promising potential, many third-generation PV technologies remain in the experimental phase, facing challenges related to material stability, large-scale production, and long-term performance. Nevertheless, they hold the promise of reshaping the future of solar energy by enabling more efficient, flexible, and versatile applications compared to their predecessors.

- **The third generation of solar cells encompasses:**

IV.3. 2 - Nano-crystalline solar cells [108]

IV.3. 3 - Polymer Solar Cells (PSC) [108]

IV.3. 4 - Organic Solar Cells (OSC) [108]

IV.3. 5 - Perovskite Solar Cells (PSC) [108]

IV.3. 6 - Dye-sensitized Solar Cells (DSSC) [103]

IV.3. 7 - Quantum Dot (QD) Solar Cells [109]

IV.3. 8 - Multi-junction Solar Cells [108] , [109]

Third-generation photovoltaic cells are often described as 'emerging concepts' due to their limited market penetration, despite some having been studied for over 25 years **[110].**

IV.4-The Fourth-Generation of Photovoltaic Technologies (PV Solar Cells)

Fourth-generation photovoltaic (PV) technologies, known as hybrid inorganic cells or nano photovoltaics, integrate low-cost, flexible materials with durable and stable nanostructures. These technologies combine the lightweight and cost-effective properties of polymer thin films with the enhanced stability and functionality of advanced inorganic and organic nanomaterials. Key components include metal oxides, metal nanoparticles, and carbon-based nanostructures, such as graphene, carbon nanotubes, and their derivatives **[109],[111-112].**

By integrating these innovative materials, fourth-generation PV cells address critical challenges faced by earlier generations, such as material stability, efficiency, and scalability. The incorporation of nanostructured materials enables unique properties, including:

- Improved light absorption and scattering using nanomaterials such as metal nanoparticles and graphene derivatives to capture a broader spectrum of sunlight.
- Enhanced charge transport and carrier mobility due to graphene's and carbon nanotubes' superior conductivity.
- These cells have customizable flexibility and durability, making them suitable for emerging applications like wearable devices, portable solar panels, and building-integrated photovoltaics (BIPV).

Fourth-generation photovoltaic technologies strive to combine high efficiency with low costs, positioning them as promising candidates for widespread solar energy adoption. Although many of these devices are still in experimental or early development stages, They hold the potential to transform solar energy systems by integrating the best features of both organic and inorganic materials .

V. Structure of Photovoltaic Cell Generations

In the past decade, photovoltaics have become a significant contributor to the ongoing energy transition. Advances in materials and manufacturing methods have greatly facilitated this progress. However, several challenges remain before photovoltaics can provide cleaner, low-cost energy.

The main function of a photovoltaic cell is to capture solar radiation as light and convert it into electrical energy through a process known as the photovoltaic effect. Multiple technologies are involved in the manufacturing process of photovoltaic cells, which utilize material modifications that vary in photoelectric conversion efficiencies within the cell components. With the emergence of various non-conventional manufacturing methods for creating functional solar cells, photovoltaic technologies can be categorized into four main generations, as illustrated in **Fig II.11 [113].**

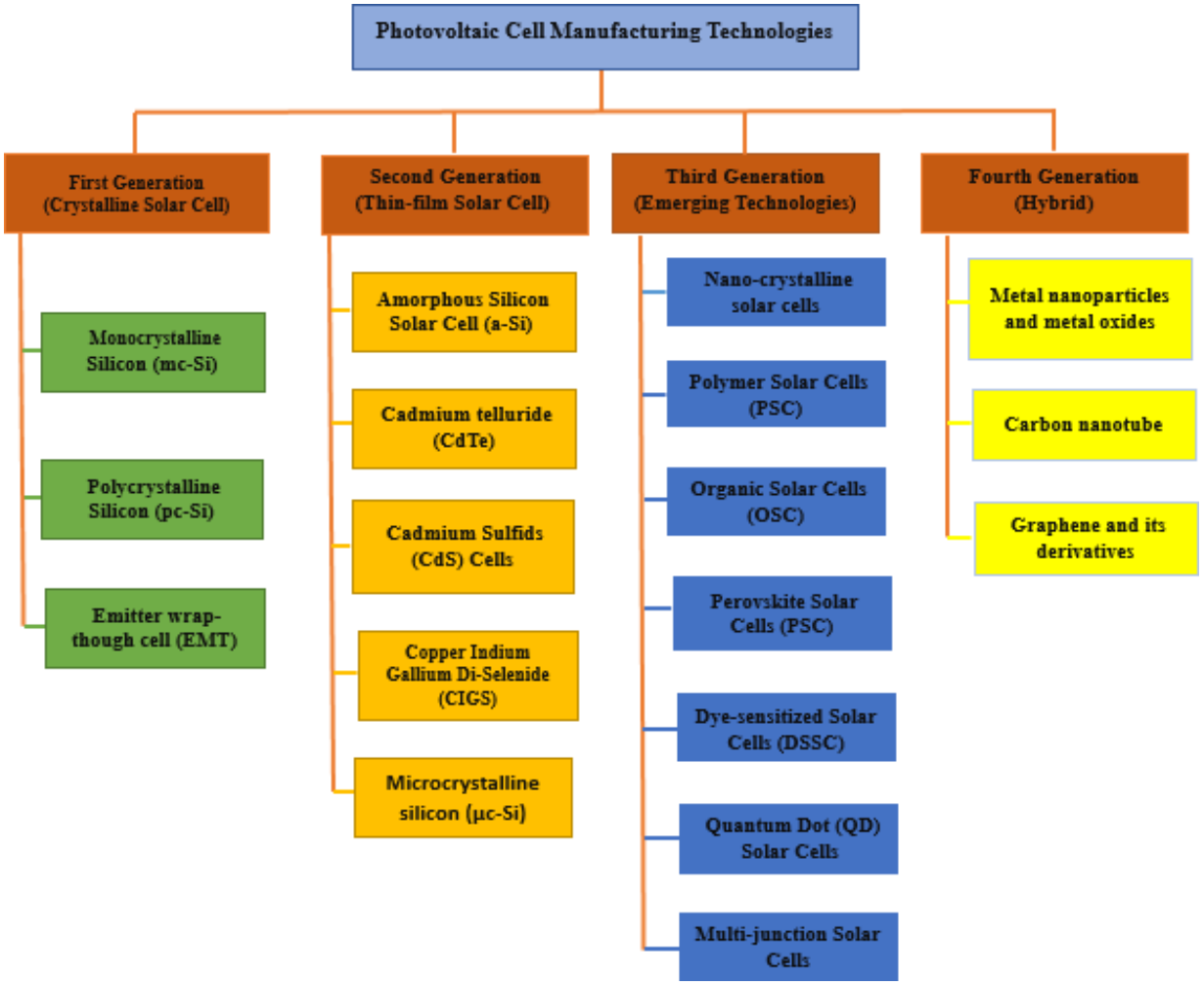

Fig II .11 . Evolutionary Different types of solar cells and the latest advancements in this field **[109-114].**

VI. Photovoltaic Generation Technologies: Efficiency, Advantages, and Disadvantage

Photovoltaic (PV) efficiency refers to the capability of a photovoltaic device, such as a solar cell or solar panel, to convert sunlight into usable electrical energy . It is expressed as a percentage, representing the ratio of electrical power output to the input of sunlight (solar energy).Photovoltaic efficiency is calculated by measuring the electrical power output of solar cells or panels under standard test conditions (STC), which involve specific light intensity and temperature. Efficiency is computed by dividing the electrical power output by the incident solar power. The resulting value is then multiplied by 100 to express it as a percentage. Multiple factors affect the efficiency of photovoltaic devices: the properties of materials, cell design, temperature, solar spectrum, losses from reflection and absorption, dirt, and shading, inverter efficiency **[115].**

Each generation of photovoltaic cells has its advantages and limitations, and research continues to improve efficiency, durability, and cost-effectiveness **[116].**

The adoption of solar photovoltaic (PV) technology encounters several challenges. These include high costs for energy storage, intermittency , resource constraints, competition from other energy sources, initial cost barriers, difficulties integrating into existing infrastructure, and environmental concerns. To ensure the sustained growth and widespread adoption of solar PV technology, it is essential to address these challenges through research, innovation, and supportive policies **[117].**

The table below highlights the advantages and disadvantages of each generation of technology, along with the efficiency levels of different solar cell generations.

Table II. 2. Comparative Analysis of the Three Generations of Photovoltaic Solar Cells: Efficiency Ranges, Advantages, and Disadvantages **[108-109],[118-120].**

Photovoltaic Cells					
First Generation Crystalline Solar Cell					
Photovoltaic Technologies	**Efficiency (%)**	**Band gap**	**Life Span**	**Advantages**	**Disadvantages**
Monocrystalline silicon (m-Si)	15 to 24%	~1.1 eV	25 years	- Stability -high performance - long service life	- High manufacturing cost. - More temperature sensitivity. - Absorption problem. - Material loss.7
Polycrystalline silicon (p-si)	10 to 18%	~1.7 eV	14 years	- Manufacturing procedure is simple - Profitable . - Decreases the waste of silicon. - Higher absorption compared to m-si .	- Lower efficiency - Higher temperature - Sensitivity.
Single III-V junctions (GaAs)	28 to 30%	~1.43 eV	18 years	- High stability - Lower temperature sensitivity. - Better absorption than m-si . - High efficiency.	- Extremely expensive

Emitter wrap Though (EWT)	15 to 20%	~1.1 eV	20–30 years	-Increased Efficiency(By eliminating front metal contacts). -Improved Aesthetics (The absence of visible front metal lines) - Enhanced Light Absorption (The design allows more solar radiation to be captured).	- High Series Resistance (limiting the fill factor and reducing overall performance). - Complex Fabrication - Potential Heat Generation (lead to localized heating, which can degrade performance over time).
Second Generation Thin-Film Solar Cell					
Photovoltaic Technologies	**Efficiency (%)**	**Band gap**	**Life Span**	**Advantages**	**Disadvantages**
Amorphous silicon (a-si)	5 to 12%	~1.7 eV	15 years	- Less expensive. - Available in large quantities. - Non-toxic. - High absorption coefficient .	- Lower efficiency. - Difficulty in selecting dopant materials. - Poor minority carrier lifetime.
cadium telluride/cadium sulfide (CdTe/CdS)	15 to 16%	~1.45 eV	20 years	- High absorption rate. - less material required for production	- Lower efficiency. - Cd being extremely toxic, Te being limited. - More temperature sensitive.
copper indium gallium selenide (CIGS)	20%	~1.7 eV	12 years	- Less material required for production	- Very high-priced. - Not stable. - More temperature-sensitive. - Highly unreliable
The Third-Generation Emerging technologies Solar Cell					
Photovoltaic Technologies	**Efficiency (%)**	**Band gap**	**Life Span**	**Advantages**	**Disadvantages**
Nano-Crystalline Solar Cell (Quantum dots (QD))	16.6%	1.2 to 1.7 eV	05 years	- Lightweight and Flexible. - High Absorption Coefficient . - Band Gap Tunability	- Lower Stability in Outdoor Conditions -Efficiency Degradation Over Time.

				(Allows for better solar spectrum utilization).	-Thermal Instability (sensitive to temperature fluctuations)
Polymer Solar Cells	3 to 8 %	~1.4 eV to ~ 2 eV	05 years	- Light weight and flexible, thus easy to size and shape . - Ease of storage and transportation. - Organic in nature, hence are environmentally friendly.	- Very low efficiency. - Faster degradation in outdoor situations. - Shorter lifespan .
Organic and polymeric photovoltaic cells (OPC).	9 to 11%	~1.4 eV to ~ 2.0 eV	- 05 years (advancements have extended this to approximately 15–20 years as of 2020).	- Low processing cost. - Lighter weight, flexibility. - Thermal stability.	- Low efficiency.
- Perovskite Solar Cells	21%	~ 1.5 eV to ~ 2.3 eV	- 05 years	- Low-cost and simplified structure. - Light weight, - Flexibility, - High efficiency. -Low manufacturing cost.	- Unstable. -Toxicity (Many perovskite materials contain lead). - Scalability Issues.
Dye-sensitized photovoltaic cells (DSSC)	5 to 20%	/	-10 years (recent advancements have extended this to 15–30 years as of 2020) .	- Lower cost. - low light and wider-angle operation. - lower internal temperature operation, - robustness, and extended lifetime	-Problems with temperature stability. - poisonous and volatile substances
quantum dots solar cells (QDSC)	11 to 17%	~ 0.5 eV to ~2.5 eV .	- 1 to 10 years (ongoing research aims to extend this to 25 years).	- Low production cost. - low energy consumption	- High toxicity in nature. - degradation.
Multi-junction solar cells	36% and higher	~0.7 eV to ~1.9 eV.	20 –30 years.	- High performance	- Complex. - expensive

VII . Advantages and Disadvantages of the Fourth Generation of Solar Cell (Hybrid) .

This research paper provides a general overview of the different generations of solar cells. Currently, fourth-generation technologies including graphene and its derivatives, carbon nanotubes, metal nanoparticles, and metal oxides are still in the research and development phase. Due to the experimental nature of these materials and its components , precise data regarding their lifespan, bandgap values, and efficiency are not yet consistently defined across various studies. Consequently, this section will outline the general advantages and disadvantages of each fourth-generation solar cell technology discussed in this chapter.

VII.1- Metal Nanoparticles and metal oxides in Solar Cells

Advantages

- ✓ Enhanced light-harvesting efficiency due to improved optical properties.
- ✓ Potential to reduce the thickness of active layers, contributing to material and cost savings.

Disadvantages

- ✓ Compatibility Limited compatibility with existing solar cell materials, requiring advanced integration techniques.
- ✓ High cost of noble metals such as gold and silver, which can impact scalability.

VII.2- Carbon Nanotubes (CNTs) in Solar Cells

Advantages

- ✓ High electrical conductivity and excellent charge transport properties.
- ✓ Flexibility and lightweight nature.

Disadvantages

- ✓ Difficulty in large-scale production and uniformity.
- ✓ Integration with other solar cell materials can be complex.

VII.3- Graphene and Its Derivatives in Solar Cells

Advantages

- ✓ High electrical conductivity and flexibility.

- ✓ Potential to replace indium tin oxide (ITO), reducing costs.

Disadvantages

- ✓ Achieving uniform and defect-free graphene layers.
- ✓ High-quality synthesis methods remain expensive.

❖ Each technology's efficiency, cost, lifespan, and application can vary widely based on the specific product and manufacturer **[121] .**

The efficiency of solar cells can be improved by reducing various losses that affect their overall performance. Since 1976, the National Renewable Energy Laboratory (NREL) has maintained a record of the highest verified research cell conversion efficiencies across different photovoltaic technologies see **Fig II.12.** Cell Efficiency results for various semiconductor families are presented, including multi-junction cells, gallium arsenide single-junction cells, crystalline silicon cells, thin-film technologies, and emerging photovoltaic technologies. The most recent world record for each specific technology is highlighted by a flag on the right edge, which includes the efficiency value and the corresponding technology symbol **[122].**

This chart, known as the Best Research-Cell Efficiency Chart, is regularly updated to reflect the latest findings in research **[122].** See **Fig II.12.**

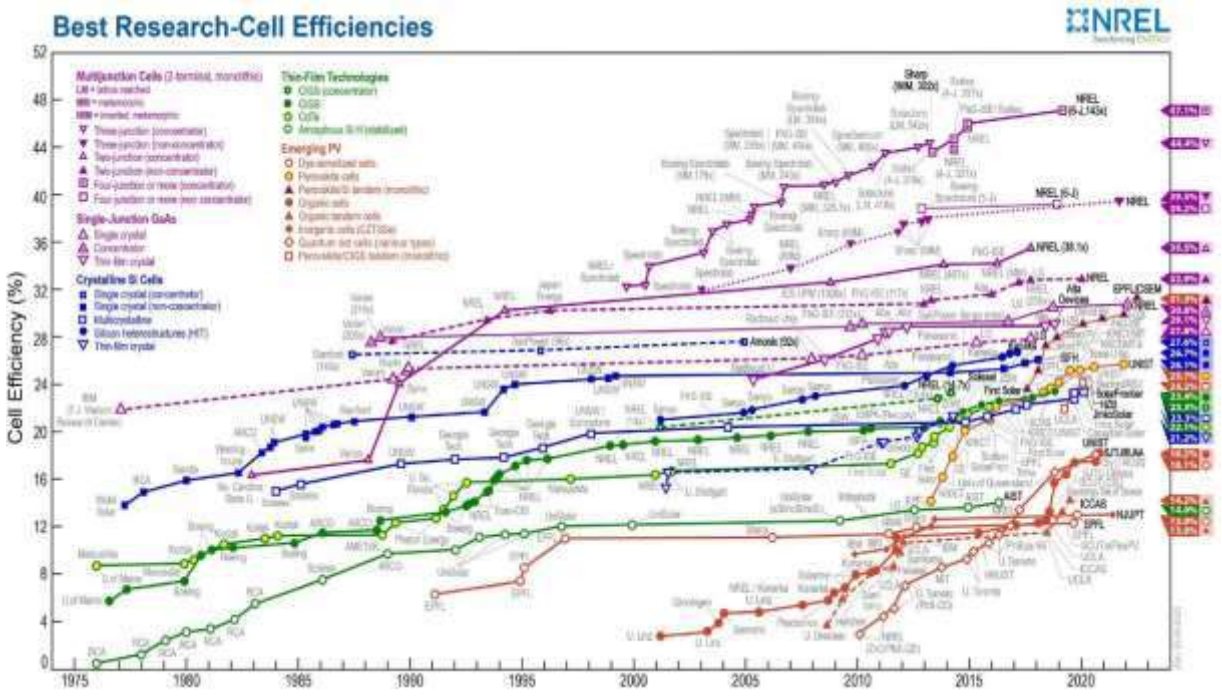

Fig II .12.NREL Best Research-Cell Efficiencies chart **[122].**

- ✓ Here are the current highest confirmed efficiency values for different types of solar cells, as listed on the NREL chart:
  - **Multijunction Solar Cells: 47.1% (research grade).**
  - **Concentrator Solar Cells: 46.1% (research grade).**
  - **Silicon Solar Cells (single junction): 27.6% (commercial grade).**
  - **Tandem Perovskite/Silicon Solar Cells: 29.5% (research grade).**
  - **Organic Solar Cells: 18.9% (research grade).**

These efficiency values pertain to research-grade solar cells and may not accurately reflect the commercial products currently available on the market **[123]** . Furthermore, these values may not be achievable in all conditions and can vary depending on the specific application and location **[124].** However, these values reflect the latest advancements in solar cell research and development, highlighting the potential for further improvements in solar energy technology .

VIII. Applications of photovoltaic cells

The applications of photovoltaic (PV) cells are broad and varied. While they are primarily designed to convert solar energy into electrical power, their use extends to several sectors, including residential buildings, industrial facilities, agriculture, transportation, and military operations. PV cells provide a source of clean, renewable energy, making them crucial in addressing global energy demands while reducing environmental impact. As the focus on sustainable energy solutions grows, PV technology is increasingly being integrated into emerging areas, such as remote power systems, portable electronics, and grid-connected infrastructure.

VIII.1 – Household Applications of Solar Cells

Photovoltaic solar cells are a modern and efficient solution that is increasingly adopted in both residential and commercial buildings. They offer numerous advantages, including reduced energy costs, enhanced environmental sustainability, and decreased reliance on traditional energy sources. In the residential sector, solar energy has diverse applications. These include electricity generation through the installation of photovoltaic panels on rooftops or adjacent land, which can power household appliances as well as heating and

cooling systems. In addition, solar thermal systems are employed for domestic hot water production, supplying showers, taps, and underfloor heating. Other common uses include outdoor solar lighting equipped with rechargeable batteries and solar-powered ventilation systems that expel hot and humid air from enclosed spaces.

Furthermore, PV panels can be architecturally integrated into building elements such as facades, roofs, or railings, combining aesthetic design with functional energy production. To maximize efficiency, solar cells are often coupled with residential energy storage systems, such as home batteries, which store electricity for use during periods of low solar availability or power outages. These varied applications highlight the versatility and growing importance of solar cells in supporting the transition toward cleaner, more sustainable energy within the residential sector **[125].**

VIII. 2- Integration of solar energy in industrial and agricultural applications

Solar energy is increasingly being utilized across various industrial sectors to meet energy demands, reduce costs, and promote environmental sustainability. In agriculture, solar energy powers water pumps, irrigation systems, and greenhouses, which reduces reliance on fossil fuels and lowers associated costs. In manufacturing, solar energy is harnessed to power production processes, helping to decrease energy expenses and carbon footprints. In construction, solar panels are used to power electrical equipment on construction sites and in completed buildings. They can be integrated into roofs, facades, and structural elements, providing a renewable energy source and contributing to cost savings.

In information and communications technology, solar energy powers data centers and telecommunications networks, reducing operating costs and reducing carbon footprint. It is also used in the transportation sector to power signaling and road lighting systems, charging infrastructure for electric vehicles and electrified public transit systems although its direct use to power vehicles remains limited.

In the oil and gas industry, solar energy powers drilling, pumping, and processing facilities, reducing dependence on diesel generators and fossil fuel-based energy sources. Likewise, in the mining industry, solar energy provides electricity for equipment at extraction sites, leading to cost savings and lower carbon emissions.

Across these sectors, solar energy significantly contributes to reducing greenhouse gas emissions, mitigating the impacts of climate change, and promoting environmental sustainability, providing a reliable, clean, and renewable energy alternative **[126].**

VIII.3- Applications of Photovoltaic Cells in the Military Sector

Photovoltaic cells are primarily used in the military sector to provide autonomous, stable, and reliable power to military bases and camps, particularly those located in remote locations or difficult-to-access environments. This technology helps reduce dependence on fossil fuels and strengthen the resilience and energy continuity of military infrastructure while reducing costs and environmental impact.

Among these systems, the Eneria Hybrid Sunbox provides a compact and rapidly deployable solution for military sites. In France, the Ministry of the Armed Forces is heavily investing in solar projects that cover the rooftops of military buildings, such as the 5,600 m^2 photovoltaic panel installation at the Hexagone Balard site. This initiative generates significant energy savings and reduces dependence on electricity produced from fossil fuels. The eco-camp concept aims to integrate solar energy production and storage to enhance the self-sufficiency and energy efficiency of military bases, especially during external operations. In addition to electricity generation, solar thermal panels supply hot water to military camps even during cloudy conditions, improving living standards and comfort on site **[126-127].**

IX. Conclusion

This chapter reviewed the key types of solar cells, emphasizing their impact on solar panel performance and operation. It examined materials, manufacturing processes, construction, configurations, and working principles, providing a comprehensive understanding of photovoltaic (PV) technologies.

A comparative analysis of current and emerging PV technologies was presented, highlighting efficiency, fabrication methods, and technological advancements. Innovations in materials and cell design offer more cost-effective, efficient power generation solutions to address future energy demands.

In conclusion, PV technologies hold significant potential to transform the energy sector by providing clean, efficient, and cost-effective electricity. Continued development and implementation of advanced PV solutions are crucial for advancing a sustainable energy future.

CHAPTER III

PERFORMANCE COMPARISON OF PHOTOVOLTAIC SUBFIELDS USING EXPERIMENTAL DATA

I. Introduction

This study investigates the performance and adaptability of photovoltaic (PV) subfields at the OUED-NECHOU power plant in Ghardaïa, considering the plant's location, climatic conditions, installed PV technologies, and operational system from DC generation to grid injection. It focuses on the influence of real-time weather parameters- including solar irradiation at a 30° tilt, module and ambient temperatures, wind speed, and relative humidity on PV performance across winter, spring, summer, and fall.

Four fixed PV subfields (mc-Si, pc-Si, a-Si, and CdTe, each 100 kWp) are evaluated, alongside a comparison with single-axis tracking systems using mc-Si and pc-Si technologies. Key metrics, including peak output power, long-term daily production (kWh/day), and average daily output, were measured at four-minute intervals and analyzed under real Saharan conditions. The performance gains of tracking systems over fixed subfields are quantified using an augmentation percentage factor, demonstrating the effectiveness of tracking mechanisms in enhancing energy yield and overall system efficiency.

PV power output is simulated in MATLAB and compared with experimental measurements, with the method for injecting daily energy into the medium-voltage grid

II. Description of the photovoltaic installation at the photovoltaic power plants in OUED-NECHOU, Ghardaïa .

The Ghardaïa photovoltaic solar power plant**,** constructed by the Algerian Electricity Production Company (SPE)**,** is located approximately 15 km north of Ghardaïa**,** near the village of OUED-NECHOU**.** Spanning ten hectares**,** this facility is designed to harvest and directly convert sunlight into electricity**,** contributing to Algeria's renewable energy development program.

With a nominal capacity of approximately 1100 kWp**,** the plant serves as a pilot project aimed at evaluating the performance of different photovoltaic (PV) technologies under the extreme conditions of southern Algeria**,** where high solar radiation and temperature variations significantly impact efficiency. The project is divided into eight subfields**,** each incorporating four different photovoltaic module technologies and two types of structures (Fixed and Single-axis). The installation is south-oriented (azimuth angle = 0°) with a tilt angle of 30°**.**

Fig. III.1 presents an overview of the photovoltaic (PV) accessory center at OUED-NECHOU, highlighting the main solar technologies installed at the site. The PV subfields are tilted at a 30° angle and oriented south to optimize solar energy capture. This pilot plant serves as a testing ground to evaluate the performance and adaptability of different PV technologies under desert climate conditions. It also plays a strategic role in assessing the economic viability of these systems before their implementation in larger-scale photovoltaic station projects across the country, particularly in southern Algeria.

Fig III. 1: Photovoltaic Installation of OUED-NECHOU, Ghardaïa.

II.1. Photovoltaic Technologies and System Components

The power plant integrates multiple photovoltaic (PV) technologies, distributed across eight subfields with different module types and structural configurations. The total installed capacity is as follows:

- **Monocrystalline silicon panels: 452 kWp.**
- **Polycrystalline silicon panels: 452 kWp.**
- **Amorphous silicon (a-Si) panels: 100 kWp.**
- **Thin-film panels (Cadmium Telluride, CdTe): 100 kWp .**

The power plant is a pilot project divided into eight (08) subfields, each incorporating four (04) different photovoltaic module technologies and two (02) types of structures fixed and motorized. All PV subfields are inclined at 30° facing south to optimize solar energy capture. For monocrystalline and polycrystalline technologies, 30% of the panels are installed on adjustable (motorized) supports, while 70% are on fixed supports. In contrast, CdTe and amorphous technologies are entirely mounted on fixed supports.

- **Subfield (1):** 105 kWp in monocrystalline silicon with a motorized structure.
- **Subfield (2):** 98.7 kWp in polycrystalline silicon with a motorized structure.
- **Subfield (3):** 100.8 kWp in thin-film (cadmium telluride Cd-Te) with a fixed structure.
- **Subfield (4):** 100.116 kWp in amorphous silicon with a fixed structure.
- **Subfield (5):** 105 kWp in monocrystalline silicon with a fixed structure.
- **Subfield (6):** 98.7 kWp in polycrystalline silicon with a fixed structure.
- **Subfield (7):** 255 kWp in monocrystalline silicon with a fixed structure.
- **Subfield (8):** 258.5 kWp in polycrystalline silicon with a fixed structure.

This technical distribution provides a representative layout of the subfields in the PV center at OUED-NECHOU, allowing for a comprehensive assessment of PV technologies under real-world conditions. **Fig III.2.** Illustrates the technical distribution and representation of the subfields within the OUED-NECHOU PV center

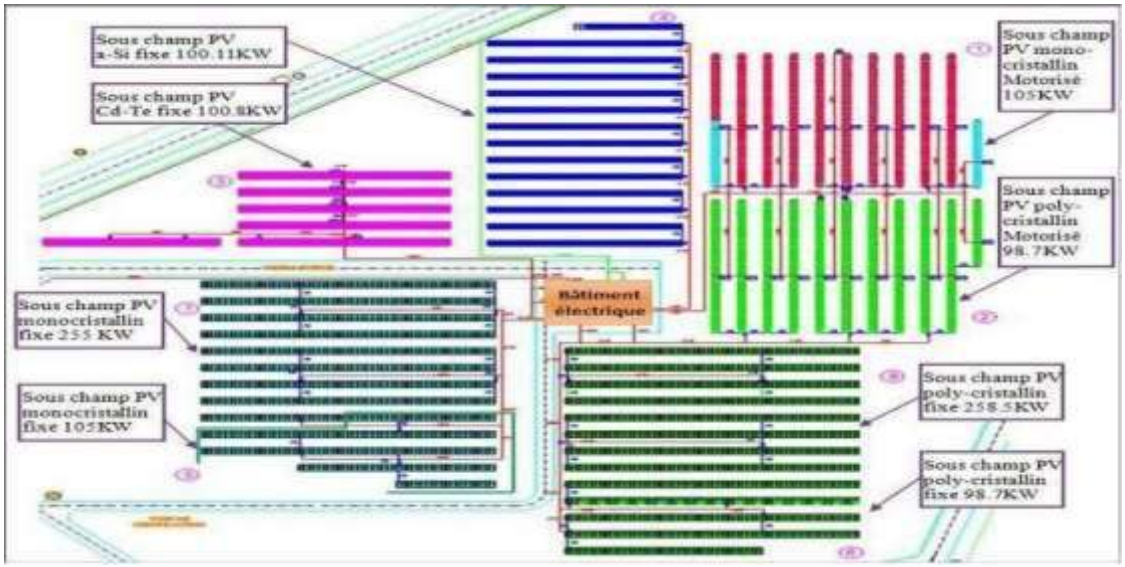

Fig III. 2 : Distribution of Subfields in the OUED-NECHOU Photovoltaic Center, Ghardaïa City.

Additionally, the facility includes essential infrastructure:

- A Guard Post
- A Control Unit
- A Power evacuation station

II.2. General Overview:

❖ **The project followed a structured development timeline:**

- **Location:** Algeria – Ghardaïa – Oued Nechou
- **Geographical Coordinates:** 32°24'N, 03°48'E
- **Total Area:** 10 hectares
- **Peak Power Capacity:** 1,100 kWp Or 1.1 MW
- **Injection Voltage:** 30 KV
- **Project Owner:** Algerian Electricity Production Company (SPE)
- **Final Project Owner:** Shariket Kahraba wa Taket Moutadjadida (SKTM)
- **Engineering Company:** Electricity and Gas Engineering Company (CEEG)
- **Installation Company:** ETTERKIB
- **Control Organization:** CTC Sud
- **Construction Company:** SNC IDÉAL BATISSE COMPAGNIE
- **Service Provider:** ABB Group (ABB SpA Italy – ABB Algérie Spa)
- **Project Duration:** 12 months
- **Contract Number:** 06/2012/SPE 2012/02/KD.ER12 months

II.3. Development Timeline:

- **Start of Engineering Study** (ABB Italy / ABB Algeria): February 12, 2012
- **Start of Civil Engineering Works** (SNC IDÉAL BATISSE): May 28, 2012
- **Start of Installation Works** (ETTERKIB): August 22, 2013
- **Commissioning Tests:** March 27, 2014
- **Partial Commissioning:** June 11, 2014
- **Semi-Industrial Commissioning (MSSI):** Not yet declared

The **Fig** below **III.3** presents an illustrative representation of the OUED-NECHOU Photovoltaic Power Plant in Ghardaïa , Algeria. It highlights the project's geographical location, technical specifications, and structured development timeline. The image offers an overview of the installation site, highlighting its peak power capacity, injection voltage, and the different stakeholders involved in its implementation.

Fig III. 3: Geographical location of the photovoltaic power plants: 1.1 MWp OUED-NECHOU, Ghardaïa **[128]**.

III. Photovoltaic Technologies at Oued Nechou Power Plant: Technological Aspects and Structure, Configuration.

This technical report aims to outline the fundamental principles and identify the main components of a photovoltaic solar power plant. It examines four distinct photovoltaic technologies, all installed on the same site and integrated into both fixed and motorized mounting structures to enhance energy capture and overall performance.

a)- Sub-field (1) has a capacity of 105 kWp and features a motorized monocrystalline silicon (mc-Si) structure. The peak power output of each photovoltaic (PV) panel is 250

Wp. This sub-field comprises 420 photovoltaic modules organized into 21 chains, with each chain consisting of 20 modules. The module efficiency is 15.35%.

b)- Sub-field (2): has a capacity of 98.7 kWp with a Motorized polycrystalline silicon structure (pc-Si), and the peak power output of the PV panel is 235 Wp. This sub-field comprises 420 photovoltaic modules organized into 21 chains, with each chain consisting of 20 modules. The module efficiency is 14.43%.

c) - Sub-field (3) has a capacity of 108 kWp with a fixed thin-film structure using Cadmium Telluride (CdTe), and the peak power output of the PV panels is 80 Wp. This sub-field comprises 1260 photovoltaic modules, organized into 105 chains, with each chain consisting of 12 modules. The module efficiency is 11.10%.

d)- Sub-field (4): This sub-field has a capacity of 100,116 kWp and a fixed amorphous silicon structure (a-Si). The peak power output of the PV panel is 103 Wp. This sub-field comprises 972 photovoltaic modules organized into 54 chains, each chain consisting of 18 modules. The module efficiency is 15.35%.

e)-Sub-field (5) has a capacity of 105 kWp with a Fixed monocrystalline silicon structure (mc-Si), and the peak power output of the PV panel is 250Wp. This sub-field comprises 420 photovoltaic modules organized into 21 chains, with each chain consisting of 20 modules. The module efficiency is 15.35%.

f)-Sub-field (6): has a capacity of 98.7 kWp with a Fixed polycrystalline silicon structure (pc-Si), and the peak power output of the PV panel is 235 Wp. This sub-field comprises 420 photovoltaic modules organized into 21 chains, with each chain consisting of 20 modules. The module efficiency is 15.35%.

g)- Sub-field (7): has a capacity of 255 kWp with a Fixed monocrystalline silicon structure (mc-Si), and the peak power output of the PV panel is 250 Wp. This sub- field comprises 1020 photovoltaic modules, organized into 51 chains, with each chain consisting of 20 modules. The module efficiency is 15.35%.

h)- Sub-field (8): has a capacity of 258.5 kWp with a Fixed polycrystalline silicon structure (pc-Si), and the peak power output of the PV panel is 235 Wp. This sub-field

comprises 1100 photovoltaic modules organized into 55 chains, with each chain consisting of 20 modules. The module efficiency is 14.43%.

The Ghardaïa photovoltaic (PV) power plant has a total installed capacity of 1100 kW and consists of several subfields with a combined total power output of 1174.016 kW. The entire system is composed of 6032 photovoltaic modules organized into 349 chains, each chain containing 150 modules. This large-scale solar installation is designed to efficiently capture and convert solar energy, contributing to renewable energy production in the region.

Table III.1 below presents a comprehensive configuration of the Ghardaïa photovoltaic (PV) power plant. It includes technical specifications such as installed capacity, the types of photovoltaic technologies used, and structural configurations. The table highlights the distribution of modules, power output, and efficiency of each subfield, providing valuable insights into the overall system design.

Table III.1: Configuration and Technical Specifications of the Ghardaïa Photovoltaic Power Plant (1100 kWp)

Ghardaïa OUED-NECHOU Photovoltaic Power Plant 1.1 MWp								
Sub-field number	**Type**	**Structure**	**Sub-field power**	**Number of modules / sub-field**	**Number of strings / sub-field**	**Number of modules / string**	**Module power**	**Module efficiency/ Type**
1	Mono	Motorized	105000 Wc	420	21	20	250 Wc	15.35%
2	Poly	Motorized	98700 Wc	420	21	20	235 Wc	14.43%
3	Cd-Te	Fixed	108000 Wc	1260	105	12	80 Wc	11.10%
4	a-Si	Fixed	100116 Wc	972	54	18	103 Wc	7.10%
5	Mono	Fixed	105000 Wc	420	21	20	250 Wc	15.35%
6	Poly	Fixed	98700Wc	420	21	20	235 Wc	14.43%
7	Mono	Fixed	255000 Wc	1020	51	20	250 Wc	15.35%
8	Poly	Fixed	258000 Wc	1100	55	20	235 Wc	14.43%
TOTAL			1174016 Wc	6032	349	150		

IV. General Overview and Technical Characteristics of PV Technologies Used in the Photovoltaic Station OUED-NECHOU .

At the OUED-NECHOU, Ghardaïa power plant, four different types of panels will be utilized to analyze the behavior of various photovoltaic equipment and technologies in the southern Algerian environment. The electrical specifications of the PV modules are set under standard test conditions.(1000 W/m², 25°C, AM 1.5) are outlined below for the four technologies employed: monocrystalline silicon (mc-Si), polycrystalline silicon (pc-Si), amorphous silicon (a-Si), and cadmium telluride (Cd-Te). It's important to note that both the monocrystalline and polycrystalline technologies follow the same manufacturer's specifications for fixed and single-axis tracking systems.

IV.1. Monocrystalline silicon panels

Monocrystalline cells are first-generation photovoltaic technologies made from a single-crystal silicon block. These cells are typically round or nearly square and exhibit a uniform color when observed up close. Despite the labor-intensive production process, they are widely adopted in modern solar installations due to their high efficiency. In the Ghardaïa installation, monocrystalline panels of the Solaria brand, model S6M-2G, were selected. See **Fig. III.4** below.

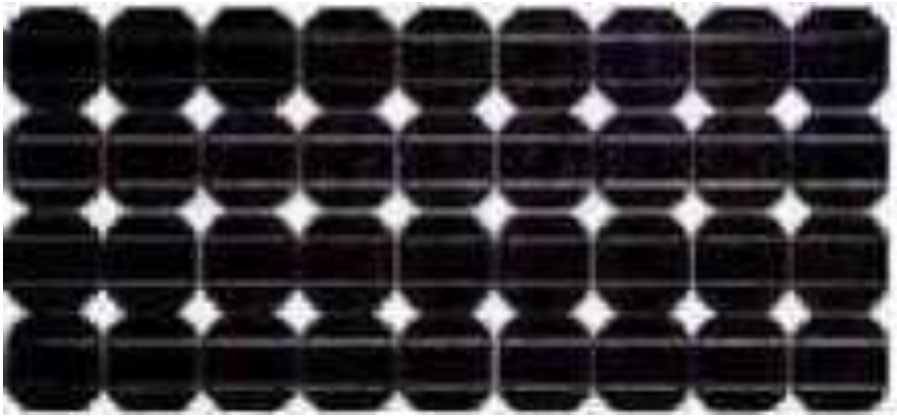

Fig III . 4 : Monocrystalline PV Panel (Solaria S6M-2G) Deployed at the OUED-NECHOU Site , Ghardaïa .

IV.2. Polycrystalline silicon panels

Polycrystalline solar cells are manufactured from a silicon block composed of multiple crystal grains. When viewed up close, variations in crystal orientation appear as different tones. Although their production is more cost-effective than that of monocrystalline cells, polycrystalline cells typically exhibit slightly lower performance. At the Ghardaïa site, polycrystalline panels of the Solaria brand, model S6P-2G, were selected. See **Fig. III.5.**

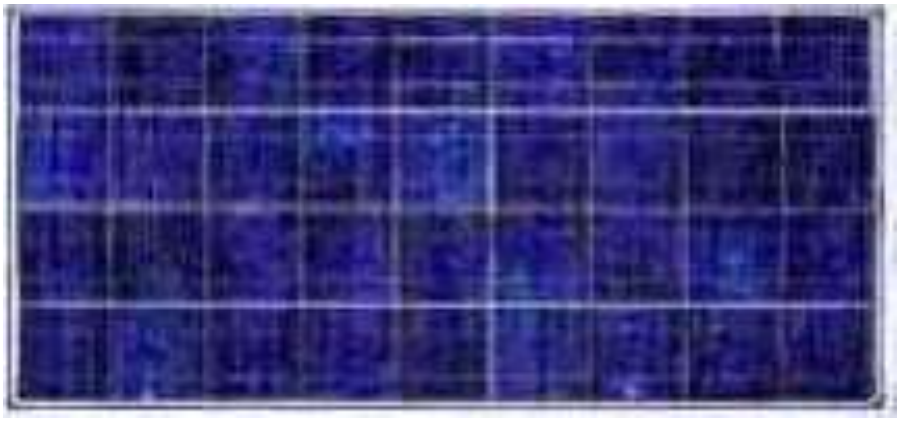

Fig III . 5: Polycrystalline PV Panel (Solaria S6P-2G) Deployed at the OUED-NECHOU Site, Ghardaïa.

IV.3. Amorphous Silicon (a-Si) Panels

Amorphous photovoltaic modules are characterized by significantly lower production costs. This technology employs very thin layers of silicon deposited onto glass, flexible plastic, or metal substrates using a vacuum vapor deposition process. At the Ghardaïa site, amorphous silicon panels of the SCHOTT brand, model ASI 103, were selected. See **Fig. III.6.**

Fig III . 6: Amorphous Silicon PV Panel (SCHOTT ASI 103) Deployed at the OUED-NECHOU Site, Ghardaïa.

IV.4. Thin-Film Panels (Cd-Te)

Thin-film photovoltaic modules, such as those based on cadmium telluride (CdTe), can absorb a broader range of the light spectrum. They demonstrate high sensitivity under low-light conditions and have a low-temperature coefficient, enhancing their performance across varying climatic conditions. At the Ghardaïa site, the installed thin-film panels are of the FIRST SOLAR brand, model FS-380. See **Fig. III.7**

Fig III .7: Cadmium Telluride (CdTe) Thin-Film PV Panel (First Solar FS-380) Deployed at the OUED-NECHOU Site, Ghardaïa .

Providing a comparative overview of efficiency and technical specification parameters, the following table summarizes the key characteristics of each photovoltaic technology used at the Ghardaïa power station.

Table III.2: PV Modules Technical Specifications and Characteristics

Photovoltaic Technologies	Monocrystalline (mc-Si)	Polycrystalline (pc-Si)	Amorphous (a-Si)	Cadmium Telluride (CdTe)
Electrical Characteristics				
Type	SOLARIA S6M-2G	SOLARIA S6P-2G	SCHOTT PROTECT ASI-103	FIRST SOLAR FS-380
Peak power	245 Wc	235 Wc	103 Wc	80 WC
Peak power tolerance	0 / +5 Wc	0 / +5 WC	7,1%	±5%
Module performance	15%	14.4%	30,4 V	11.1%
Max voltage (Vmpp)	30.33 V	30.49 V	30.9 V	48.5V
Max intensity (Impp)	8.08 A	7.71 A	3.33 A	1.65 A
Open circuit voltage	37.82 V	37.62V	41.1 A	60.8V
Short circuit current	8.52 A	8.40 A	3.94 A	1.88A
Max system voltage	1000 V	1000 V	1000 V	1000 V
Reference Standards	IEC 61730-1, IEC 61730-2, IEC 61215	IEC 61730-1, IEC 61730-2, IEC 61215	IEC 61730, IEC 61646	IEC 61730, IEC 61646
Thermal Characteristics				
NOCT (Nominal Operating Cell Temperature)	46 +/- 2 [°C]	46 +/- 2 [°C]	49 [°C]	45 [°C]
Temperature coefficient Isc	+0,015% [°K]	+0.02% [°K]	+0,08% [°K]	+0,04% [°K]
Temperature coefficient Voc	- 0,31% [°K]	- 0.29% [°K]	- 0,33% [°K]	- 0,27% [°K] to - 0,20% [°K]
Temperature coefficient Pmax	-0,46% [°K]	-0.43% [°K]	-0,20% [°K]	-0,25% [°K]
Mechanical Characteristics				

Dimensions(+/-3mm))	1646 x 991 x 38 mm	1646 x 991 x 38 mm	1308 x 1108 x 35 mm	1200 x 600 x 6,8 mm
Weight	19 kg	19 kg	20,8 kg	12 kg
Cells	60 (6 pouces), connectées en série, matrice 6x10	60 (6 inches), connected in series, matrix	72 (3x24)	154
Max load	5400 Pa	5400 Pa	5400 Pa (N / m2)	2400 Pa (N / m2)
Conditions Opératives				
Maximum operating temperature	-40 / +90 [°C]	-40 / +90 [°C]	-40 / +85 [°C]	-40 / +90 [°C]
Electrical Connections				
Connection Box	IP65	IP65	IP65	IP65 or IP67
Protection Diodes	3 bypass diodes, 11 A	3 bypass diodes, 11 A	/	Maximum series fuse rating: 3.5 A
Connectors	100 cm long cables IP67 quick connectors	100 cm long cables IP67 quick connectors	80 cm long cables . LC4 connectors	Avec câbles de 61 cm de longueur, 4 mm^2. MC4

V. Design of Fixed and Tracking Support Structures for Subfield Installations.

V.1. Fixed Photovoltaic Support Subfields

The Ghardaïa photovoltaic plant, serving as the experimental site, was selected to accommodate four different types of photovoltaic modules and two types of mounting structures: fixed and motorized (tracking) systems.

The fixed support structures are used for monocrystalline (mc-Si), polycrystalline (pc-Si), cadmium telluride (Cd-Te), and amorphous silicon (a-Si) panels. Both the fixed and tracking subfields are described in the layout and mounting plans. All structures, whether fixed or motorized, are ground-mounted using concrete blocks. They are constructed from galvanized steel and dimensioned according to the specific site conditions. The fixed structures are oriented southward with a tilt angle of 30°, which is close to the optimal tilt angle for the region , optimizing solar exposure, as illustrated in **Fig. III.8.**

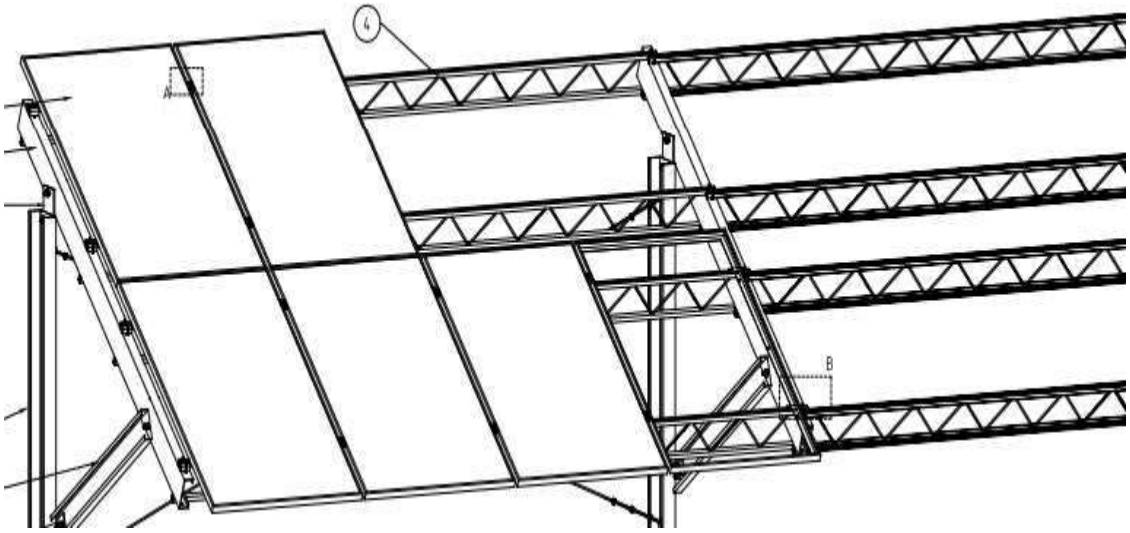

Fig III .8: Structural Diagram of the Fixed PV Support Structure.

Fig III.9 displays the various fixed support structures used for four photovoltaic technologies. These authentic images were captured on-site at the OUED-NECHOU station during an experimental investigation conducted over an average period of five years. They serve as practical illustrations of the installed systems. The configurations illustrate both the layout and mounting arrangements, emphasizing structural integrity and a south-facing orientation tilted at 30°. This tilt angle was chosen to optimize solar energy capture, as it closely matches the region's optimal inclination, thereby maximizing solar radiation exposure throughout the year.

Fig. III.9: Real Images of Fixed Support Structures for mc-Si, pc-Si, CdTe, and a-Si Photovoltaic Technologies at the OUED-NECHOU Site.

V.2. Single-Axis Tracking Photovoltaic Subfields

The tracking systems used in this study are single-axis trackers with the axis oriented along the north-south direction. Each tracker follows the sun's daily path from east to west via azimuthal movement. The photovoltaic panels mounted on these trackers are tilted at 30° to optimize sunlight capture. This configuration maximizes the solar radiation's angle of incidence throughout the day, enhancing the overall efficiency and power output of the photovoltaic system compared to fixed-tilt setups.

The single-axis tracking system is implemented in Subfields 1 and 2, which correspond to the motorized monocrystalline (mc-Si) and polycrystalline (pc-Si) technologies, respectively. **Fig III.10** shows an illustrative view of the single-axis support structures installed at the OUED-NECHOU station.

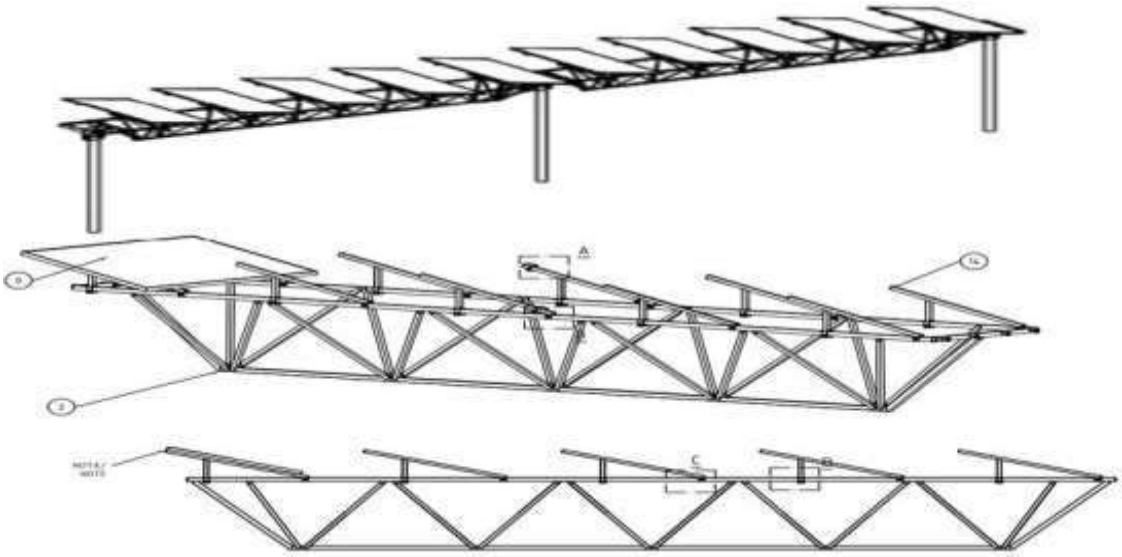

Fig. III.10: Structural Diagram of the Single-Axis Tracking PV Support System.

Fig III.11 presents real photographs of the single-axis tracking systems installed in Subfields 1 and 2, which are equipped with motorized monocrystalline (mc-Si) and polycrystalline (pc-Si) technologies. These images were captured on-site at the OUED-NECHOU station during the five-year experimental investigation, providing a visual representation of the systems under real operating conditions.

The photographs emphasize key physical features, including structural design, mounting configuration, and tracking mechanism alignment. Importantly, the panels are tilted at a 30° angle to optimize solar exposure, closely aligned with the region's ideal inclination.

This visual documentation supports the technical analysis by illustrating the practical implementation of the tracking systems and their contribution to enhancing energy yield.

Fig III. 11: Single-Axis Tracking Structures for mc-Si and pc-Si PV Subfields at the OUED-NECHOU Station **.**

V.3. Motorization System of the Ghardaïa Photovoltaic Power Plant (SILVER Electric Motors and Automation).

V.3.1. Description of the SILVER Tracking System

Each tracking system is driven by an electric motor integrated into the support structure and powered by a low-voltage (LV) panel within the photovoltaic power plant (see **Fig III. 12**). The movement of the trackers is synchronized using a proprietary programmable logic controller (PLC). For safety, the system automatically returns the PV modules to a horizontal position when high wind speeds are detected.

Fig. III.12: SILVER Single-Axis Tracking System Installed at the OUED-NECHOU Experimental Site in The Experiment.

V. 3.2- Programmable Logic Controller (PLC) for Tracking System Operation in the Ghardaïa Photovoltaic Power Plant.

The tracking system at the Ghardaïa photovoltaic power plant operates based on estimations of sunrise, sunset, and the sun's hourly trajectory derived from an eight-month site-specific study. This study, conducted by a Spanish company, was later translated into a control program embedded within a programmable logic controller (PLC), which governs the movement of the photovoltaic panels. The panel orientation is adjusted approximately every four to five minutes. The subfield consists of ten horizontal support bars, each fitted with photovoltaic modules. Each bar is equipped with an individual motor that enables the rotation of the PV panels. To optimize energy consumption, the motors are activated sequentially rather than simultaneously.

Fig III.13 illustrates the programmable logic controller (PLC) used to manage the tracking system, highlighting the essential role of automation in maintaining optimal panel alignment with the sun throughout the day

Fig. III.13: Programmable Logic Controller (PLC) Governing the Solar Tracking System

V.4. Electrical Connections of the Photovoltaic Generator

In the Ghardaïa photovoltaic power plant, the photovoltaic (PV) modules are connected in a series configuration to form module strings. This configuration increases the overall voltage output by connecting the positive output of one module directly to the negative input of the subsequent module .

Each panel is equipped with positive and negative output cables located on its rear side, allowing for direct interconnection between adjacent modules. For the terminal panels at

each end of the string, solar-grade cables are used to connect the string to the nearest junction box.

These solar cables are rated for a nominal voltage of $U_0 \geq 1$ kV DC and are identified by the FG21M21 designation, in accordance with IEC 20-29 standards.

The configuration of the module strings used in the Ghardaïa plant is summarized in Table III.3.

Table III.3: PV String Configuration and Output Voltage by Technology – Ghardaïa Photovoltaic Plant.

Type of PV Panel	Number of Panels Per String	String Voltage
Monocrystalline Silicium (mc-Si)	20	756.4
Polycrystalline Silicium (pc-Si)	20	752.4
Amorphous Silicium (a-Si)	19	780.9
Cadmium Telluride (CdTe)	13	790.4

The photovoltaic strings are arranged in parallel and connected to a junction box located on the module mounting frame, designed to accommodate a maximum of 16 series.

VI. Junction boxes and DC Combiner Boxes

VI . 1. Junction Boxes

The junction box, also known as the combiner box, is the central element where the wiring connections of the photovoltaic field are made. It enables the parallel connection of photovoltaic module strings in order to increase the total current output from the subfield. It also routes the cables toward the DC combiner box.

Each box can accommodate up to eight (8) strings (+ and −) at most. At its output, there is a main cable (+ / −) of larger cross-section, intended to supply the solar inverter.

The junction box is generally mounted on the module support structure or an adjacent stand. It is made of durable plastic and constructed to maintain a fully sealed enclosure to avoid any ingress of dust or moisture. This is achieved through compliance with the IP65 protection rating, which guarantees complete sealing against dust and protection from low-pressure water jets.

- **The junction box contains:**
  - Terminals for each string in the subfield
  - A fuse for each series of photovoltaic modules and for each polarity
  - A disconnect switch

- A surge protector
- Test points for each branch
- A transducer for measuring the current and voltage of the corresponding module strings.

To provide a clearer understanding of the junction box's configuration, its essential components are detailed in **Table III.4.**

Table III. 4 : Junction Box Components of the PV Subfields

Component	Description	Description	Description
01	Double Fuse Holder 32A	**07**	Main Switch
02	300 mm² Terminal Block	**08**	35 mm² Blue Terminal Block
03	Power Supply	**09**	35 mm² Grey Terminal Block
04	35 mm² Yellow-Green Terminal Block	**10**	Converter / Inverter
05	End Stop Block	**11**	PLC Module AI531-XC
06	Surge Arrester	**12**	PLC Module AI541-XC
13	PLC Plate TU516-XC	**17**	6 mm² Trimmable Terminal Block
14	PLC Plate TU518-XC	**18**	Separator
15	Parallel Shunts	**19**	Voltmeter Transducer
16	6 mm² Yellow-Green Terminal Block	**20**	Upper End Stop Block

The following **Fig III.14** illustrates the internal layout and components of the junction box used in the PV subfields, providing a clearer understanding of its configuration and wiring

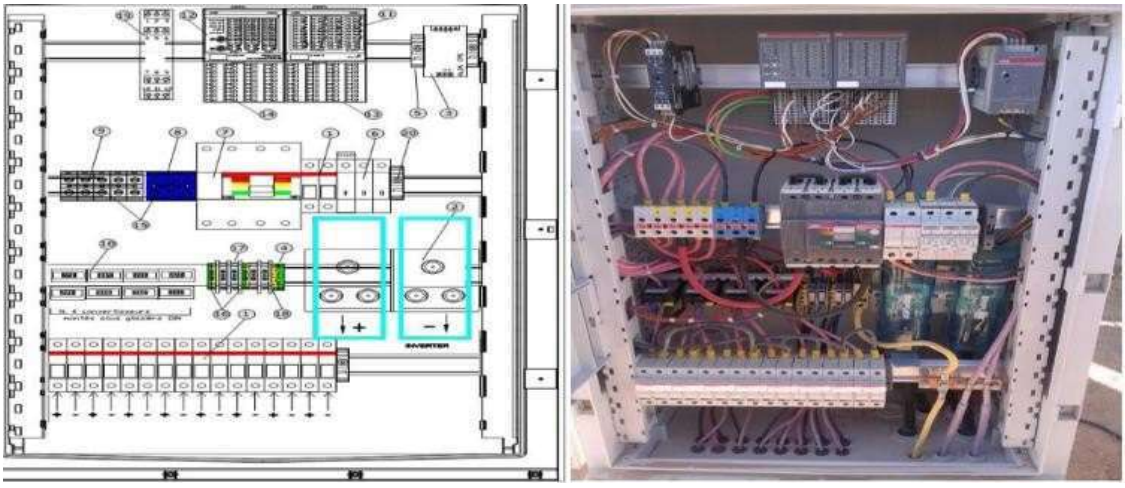

Fig III.14: Internal Elements of the Junction Box: Real and Schematic View.

After the connection is made at the junction box level, all the boxes within a subfield are connected in parallel to the DC combiner box .

VI.2 DC Combiner Box

Each junction box is connected via an FG7OR cable (U0/U = 0.6/1 kV) to a DC combiner box, which is installed near the reference inverter inside the technical (or electrical) building. Inside the DC combiner box, the outputs from all the junction boxes belonging to a specific subfield are connected in parallel.

The output of the combiner box consists of a main positive (+) and negative (–) terminal for each subfield. This output is then directly connected to the inverter.

Within the combiner box, a set of fuses is arranged in parallel. For each fuse, one side is connected to the DC cable coming from the corresponding junction box, while the other side is connected in parallel with the other fuses through a copper busbar. This configuration ensures safe and efficient aggregation of currents from the entire subfield before feeding them to the inverter.

Fig III.15 presents an on-site view of the DC combiner box used at the Ghardaïa photovoltaic site. This box collects the DC outputs from various junction boxes (connected to PV strings) and consolidates them before forwarding the combined output to the inverter.

Fig. III.15: On-site view of a DC combiner box used to aggregate and route DC power from multiple photovoltaic strings to the inverter at the Ghardaïa PV plant.

VII. Detailed Description, Operation, and Main Function of the Photovoltaic Power Plant

VII.1. Configuration and Operation of the Photovoltaic Generator

The photovoltaic generator at the OUED-NECHOU power station in Ghardaïa is composed of an integrated system of photovoltaic (PV) panels designed to convert solar radiation into direct current (DC) electricity.

This conversion process forms the core of the station's renewable energy generation, supporting real-time injection of power into the national grid.

The energy transformation process begins when solar radiation is captured by an array of PV panels arranged in multiple subfields. These panels are mounted on support structures optimized for solar exposure. The DC electricity generated is then collected via junction boxes and DC combiner boxes, which consolidate and protect the electrical flow from multiple strings of panels.

This collected DC energy is directed to the plant's control and command system, managed through a Programmable Logic Controller (PLC) specifically an AC500 module. This system guarantees continuous monitoring, safety management, and dynamic regulation of operational conditions.

Inverters convert the stabilized direct current (DC) into alternating current (AC) and communicate via the RS-485 protocol to ensure synchronized functionality and real-time system monitoring. After the AC conversion, the electrical power is routed to a step-up transformer that raises the voltage to 30 kV, suitable for medium-voltage distribution and efficient grid integration.

The OUED-NECHOU plant has an installed capacity of 1.1 MW and delivers electricity instantaneously based on incoming solar irradiance. The entire process, from capturing solar energy to producing high-voltage output, is fully automated and equipped with instrumentation systems that ensure reliable performance, optimal conversion efficiency, and operational safety.

This explanation corresponds directly to **Fig III.16,** which illustrates the complete structure of the photovoltaic generator at OUED-NECHOU. The figure visually presents each component in the energy conversion chain: from the photovoltaic panels and junction boxes to the control system, inverters, transformer, and finally to the grid connection point. Together, this system enables continuous, efficient injection of clean energy into the medium-voltage distribution network

.

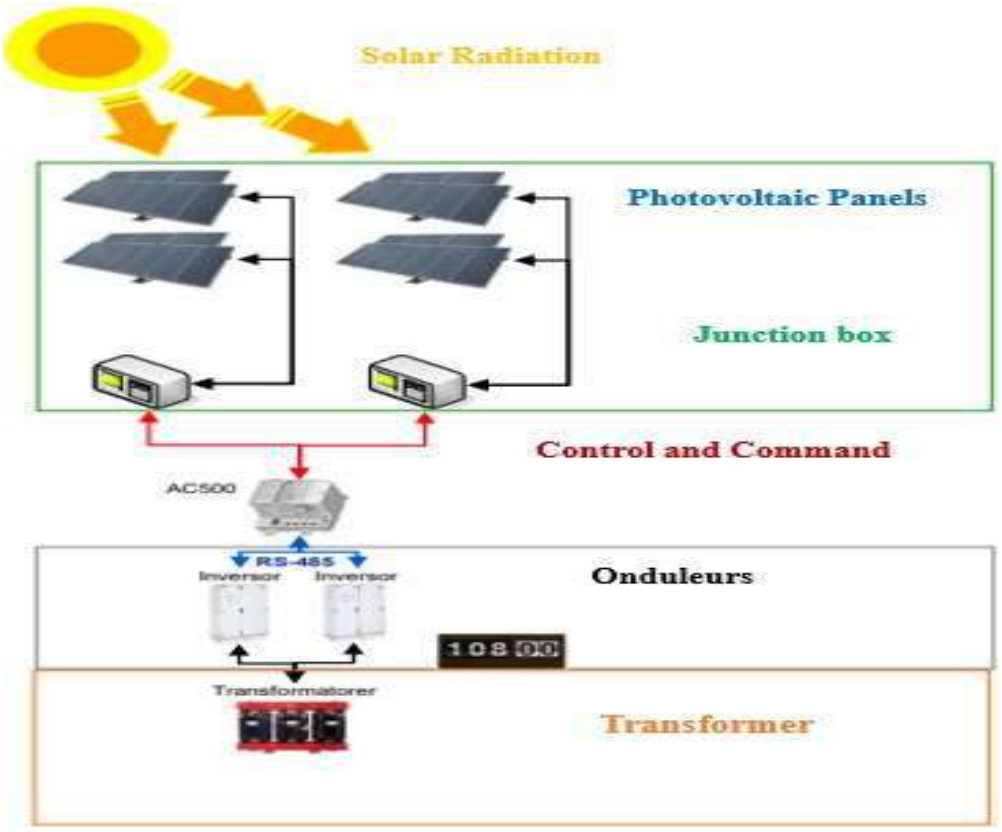

Fig III.16: Photovoltaic Generator and Grid Injection System Schematic at OUED-NECHOU, Plant.

VIII. Comparative Evaluation of Fixed and Tracking PV Systems Using Real Performance Data from Oued-Nechou, Ghardaïa .

The present work provides a technical comparison and performance evaluation of four fixed photovoltaic (PV) subfields and tracking systems using real operational data from OUED-NECHOU, Ghardaïa . It examines how different tracking mechanisms influence power and energy output under the unique environmental conditions of the site. The objective is to identify the most suitable PV technology and mounting configuration for photovoltaic plants in similar Saharan regions, which are characterized by harsh and variable climates. Additionally, the study considers the effect of a fixed installation angle of approximately 30°, deemed close to the optimal tilt for maximizing solar energy capture in this environment. This assessment aims to recommend the most efficient and reliable photovoltaic (PV) technology and system design to enhance energy production and sustainability in desert and semi-arid regions such as Ghardaïa . The analysis covers the entire process, from capturing solar energy to injecting it into the grid, ensuring a thorough evaluation of photovoltaic system performance under real-world conditions.

IX. Geographical and Meteorological Data of Photovoltaic Power Plants in OUAD-NECHOU, Ghardaïa.

IX.1. Geographical Data of OUAD-NECHOU.

The Ghardaïa photovoltaic solar power plant, located in southern Algeria, is part of the renewable energy development program initiated by the supervisory ministry. It is situated near the village of OUED-NECHOU, 15 km north of Ghardaïa along National Road No. 01, with a nominal power capacity of approximately 1100 kWp. The site is bordered by National Road No. 01 to the north and west, and vacant land to the east and south. The plant's precise coordinates are 32°34'43.79" N latitude and 3°41'55.36" E longitude, at an altitude ranging from 450 to 566 meters. The closest wilayas are Laghouat and Ouargla. The topography of the site is relatively flat, with a gentle east-west slope.

IX.2. Meteorological Data of OUAD-NECHOU

Ghardaïa's hot, dry climate presents extreme environmental conditions, with temperatures ranging from -5°C to +50°C in the shade. Wind speeds can reach up to 28 m/s, and the maximum recorded relative humidity is 74% at 25°C. Solar irradiations during the summer months can reach 900-1000 W/m². The area also experiences significant temperature fluctuations between day and night 15 to 20°C and frequent winds carrying fine sand particles, factors critical for plant design and maintenance. Despite these challenges, the plant is located in seismic zone 0, indicating low seismic risk as per Algerian regulations (RPA 99).

Fig III.17 below illustrates the geographical location of the OUED- NECHOU photovoltaic power plant, situated in the Ghardaïa region of southern Algeria. This map serves to provide spatial and environmental context for the study area where the experimental data used in this research was recorded.

The specific geographical setting of the plant is particularly important, as the region's unique climatic and meteorological conditions such as high solar irradiance, temperature variations, and wind patterns play a significant role in influencing the performance and energy output of photovoltaic technologies. By identifying the exact location of the installation, this figure supports a better understanding of the environmental factors that affect the efficiency and reliability of the photovoltaic systems evaluated in this work.

Fig III. 17 : Geographical location of the photovoltaic power plants: 1.1 MWp OUED-NECHOU, Ghardaïa City **[128].**

In this section, following the presentation of the geographical and meteorological data of the OUED-NECHOU photovoltaic power plant, this study provides a comprehensive analysis and evaluation of the performance of four fixed photovoltaic subfields: monocrystalline silicon (mc-Si), polycrystalline silicon (pc-Si), amorphous silicon (a-Si), and cadmium telluride (CdTe). In addition, it presents an experimental performance evaluation of four other photovoltaic subfields, each employing different configurations: two with single-axis tracking systems and two with fixed systems, using both mc-Si and pc-Si technologies.

The research was conducted in the Saharan environment of OUED-NECHOU Ghardaïa, at the SKTM Electricity and Renewable Energy Company unit, focusing on real weather conditions rather than Standard Test Conditions (STC). The study emphasizes key performance indicators, including peak output power (kW), long-term daily power production (kW), and average daily output power (kW) recorded over four experimental days, accounting for seasonal variations. It also evaluates the power output differences

among the fixed photovoltaic subfields in terms of power enhancement, as well as the improvement achieved by single-axis tracking systems compared to fixed systems, with particular attention to the percentage gain in output power.

To ensure accurate data collection and analysis, daily energy generation (kWh) was measured at four-minute intervals. Additionally, the study investigates the impact of real-time meteorological parameters recorded at the same intervals on subfield performance. These parameters include solar irradiation at a 30° tilt (W/m²), ambient temperature (°C), module temperature (°C), wind speed (m/s), and relative humidity (%). The analysis takes into account seasonal climatic variations and their influence on these meteorological factors during selected experimental days in winter, spring, summer, and fall.

XI.3. Experimental Analysis of Real Wind Speed (m/s) and Relative Humidity (%) Data in the OUED-NECHOU Area .

Researchers and professionals in photovoltaic technology and power plant performance emphasize the importance of understanding regional environmental conditions. Constance Kalu et al., **[129]** utilize 22 years of meteorological data from NASA's global database, including solar insolation and air temperature, to perform a comparative analysis of polycrystalline, monocrystalline, and thin-film PV technologies using PVsyst version 5.21. Similarly, A. Allouhi et al., **[130]** employed METEONORM 7 data, including wind velocity, ambient temperature, and solar irradiance, to compare the performance of monocrystalline and polycrystalline PV technologies. Their study evaluates a 2 kWp grid-connected PV plant in Meknes, Morocco, combining recorded data from 2015 and simulated results to assess the power generation capabilities of these technologies. A. Al-Otaibi et al., **[131]** assessed the performance of CIGS thin-film PV systems installed on rooftops in Kuwait by monitoring key meteorological parameters such as solar radiation, ambient temperature, wind speed, and module temperature. Using a reference cell and pyranometer for solar radiation measurements, the study recorded data at five-minute intervals over twelve months to evaluate the impact of environmental factors on PV system efficiency in Kuwait's climate.

It is crucial to have accurate weather data to evaluate and optimize the performance of photovoltaic systems. This necessitates using advanced technical instruments to gather experimental data on local weather conditions.

The meteorological station's data acquisition system is installed on the rooftop of the Technical Room at the photovoltaic power plant. It is equipped with devices that provide essential climatic information, including 30° tilted solar irradiance (W/m2), ambient temperature (°C), wind speed (m/s) and direction, and relative humidity (%). Data were collected every 4 minutes from 06:00 AM to 19:52 PM on January 1ST, May 1ST, July 1ST, and October 1ST, representing different seasons (Winter, Spring, Summer, and Fall). **Table III.5** . Shows a list and specifications of instruments used by manufacturers.

Table III.5 : Technical Parameters of the Measuring Instruments

Measurement Instruments Parameters	**Thermo-hygrometer**	**Anemometer sensor**	**Pyranometer (Inclined radiation)**
Brand	LSI LASTEM	LSI LASTEM	LSI LASTEM
Model	DMA 672.1	DNA 121#C	DPA 053
County of Origin	Italy	Italy	Italy
Measurements	Relative Humidity (%)	Wind Speed radiation Outputs (m/s)	Solar radiation
Measurement range	0 to 100%	0 to 60 m/s	0-1300W/m^2
Precision	3.00%	0 to 3 m/s =1.5 % >3m/s =1%	5 W/m^2
Resolution	0.5 %	0.07 m/s	10 W/m^2

IX.3.1. Analysis of Relative Humidity (%) Across Experimental Days

Fig. III.18 . Presents experimental relative humidity (%) data measured with a thermo-hygrometer over four days, with recordings taken from 06:00 AM to 19:52 PM. Each curve corresponds to a different experimental day. The results reveal a consistent diurnal pattern, characterized by higher humidity levels in the early morning and late evening, followed by a noticeable decrease during midday and afternoon hours, indicating a regular daily cycle.

On October 1st , relative humidity peaked at 90% at 06:00 AM and gradually declined to 42% by 19:52 PM. A similar trend was observed on January 1st , with RH starting at 67% at 06:00 AM and dropping to 45% by 19:48 PM. On May 1st and July 1st , relative humidity was significantly higher in the early morning, with readings of 42% at 06:00 AM on May 1st and 35% at the same time on July 1st . Throughout the day, humidity levels steadily

decreased, reaching 17% by 19:52 PM on May 1st and dropping to 10% by 19:52 PM on July 1st .

The fluctuations in relative humidity (RH) in the OUED-NECHOU region are primarily driven by pronounced diurnal temperature variations, as illustrated in Figures I.14 to I.17. During the day, intense solar heating causes a significant decrease in RH, while sharp drops in temperature in the early morning and at night result in a temporary rise in RH. This pattern reflects a clear inverse relationship between temperature and relative humidity: as temperature increases, RH decreases, and vice versa.

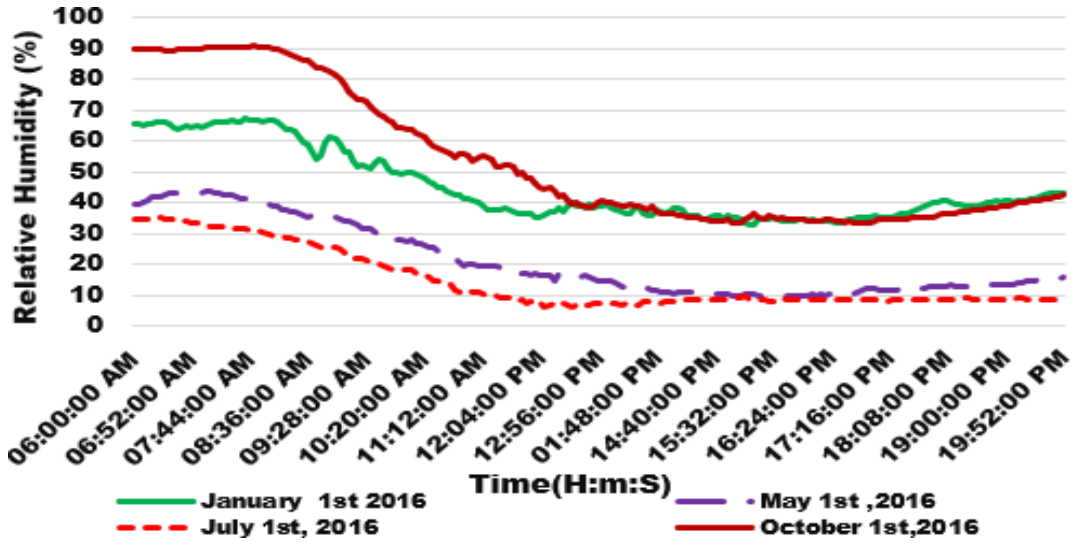

Fig III.18: Relative humidity data (%) over four experimental days , each representing a different season in 2016 .

IX.3.2. Analysis of Wind Speed (m/s) Across Experimental Days

Fig III. 19. Showcases experimental wind speed data recorded by an anemometer from 06:00 AM to 19:52 PM across four days, each representing a different season. The data illustrates the diurnal wind speed profiles for January 1st , May 1st , July 1st , and October 1st , 2016.

On January 1st , the wind speed remains consistently low throughout the day. It begins at 0.02 m/s at 06:00 AM and gradually rises to reach a peak of 2.56 m/s at approximately 06:32 PM, reflecting the calm wind conditions typical of winter. On May 1st , wind speed is more variable. It peaks twice in the morning, with the highest value of 8.37 m/s observed around 07:20 AM and again near 09:16 AM. After these peaks, the wind speed steadily declines to approximately 4.16 m/s in the late afternoon, indicating a transition from turbulent morning conditions to a more stable evening atmosphere. On July 1st , the wind profile shows a steep increase from 7.22 m/s at 06:00 AM to a maximum of 9.05 m/s at

07:24 AM the highest value recorded among all days. This is followed by a significant decline, reaching a minimum of 1.03 m/s around 05:30 – 06:00 PM. The sharp morning rise and afternoon fall highlight strong thermal activity and atmospheric instability typical of summer. On October 1st , the wind speed shows a smoother trend. It increases gradually to a peak of 7.20 m/s around 11:36 AM, then steadily decreases to 2.67 m/s by 07:48 PM, indicating moderate and stable autumn wind patterns.

Seasonal variations in wind speed are closely linked to atmospheric pressure gradients driven by temperature differences. During summer, intense solar heating over the Sahara Desert generates strong thermal gradients and upward air motion, leading to enhanced wind speeds, as observed on July 1st . In contrast, the more astonishing winter season results in weaker pressure differentials and reduced wind activity, as seen on January 1st . Spring and autumn exhibit transitional wind patterns characterized by moderate turbulence and evolving atmospheric stability.

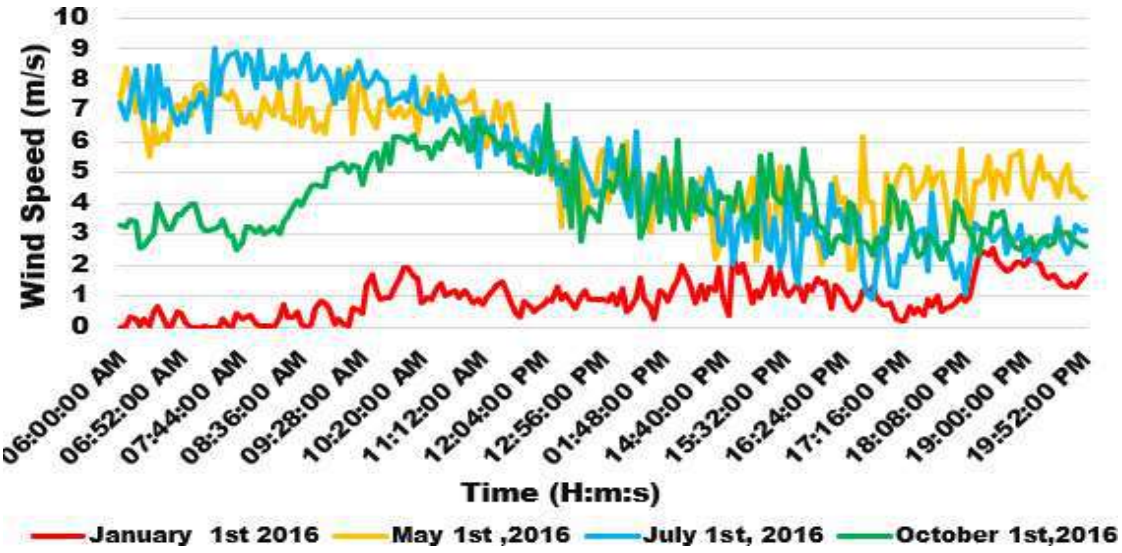

Fig III.19: Wind Speed data (m/s) over four experimental days , each representing a different season in 2016 .

Figs 18 and **19** clearly demonstrate a significant inverse correlation between relative humidity (%) and wind speed (m/s) in the OUED-NECHOU region. Specifically, during the spring and summer months (May 1st and July 1st), high wind speeds coincide with lower relative humidity, whereas in the winter and fall months (January 1st and October 1st) , lower wind speeds are observed alongside higher humidity levels. This seasonal pattern suggests that as wind speed increases, relative humidity tends to decrease, likely due to intensified evaporation and air mixing effects in warmer months.

These findings underscore the impact of seasonal temperature variations on atmospheric moisture and wind dynamics in the region, highlighting the complex interplay between temperature, wind speed, and humidity in shaping local climate characteristics.

IX.4. Performance Assessment Methods for Photovoltaic Subfields

In this section, we present a comprehensive evaluation of the performance of photovoltaic (PV) subfields installed at the PV accessory center in the OUED-NECHOU region of Ghardaïa, Algeria. The objective is to identify the most effective configuration for deployment in desert environments by examining two comparative approaches: (1) between four fixed-tilt PV subfields employing different photovoltaic technologies, and (2) between fixed and single-axis tracking configurations.

Each of the four subfields in the fixed configuration features a uniform nominal capacity of 100 kW and is installed facing south at a tilt angle of 30°, closely aligned with the region's optimal inclination for solar capture. The study focuses on four critical performance indicators: (I) Output Power analyzing both peak values and the full-day production from sunrise to sunset, (II) Environmental Factors Influencing Performance such as temperature, irradiance, wind speed, and humidity, (III) Augmentation Percentage reflecting the gain in power output relative to baseline performance, and (IV) Daily Energy Yield.

The experimental campaign involved high-frequency data collection every four minutes between 06:00 AM and 19:52 PM, allowing for detailed monitoring of system behavior. The investigation was carried out across four representative days January 1st (Winter), May 1st (Spring), July 1st (Summer), and October 1st (Fall) to capture seasonal variability. On average, the mornings provided 6 hours and 50 minutes of solar generation, while the evenings contributed approximately 6 hours and 36 minutes.

The results, presented in Figures 22 to 25, illustrate the output power comparison among the four fixed-tilt photovoltaic (PV) subfields. In contrast, Figures 26 to 29 highlight the performance differences between fixed and single-axis tracking systems. This dual analysis offers valuable insights into the most efficient and economically viable PV technologies and configurations for large-scale deployment in Algeria's arid regions.

IX.4.1 Analysis of Experimental Results: Peak Output Power (kW) and Long-Term Daily Performance

The comparison of photovoltaic (PV) technologies in terms of energy productivity [**132-133**] and grid energy injection [**134-136**] has been the focus of numerous previous studies conducted in both research laboratories and operational photovoltaic power plants

[**137-139**]. The performance of grid-connected PV systems is typically evaluated using key indicators such as final yield (Yi), array yield (Ya), reference yield (Yr), performance ratio (PR), and the total energy generated by the system **[133], [140-141].** Assessments may also rely on experimental data, including peak output power and average daily or seasonal power output.

In line with this evaluation approach, Constance Kalu et al. **[129]** conducted a simulation- based study using PVsyst version 5.21 and NASA meteorological data, alongside a hypothetical load demand. Their analysis compared polycrystalline (pc-Si), monocrystalline (mc-Si), and thin-film PV technologies. The findings revealed that thin-film technology, although offering low array losses, favorable performance metrics, and a low unit cost of energy, required significantly more surface area for installation. In contrast, polycrystalline PV modules, which provide higher efficiency and require less space, were considered more suitable for the specific site conditions due to their balanced performance and compact design Furthermore, Allouhi et al., (2016) **[130]** assessed the performance, economic feasibility, and environmental impact of 2 kWp grid-connected PV systems (Poly-Si and Mono-Si) installed at the High School of Technology, Meknes, Morocco. The two PV fields are oriented south at a fixed tilt angle of 30°. Using METEONORM data and PVSYST simulations, the study found Poly-Si modules slightly outperform Mono-Si, with a higher annual average daily final yield. The Meknes systems perform better than those in Greece, Ireland, India, South Africa, and the UAE. Economically, Poly-Si has a lower levelized cost of electricity ($0.073/kWh) and shorter payback time (11.10 years) compared to Mono-Si ($0.082/kWh and 12.69 years). The systems also offer significant environmental benefits, reducing CO2 emissions by about 5.01 tons annually. The International Electrotechnical Commission (IEC) recommends several parameters for assessing PV power plant performance, as outlined in IEC-61724 standards. Key parameters include the final yield (Yf), reference yield (Yr), performance ratio (PR), and capacity factor (CF) Cubukcu & Gumus., 2020 **[141].** Pirzadi & Ghadimi ., 2020 **[142].** Veerendra Kumar et al., 2022 **[43].** Ismail Bendaas et al., 2023 **[144]** ,IRFAN JAMIL et al.,2022 **[145],** A. Fezzani et al.,2022 **[146], [142],[147 - 151].** These indicators are crucial for evaluating the efficiency and profitability of various PV power plants under different climatic conditions and for detecting potential issues or failures.Building on this. El Mehdi Karami et al., (2018) **[152]** evaluated the performance of grid-connected PV systems with monocrystalline, polycrystalline, and amorphous silicon modules in Casablanca, using 2016 data and PV syst

simulations. They assessed performance parameters such as annual energy generation, final yield, reference yield, performance ratio, and capacity factor. Results indicated that simulations were accurate for energy production and irradiation but less accurate for ambient temperature. Performance ratios were 76.94% for p-si, 78.02% for c-si, and 67.28% for a-si, with final yields of 4.61, 4.68, and 4.02 kWh/kWp/day, respectively. The study confirms PVsyst's reliability but suggests using on-site temperature measurements for better simulation accuracy. Assessing solar panel performance by analyzing output power, a critical electrical parameter, is essential for comparative studies, especially when considering the specific meteorological conditions of a given location. El Mehdi Karami et al., (2018) **[152]** conducted additional research to evaluate the performance of different solar panel technologies. They assessed the DC power output from the modules and the AC power from the inverters using real-time measurements under various weather conditions clear, cloudy, and rainy. Additionally, Layachi Zaghba et al.,(2022) **[153]** conducted an experimental study on an 11.28 kWp grid-connected solar system with sun tracking over one year at the Applied Research Unit of Renewable Energy in Ghardaia, Algeria. The study combines simulation data from PVSYST with experimental results and features three 3.76 kWp solar tracker configurations: fixed-axis, one-axis, and dual-axis. In a specific section, it compares the power output of single-axis and dual-axis trackers with fixed-axis systems under varying weather conditions, including clear and cloudy skies. Arechkik Ameur et al.,(2019)**[154]** aimed to analyze and compare various indices for evaluating the performance of three grid-connected photovoltaic technologies (a-Si, pc-Si, and mc-Si) in Ifrane, Morocco, at Al Akhawayn University. The study examines systems generating 2 kWp each, installed facing south on a flat surface, tilted at 32°, with zero azimuth. It evaluates AC power output under sunny and snowy conditions, considering the impact of temperature on power output.

IX.4.1.1. Comparative Daily Power Analysis (kW) of Four Fixed PV Subfields (mc-Si, pc-Si, a-Si, and CdTe) .

This section presents a comparative performance analysis of four stationary photovoltaic subfields, each with an identical capacity of 100 kW, installed at the PV center. The objective is to evaluate the effectiveness of different PV technologies under the region's specific climate conditions. All subfields are south-facing and tilted at 30°, an angle selected

to match the site's optimal orientation for maximizing solar energy capture and reflecting seasonal performance variations. Data collection was conducted every 4 minutes, from 06:00 AM to 19:52 PM, to ensure high-resolution monitoring and accurate performance assessment. Each experimental day corresponds to one of the four seasons in 2016: January 1st (Winter), May 1st (Spring), July 1st (Summer), and October 1st (Fall). The output power results for the four subfields across these representative days are illustrated in the figures below.

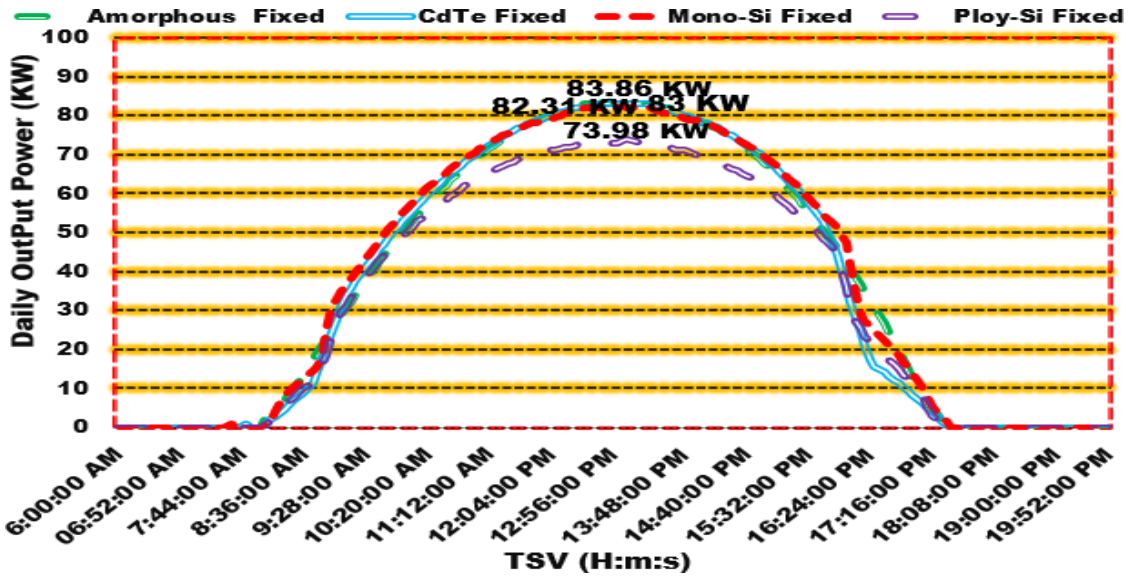

Fig III.20. Comparison of Output Power (kW) Among Four Fixed PV Subfields (mc-Si, pc-Si, a-Si, and CdTe) on January 1st , 2016 A Winter Day .

Fig. 20 illustrates the output power profiles of four fixed-tilt photovoltaic subfields (a-Si), (CdTe), (mc-Si), and (pc-Si) recorded on January 1st , 2016, representing winter conditions. At the beginning of the day, the power outputs of all four PV technologies were nearly identical, indicating similar performance during low irradiance periods. As solar irradiance increased toward midday, noticeable performance variations emerged. Around 13:00 PM, the a-Si subfield delivered the highest peak output, reaching 83.86 kW, closely followed by CdTe at 83.00 kW, mc-Si at 82.31 kW, and pc-Si trailing behind at 73.98 kW. These differences in peak performance reflect the varying efficiencies and spectral responses of each PV technology under the specific climatic conditions of the winter season. Notably, mc-Si demonstrated superior output, likely due to its high conversion efficiency and favorable temperature coefficient under clear winter skies.

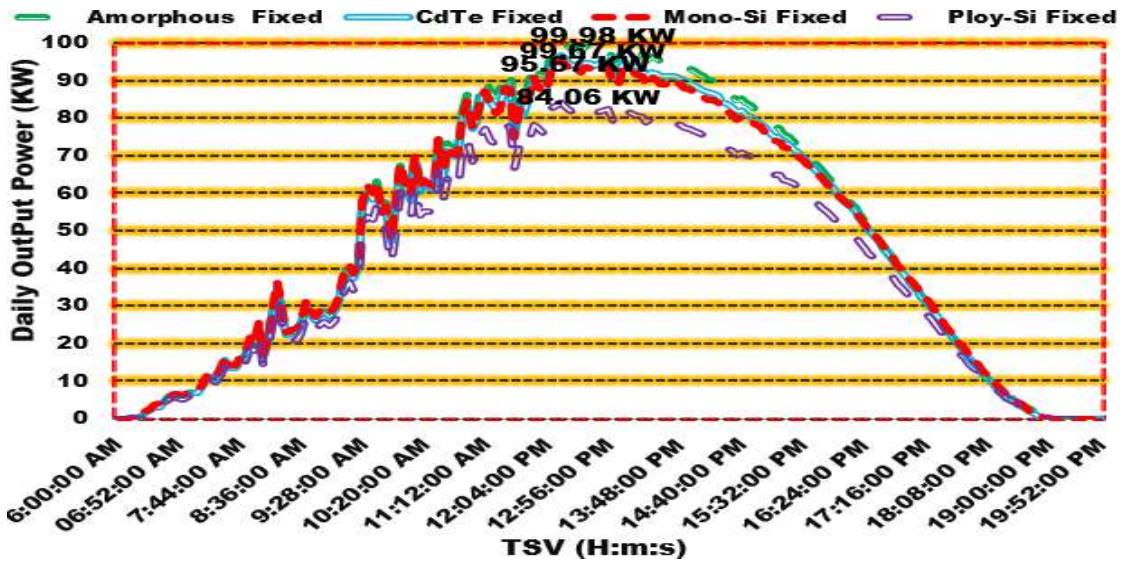

Fig III.21. Comparison of Output Power (kW) Among Four Fixed PV Subfields (mc-Si, pc-Si, a-Si, and CdTe) on May1st , 2016 A Spring Day .

On May 1st , 2016, a typical spring day, the performance of four fixed photovoltaic subfields a-Si, CdTe, mc-Si, and pc-Si was monitored, and **Fig III. 21** illustrates this. The figure captures the full-day output power curves, highlighting the peak values attained by each technology under identical environmental conditions.

From 06:00 AM to 12:00 PM**,** the a-Si, CdTe, and mc-Si subfields exhibited closely aligned performance trends, reflecting similar irradiance responses under favorable spring conditions. Among them, the a-Si subfield reached the highest peak output of 99.98 kW**,** nearly achieving its rated capacity of 100 kW. This exceptional performance may be attributed to the stable ambient temperature and consistent solar irradiance during this season. The CdTe and mc-Si subfields followed closely, with outputs of 96.67 kW and 95.67 kW**,** respectively, indicating their strong performance and high efficiency under spring conditions. Conversely, the pc-Si subfield lagged, recording a lower peak output of 84.06 kW**,** which may point to either higher thermal sensitivity or reduced efficiency compared to the other technologies under similar conditions.

These results underscore the influence of both material properties and environmental factors on PV system performance, providing valuable insight into the seasonal behavior of different PV technologies.

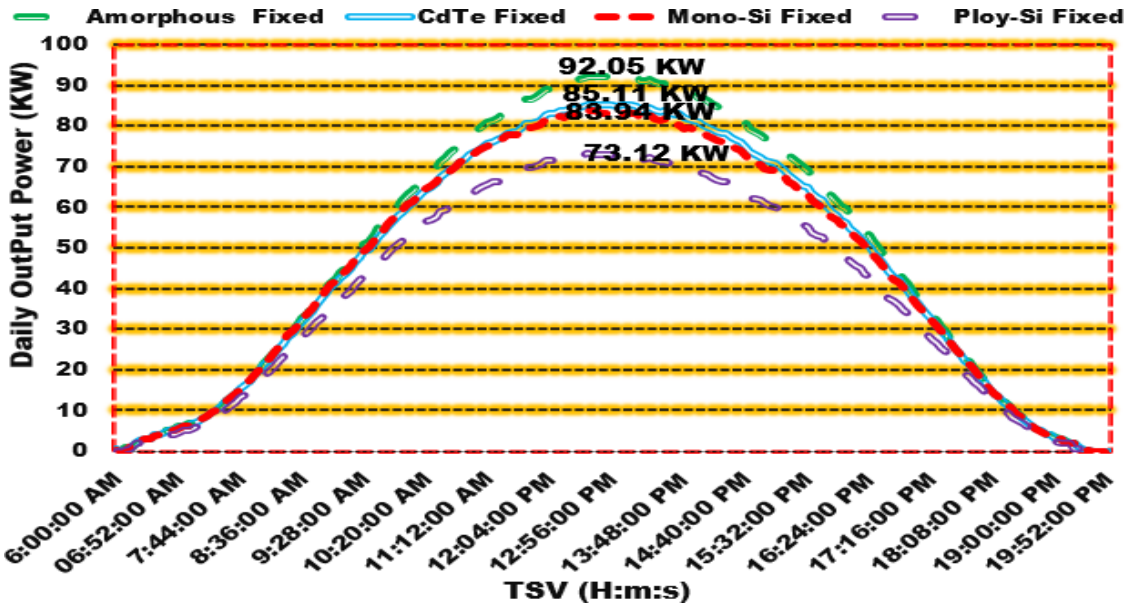

Fig III .22. Comparison of Output Power (kW) Among Four Fixed PV Subfields (mc-Si, pc-Si, a-Si, and CdTe) on July 1st , 2016 A Summer Day .

Fig III. 22. Presents the power output profiles of the four fixed photovoltaic (PV) subfields amorphous silicon (a-Si), cadmium telluride (CdTe), monocrystalline silicon (mc-Si), and polycrystalline silicon (pc-Si) on July 1st , 2016, a typical summer day. The a-Si subfield exhibited the highest peak performance, reaching 92.05 kW, which is close to its optimal capacity. CdTe and mc-Si followed with peak outputs of 85.11 kW and 83.84 kW, respectively. Meanwhile, the pc-Si subfield delivered the lowest peak output at 73.12 kW. In terms of overall curve profiles, all technologies exhibited a symmetrical bell-shaped curve, reflecting stable and clear irradiance conditions throughout the day. Notably, the a-Si and CdTe subfields not only peaked higher but also maintained elevated power levels over a longer period around midday, indicating better performance in high-temperature summer conditions. This suggests that thin-film technologies, particularly a-Si, might have superior thermal behavior compared to crystalline silicon technologies under elevated ambient temperatures.

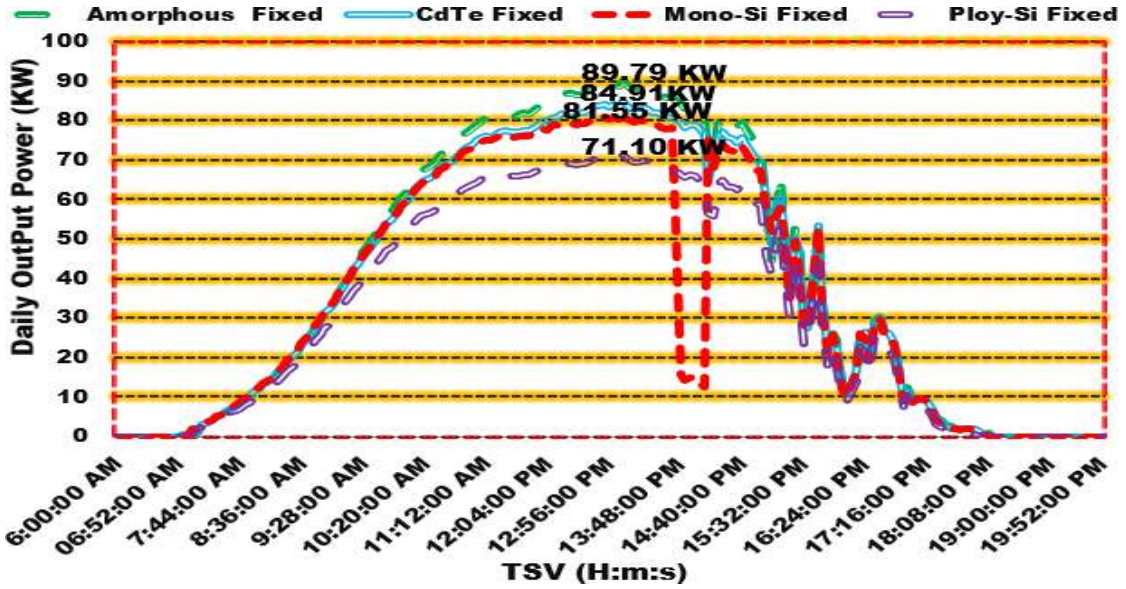

Fig III .23. Comparison of Output Power (kW) Among Four Fixed PV Subfields (mc-Si, pc-Si, a-Si, and CdTe) on October 1st , 2016 A Summer Day .

Full-day monitoring of output power for four fixed photovoltaic subfields (a-Si, CdTe, mc-Si, and pc-Si) on October 1st under real operating conditions, as presented in **Fig. 23**. The experimental results show that among the four fixed photovoltaic subfields, the amorphous silicon (a-Si) subfield delivered the highest peak output power, reaching 89.97 kW. This was followed by the cadmium telluride (CdTe) subfield with 84.91 kW, then the monocrystalline silicon (mc-Si) with 81.55 kW, while the polycrystalline silicon (pc-Si) subfield recorded the lowest peak, at 71.10 kW.

These results suggest that a-Si and CdTe technologies are more efficient under the specific conditions of October 1st , which likely included lower ambient temperatures and moderate irradiance levels, common during early autumn. The superior performance of a-Si and CdTe may be attributed to their favorable temperature coefficients, which make them less sensitive to performance losses in cooler environments.

Based on real performance data collected over four experimental days, January 1st , May 1st , July 1st , and October 1st , a clear distinction emerged among the four fixed photovoltaic subfields (a-Si, CdTe, mc-Si, and pc-Si). Across all measured dates, the amorphous silicon (a-Si) subfield consistently demonstrated the highest output power, outperforming the other technologies regardless of seasonal variation. This consistent performance highlights the robustness of a-Si technology under varying environmental conditions, particularly in terms of temperature fluctuations and solar irradiance levels.

The CdTe subfield followed closely behind a-Si in several instances, showcasing stable performance, particularly in moderate weather conditions. Meanwhile, the monocrystalline silicon (mc-Si) subfield exhibited intermediate output levels but showed improved efficiency during periods of high irradiance. Lastly, the polycrystalline silicon (pc-Si) subfield registered the lowest power output across all experimental days, indicating comparatively lower efficiency under the same conditions.

These findings reinforce the suitability of amorphous silicon as a highly effective and reliable option for photovoltaic power generation, particularly in regions with diverse seasonal conditions. Its favorable temperature coefficient and ability to maintain stable output throughout the year reaffirm its viability for deployment in fixed-mount solar systems in the region (The Photovoltaic Station). As such, this technology stands out as the optimal choice among the tested subfields for consistent, high-yield energy production.

IX.4.1.2. Experimental Comparison of Daily Power Output from Fixed and Single-Axis mc-Si and pc-Si PV Subfields .

Two different crystalline silicon photovoltaic technologies monocrystalline silicon (mc-Si) and polycrystalline silicon (pc-Si) were evaluated under two types of mounting configurations: fixed-axis and single-axis tracking systems, both installed at a tilt angle of 30°. Each PV subfield consisted of identical 100 kW systems to ensure a fair comparison. Real-time data were collected every four minutes using calibrated field measurement instruments, with the recorded results visualized in **Fig III. 26–29.** The comparative analysis focused on two primary metrics: the peak DC output power and the long-term daily power generation. Measurements were conducted on four specific dates, January 1st , May 1st , July 1st , and October 1st , which were chosen to represent seasonal variations in solar irradiance and ambient temperature. This approach allowed for the evaluation of how both PV technology and structural design respond to varying environmental conditions throughout the year. Notably, the use of single-axis tracking systems aimed to enhance solar capture by enabling the modules to follow the sun's daily path from east to west, thereby improving energy yield in comparison to fixed installations.

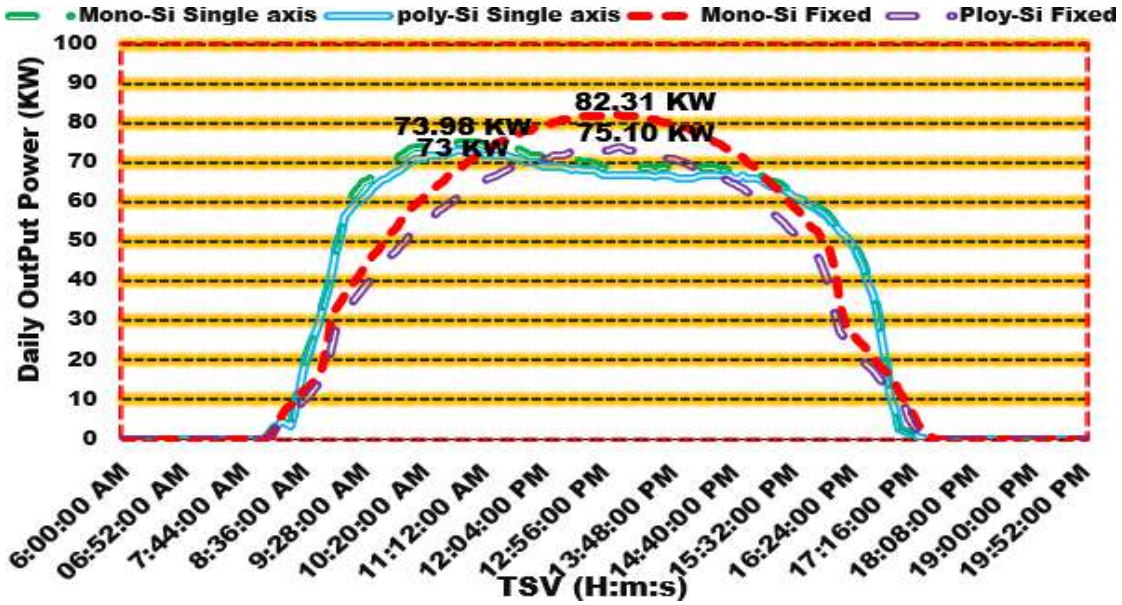

Fig III.24. Comparison of Output Power (kW) Between Fixed and Single-Axis PV Subfields for mc-Si and pc-Si on January 1st , 2016. A Winter Day .

After confirming the accuracy of the real performance data of the photovoltaic (PV) subfields, **Fig.III 24** presents the experimental comparison of daily output power between fixed-axis and single-axis tracking systems for monocrystalline (mc-Si) and polycrystalline (pc-Si) technologies on a winter day January 1st , 2016.

At approximately 12:56 PM, the fixed mc-Si subfield achieved its peak output of 82.31 kW, marking the highest power generation of the day. Earlier in the day, at 10:37 AM, the single- axis mc-Si subfield recorded a slightly lower output of 75.10 kW. Meanwhile, the fixed pc- Si subfield produced 73.98 kW at 12:56 PM, and the single-axis pc-Si configuration yielded the lowest peak output of 73.00 kW at 10:50 AM.

This performance pattern may be partially attributed to winter meteorological conditions such as low solar altitude and diffuse radiation. This helps explain why single-axis systems underperformed compared to fixed systems on this particular winter day. These variations highlight the effect of tracking and module technology on power generation performance under winter solar conditions.

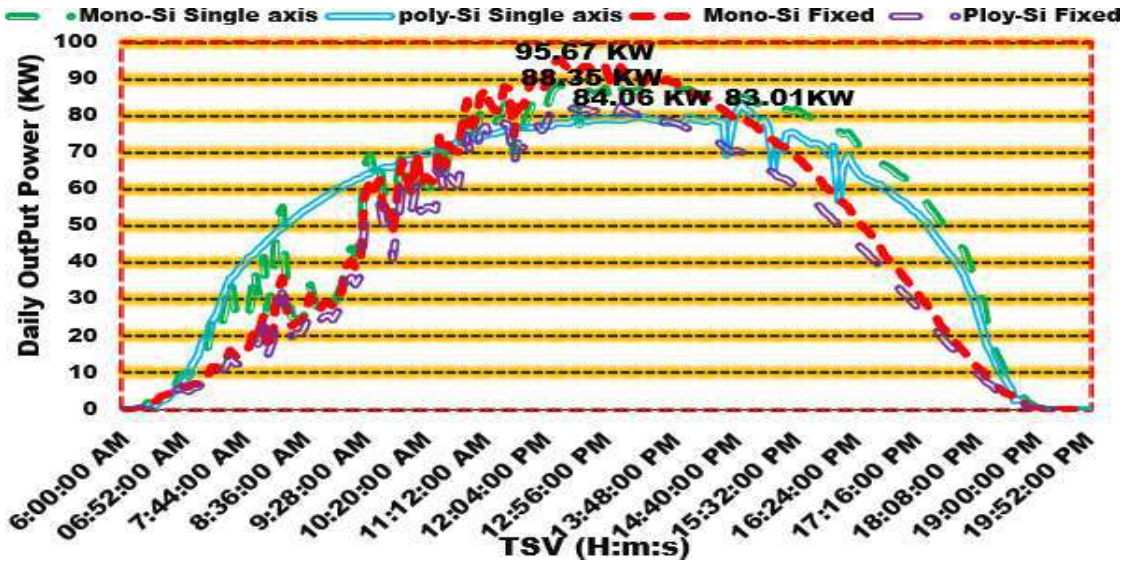

Fig III. 25 .Comparison of Output Power (kW) Between Fixed and Single-Axis PV Subfields for mc-Si and pc-Si on May 1st , 2016. A Spring Day .

Fig III. 25 presents the findings from the four PV subfields on May 1st, 2016 a spring day showing the maximum power output recorded during the four-day pilot study. At 12:23 PM, the fixed mc-Si subfield achieved the highest peak output, reaching 95.67 kW. This was followed by the motorized mc-Si subfield, which generated 88.35 kW at 12:20 PM. At the same time, the fixed pc-Si subfield recorded 84.06 kW, while the motorized pc-Si subfield reached 83.01 kW at 14:40 PM.

Beyond these peak values, the analysis reveals that single-axis tracking systems especially the mc-Si configuration maintained higher output levels over a longer duration throughout the day compared to fixed systems. The power curve of the motorized mc-Si subfield demonstrates a broader and more sustained generation period, suggesting a higher total daily energy yield despite a slightly lower peak value. This extended duration of power generation from sunrise to sunset emphasizes the advantage of solar tracking systems in capturing more irradiance, particularly in the early morning and late afternoon hours.

Interestingly, the motorized pc-Si subfield exhibited a delayed peak at 14:40 PM, possibly indicating alignment issues or less responsiveness to tracking adjustments. The relatively small difference in peak performance between fixed and motorized pc-Si systems also suggests that polycrystalline silicon technology may not benefit from single-axis tracking to the same extent as monocrystalline systems. Overall, the performance trends across the four configurations highlight the importance of peak output and temporal

distribution of power generation when evaluating system efficiency under real operating conditions.

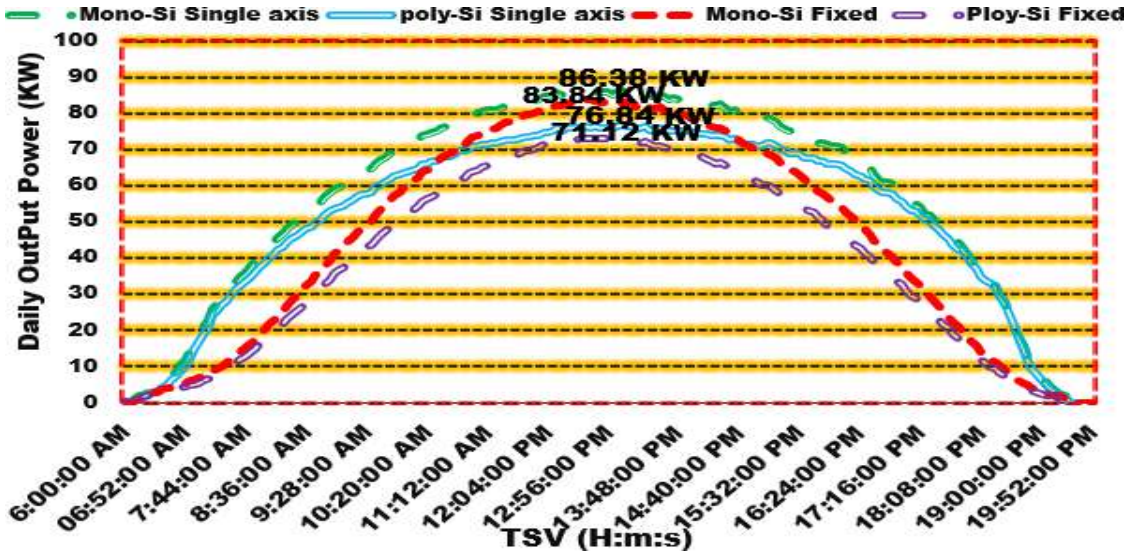

Fig III. 26. Comparison of Output Power (kW) Between Fixed and Single-Axis PV Subfields for mc-Si and pc-Si on July 1st , 2016. A Summer Day.

Fig III . 26. Illustrates the comparison of output power curves from four subfields: one-axis and fixed-axis mc-Si and pc-Si, using real data from July 1st, a summer day. The experimental results on this day differed from those of the previous day. The one-axis mc-Si subfield yielded the highest power output, producing 86.38 kW at 12:56 PM. This was followed by the fixed mc-Si subfield, which generated 83.84 kW at 12:46 PM. The motorized pc-Si subfield produced 76.84 kW at 13:28 PM, while the fixed pc-Si subfield achieved 71.12 kW.

The data presented in **Fig III . 26** highlights the clear advantages of one-axis tracking systems, particularly when paired with high-efficiency mc-Si modules. The one-axis mc-Si subfield achieved the highest power output, demonstrating the significant benefits of tracking in maximizing solar radiation capture throughout the day. While the fixed mc-Si subfield also performed well, the motorized pc-Si subfield showed that tracking can still enhance the performance of lower-efficiency modules, although to a lesser extent. Overall, these results emphasize the importance of combining efficient technologies with tracking mechanisms to optimize photovoltaic system performance.

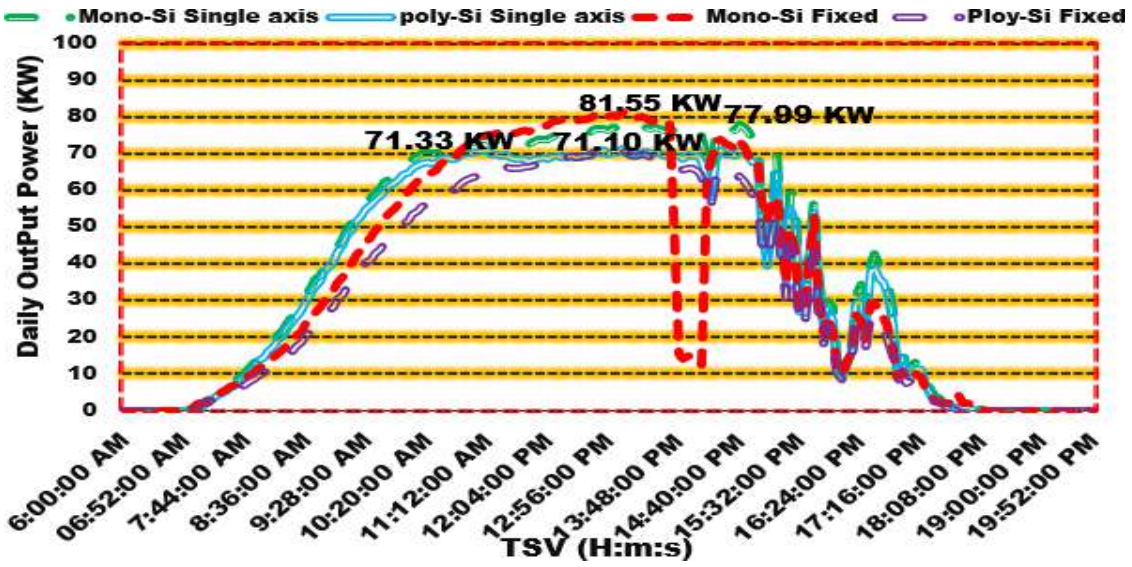

Fig III.27. Comparison of Output Power (kW) Between Fixed and Single-Axis PV Subfields for mc-Si and pc-Si on October 1st , 2016. A Fall Day .

Fig III. 27. Presents experimental real data on output power for fixed-axis and one-axis PV subfields from October 1st , 2016, covering a full day. The curves reveal that the fixed-axis mc-Si subfield yielded the highest output power compared to other subfields, achieving 81.55 kW at 12:56. Following this, the one-axis mc-Si subfield delivered 77.99 kW at 14:30. The data for the two subfields, motorized pc-Si and fixed pc-Si, show a close similarity in their maximum output power. The one-axis pc-Si subfield yielded 71.33 kW at 11:12, while the fixed pc-Si subfield delivered 71.10 kW at 13:10.

This data suggests that on October 1st , the fixed-axis mc-Si subfield outperformed its one-axis counterpart, indicating that fixed high-efficiency modules can be more effective than tracking systems under certain seasonal conditions. Moreover, the nearly identical peak outputs of the one-axis and fixed pc-Si subfields reveal the limited benefit of tracking for lower-efficiency technologies like pc-Si in autumn. These findings underscore the importance of both seasonal variation and module efficiency when assessing the value of tracking systems.

Remarkably**,** the output power curves exhibit noticeable fluctuations across all subfields from 14:10 to 18:00. These fluctuations are likely due to intermittent cloud cover or shifting atmospheric conditions during the late afternoon, which significantly affect irradiance levels. Despite this, the single-axis mc-Si subfield demonstrated relatively stable and strong power output throughout the fluctuations, highlighting its resilience and consistent performance under partially cloudy conditions.

When comparing the DC output power performance of four conventional PV subfields in this section, the results from four experimental days indicate that on each of these days, the power output of the solar panels was monitored from sunrise to sunset, between 06:00 AM and 19:52 PM. Among the subfields, the fixed monocrystalline (mc-Si) consistently generated the highest output power, with a peak value of 95.67 kWp recorded on May 1st , close to the subfield's optimal power. Additionally, on July 1st , the single-axis monocrystalline (mc-Si) subfield demonstrated a peak output power of 88.35 kWp.

Notably, the single-axis solar tracker consistently increased the amount of power generated throughout all experimental days, from sunrise to sunset, by capturing more solar radiation compared to a fixed module. This effect was particularly evident on January 1st , May 1st , and July 1st . As a result, by implementing single-axis tracking systems in our mc-Si and pc-Si subfields, the PV panels were able to continuously track the sun. These systems ensure that the panels remain optimally aligned with the sun throughout the day and across the year, maximizing the exposure of the panel’s surface. This alignment leads to increased conversion efficiency and, consequently, higher electricity generation (output power). Additionally, tracking systems optimize land area usage for electricity production compared to non-tracking systems, making them a more efficient choice. This finding is consistent with those obtained by many authors who have studied solar tracking systems. Hafez et al. (2015) **[156]** introduced an innovative solar single-axis tracking system powered by a Stirling engine, which was used to evaluate the performance of solar panels in Giza, Egypt. The East-West axis system achieved higher output power than the fixed system. Research carried out by Layali Abu Hussein et al. (2021) **[157]** in Amman, Jordan, looked into the performance improvement of standard fixed photovoltaic (PV) solar systems by using single and dual-axis sun tracking mechanisms. They compared these systems to concentrated photovoltaic (CPV) systems, which inherently use tracking systems. The study included an experimental analysis, characterization, and performance comparison of four mounting types of standard PV systems. The PV panels were installed using either a fixed mount, single-axis (East-West tracking), single-axis (North-South tracking), or dual-axis tracking. The study's findings confirmed that electrical power generation on tracking surfaces was significantly higher than on a fixed surface. Additionally, the study demonstrated that both East-West and North-South tracking systems produced more power compared to a fixed surface inclined at 26° to the south.

IX.4.2. Influence of Environmental Factors (Solar Irradiance at 30° Tilt, Temperature, Wind Speed, and Relative Humidity) on Subfield Performance .

IX.4.2.1. Solar irradiance and Temperature data analysis

Climatic, environmental, and operational conditions, along with geographical locations, play a crucial role in the energy yield of photovoltaic (PV) systems. This concept has driven research focused on quantifying and modeling the output power of PV systems under diverse conditions. Researchers globally aim to understand better how these parameters affect PV system performance. According to Elkholy et al., (2016) **[157],** reduced solar irradiation significantly influences the energy quality produced by photovoltaic systems .Dabou et al., (2016) **[158],** conducted a study examining the impact of climatic conditions on the performance of grid-connected photovoltaic systems. The findings indicate that performance is influenced on cloudy and sandy days due to the rapid and successive changes in cloud cover and sand exposure, which affect both the energy output and the stability of the photovoltaic system. In their 2014 study, Panagea et al **[159]** . discovered a clear inverse link between PV power and temperature in Greece. They also observed that as irradiance intensity rises, so does PV power. As reported by Schwingshackl et al., (2013) **[160]** and Kaplani and Kaplanis (2014) **[161],** wind speed significantly enhances PV performance by cooling the PV surfaces, which in turn reduces the parallel resistance within the PV circuit model. Humidity decreases PV output by diminishing the amount of solar irradiance received. Nevertheless, when combined with wind speed, humidity significantly contributes to cooling PV surfaces, thereby enhancing PV efficiency in hot climates Zainuddin et al., 2010 **[162].**

Currently, no published studies provide experimental results on the performance of photovoltaic systems and their interaction with environmental factors in the OUED-NECHOU region, Ghardaïa. This section presents a comparative analysis of the influence of meteorological parameters on the performance of photovoltaic subfields based on real experimental data. The study evaluates the effects of solar irradiance at a 30° tilt, cell irradiation at the same angle, ambient temperature, cell temperature, relative humidity (Fig. 20), and wind speed (Fig. 21) on DC power output.

Furthermore, the performance of the four fixed subfields (mc-Si, pc-Si, a-Si, and CdTe) in Section One, along with the fixed and motorized (single-axis tracking) subfields in Section Two, is analyzed to determine which technology performs most effectively under

the specified environmental conditions. Real-time meteorological data were collected using sensors installed at the weather station (Table III.7) located on the roof of the control room. An experimental analysis was also conducted to compare the meteorological data obtained from the weather station sensors with the cell calibrators installed in the subfield areas. Measurements were recorded at four-minute intervals on January 1st , May 1st , July 1st , and October 1st , each representing a different season. The collected data were subsequently displayed and analyzed, as shown in **Figures** 20, 21, 30, 31, 32, and 33.

- **Fig III.18** and **Fig III.19** illustrate the variations in wind speed (m/s) and relative humidity (%), which were previously discussed in detail.
- Figures **III.28** and **Fig III.29** present the environmental parameters irradiance and temperature that influence the performance of the fixed PV subfields. Specifically, **Fig III.28** displays both ambient and cell solar irradiance, measured on a surface tilted at 30°. **Fig III.29** illustrates ambient and cell temperatures (°C), providing a comparative basis for analyzing the thermal behavior of different fixed PV technologies.
- Figures **III.30** and **III.31** compare fixed and single-axis tracking subfields using monocrystalline (mc-Si) and polycrystalline (pc-Si) technologies. **Fig III.30** presents ambient and cell irradiance data measured on surfaces tilted at 30°, while **Fig III.31** illustrates ambient and cell temperature variations (°C), highlighting the influence of mounting configuration and tracking mechanisms on thermal conditions.

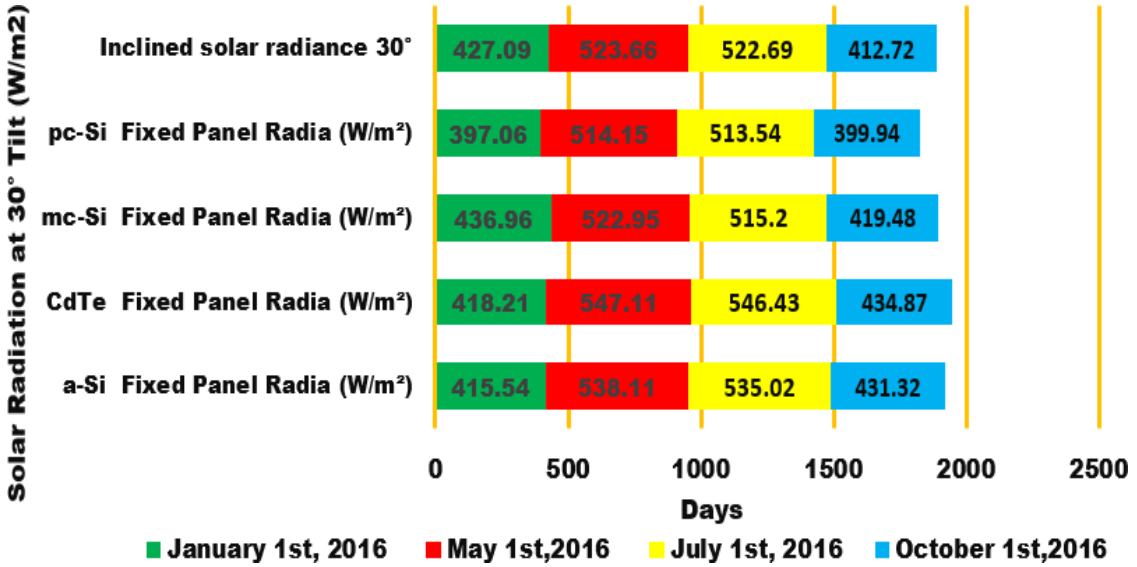

Fig. III.28. Daily Measurements of Average Tilted Solar Irradiance (W/m²) and Calibrated Cell Radiation (W/m²) for Four Fixed Subfields on Representative Days, Measured at a 30° Tilt Angle.

The daily average inclined solar irradiance, measured by a pyranometer, is compared with the calibrated cell-level irradiance for four photovoltaic (PV) subfields: mc-Si , pc-Si , CdTe , and a-Si . Additionally, ambient irradiance is included in this comparison. The data was collected over four representative seasonal days at a fixed tilt angle of 30°, as illustrated in **Fig. III.28 .**

- On January 1st , the pyranometer recorded an inclined ambient irradiance of 427.09 W/m² under typical winter conditions. Among the fixed-tilt PV subfields, the monocrystalline silicon (mc-Si) module achieved the highest cell-level irradiance at 436.96 W/m², while the polycrystalline silicon (pc-Si) module registered the lowest at 397.06 W/m². This winter scenario, characterized by a low solar angle and a diffuse-rich atmosphere, tends to favor crystalline-Si technologies, with mc-Si exhibiting slightly better irradiance capture. By May 1st , ambient irradiance increased to 523.66 W/m², reflecting clearer skies and higher solar elevation. Under these spring conditions, thin- film technologies demonstrated superior performance: the CdTe module reached 547.11 W/m², and the a-Si module recorded 538.11 W/m². In comparison, mc-Si and pc- Si captured 522.95 W/m² and 514.15 W/m², respectively. These results highlight the enhanced diffuse light response and broader spectral sensitivity of thin-film modules. On July 1st , ambient irradiance slightly decreased to 522.69 W/m², possibly due to seasonal haze or higher humidity. Despite this, CdTe and a-Si technologies continued to outperform crystalline-Si, with values of 546.43 W/m² and 535.02 W/m², respectively, compared to 515.20 W/m² (mc-Si) and 513.54 W/m² (pc-Si). These findings confirm the consistency of thin-film modules in capturing higher irradiance even under plateauing or mildly reduced ambient conditions. Finally, on October 1st , ambient irradiance declined to 412.72 W/m² due to shorter days and increased cloud cover. Thin-film technologies again led in performance, with CdTe and a-Si recording 434.87 W/m² and 431.32 W/m², respectively. Meanwhile, mc-Si and pc-Si registered 419.48 W/m² and 399.94 W/m². This autumn drop further underscores the ability of thin-film PV modules to maintain performance under diffuse and lower irradiance conditions.
- Throughout the four seasonal days, the highest cell-level irradiance was recorded by CdTe (547.11 W/m² on May 1st), followed by a-Si (538.11 W/m²), mc-Si (522.95 W/m²), and pc-Si (514.15 W/m²), demonstrating the superior irradiance capture capability of thin-film technologies under varying seasonal conditions.

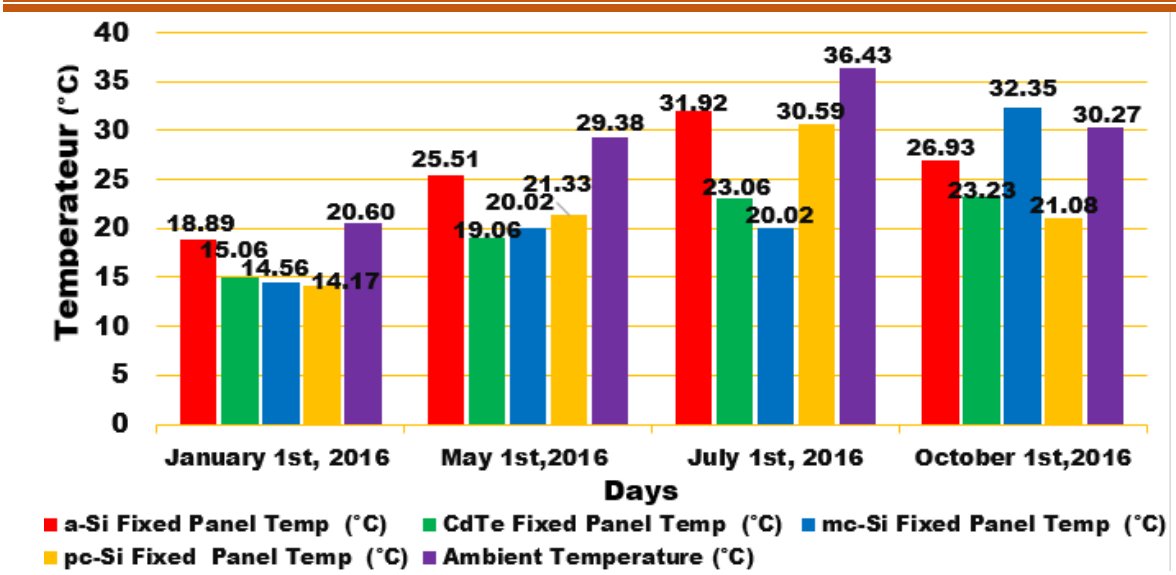

Fig III.29. Experimental Daily Ambient and Module Cell Temperatures (°C) Across Four Representative 2016 Days each represents a Season .

- **Fig III.29** shows a seasonal comparison between ambient temperature and the average cell temperatures of four fixed photovoltaic (PV) technologies namely a-Si, CdTe, mc-Si, and pc-Si recorded over four distinct days using cell-mounted sensors and a thermo-hygrometer.

January 1st , 2016 (Winter) Under cold winter conditions, the ambient temperature was relatively low at 20.60°C. Among the PV technologies, the a-Si module exhibited the highest surface temperature at 18.89°C, followed by CdTe (15.06°C), mc-Si (14.56°C), and pc-Si (14.17°C). The narrow temperature range across all technologies on this day reflects the limited solar irradiance and low environmental heat, with a-Si showing a slightly greater thermal response.

May 1st , 2016 (Spring): As ambient temperatures increased to 29.38°C, PV module temperatures also rose. The a-Si module again registered the highest temperature at 25.51°C, consistent with its known higher thermal absorption. This was followed by mc-Si (21.33°C), CdTe (20.02°C), and pc-Si (19.06°C). The observed differences are influenced by material-specific heat absorption characteristics, with a-Si more sensitive to thermal buildup due to its structure.

July 1st , 2016 (Summer) Summer conditions led to the highest recorded ambient temperature of 36.43°C. The a-Si module reached its peak surface temperature of 31.92°C, while pc-Si followed closely with 30.59°C. mc-Si and CdTe registered lower temperatures at 26.93°C and 23.06°C, respectively. These findings highlight how thin-film modules,

particularly a-Si, heat up more significantly under intense solar radiation, which can impact performance efficiency through temperature-related losses.

October 1st , 2016 (Fall) As temperatures declined slightly to an ambient 30.27°C, module surface temperatures remained elevated. mc-Si surprisingly exhibited the highest panel temperature at 32.35°C, exceeding the ambient level potentially due to prolonged exposure or thermal retention. a-Si followed at 23.23°C, with CdTe and pc-Si recording 21.08°C and 20.02°C, respectively. This shift may be linked to the specific thermal dynamics of mc-Si during moderate irradiance and cooling conditions.

The highest ambient temperature was 36.43°C on July 1st , while the maximum cell temperatures recorded were 31.92°C for a-Si on July 1st , 23.23°C for CdTe on October 1st , 32.35°C for mc-Si on October 1st , and 30.59°C for pc-Si on July 1st .

This section extends the analysis by comparing fixed and single-axis tracking photovoltaic (PV) subfields, focusing on key parameters irradiance and temperature across the same representative days. The comparison highlights the impact of tracking systems on solar energy collection and module thermal behavior.

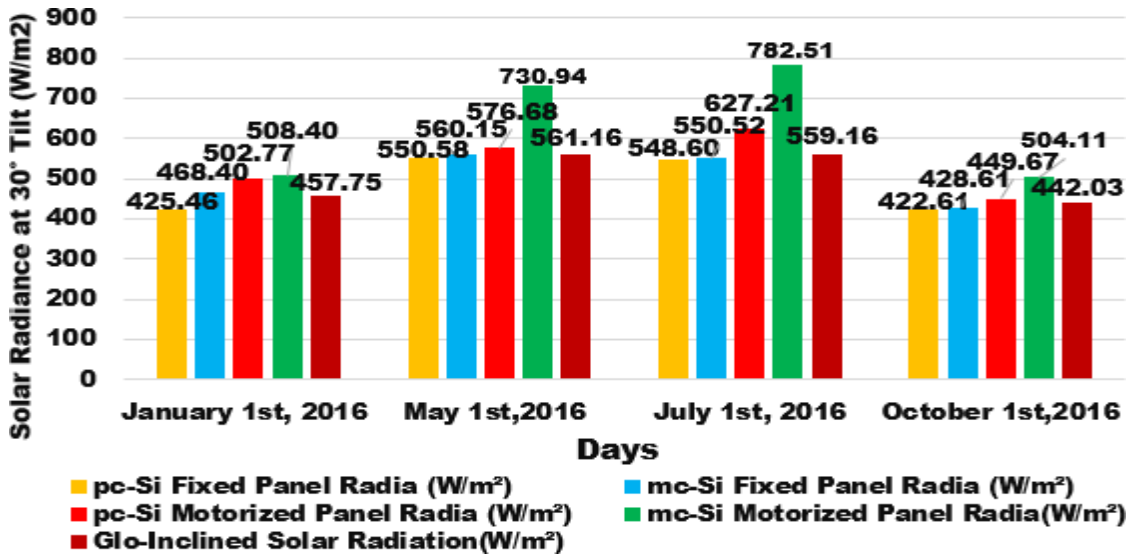

Fig. III.30: Daily Average Inclined Solar Irradiance and Calibrated Cell-Level Irradiance for Fixed and Single-Axis PV Subfields Over Four Seasonal Days at a 30° Tilt.

- Seasonal Comparison of Inclined Solar Irradiance Measured by Pyranometer and Calibrated Cells at a 30° Tilt Angle Over Four Experimental Days in **Fig III.30.**

On this cold winter day (January 1st), the motorized mc-Si subfield recorded 508.40 W/m², while its fixed counterpart captured 468.40 W/m², indicating an 8.5% increase due to the use of single-axis tracking. Similarly, the motorized pc-Si subfield measured 502.77

W/m², compared to 425.46 W/m² from the fixed pc-Si, resulting in an even more notable 18.2% gain. Interestingly, both motorized subfields exceeded the pyranometer's reading of 457.75 W/m², which emphasizes their effectiveness in maximizing solar irradiance capture even during winter conditions with low sun angles.

On this bright spring day (May 1st), the motorized mc-Si subfield recorded a significantly higher irradiance of 730.94 W/m², compared to 560.15 W/m² for its fixed counterpart showing a remarkable 30.5% gain due to single-axis tracking. For the pc-Si technology, the motorized version measured 576.68 W/m², while the fixed pc-Si reached 550.58 W/m², indicating a more modest 4.7% increase. Notably, all motorized subfields exceeded the pyranometer's reading of 561.16 W/m², especially the motorized mc-Si, highlighting the strong advantage of solar tracking under clear springtime conditions with higher solar angles.

On this summer solstice day (July 1st), single-axis tracking demonstrated its strongest impact. The motorized mc-Si subfield recorded a peak irradiance of 782.71 W/m², compared to just 550.52 W/m² for the fixed mc-Si module showing a substantial 42.2% increase due to solar tracking. Similarly, the motorized pc-Si subfield measured 627.21 W/m², while the fixed version reached 548.60 W/m², resulting in a 14.3% improvement. Notably, all motorized subfields outperformed the pyranometer's reading of 559.16 W/m², confirming that tracking systems significantly boost solar irradiance capture during summer conditions with high solar altitude and intense direct radiation.

In autumn's mixed sky conditions, the motorized mc-Si subfield achieved an irradiance of 504.11 W/m², while its fixed counterpart dropped to 428.61 W/m² showing a 17.6% gain with single-axis tracking. For the pc-Si technology, the motorized system recorded 449.67 W/m² compared to 422.61 W/m² for the fixed subfield, resulting in a 6.4% increase. Notably, both motorized subfields surpassed the pyranometer's measurement of 442.03 W/m², emphasizing that even as daylight hours shorten and diffuse radiation increases, tracking systems maintain a clear advantage particularly for mc-Si modules.

These measurements illustrate the variability in irradiance captured by different PV technologies, highlighting the pyranometer's role as a benchmark for evaluating the performance of photovoltaic subfields in capturing solar radiation.

Single-axis tracking systems improve solar irradiance capture by aligning PV modules with the sun's path throughout the day, maximizing direct sunlight exposure and increasing

energy yield, especially under clear skies and high solar angles. Even in diffuse or lower-light conditions, tracking systems typically outperform fixed setups, offering consistent performance gains.

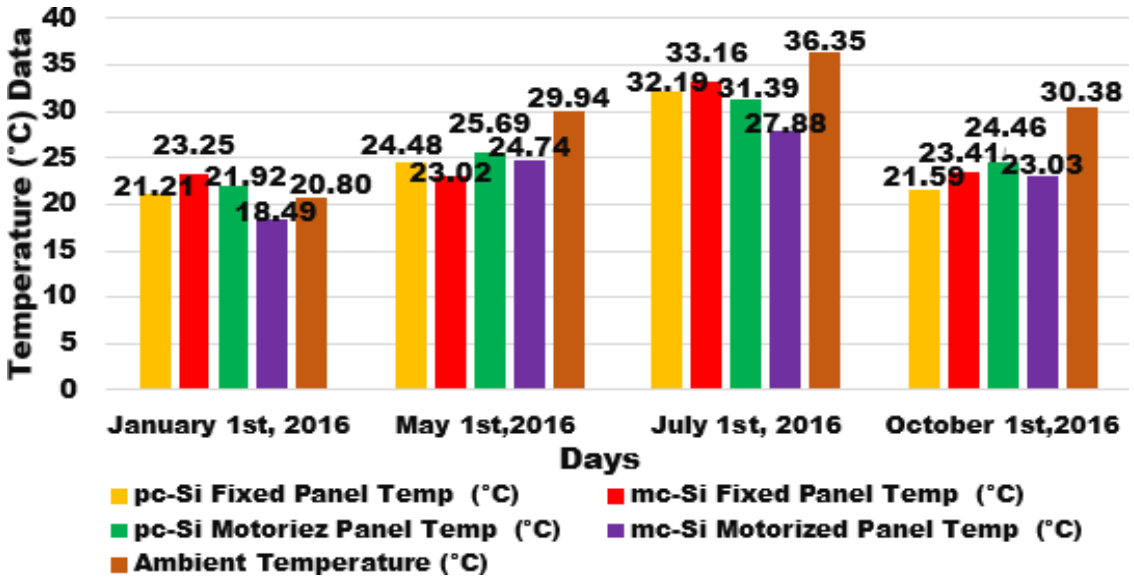

Fig. III. 31: Seasonal Variation of Daily Average Ambient and PV Module Temperatures from Four Experimental Days .

Fig. III.31 presents experimental data collected on four separate days, representing different seasons. It includes ambient temperature readings recorded by a thermo-hygrometer at the weather station, along with PV module temperatures from both fixed and motorized systems, measured using cell sensors installed in the subfields. The analysis shows that ambient temperatures consistently exceeded PV module surface temperatures on all four days. Moreover, module temperatures increased in response to higher ambient conditions, with the most notable rise occurring on July 1st .

On this winter day, January 1st , the ambient temperature reached 20.80°C, the lowest among the four experimental dates. The fixed mc-Si module recorded the highest surface temperature at 23.25°C, likely due to its continuous exposure to available winter sunlight. In contrast, the motorized mc-Si module exhibited the lowest value at 18.49°C, possibly influenced by its varying orientation and enhanced convective cooling during tracking. The pc-Si modules operated close to ambient levels, with the motorized system slightly warmer (21.92°C) than the fixed one (21.21°C). These results indicate relatively stable and mild thermal conditions, typical of low-angle solar incidence in winter.

On May 1st , during spring, ambient temperature reached 29.64°C. The motorized pc-Si panel exhibited the highest module temperature at 25.69°C, followed by the fixed pc-Si at

24.48°C and motorized mc-Si at 24.74°C. The fixed mc-Si showed the lowest panel temperature at 23.02°C. All modules remained below ambient levels, reflecting typical cooling effects due to air circulation and module efficiency. The slightly elevated temperatures in motorized panels, especially pc-Si, indicate improved solar capture from optimized sun tracking. This highlights how both PV technology and mounting type affect thermal behavior under spring conditions.

On July 1st , the ambient temperature peaked at 36.35°C, the highest among the four experimental days, resulting in the most significant increase in PV module surface temperatures. The fixed mc-Si panel reached 33.16°C, followed by the fixed pc-Si at 32.19°C. Among the motorized systems, pc-Si measured 31.39°C, while the mc-Si tracker recorded the lowest panel temperature at 27.88°C.

This data reveals two key patterns: First, all modules operated below ambient temperature, confirming the cooling effect from natural convection. Second, the motorized mc-Si module exhibited the lowest surface temperature among all configurations, likely due to enhanced airflow from continuous tracking movement. In contrast, the slightly higher temperature observed in the motorized pc-Si panel indicates more effective solar capture due to optimal sun alignment under intense summer irradiance. These results highlight how PV technology and mounting configuration influence thermal behavior. While tracking systems promote cooling through airflow, they also enhance irradiance capture, especially in pc-Si modules. This demonstrates a performance balance between thermal regulation and energy absorption during high-temperature conditions.

By October 1st , during autumn, the ambient temperature had decreased to 30.38°C. The fixed mc-Si panel recorded the highest surface temperature at 24.46°C, followed closely by the motorized pc-Si at 24.41°C. The motorized mc-Si and fixed pc-Si panels registered slightly lower values at 23.03°C and 21.59°C, respectively. Although ambient temperatures remained elevated, the reduced solar angle and weaker irradiance typical of autumn resulted in lower thermal loading across all systems. The relatively small differences between fixed and motorized configurations reflect the seasonal transition, during which tracking provides limited thermal benefits due to less direct sunlight.

The analysis shows that PV module temperatures are affected by ambient conditions, panel type, and mounting configuration. All modules stayed below ambient temperature due to convective cooling, with motorized systems, especially mc-Si, benefiting from better

airflow and lower heat buildup. In contrast, motorized pc-Si panels sometimes exhibited slightly higher temperatures, reflecting improved solar capture. Seasonal changes also played a role, with summer conditions causing the highest thermal stress and autumn reducing temperature differences due to lower solar intensity.

IX.4.2. 2. Influence of Meteorological Factors on the Power Output of Fixed PV Systems .

- On January 1st , PV performance was primarily constrained by high relative humidity, which increased atmospheric attenuation and reduced the solar irradiance reaching the modules. Although wind speeds were low, module temperatures remained lower due to the cool ambient air, so thermal losses were minimal. Consequently, the reduced irradiance transmission was the main factor behind the lower energy conversion efficiency and the diminished power output observed on this day.

The mc-Si, a-Si, and CdTe, pc-Si technologies exhibited nearly identical performance throughout the day, with only variations observed around solar noon in their respective peak output values at 13:04 PM. Where the fixed a-Si subfield recorded the highest power output of 83.00 kW at 13:00 PM. This performance was supported by the day's highest cell irradiance (415.54 W/m²) and low thermal stress, with ambient and cell temperatures of 20.60 C and cell temperature of 18.89 °C, respectively, which favored a-Si efficiency due to its low-temperature coefficient, allowing it to perform effectively under higher temperatures. Although the CdTe modules received adequate irradiance (418.21 W/m²), their output power remained lower due to their inherently lower conversion efficiency. Furthermore, the cool ambient temperature (15.06°C) reduced the thermal advantage typically associated with CdTe technology, which performs better under higher temperatures. The additional impact of elevated relative humidity and low wind speed likely contributed to increased thermal stress, further limiting performance. Similarly, the mc-Si subfield, which typically performs well under low- temperature and direct irradiance conditions, was unable to fully capitalize on its potential under the clear and cold winter conditions. It reached a moderate peak power output of 82.31 kW, corresponding to the highest irradiance level among the subfields (436.96 W/m²) and a relatively low ambient temperature of 14.56 °C. However, the performance may have been constrained by high atmospheric pressure and limited wind-induced cooling, which reduced thermal dissipation.

In contrast, the fixed pc-Si subfield exhibited noticeably lower performance, reaching a peak output of only 73.98 kW. This reduced output can be attributed to both the lower average irradiance it received (497.06 W/m²) and a relatively cool cell temperature of 14.17 °C. While pc-Si modules typically have a slightly higher temperature coefficient, making them more sensitive to performance losses at high temperatures, in this case, the environmental conditions were not favorable enough for the module to operate at optimal efficiency.

- On May 1st , 2016, the effect of environmental conditions on the performance of four fixed PV subfields (mc-Si, pc-Si, CdTe, and a-Si) was comparatively evaluated at a 30° tilt angle.

The increase in power production on this day is primarily attributed to low relative humidity and elevated wind speed. Higher wind speeds enhance convective cooling, reducing module temperatures and thereby improving energy conversion efficiency. Simultaneously, lower humidity allows more solar irradiance to reach the PV modules with minimal atmospheric attenuation.

Midday conditions, characterized by stable wind and reduced humidity, supported optimal power output. In contrast, the slight morning perturbations of the output power that were observed between 06:00 AM and 12:04 PM are likely due to transient cloud cover and variable wind patterns. Overall, all four PV subfields demonstrated highly similar power output profiles throughout the day, reflecting consistent irradiance and confirming the influence of favorable environmental conditions. A sharp peak was observed at 12:56 PM, and the stable afternoon curves confirm consistent irradiance and validate the effectiveness of the 30° tilt angle. Among the technologies, amorphous silicon (a-Si) achieved the highest peak power output of 99.98 kW, operating under an average irradiance of 538.11 W/m² and a module temperature of 25.51°C, which is close to standard test conditions (STC). Cadmium telluride (CdTe) followed closely with a peak output of 99.67 kW, benefiting from higher average irradiance (547.11 W/m²) and a lower module temperature (19.06°C), which enhanced its solar energy absorption.

The mc-Si subfield recorded a high peak output of 95.67 kW, demonstrating strong performance under the given conditions. In contrast, pc-Si exhibited the lowest peak output at 84.06 kW. These systems operated under average irradiance levels of 522.95 W/m² (mc-Si) and 514.15 W/m² (pc-Si), with corresponding module temperatures of 20.02°C and

21.33°C. Although these temperatures are generally favorable for crystalline PV technologies, the relatively lower irradiance absorption especially for pc-Si contributed to its reduced power generation compared to a-Si, CdTe, and even mc-Si.

- On July 1st , 2016, typical summer conditions high ambient temperature (36.43 °C), very low relative humidity (down to 10%), and strong wind speeds (6–9 m/s) shaped PV performance across all subfields. Low humidity enhanced solar radiation transmission and wind-driven cooling reduced thermal losses. CdTe and a-Si technologies benefited from thermal stability, while mc-Si maintained strong output due to effective cooling. In contrast, pc-Si underperformed, as higher module temperatures and lower irradiance limited its efficiency despite the wind effect.

The amorphous silicon (a-Si) subfield achieved the highest peak output at 92.05 kW, supported by high irradiance (535.02 W/m²) and a moderate module temperature (31.92 °C). Known for its thermal stability and efficient use of diffuse light, a-Si maintained strong performance under high ambient conditions. The low relative humidity further improved atmospheric clarity, enhancing irradiance and supporting its output, which also enhanced solar transmittance. The CdTe (cadmium telluride) subfield performed strongly, reaching a peak output of 85.11 kW. This was driven by the highest recorded irradiance (546.43 W/m²) and the lowest module temperature (23.06 °C), aided by sustained wind speeds of 6–9 m/s that enhanced cooling. CdTe's thin-film structure, known for its thermal stability, benefited further from low relative humidity (10–35%), which improved atmospheric transparency and solar energy transmission. The mc-Si subfield, despite receiving lower irradiance (515.20 W/m²) compared to a-Si and CdTe, which reduced its potential for power generation, still achieved a peak output of 83.94 kW. This performance was supported by the lowest module temperature (20.02 °C), mainly due to effective cooling from sustained high wind speeds. Since mc-Si technology is sensitive to temperature increases, the low module temperature helped mitigate the negative impact of reduced irradiance, allowing for relatively high power output. In contrast, the (pc-Si) subfield recorded the lowest peak output (73.12 kW), with noticeably reduced power generation during midday. This underperformance is primarily due to a combination of low irradiance (513.54 W/m²) and a relatively high module temperature (30.59°C), both of which negatively impacted efficiency. Like mc-Si, pc-Si is sensitive to elevated temperatures. In this case, the available cooling from wind was insufficient to mitigate the thermal losses and compensate for the reduced solar input.

The data show that high solar irradiance, moderate to low module temperatures, and strong wind significantly enhance PV performance. Technologies with better thermal stability, such as a-Si and CdTe, maintained stronger power output throughout the day. Additionally, the decrease in relative humidity to 10% improved solar radiation transmission, benefiting technologies that perform well under both direct and diffuse irradiance.

- On October 1st , relative humidity in the OUED-NECHOU region was notably high in the early morning, reaching 90% at 06:00 AM, and gradually decreased to 42% by evening. Throughout the day, wind speeds remained consistently low characteristic of the fall season reflecting reduced air mixing and evaporation rates. These stable but humid atmospheric conditions contributed to a power fluctuation observed across all PV subfields between 13:48 PM and 18:08 PM. This fluctuation was most likely due to intermittent cloud cover and low wind activity, which limited solar irradiance and resulted in unstable power output during the afternoon period.

Full-day observations on the same date recorded an average ambient inclined solar irradiance of 412.72 W/m² and an average temperature of 30.27 °C. Among the four photovoltaic subfields, the amorphous silicon (a-Si) technology achieved the highest overall performance, with a peak power output of 92.05 kW and an average irradiance of 431.32 W/m². The system's relatively moderate average module temperature of 26.93 °C further contributed to its efficiency. The superior performance of the a-Si system is attributed to its favorable behavior under diffuse light and its low-temperature coefficient, which enables it to excel in conditions of moderate irradiance and temperature. The CdTe technology ranked second in performance, exhibiting a power generation curve closely resembling that of the a-Si system. It reached a maximum power output of 84.91 kW, benefiting from the highest recorded average daily irradiance of 434.87 W/m² and the lowest average module temperature of 23.23 °C. Although CdTe modules are primarily known for maintaining efficiency under high-temperature conditions due to their low-temperature coefficient, on this day, their strong performance was further supported by high irradiance and cooler module temperatures, which together enhanced power output in the OUED-NECHOU environment . The mc-Si followed in third place, with a peak power output of 81.55 kW. Despite having a comparable power curve to CdTe, the mc-Si subfield experienced a lower average daily irradiance of 419.48 W/m² and a higher average module temperature of 32.35 °C.

This elevated temperature, combined with the mc-Si module's relatively high-temperature coefficient, contributed to a noticeable drop in efficiency highlighting the technology's sensitivity to heat stress under such conditions.

Lastly, the pc-Si technology demonstrated the lowest performance, with a peak power output of 71.10 kW. It operated under the lowest average daily irradiance of 399.94 W/m², which significantly constrained its energy generation. Although it maintained a favorable average module temperature of 21.08 °C well-suited to pc-Si's moderate temperature sensitivity the low solar irradiance ultimately limited its performance.

On October 1st , the photovoltaic technologies in OUED-NECHOU responded differently to moderate irradiance, high ambient temperatures, low wind speeds, and decreasing relative humidity. Amorphous silicon (a-Si) performed the best due to its high tolerance to heat and diffuse light. It also absorbed the highest recorded solar irradiance, and its surface temperature remained close to the standard test condition (STC) value of 25°C. Cadmium telluride (CdTe) also delivered strong output, supported by high irradiance and its low sensitivity to temperature. In contrast, monocrystalline (mc-Si) and polycrystalline silicon (pc-Si) underperformed due to their greater thermal sensitivity and limited irradiance absorption, respectively. These findings highlight the significant impact of environmental factors, particularly temperature, irradiance, wind speed, and humidity, on photovoltaic performance.

IX.4.2. 3. Influence of Meteorological Factors on the Power Output of Fixed and Single-axis PV Subfeilds .

This section delivers a compelling experimental comparison of the power output performance across four distinct photovoltaic (PV) subfields, featuring both fixed and single-axis tracking configurations. Drawing on actual performance data collected over four strategically chosen days, this study evaluates four cutting-edge technologies: fixed monocrystalline silicon (mc-Si), fixed polycrystalline silicon (pc-Si), single-axis tracking mc-Si, and single-axis tracking pc-Si. Power measurements were meticulously recorded every four minutes from sunrise to sunset, facilitating an in-depth analysis of daily power curves, peak power, and total energy production. Beyond merely contrasting mounting configurations, this comprehensive analysis delves into the impact of crucial meteorological factors such as solar irradiance, ambient temperature, wind speed, and relative humidity on

the power output of each subfield under identical environmental conditions. This multifaceted approach not only highlights the advantages of different technologies but also emphasizes the importance of understanding the environmental influences on photovoltaic performance, making a strong case for informed decisions in PV system deployment and optimization.

This study selects the OUED-NECHOU pilot center as a key reference site to assess the impact of meteorological factors on the performance of the implemented photovoltaic technologies. By focusing on this location, we aim to provide valuable insights into how environmental conditions influence solar energy performance.

- After detailed research, the experimental results indicate that single-axis tracking solar subfields consistently generate more power from sunrise to sunset compared to fixed subfields. This increase in power production was particularly evident on January 1st , May 1st , and July 1st . The east-west alignment of single-axis panels optimizes solar energy absorption by improving the polarization angle of incoming solar radiation.

Natural factors clearly influence this variation in power production. Extensive studies have confirmed these findings, including those by Karami et al. (2017) **[163],** Al-Otaibi et al. (2015) **[131],** Moafaq K.S. et al. (2022) **[164],** and Layali Abu Hussein et al. (2021) **[157].**

During the experimental study, the average temperatures of the photovoltaic (PV) technologies remained close to the optimal Standard Test Condition (STC) of 25°C, occasionally exceeding this temperature. Notably, on July 1st , higher temperatures contributed to significant DC power generation, indicating favorable conditions for efficient operation. Despite the increase in temperature, power output rose, with the single-axis subfields achieving more significant gains than the fixed subfields. It suggests that elevated temperatures did not hinder performance but enhanced productivity. On July 1st , conditions were particularly advantageous for both fixed and motorized panels, leading to higher energy yields. A similar trend was observed on May 1st , where rising temperatures also correlated with increased power output. The recorded average temperatures on these days remained within the optimal range for solar panel performance. High temperatures negatively affect the performance of solar panels, as they reduce their efficiency and power output. The evidence for this previous study conducted in Southeast China by Du et al. (2012) **[165]** showed that temperatures above 60°C significantly reduce panel power output while lowering the temperature below this threshold increases efficiency and power

generation. The panels operated near their optimal capacity since such extreme temperatures were not observed in our experimental study, especially for this section.

Since rising temperatures adversely affect the performance of solar panels, finding practical solutions to alleviate this impact is crucial. Researchers such as Mohamed R. Gomaa et al. (2020) **[166],** Their study experimentally evaluated two cost-effective cooling methods to enhance PV system performance: direct active cooling using water and passive cooling with fins. A non-cooled PV module was used as a reference for comparison. The findings showed that the water cooling method reduced the module surface temperature to 38°C, while the fin cooling method brought it down to 55°C, compared to 58°C for the non-cooled module. These cooling techniques enhanced energy performance, resulting in a 10.2% increase in daily harvested energy for the water-cooled module and a 7% increase for the fin-cooled module. Additionally, the performance ratio improved to 84% with water cooling and 81% with fins, while the non-cooled module had a performance ratio of 77%. Furthermore, wind speed and humidity significantly impact the efficiency of photovoltaic subfields. During the experimental period, we observed that higher wind speeds and lower humidity levels improved solar panels output. Increased airflow effectively reduced localized humidity on May 1st and July 1st by promoting continuous air movement over the panels. It led to increased power generation. Additionally, motorized subfields outperformed fixed subfields due to the cooling effect of wind, lower atmospheric moisture, and better solar absorption, resulting in consistently superior performance. Our experimental analysis confirmed an inverse relationship between wind speed and relative humidity: as wind speed increased, humidity levels decreased, further supporting these findings. Water condensation on solar panels can decrease their efficiency by causing moisture build-up. To address this issue, we optimize the tilt angle in our subfields , where photovoltaic panels are installed at a fixed tilt of 30°. which allows water droplets to run off rather than accumulate, thus minimizing prolonged moisture exposure. Additionally, natural airflow in well-ventilated areas enhances this effect. On May 1st and July 1st , increased airflow effectively reduced localized humidity by promoting continuous air movement over the panels. This led to higher power gains for the single-axis tracking system and improved overall power generation.

In regions with high relative humidity that are considered hot and dry, like Oued Nechou, additional solutions focus on improving air circulation around photovoltaic panels to reduce

moisture buildup. It can be done by installing small fans or passive ventilation systems that operate intermittently, activated by sensors that detect elevated humidity levels. When needed, these fans help remove water droplets from the panel surface while keeping energy consumption minimal. This approach ensures efficient panel operation without compromising the primary goal of maximizing power generation, especially in single-axis tracking systems designed to optimize solar absorption.

In conclusion, meteorological factors strongly influence the performance of single-axis and fixed photovoltaic (PV) subfields. Solar irradiance, which is the primary driver of photovoltaic (PV) performance, and tracking mechanisms play a critical role in maximizing energy capture. The irradiance values recorded during the experimental days clearly show that the single-axis tracking system outperformed the fixed system in capturing solar energy, resulting in higher power generation throughout the day. Notably, on May 1st and July 1st , both solar irradiance and power output were significantly higher. This confirms the direct relationship between increased solar irradiance and enhanced power generation in the PV subfields.

Additionally, the cell temperatures recorded during the experimental days were generally close to the Standard Test Condition (STC) threshold, contributing to stable and efficient photovoltaic performance. Notably, July 1st registered the highest ambient and cell temperatures due to typical summer conditions; however, this did not negatively affect performance. On the contrary, field productivity peaked on this day, indicating that the recorded temperatures remained within a range that supports optimal panel operation. Although elevated ambient temperatures are known to reduce PV efficiency by increasing cell temperature, leading to lower voltage and overall output, the experimental data did not reveal any extreme values that would significantly hinder performance. In fact, all temperature readings fell within an optimal operational range, enabling consistent and effective energy generation across all subfields.

Furthermore, wind speed proved to be a beneficial factor, as it helped cool the panel surfaces and reduce thermal stress. On days with higher wind speeds, the photovoltaic subfields, particularly the single-axis tracking systems, performed well due to the enhanced cooling effect and the favorable east-west orientation of the panels. This was especially evident on May 1st and July 1st , when the single-axis system generated more daily power compared to the fixed system. Lower humidity levels also played a positive role by

minimizing atmospheric absorption and scattering, allowing more direct solar radiation to reach the panel surfaces.

Overall, favorable meteorological conditions characterized by high solar irradiance, moderate wind speeds, low humidity, and average surface temperatures greatly contributed to the energy yield of PV systems. Among these, single-axis tracking technologies demonstrated a superior capacity to take advantage of these conditions, leading to improved performance and power generation throughout the day.

X. Augmentation Percentage

The term "Augmentation Percentage" in renewable energy, especially in photovoltaic technologies, refers to the relative improvement in the performance of a specific technology or system compared to a reference or baseline technology. This metric is determined by calculating the percentage increase or decrease in a specific performance indicator (such as power output or efficiency) of the new or alternative technology relative to the baseline **[156].**

Baseline Technology refers to the standard photovoltaic (PV) system that serves as a reference point for evaluating performance. This system typically represents the most commonly installed and widely accepted configuration in the given study context. By establishing this baseline, it becomes possible to assess the relative improvements or enhancements achieved by alternative technologies or mounting systems, such as different fixed-tilt configurations or single-axis tracking systems.

In this study, we analyze the concept of augmentation percentage, defined as the percentage gain in power (%), across two key scenarios.

- First, the power output of four fixed-tilt subfields (a-Si, CdTe, mc-Si, and pc-Si) was compared over four experimental days. For each day, the most productive subfield was selected as the baseline reference, and the performance of the remaining subfields was evaluated relative to it.
- Second, the increase in power output from a single-axis tracking system was evaluated in comparison to its corresponding fixed-tilt configuration, with both systems installed at a 30° tilt. This analysis focused on monocrystalline (mc-Si) and polycrystalline (pc-Si) technologies, each tested over four experimental days. The motorized tracking configuration, selected daily for its higher average power output, served as the baseline against which the fixed system was assessed.

➢ The percentage of augmentation would be calculated as follows:

$$\mathbf{AP\ (\%) = \frac{P_{baseline} - P_{new}}{P_{baseline}}} \qquad \mathbf{(III.1)}$$

AP: Augmentation Percentage (%).

$P_{baseline}$: Mean Output Power (KW) of the baseline (reference) technology or subfield.

P_{new} : Mean Output Power (KW) of the new technology or subfield .

Next, the percentage of power gain (%) is used to compare the performance of four fixed photovoltaic technologies (a-Si, CdTe, mc-Si, and pc-Si) on January 1st , May 1st , July 1st , and October 1st , 2016. This comparison relies on daily average output power, derived from measurements recorded every four minutes between 06:00 AM and 8:00 PM. The results are presented in the bar charts below.

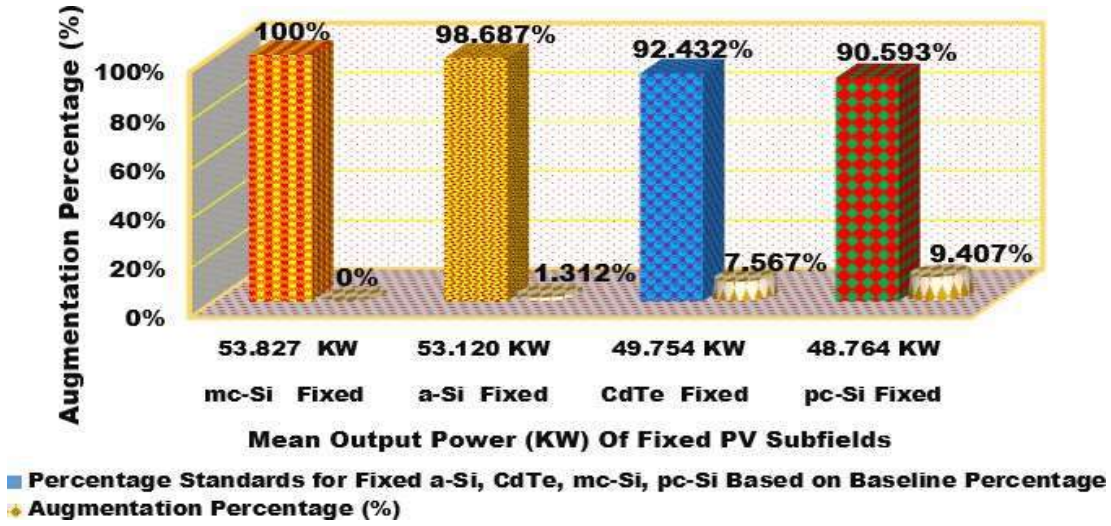

Fig. III.32 : Percentage Increase in Mean Output Power for Fixed and Single-Axis Tracking Subfields (mc-Si, pc-Si) on January 1st , 2016 (Winter Day).

On January 1st , representing winter conditions, **Fig III.32** presents the percentage differences in mean output power among four fixed-tilt photovoltaic subfields: amorphous silicon (a-Si), monocrystalline silicon (mc-Si), polycrystalline silicon (pc-Si), and cadmium telluride (CdTe). The mc-Si subfield, which achieved the highest average output power of 53.8274 kW, is used as the reference (100%). The a-Si subfield produced 53.1209 kW, corresponding to a marginal decrease of 1.312%. CdTe followed with 49.7542 kW, reflecting a 7.567% reduction, while pc-Si recorded the lowest output at 48.763 kW, indicating a 9.406% drop. These results reveal performance variations among technologies and underscore the seasonal influence on photovoltaic efficiency.

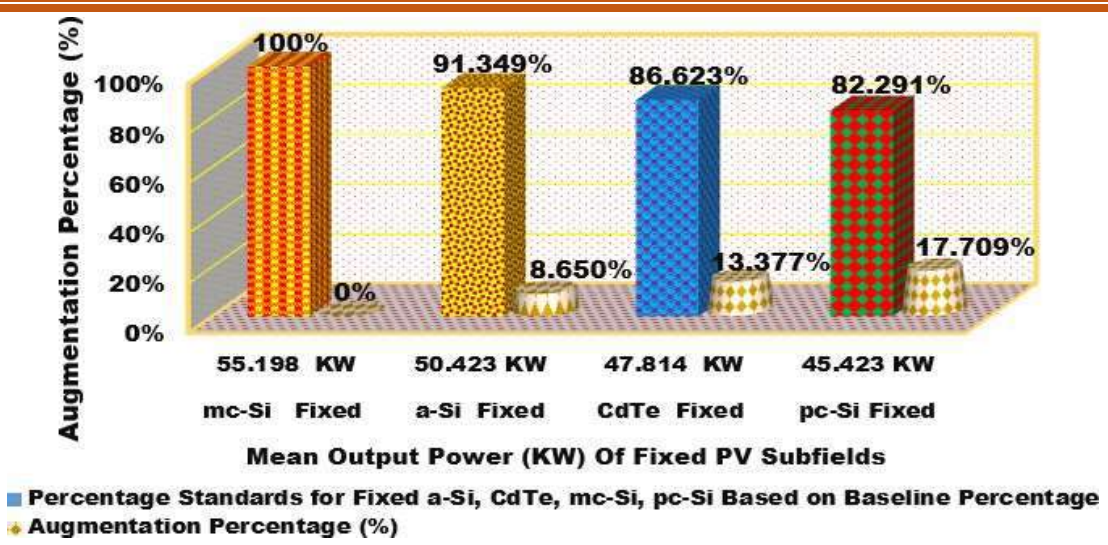

Fig. III.33 : Percentage Increase in Mean Output Power for Fixed (a-Si, CdTe, mc-Si, pc-Si) on May 1st , 2016 (Spring Day).

On May 1st , a spring day, **Fig III.33** illustrates the percentage difference in mean output power (in kW) among four fixed photovoltaic subfields: mc-Si, pc-Si, a-Si, and CdTe. The mc-Si subfield, with an average output of 55.198 kW, serves as the baseline reference (100%). The a-Si subfield generated 50.423 kW, reflecting an 8.650% decrease relative to the baseline. The CdTe subfield produced 47.814 kW, corresponding to a 13.376% reduction, while the pc-Si subfield recorded 45.423 kW, indicating the most significant drop at 17.708%. These findings highlight the mc-Si technology's superior spring performance and the importance of accounting for seasonal effects in PV technology selection

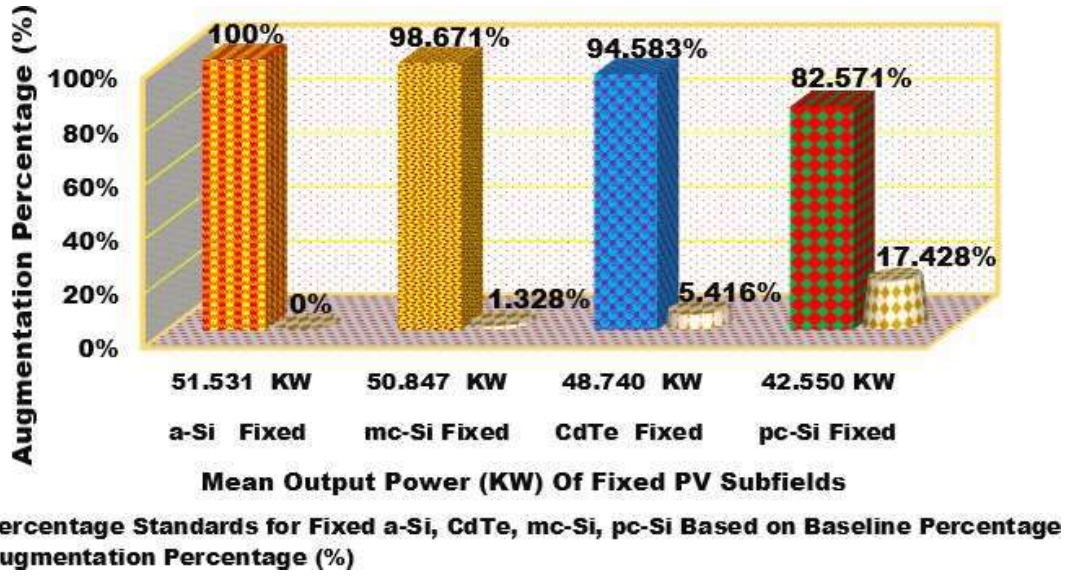

Fig. III.34 : Percentage Increase in Mean Output Power for Fixed Subfields (a-Si, CdTe, mc-Si, pc-Si) on July 1st , 2016 (Summer Day).

. On July 1st , a summer day, **Fig III.34** presents a comparative analysis of the mean output power (in kW) from four fixed photovoltaic subfields: mc-Si, pc-Si, CdTe, and a-Si. The a-Si subfield, with an average output of 51.531 kW, serves as the performance benchmark (100%). The mc-Si subfield followed closely with 50.847 kW, showing a slight decrease of 1.328%. In contrast, the CdTe and pc-Si subfields yielded lower outputs of 48.7404 kW and 42.550 kW, corresponding to reductions of 5.416% and 17.428%, respectively. These results highlight the strong performance of a-Si technology under high- irradiance summer conditions, slightly surpassing mc-Si. While mc-Si remained competitive, the lower efficiency observed in CdTe and pc-Si underscores the variability in photovoltaic performance during peak solar conditions

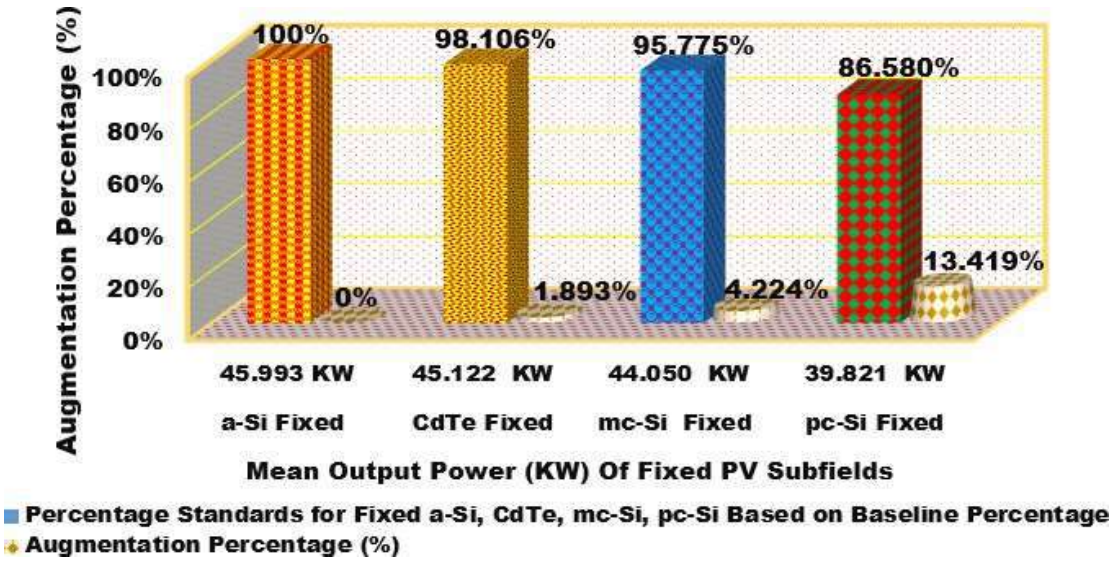

Fig. III.35 : Percentage Increase in Mean Output Power for Fixed Subfields (a-Si, CdTe, mc-Si, pc-Si) on October 1st , 2016 (Full Day).

On October 1st , a fall day characterized by lower irradiance levels, cloudy conditions, and comparable wind speeds, **Fig III.35** presents a comparative analysis of the mean output power (in kW) from four fixed photovoltaic subfields: mc-Si, pc-Si, CdTe, and a-Si. The a-Si subfield recorded the highest mean output of 45.993 kW and serves as the performance benchmark (100%). The CdTe subfield closely followed with 45.122 kW, showing a slight decrease of 1.893%. The mc-Si and pc-Si subfields produced 44.050 kW and 39.821 kW, corresponding to reductions of 4.224% and 13.419%, respectively. These findings suggest that under diffuse irradiance and cloudy conditions typical of fall, a-Si and CdTe technologies exhibit a relative performance advantage, likely due to their favorable spectral response and efficiency in low-light environments.

❖ The highest recorded power gain of 9.775 kW was observed on May 1st between the monocrystalline silicon (mc-Si) The highest recorded power gain of 9.775 kW was observed on May 1st between the monocrystalline silicon (mc-Si) subfield (55.198 kW) and the polycrystalline silicon (pc-Si) subfield (45.423 kW). A similarly substantial gain of 8.981 kW occurred on July 1st between amorphous silicon (a-Si) (51.531 kW) and pc-Si (42.550 kW). In contrast, the lowest gain was recorded on January 1st , with a marginal difference of only 0.7065 kW between mc-Si (53.8274 kW) and a-Si (53.1209 kW). These results highlight the combined impact of seasonal variation and photovoltaic technology choice on performance, reinforcing the importance of matching PV technologies to prevailing environmental conditions to maximize energy output.

❖ The performance improvement of two single-axis tracking subfields was evaluated against two fixed photovoltaic subfields during a four-day experimental period in 2016, with each day representing a different season. Monocrystalline (mc-Si) and polycrystalline (pc-Si) silicon technologies were used. For each system configuration, Mean output power was measured for both subfield types, and the percentage increase was calculated to quantify performance gains. The results are presented in the charts below .

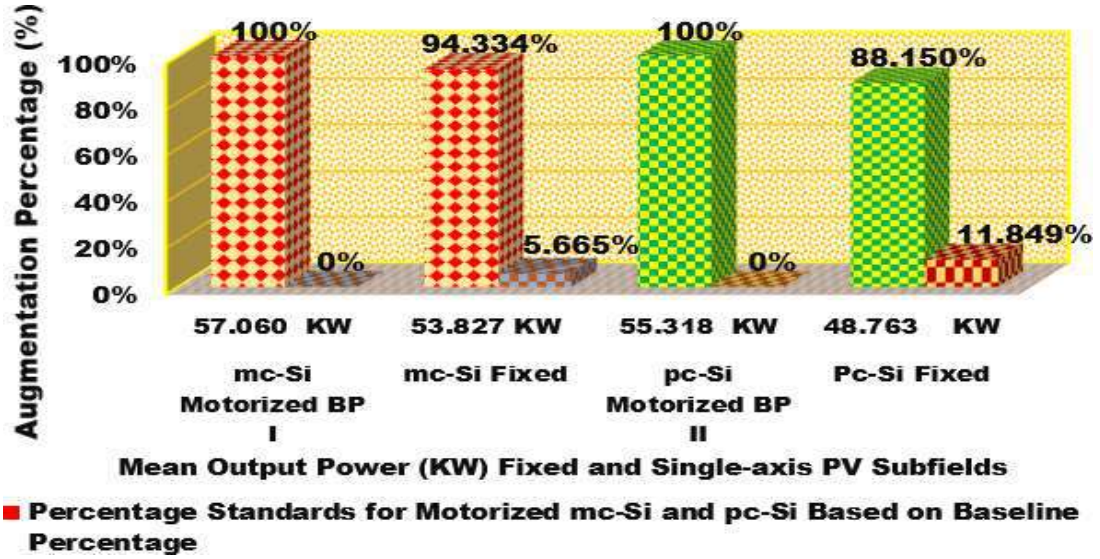

Fig . III. 36: Percentage Increase in Mean Output Power for Fixed and Single-Axis Tracking Subfields (mc-Si, pc-Si) on January 1st , 2016 (Winter Day).

Data from January 1st , 2016, shown in **Fig.36**. Illustrates the increase in mean output power (in kW) for single-axis tracking systems compared to fixed systems for mc-Si and pc-Si sub-fields. The single-axis tracking sub-fields served as baseline technologies for comparison. The mc-Si single-axis tracking system achieved a mean output power of 57.060 kW, representing a 5.566% increase over the fixed sub-field output of 53.827 kW. Similarly,

the pc-Si single-axis tracking system generated 55.318 kW, resulting in an 11.849% increase compared to the fixed sub-field output of 48.763 kW. These increases in mean output power highlight the effectiveness of solar tracking systems in enhancing energy yield, especially during winter days with lower solar angles.

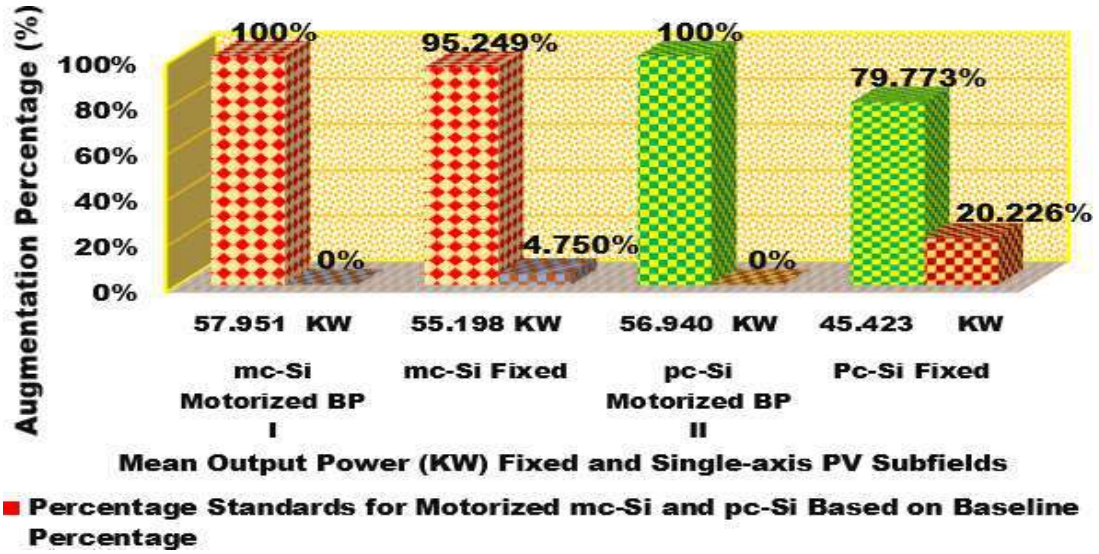

Fig . III. 37: Percentage Increase in Mean Output Power for Fixed and Single-Axis Tracking Subfields (mc-Si, pc-Si) on May 1st , 2016 (Spring Day).

Fig III.37 illustrates the results of an experiment conducted on May 1st , 2016, aimed at comparing the mean output power of fixed and single-axis tracking systems for multi-crystalline silicon (mc-Si) and polycrystalline silicon (pc-Si) subfields during the spring season. The single-axis tracking systems labeled Baseline I for mc-Si and Baseline II for pc-Si demonstrated significantly higher performance compared to their fixed system counterparts. Specifically, the mc-Si single-axis tracking system achieved a mean output power of 57.951 kW, representing a 4.750% increase over the fixed system's output of 55.198 kW. Likewise, the pc-Si single-axis tracking system produced 56.940 kW, resulting in a 20.226% increase compared to the fixed system's output of 45.423 kW. The results highlight that single-axis tracking systems significantly enhance energy capture during spring due to better alignment with the sun's elevated path. The performance gain was more pronounced for pc-Si technology, indicating its greater responsiveness to seasonal tracking benefits compared to mc-Si.

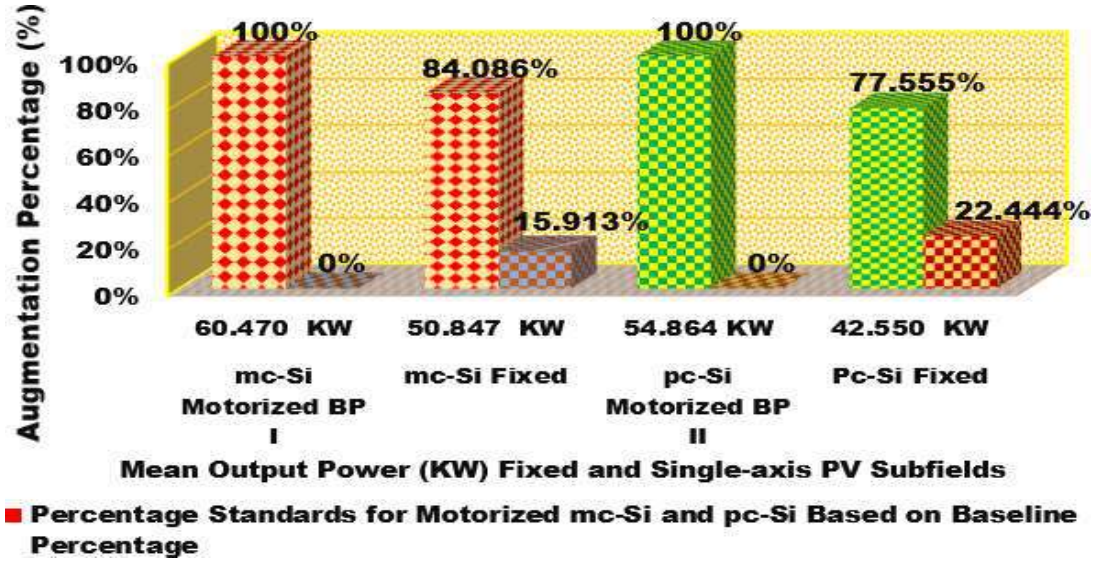

Fig . III. 38: Percentage Increase in Mean Output Power for Fixed and Single-Axis Tracking Subfields (mc-Si, pc-Si) on July 1st , 2016 (Day).

Fig. III.38. Presents data on the percentage increase in mean output power (in kW) for single-axis tracking and fixed systems using mc-Si and pc-Si subfields on July 1st , a summer day. The mc-Si single-axis tracking system considered Baseline I, achieved a mean output power of 60.470 kW, representing a 15.913% increase over the fixed system's output of 50.847 kW. Similarly, the pc-Si single-axis tracking system, established as Baseline II, generated 54.864 kW, resulting in a 22.444% increase compared to the fixed system's output of 42.550 kW. During the summer season, high solar angles and extended daylight hours enhance the effectiveness of sun-tracking systems.

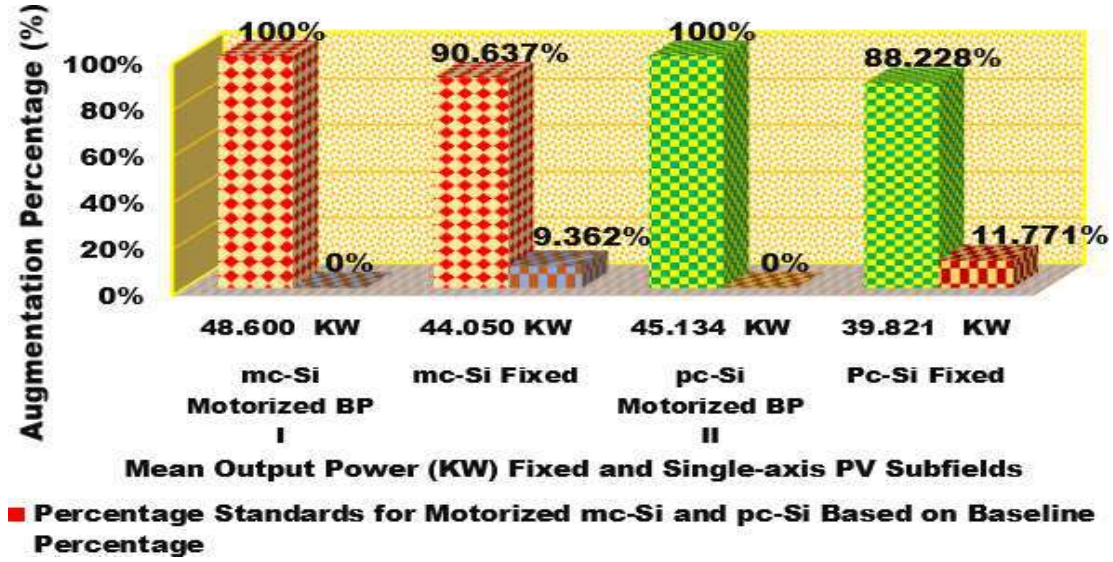

Fig . III. 39: Percentage Increase in Mean Output Power for Fixed and Single-Axis Tracking Subfields (mc-Si, pc-Si) on October 1st , 2016 (Day).

On October 1st , a fall day**, Fig III.39** presents the percentage increase in average output power (in kW) achieved by single-axis tracking systems compared to fixed systems using monocrystalline silicon (mc-Si) and polycrystalline silicon (pc-Si) subfields. The tracking configurations are designated as Baseline I (mc-Si) and Baseline II (pc-Si). The mc-Si tracking system delivered a mean output power of 48.600 kW, representing a 9.362% increase over the fixed system's 44.050 kW. Similarly, the pc-Si tracking system achieved 45.134 kW, corresponding to an 11.771% gain over the fixed system's 39.812 kW. These findings demonstrate the performance advantage of single-axis tracking technologies under fall irradiance and environmental conditions.

The maximum power gain for mc-Si single-axis tracking compared to its fixed counterpart was recorded on July 1st, reaching 15.913% (60.470 kW vs. 50.847 kW). For pc-Si, the highest gain occurred on May 1st , with a 20.226% increase (56.940 kW vs. 45.423 kW). These peak improvements demonstrate the superior performance of tracking systems, especially during periods of elevated solar intensity and favorable sun paths.

A consistent pattern emerged showing that single-axis tracking systems captured significantly higher solar irradiance than fixed systems; on May 1st and July 1st, single-axis tracking systems consistently captured higher solar irradiance than fixed systems. The mc-Si tracker reached 730 W/m² and 782.57 W/m², compared to 550.58 W/m² and 550.52 W/m² for the fixed system, while the pc-Si tracker recorded 576.57 W/m² and 627.21 W/m² versus 550.58 W/m² and 548.60 W/m², respectively.

The findings demonstrate that single-axis tracking systems significantly enhance photovoltaic energy yield by maintaining optimal module orientation throughout the day, particularly during spring and summer when solar irradiance is most intense. The consistent power gains achieved with single-axis tracking systems demonstrate their operational advantage over fixed installations. This validates the use of tracking technology in locations with marked seasonal sunlight variations, dynamic solar paths, and supportive environmental conditions.

XI. Daily Energy Production Analysis of the Photovoltaic Plant at OUED-NECHOU

The Oued-Nechou photovoltaic power plant in Ghardaïa, developed by the Algerian Electricity Production Company (SPE), has a nominal peak capacity of 1.1 MW and is connected to the 30 kV medium-voltage grid for energy injection and distribution.

Established to both reinforce the local grid and evaluate diverse PV technologies under the southern Algerian climate, the plant comprises eight identical 100 kW subfields.

As previously mentioned, this facility was established with a dual purpose: to reinforce the existing electrical grid and to evaluate the performance of various photovoltaic (PV) technologies under the specific climatic conditions of southern Algeria. This study is divided into two main sections focusing on daily energy generation (kWh/day) measured from sunrise to sunset (06:00–20:00) on four days in 2016, each representing a different season. Real-time energy data were collected at four-minute intervals, enabling high-resolution analysis of diurnal performance across PV subfields and configurations.

- Section One compares daily energy output from a-Si, CdTe, mc-Si, and pc-Si subfields to identify the highest performer and assess seasonal effects on grid contribution.
- Section Two compares the daily energy production (kWh/day) of fixed and single-axis tracking systems for mc-Si and pc-Si technologies, emphasizing the role of solar irradiance and the performance gains offered by mechanical tracking.

XI.1. Daily Energy Production (kWh/day) of Four Fixed PV Subfields

The experimental comparison of real-time daily energy generation (kWh/day) for four fixed subfields across four seasonal days in 2016 is shown in the chart below, enabling evaluation of seasonal effects on photovoltaic energy production .

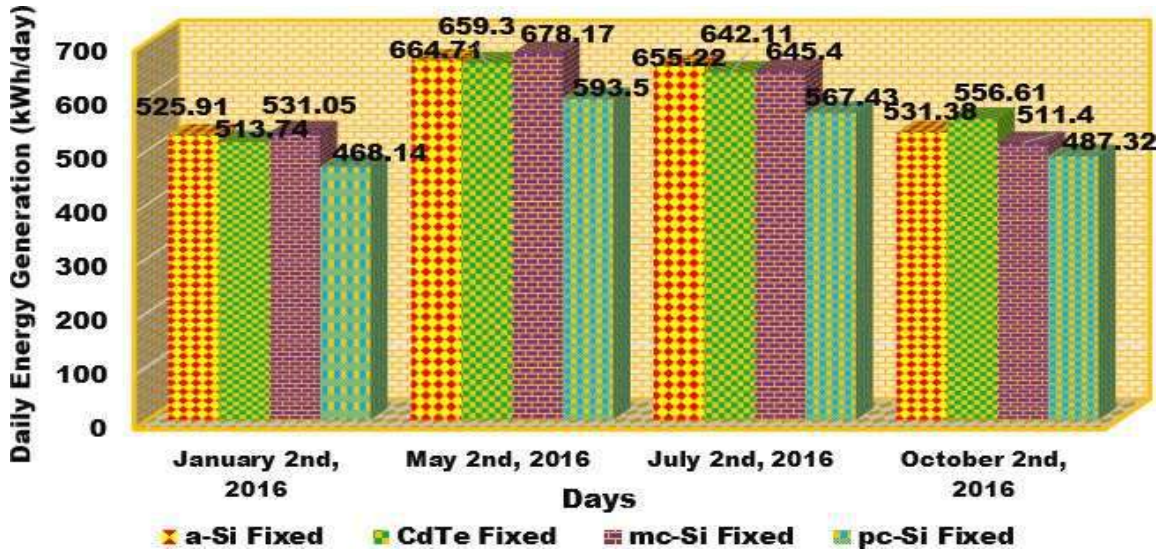

Fig. III.40 : Daily Energy Generation (kWh/m²) of Four Fixed PV Subfields Across Four Seasonal Days in 2016.

Fig III.40. Comparative Daily Energy Generation of Four Fixed PV Subfields Across Four Seasons in 2016 This chart presents the real-time daily energy output (kWh/day) of four fixed photovoltaic subfields (a-Si), (CdTe), (mc-Si), and (pc-Si) each mounted at a 30° tilt, for one representative day of each season. The analysis assesses how seasonal weather variations influence daily energy production and identifies the highest-

yielding technology under southern Algerian conditions, guiding PV system selection in similar climates.

- On this winter day, January 1st , 2016, daily energy generation was the lowest among all seasons for each subfield. The mc-Si Fixed subfield produced 531.05 kWh/day, followed closely by a-Si Fixed with 525.91 kWh/day. The CdTe Fixed subfield generated 513.74 kWh/day, while the pc-Si Fixed subfield recorded the lowest energy output at 468.14 kWh/day. This decline is mainly due to reduced solar irradiance, lower sun angle, and shorter daylight hours in winter, all of which limit energy availability and photovoltaic efficiency.

- On May 1st , 2016, a spring day marked the highest daily energy generation across all subfields. The mc-Si Fixed subfield achieved a peak value of 678.17 kWh/day, closely followed by the a-Si Fixed subfield at 664.71 kWh/day, the CdTe Fixed subfield at 659.3 kWh/day, and the pc-Si Fixed subfield at 593.5 kWh/day. The combination of extended sunshine hours, moderate temperatures, and high solar irradiance during spring created optimal operating conditions, particularly benefiting crystalline-based technologies.

- During the summer period of May 1st, 2016, energy generation remained high across all subfields, although it was slightly below the peak levels observed in spring. The mc-Si Fixed subfield led production with 655.22 kWh per day, followed closely by a-Si Fixed at 645.4 kWh per day and CdTe Fixed at 642.11 kWh per day. The subfield with the lowest energy generation was pc-Si Fixed, producing 593.5 kWh per day. Despite the high solar irradiance and extended daylight hours, the elevated ambient temperatures may have slightly reduced efficiency, particularly for silicon-based modules, due to thermal losses.

- On July 1st , 2016, the energy generation values began to decline as the season transitioned into winter. The CdTe Fixed subfield generated 546.61 kWh per day, followed closely by the a-Si Fixed subfield with 531.38 kWh per day and the mc-Si Fixed subfield, which produced 511.52 kWh per day. The pc-Si Fixed subfield recorded the lowest energy generation, with an output of 487.32 kWh per day. This decline is due to lower solar radiation levels, reduced sunlight duration, and a decreased angle of incidence, all of which hinder the photovoltaic system's efficiency in capturing and converting solar energy.

- The experimental study revealed that the highest energy generation occurred on May 1st , 2016, during the spring season, when the mc-Si Fixed subfield produced 655.22

kWh per day. Conversely, the lowest energy generation was recorded on July 1st , 2016, in the autumn season, with the pc-Si Fixed subfield generating only 487.32 kWh per day.

- Performance variations are mainly driven by solar irradiance and ambient temperature. Spring conditions, with higher irradiance and moderate temperatures, enhance energy generation. In contrast, autumn and winter are marked by reduced irradiance, shorter daylight hours, and a lower solar angle, all of which limit energy production. Additionally, high summer temperatures can reduce efficiency due to thermal losses in silicon-based modules.

XI.2. Daily Energy Production (kWh/day) of Fixed and Single-Axis Tracking PV Subfields (mc-Si and pc-Si) .

The performance assessment compares real-time daily energy production (kWh/day) from photovoltaic subfields using fixed and single-axis tracking systems with monocrystalline (mc-Si) and polycrystalline (pc-Si) silicon technologies, both mounted at a 30° tilt. Based on data collected over four representative seasonal days in 2016, the analysis illustrates the impact of seasonal variation on energy output. The findings also demonstrate the performance advantage of single-axis tracking, which improves solar energy capture by continuously optimizing panel orientation throughout the day, as shown in the chart below.

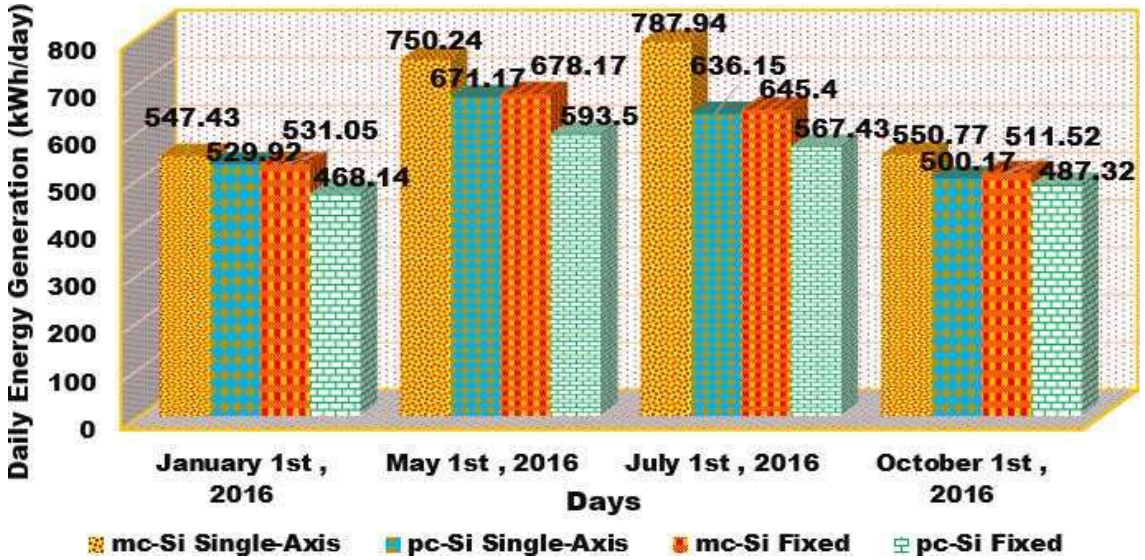

Fig. III.41: Comparison of Daily Energy Generation in Fixed and Single-Axis Tracking PV Subfields Across Four Experimental Days in 2016 .

All photovoltaic (PV) subfields are designed with equal power capacity, each rated at an instantaneous output of 100 kW. **Fig III.41** presents the results of a comparative

between fixed and single-axis tracking configurations. This investigation explores the influence of solar irradiance on energy output, highlighting the performance gains achieved through mechanical tracking systems. To ensure precision and consistency, energy generation was monitored at four-minute intervals throughout the daily measurement period.

- On January 1st , 2016, during the winter season, the single-axis mc-Si subfield recorded the highest daily energy output at 547.73 kWh/day, surpassing its fixed counterpart, which generated 529.92 kWh/day. The single-axis pc-Si system followed closely with an output of 531.05 kWh/day, also outperforming its fixed version, which had the lowest energy output among all configurations at 468.14 kWh/day. These findings emphasize the superior performance of single-axis tracking systems compared to fixed installations, particularly under winter conditions where reduced solar irradiance and shorter daylight durations.
- According to the data recorded on May 1st , the mc-Si technology equipped with a single-axis tracking system achieved the highest energy output, generating 750.24 kWh. In comparison, the fixed mc-Si configuration produced 678.17 kWh, demonstrating a significant performance improvement due to the tracking mechanism. Similarly, the polycrystalline (pc-Si) single-axis system generated 671.17 kWh, outperforming its fixed counterpart, which yielded 593.50 kWh. These results demonstrate that the use of single-axis tracking significantly enhances energy production for both mc-Si and pc-Si technologies.
- The highest recorded energy output was achieved based on measurements taken on July 1st,2016 , during the summer season. The mc-Si single-axis subfield reached a peak generation of 787.94 kWh/day, significantly outperforming its fixed counterpart, the mc-Si fixed subfield, which generated 636.15 kWh/day. This performance difference can largely be attributed to the solar irradiance captured by the single-axis tracking system. The pc-Si single-axis system also performed well, producing 715.17 kWh/day, while the fixed pc-Si subfield recorded the lowest output during this period at 553.43 kWh/day. This rise in performance correlates with the longer daylight hours and elevated solar irradiance levels typical of the summer season.

- As fall began on October 1st ,2016, a seasonal decline in energy generation was recorded. Among the configurations, the mc-Si single-axis subfield delivered the highest output at 550.77 kWh, outperforming its fixed counterpart, which produced 500.17 kWh. Similarly, the pc-Si single-axis system generated 511.52 kWh, exceeding the fixed pc-Si subfield's output of 487.32 kWh. These results highlight the continued advantage of single-axis tracking systems over fixed installations, even under lower irradiance conditions recorded with the autumn season .

- Among the four experimental days in 2016, the most significant daily energy generation gap between single-axis and fixed systems occurred on July 1st . The mc-Si single-axis subfield generated 787.94 kWh/day, while its fixed counterpart produced 645.40 kWh/day, resulting in a notable difference of 142.54 kWh/day. The second-largest gap was recorded on May 1st for the pc-Si technology, where the single-axis system generated 671.17 kWh/day, compared to 593.50 kWh/day from the fixed system, yielding a difference of 77.67 kWh/day. These results underscore the enhanced energy yield of tracking systems, particularly under high solar irradiance conditions.

- The enhanced energy output of single-axis tracking systems stems from their ability to continuously align with the sun’s trajectory throughout the day, thereby maximizing solar irradiance collection. This dynamic positioning minimizes incidence angle losses and ensures that photovoltaic (PV) panels maintain optimal exposure to sunlight, particularly during low-angle periods in the early morning and late afternoon, when fixed-tilt systems typically underperform.

Furthermore, fine-tuning the mechanical tilt of the modules promotes more efficient absorption of direct sunlight, contributing to higher energy yields. Seasonal meteorological conditions such as extended daylight duration, higher sun elevation angles, and decreased cloud frequency further enhance the performance advantage of tracking systems over stationary configurations. These observations emphasize the effectiveness of single-axis tracking technologies, particularly in high-irradiance regions where solar availability varies throughout the year.

XII. Grid Integration of PV Subfield Energy at OUED-NECHOU into the Medium Voltage Network

The OUED-NECHOU photovoltaic power plant, located in Ghardaïa, was developed by the Algerian Electricity Production Company (SPE). With a nominal peak capacity of

approximately 1.1 MW, the plant is connected to the 30 kV medium-voltage grid for energy injection.

As stated at the beginning of this chapter, the plant was built with two main objectives: to strengthen the regional electricity grid and to assess the performance of various photovoltaic (PV) technologies and equipment under the specific climatic conditions of southern Algeria.

The facility consists of multiple PV subfields, each rated at 100 kW, along with two additional subfields rated at 250 kW. These subfields are designed to deliver their respective instantaneous power outputs, enabling comparative performance evaluation.

The plant's primary goal is to produce clean electrical energy with minimal harmonic distortion and to maintain generation for the maximum possible duration throughout the day. The electrical energy generated is injected directly into the 30 kV distribution network (SDC).

The selling price of one kilowatt-hour (kWh) exported from the PV plant is 12.00 Algerian Dinars (DA), while the purchasing price for one kWh imported from the SDC distribution network is 4.00 DA. This pricing scheme highlights SONELGAZ's strategic objective to promote investment in and adoption of renewable energy technologies.

Fig III.42 presents the meter that records the cumulative energy generated by the plant and injected into the grid since the station's commissioning.

Fig III.42: Instrumentation Meter Measuring (Recording) Cumulative Energy Generated and Delivered to the Grid .

Building on the previous discussion regarding energy injection into the 30 kV medium-voltage grid, this section emphasizes the critical components that facilitate this process. A key element in integrating photovoltaic-generated power is the inverter, which serves as the essential interface by transforming the direct current (DC) output generated by the eight subfields located at the center into alternating current (AC) power that complies with grid standards. Additionally, the inverter ensures that the output is synchronized with the grid's voltage and frequency parameters, thus allowing for seamless and reliable energy transfer to the utility network. The explanation below offers a more detailed description of the inverters used at the center, along with a table of their technical parameters.

XII.1. The PV Center Inverters

XII.1.1- Operation and Characteristics of Inverters at the OUED-NECHOU Photovoltaic Power Plant, Ghardaïa .

Inverters are vital components in the energy conversion chain of a photovoltaic (PV) power plant. Their primary role is to convert the direct current (DC) electricity produced by the PV modules into alternating current (AC), which is compatible with the public electrical grid. This conversion is a prerequisite for feeding solar energy into the distribution network, following a voltage step-up via dedicated transformers. In addition to conversion, inverters also help stabilize grid voltage and contribute to its regulation.

At the Ghardaïa photovoltaic power plant (OUED-NECHOU site), eight high-efficiency inverters manufactured by ASI (Ansaldo Sistemi Industriali) are deployed. These include six PV8L121 models (100 kW) and two PV8M291 models (250 kW) designed explicitly for large-scale solar installations. The inverters are installed within a central technical building located in the middle of the solar field, with each subfield connected to a dedicated inverter, ensuring decentralized and efficient energy management.

According to the general single-line diagram, the six PV8L121 inverters are connected in parallel through a low-voltage (LV) switchboard, which then transmits energy to a 750 kVA 30/0.4 kV step-up transformer. Meanwhile, the two PV8M291 inverters are connected to two separate secondary windings of another transformer rated at 630 kVA, 30/0.27 kV.

The system configuration is as follows:

- Six PV8L121 (100 kW) inverters are connected in parallel through a low-voltage (LV) switchboard, with their combined output fed into a 30/0.4 kV step-up transformer rated at 750 kVA. All inverters are installed in the technical room. **Fig III.43** presents a real photograph taken on-site, showing the arrangement of the PV8L121 inverters.

- Six PV8L121 (100 kW) inverters are connected in parallel through a low-voltage (LV) switchboard, with their combined output fed into a 30/0.4 kV step-up transformer rated at 750 kVA. All inverters are installed in the technical room. **Fig III.43** presents a real photograph taken on-site, showing the arrangement of the PV8L121 inverters.

Fig III.43: Photograph of the installed PV8L121 (100 kW) inverters inside the technical room.

- According to the general single-line diagram, two inverters (model PV8M291, rated at 250 kW each) are located in the technical room. These inverters are connected to the secondary windings of a 30/0.27 kV transformer with a rated capacity of 630 kVA. **Fig III.44** provides an on-site photograph that illustrates their physical arrangement.

Fig III.44: On-site photograph of two PV8M291 (250 kW) inverters installed in the technical room.

Table III.6: The ASI PV8M291 Inverter

Electrical Characteristics of the ASI PV8L121 Inverter			
Quantity	6	Power factor	≥0,99
Nominal power on DC side	101 kW	Harmonic distortion on AC side	<3%
Recommended peak power on DC side	CC 119 kW	Nominal power on AC side	96 kW
Maximum voltage on DC side	880 Vcc	Maximum power on AC side	105 kW
MPPT Range	430 – 760 Vcc	Nominal current on AC side	210 A
Nominal current on DC side	CC 221 A	Maximum efficiency at nominal power	96,1 %
Voltage on AC side	400 V	European efficiency	95,5 %
Frequency		50 Hz	
Auxiliary power supply for the PV8L121 UPS			
Auxiliary power supply		230 V AC normal and 230 V AC uninterruptible	
Load		Approximately 400 W (230 V AC normal) + 100 W (230 V AC uninterruptible)	
System Characteristics of the ASI PV8L121 Inverter			
DC side surge protection		Yes	
DC side insulation monitoring		Yes	
DC side disconnect switch		Yes	

AC side surge protection	Yes
AC side circuit breaker	Yes
Communication protocol	Modbus with control system
Dimensions and Environmental Conditions for ASI PV8L121 Inverter	
Temperature	-10 / +50 °C
Degree of protection	IP33
Altitude	1000 m
Humidity	<95%
Dimensions (LxHxW)	1400 x 2172 x 800 mm
Weight	1500 kg
Cooling	forced (by internal fan)
Required air volume	1140 m^3/h
Additional information regarding the ASI PV8L121 inverter	
270 / 400 V AC-side transformer inside the cabinet	
Color	RAL 7035

- In addition to the **ASI PV8L121,** the second inverter installed at the site is the **ASI PV8M291. Its** technical specifications are provided in **Table III.7** to offer a comprehensive overview of the equipment used at the OUED-NECHOU power plant.

Table III.7: The ASI PV8M291 Inverter.

Electrical Characteristics of the ASI PV8M291 Inverter			
Quantity	2	Frequency	50 Hz
Rated DC Power	245 kW	Power Factor	≥0.99
Recommended DC Peak Power	288 kW	Harmonic Distortion on AC Side	<3%
Maximum DC Voltage	880 Vcc	Rated AC Power	239 kW
MPPT Range	430 – 760 V DC	Maximum AC Power	262 kW
Rated DC Current	536 A	Rated AC Current	510 A
AC Voltage	270 V AC	Maximum Efficiency at Rated Power	97.91 %
European Efficiency		97.4 %	
Auxiliary Power Supply For ASI PV8M291 UPS			
Auxiliary power supply		400 Vac normal and 230 Vac uninterruptible	
Load		Approximately 400 W (230 Vac normal) + 100 W (230 V AC uninterruptible)	

System Characteristics of the ASI PV8M291 Inverter	
DC side surge protection	Yes
DC side insulation monitoring	Yes
DC side disconnect switch	Yes
AC side surge protection	Yes
AC side circuit breaker	Yes
Modbus communication protocol with control and monitoring system	
Dimensions and Environmental Conditions for the ASI PV8M291 Inverter	
Temperature	-10 / +50 °C
Degree of protection	IP33
Altitude	1000 m
Humidity	<95%
Dimensions (LxHxW)	2000 x 2172 x 800 mm
Weight	1500 kg
Cooling	forced (by internal fan)
Required air volume	2700 m^3/h
Additional information regarding the ASI PV8M291 inverter	
Color	RAL 7035

XII.1.2- Technical Specifications and Advanced Features of the Inverters

The ASI inverters installed at the OUED-NECHOU power plant in Ghardaïa feature a set of advanced technical capabilities that contribute to optimal energy conversion and system reliability. **Fig III.45** presents a photograph illustrating the internal structure and component layout of the ASI inverter, including protection devices and wiring connections.

Fig III.45: Inverter of the PV Power Plant.

❖ **The inverter consists of:**

- **Integrated disconnection device** for the safe isolation of electrical circuits.
- **Surge protection** to safeguard the inverter during voltage spikes.
- **RFI (Radio Frequency Interference) filter** on the PV side to reduce electromagnetic interference.
- **MPPT (Maximum Power Point Tracking) function**, allowing continuous extraction of the maximum available power from the photovoltaic array.
- **Ground fault detection**, ensuring system safety and integrity.
- **PV field input protected by fuses**, providing enhanced electrical safety.
- **AC-side grid contactor** for grid interconnection.
- **AC discharge filter**, improving the quality of the injected current.

XII.1.3- Conversion Performance and Injected Current Quality

The output voltage waveform of the inverters closely approximates a pure sine wave, meeting strict power quality standards. The Total Harmonic Distortion (THD) is maintained below 3% for the overall signal and under 2% for each individual harmonic. This ensures stable and high-quality power injection into the electrical grid.

Inverter startup is controlled by monitoring the DC voltage from the photovoltaic field. The operational startup voltage range lies between 430 V and 880 V DC, with corresponding AC output of 400 V. This startup threshold can be configured either locally via a keypad interface or remotely through integrated communication protocols.

XII.1.4- Medium-Voltage System

The voltage must first be stepped up to medium (30 kV) to enable the transfer of the electrical energy generated at low voltage by the photovoltaic (PV) field to the distribution grid.

At the Ghardaïa PV power plant, this voltage transformation is achieved using two medium-to-low voltage (MV/LV) transformers located within the technical building positioned at the center of the PV field refer to the (Single-Line Diagram of the PV Power Plant, Including the Equipment Used in the Center; detailed results are provided in the appendices).

In contrast, the evacuation substation, which includes the 30 kV switchgear, is housed in a separate building at the site's edge near the perimeter fence.

The transformers are connected to the 30 kV switchgear through underground medium-voltage cables.

following tables present the key technical specifications of the medium-voltage (MV) components used in the Ghardaïa photovoltaic power plant. The first **table III.8** details the configuration of the 30 kV switchgear (MT Table), which manages the protection, control, and safe evacuation of electrical energy to the distribution grid. Additionally, a table III.18 summarizes the medium-voltage (30 kV) underground cables connecting the switchgear, ensuring safe and efficient energy transmission. Together, these components guarantee reliable power transfer in compliance with grid standards.

XII.1.4.1 – Medium-Voltage (MV) Table Specifications

Table III.8: Medium-Voltage Switchgear Specifications.

The MV switchgear will be of ABB brand, type "Safe Ring 36" insulated with SF6.	
Manufacturer	ABB
Type	Safe Ring 36 (SF6 insulated)
Reference standard	IEC 62271
Rated voltage:	36 kV
Power frequency withstand voltage test:	70 kV
Lightning impulse withstand voltage	170 kV
Rated current	630 A
Rated short-circuit current	16 kA for 1 second
Vacuum circuit breakers	1500 kg
Protection degree	IP67 (live parts, SF6 container), IP2X (control part)
Internal arc withstand	20 kA for 1 second
Auxiliary voltage	127 V DC +10% / -15%
Color	RAL 7035

XII.1.4.1 – Medium-Voltage (MV) Cable Specifications.

The following **table III.9** summarizes the key technical specifications of the medium-voltage (MV) underground cables used to connect the 30 kV switchgear to transformers TP1, TP2, and TA.

Table III.9: Medium-Voltage (MV) Underground Cable Specifications

Nominal voltage	18 / 30 kV
Conductor core	Copper
Insulation	XLPE or EPR
Shield	Copper
Armor	Galvanized steel or aluminum
Outer sheath	PVC
Reference standard	IEC 60502

XII.1.5 - Transformers Setup at OUED NECHOU Station

The Ghardaïa photovoltaic power plant at the OUED-NECHOU site is equipped with three medium-to-low voltage (MV/LV) transformers, each fulfilling a distinct role in power conversion and internal supply. Two main step-up transformers (TP1 and TP2) convert the low-voltage AC power generated by the PV field inverters into medium voltage (30 kV) for grid integration. Both transformers are ONAN type, with oil insulation and copper windings. Notably, TP2 features two secondary windings, providing enhanced operational flexibility or redundancy.

An auxiliary transformer supplies power to the plant's internal auxiliary services, including control systems, lighting, and communication devices. It shares similar construction and insulation characteristics with the main transformers.

An actual image of the auxiliary transformer, taken on-site during the experimental investigation, is shown in **Fig. III.46.**

Fig III.46 : On-site view of the auxiliary transformer used to supply the plant's internal auxiliary services at the OUED-NECHOU photovoltaic site.

The step-up transformers (TP1 and TP2) are installed in the technical building near the inverters, while the auxiliary transformer is located in the control and command building. **Fig III.47** below presents a real experimental image of these transformers as installed at the OUED-NECHOU site, illustrating their role in stepping up the energy produced to medium voltage (30 kV) for grid supply.

Fig III.47: Installed Step-Up Transformers (TP1 and TP2) at the OUED-NECHOU Photovoltaic Site.

The detailed technical specifications of TP1, TP2, and the auxiliary transformer (which supplies internal services to the plant) are summarized in Tables III.10, III.11, and III.12, respectively.

Table III.10: Technical specifications of the auxiliary transformer.

Type	ONAN
Insulation	Oil
Windings	Copper
Rated Power	160 kVA
Primary Voltage	30 kV ± 2 × 2.5%
Secondary Voltage	400 V
Insulation Level	36 kV
Vector Group (Coupling)	Dyn11
Short-Circuit Voltage	6%
Reference Standard	IEC 60076

Table III.11: Technical specifications of the main transformer TP1.

Type	ONAN
Insulation	Oil
Windings	Copper
Rated Power	750 kVA
Primary Voltage	30 kV ± 2 × 2.5%
Secondary Voltage	400 V
Insulation Level	36 kV
Winding Configuration (Vector Group)	Dy11
Short-Circuit Voltage	6%
Reference Standard	IEC 60076

Table III.12: Technical specifications of the step-up transformer TP2.

Type	ONAN
Insulation	Oil
Windings	Copper
Rated Power	630 / 315 / 315 kVA
Primary Voltage	30 kV ± 2 × 2.5%
Secondary Voltage	400 V
Insulation Level	36 kV
Winding Configuration (Vector Group):	Dy11y11
Short-Circuit Voltage	6%
Reference Standard	IEC 60076

XII.1.6- Auxiliary Systems of the Power Plant

The photovoltaic power plant is equipped with all the necessary auxiliary systems that ensure its proper operation and guarantee the safety of both equipment and personnel. These systems are essential even though they do not directly contribute to energy production. Their role is to support, monitor, protect, and maintain optimal operating conditions for the entire facility.

➢ **The key auxiliary systems include:**

- **Internal and emergency lighting** for safe visibility during normal and emergency conditions.
- **External lighting** to ensure site security and visibility at night.
- **Power outlets** distributed for maintenance and equipment use.
- **HVAC systems** to regulate temperature and ventilation in control and equipment rooms.
- **Video surveillance (CCTV)** for continuous security monitoring of the facility.
- **Fire protection systems** including detectors and alarms to manage fire risks.
- **Auxiliary Power Supply** An auxiliary power supply system is provided to ensure the continuous operation of all control and electrical systems. It delivers:
  - 400 V AC and 230 V AC for standard equipment,
  - 127 V DC for control and protection systems.

This auxiliary power is supplied via a dedicated auxiliary transformer, which steps down power from the main electrical distribution to feed these essential subsystems independently from the main PV generation circuit.

The importance of the OUED- NECHOU photovoltaic center's operations is highlighted through comprehensive documentation and experimental evaluation of its technical setup, supporting systems, and actual performance metrics. The assessment of its energy output, distribution processes, and daily operational behavior confirms that the facility performs consistently and effectively under real operating conditions, supported by robust infrastructure and seamlessly integrated auxiliary systems.

The injection of solar energy produced by the OUED- NECHOU center plays a key role in strengthening the local electricity grid and supporting SONELGAZ'S broader energy supply mission. As a photovoltaic pilot station, the center generates clean and sustainable electricity from solar radiation and delivers it directly to the medium-voltage grid. This continuous energy injection not only enhances the reliability of the local power network but also demonstrates SONELGAZ'S commitment to integrating renewable technologies into the national energy system. By supplying a consistent flow of solar-generated electricity reaching an average instantaneous power of 1.1 MW the center contributes effectively to reducing dependence on conventional energy sources, while promoting Algeria's transition toward a more sustainable and decentralized energy model.

XIII. Conclusion

The chapter evaluated four fixed PV subfields (mc-Si, pc-Si, a-Si, CdTe) and compared mc-Si and pc-Si under single-axis tracking at the OUED-NECHOU plant, analyzing 100 kWp systems over four seasonal days to assess the impact of irradiance, temperature, wind, and humidity on performance.

Results showed that seasonal variations and mounting configurations strongly influence PV output. Single-axis tracking enhances solar capture, improves thermal regulation, and increases total daily energy compared to fixed systems. Thin-film modules (a-Si, CdTe) performed best under diffuse light, while crystalline silicon (mc-Si) maintained stable efficiency across temperatures. The a-Si subfield achieved the highest peak output (99.98 kW), confirming its adaptability, while pc-Si recorded the lowest.

Single-axis tracking provided significant energy gains, with relative improvements of up to 22.44% for pc-Si and 15.91% for mc-Si. Daily energy yields highlighted the benefits: mc-Si tracking reached 787.94 kWh/day, exceeding fixed mc-Si by 151.79 kWh/day. Across seasons, mc-Si and a-Si were the most reliable fixed technologies, while tracking systems consistently maximized energy yield.

Overall, the study demonstrates that PV technology selection and mounting strategy are critical for efficient solar energy generation, mitigating climatic impacts, and ensuring reliable year-round performance.

GENERAL CONCLUSION

• GENERAL CONCLUSION AND FUTURE PERSPECTIVES

The work and results of this thesis present a comparative study of four mini photovoltaic power plants, utilizing different technologies and tilt configurations, designed for grid injection at the pilot center of OUED-NECHOU, Ghardaïa. The analysis was conducted under the region's specific climatic conditions and is based on experimental real data collected on-site.

Photovoltaic solar energy is becoming an essential part of the global transition to sustainable energy, driven by rising electricity demand and the reduction of fossil fuel reserves. It provides significant benefits, including environmental sustainability, quiet operation, and widespread accessibility. Although the high initial investment can be a challenge, continuous technological advancements and supportive policies are enhancing affordability and promoting faster adoption around the world.

This study presents a systematic comparison of experimental performance data from four fixed photovoltaic subfields: mc-Si, pc-Si, CdTe, and a-Si. In addition, a comparative analysis was carried out between two configurations of monocrystalline and polycrystalline silicon (mc-Si and pc-Si) subfields, each implemented in both fixed and single-axis tracking (East–West) systems. All subfields are installed at a tilt angle of 30° and have a nominal capacity of 100 kWp. Data acquisition was performed at a frequency of 04 minutes. Performance assessments were conducted on four carefully selected days throughout 2016, each representing a distinct season and encompassing varied meteorological conditions. Through this analysis, the influence of weather variability was quantified, and the optimal system configuration was identified. Furthermore, the enhancement of photovoltaic efficiency resulting from the implementation of single-axis tracking mechanisms was experimentally evaluated.

First, the assessment of solar resource availability is essential in the field of photovoltaic solar energy . A comparative evaluation was conducted to predict solar irradiance on a 30° inclined surface using three semi-empirical models: PERRIN DE BRICHAMBAUT, LIU & JORDEN, and CAPDEROU. Among them, PERRIN DE BRICHAMBAUT demonstrated the best overall accuracy, with a correlation coefficient (CC) between 0.9885 and 0.9965, (RMSE) ranging from 3.2261 to 7.3320 W/m², (MAE) between 55.5830 and 101.2542 W/m², and (MAPE) from 0.8928% to 3.3321%. These results highlight its strong agreement with measured data and minimal prediction error. The LIU & JORDEN model showed moderate performance, with CC values from 0.9332 to 0.9885, RMSE ranging from

5.0243 to 710.7183 W/m², (MAE) between 66.2512 and 152.336 W/m², and (MAPE) from 1.2256% to 11.251% indicating greater deviations, particularly under variable irradiance. In contrast, CAPDEROU yielded the lowest accuracy, with CC between 0.9012 and 0.9521, RMSE ranging from 10.2250 to 17.6473 W/m², MAE from 88.6321 to 155.25 W/m², and MAPE between 1.7855% and 21.225%, suggesting a more conservative estimation with less alignment to actual data. Additionally, the absolute error curve remained generally low and close to the x-axis on most days, particularly when compared to the LIU & JORDEN and CAPDEROU models, indicating that the predictions from this model closely matched the actual measurements. These findings confirm the superior predictive capability of the PERRIN DE BRICHAMBAUT model for inclined surface irradiance under Saharan conditions, making it a reliable choice for regions lacking radiometric stations.

Among the fixed-mount PV subfields, the a-Si emerged as the top-performing and most reliable technology, consistently delivering the highest peak power outputs across all four seasonal days. With a peak of 99.98 kW on May 1st , nearly reaching its rated capacity, its performance underscores excellent thermal stability and strong adaptability to changing irradiance levels. Closely following, CdTe demonstrated solid output, particularly under moderate or cooler conditions, making it the second most effective fixed technology. mc-Si, despite reaching 95.67 kW in spring, showed less consistent results over the seasons and ranked third overall. Meanwhile, pc-Si persistently recorded the lowest power generation, confirming its limited efficiency and lower adaptability. These findings clearly highlight a-Si's superiority in both performance and reliability compared to the other fixed-mount technologies.

When comparing fixed and single-axis tracking configurations, mc-Si systems showed a clear advantage with tracking. The single-axis mc-Si subfield extended power production throughout the day, especially on May 1st and July 1st, generating 88.35 kW and 86.38 kW, respectively. Although its peak power was sometimes slightly lower than fixed mc-Si, the longer daily production duration resulted in a higher overall energy yield by capturing more irradiance during morning and late afternoon hours. For the Pc-Si systems, single-axis tracking led to significantly higher daily energy production despite similar peak outputs. On October 1st , the fixed and tracking pc-Si subfields recorded nearly identical peak powers of 71.10 kW and 71.33 kW, respectively, indicating that while tracking does not increase peak power much for lower-efficiency pc-Si panels, it substantially improves total daily

productivity notable in all experiment days, by extending effective power generation periods, even under diffuse or moderate irradiance conditions.

The performance of photovoltaic (PV) systems is closely tied to meteorological conditions, with solar irradiance, cell temperature, ambient temperature, wind speed, and relative humidity playing critical roles in power generation. An analysis conducted over four specific days demonstrates that fixed PV subfields were significantly affected by these environmental variables. The a-Si consistently outperformed the other technologies, especially under conditions of high temperature or fluctuating weather, due to its low sensitivity to heat. CdTe also showed strong resilience, particularly under moderate to high irradiance. In contrast, mc-Si and especially pc-Si modules exhibited lower performance, primarily due to their higher thermal sensitivity and greater dependence on irradiance levels. Notably, systems equipped with single-axis tracking mechanisms, particularly the mc-Si tracking configuration, demonstrated superior performance across all days. This was most evident on July 1st when the highest irradiance (782.51 W/m²) and average temperatures coincided with the maximum power output. The tracking system's ability to follow the sun's path from east to west throughout the day significantly enhanced irradiance capture and energy conversion, outperforming fixed installations by maintaining optimal panel orientation. Temperature effects also proved to be critical. While moderate heat can support PV operation, excessive cell temperatures tend to reduce output voltage, thereby decreasing power. However, during the observation period, temperatures remained within or near the optimal range for solar energy production. Wind speed and relative humidity further influenced system performance: higher wind speeds helped cool PV modules, mitigating thermal losses, while low humidity improved atmospheric clarity and reduced condensation on panels. These favorable conditions were especially beneficial on May 1st and July 1st . Conversely, high humidity and low wind speeds, as seen on January 1st and October 1st , led to cloud cover and reduced irradiance, resulting in diminished power output.

Choosing the right PV module and system design is crucial. a-Si and CdTe technologies are more stable in changing weather, while single-axis tracking boosts energy capture. Combining both leads to higher energy output in real-world conditions.

Over the four experimental days, mc-Si and a-Si exhibited the most stable and consistent increases in power output among the fixed photovoltaic technologies. The most significant power gain between any two technologies occurred on May 1st **,** when mc-Si generated 55.198 kW compared to 45.423 kW for polycrystalline silicon (pc-Si) a difference of 9.775 kW**,** representing an increase of approximately 17.709%**,** which highlights mc-Si's superior

efficiency under spring conditions. Further notable gain was recorded on July 1st , when a-Si **(**51.531 kW**)** outperformed pc-Si **(**42.550 kW**)** by 8.981 kW**,** an increase of 17.428%**,** emphasizing a-Si's advantage in hot, high-irradiance environments. In contrast, the smallest performance gap appeared on January 1st , with only a 0.7065 kW difference between mc-Si and a-Si**,** reflecting more comparable output levels during winter Tracking systems generally enhance panel performance compared to fixed installations. Both monocrystalline (mc-Si) and polycrystalline (pc-Si) single-axis tracking systems consistently delivered higher power output than their fixed counterparts across all experimental days, with the most notable improvements observed on July 1st and October 1st **.** On these dates, the mc-Si single-axis subfield achieved the highest power gains, 15.913% (6.623 kW) on July 1st and 9.362% (4.550 kW) on October 1st compared to the fixed mc-Si subfield. Similarly, the pc-Si single-axis system showed its peak gains on July 1st and May 1st **,** with increases of 21.226% (11.517 kW) and 22.444% (12.314 kW), respectively, over the fixed pc-Si system. Regarding, the lowest performance gains were recorded on May 1st for mc-Si, where the tracking system produced only 4.750% (2.753 kW) more power than the fixed system. For pc-Si, the smallest gain occurred on October 1st **,** with an increase of 11.771% (5.313 kW) over its fixed counterpart.

Throughout all seasons, single-axis tracking systems consistently recorded higher irradiance values compared to fixed systems. The improvements varied depending on the module type and seasonal solar conditions, ranging from 4.7% for motorized pc-Si modules compared to their fixed counterparts, to 42.2% for motorized mc-Si modules when compared to fixed mc-Si modules. All motorized subfields surpassed the pyranometer readings, demonstrating their superior ability to capture solar radiation by dynamically following the sun's path

The highest recorded daily energy yields for fixed photovoltaic technologies in 2016 were observed on May 1st , during the spring season. Monocrystalline silicon (mc-Si) led with the highest output of 678.17 kWh/day**,** followed by amorphous silicon (a-Si) at 664.71 kWh/day, cadmium telluride (CdTe) at 659.3 kWh/day, and polycrystalline silicon (pc-Si) at 593.5 kWh/day. These results highlight mc-Si's superior energy generation under optimal spring conditions characterized by high solar irradiance and moderate temperatures.

Furthermore, a superior performance of single-axis tracking systems in daily energy production. On May 1st , these systems produced 750.24 kWh of multi-crystalline silicon (mc-Si) and 671.17 kWh of polycrystalline silicon (pc-Si). Similarly, on July 1st , they generated 787.94 kWh for mc-Si and 636.15 kWh/day for pc-Si. In contrast, fixed systems

yielded 678.17 kWh/day and 590.50 kWh/day on May 1st , as well as 645.40 kWh/day and 567.43 kWh/day on July 1st , respectively. These findings emphasized the effectiveness of tracking mechanisms in maximizing solar energy capture and enhancing energy generation. After an in-depth evaluation of experimental observations and collected data, it is evident that the single-axis polycrystalline subfield outperforms the single-axis monocrystalline subfield in terms of gaining power . Furthermore, the single-axis configuration , particularly the mc-Si system, demonstrates superior efficiency in term of energy and power generation compared to both fixed polycrystalline and monocrystalline subfields. Therefore, it is highly recommended to implement polycrystalline technology in the OUAD-NECHOU region and other Saharan areas with similar solar irradiance and environmental conditions.

Based on these findings, future improvements in power generation could focus on optimizing tilt angles and integrating adaptive control algorithms for tracking systems to enhance energy yield. Additionally, regular cleaning and continuous monitoring of photovoltaic (PV) panels are essential for maintaining efficiency, particularly in dust-prone regions such as OUED-NECHOU. This is crucial for tracking systems, which need proper maintenance for optimal performance. Future studies should also assess the long-term cost-effectiveness of single-axis tracking systems compared to fixed installations, considering both operational performance and economic feasibility. Moreover, alternative performance parameters should be utilized to enhance the study of photovoltaic technologies.

• References

[1] H. Lund, A. N. Andersen, P. A. Østergaard, B. V. Mathiesen, and D. Connolly, "From electricity smart grids to smart energy systems: A market operation-based approach and understanding," Energy, vol. 42, no. 1, pp. 96–102, 2012.

[2] I. Kaaya and G. M. Tina, "Photovoltaic energy production: A global overview," Renewable and Sustainable Energy Reviews, vol. 121, Art. no. 109667, 2020.

[3] A. Jäger-Waldau, "Snapshot of photovoltaics — March 2023," Renewable and Sustainable Energy Reviews, vol. 173, Art. no. 113103, 2023.

[4] A. B. Stambouli, Z. Khiat, S. Flazi, and Y. Kitamura, "A review on the renewable energy development in Algeria: Current perspective, energy scenario and sustainability issues," Renewable and Sustainable Energy Reviews, vol. 16, no. 7, pp. 4445 – 4460, 2012.

[5] M. Kacira, M. Simsek, Y. Babur, and S. Demirkol, "Determining optimum tilt angles and orientations of photovoltaic panels in Sanliurfa, Turkey," Renewable Energy, vol. 29, no. 8, pp. 1265–1275, 2004.

[6] Global Solar Atlas (GSA), "World – Solar irradiation and PV power potential map," World Bank / ESMAP / Solargis, 2018. [Online]. Available: https://globalsolaratlas.info/download/world. [Accessed: Dec. 06, 2025].

[7] IEA-PVPS, "Snapshot of Global PV Markets 2024," 2024. [Online]. Available: https://www.iea-pvps.org/snapshot-of-global-pv-markets-2024. [Accessed: Dec. 06, 2025].

[8] "2024: Global Solar Capacity Tops 2.2 TW, With Over 600 GW New Additions," SaurEnergy, Apr. 16, 2025. [Online]. Available: https://www.saurenergy.com/solar-energy-news/2024-global-solar-capacity-tops-2-2-tw-with-over-600-gw-new-additions. [Accessed: Dec. 06, 2025].

[9] International Renewable Energy Agency (IRENA), "Renewable Energy Market Analysis: Africa and Its Regions – Summary for Policy Makers," 2022. [Online]. Available:https://www.irena.org//media/Files/IRENA/Agency/Publication/2022/Jan/IRENA_Market_Africa_2022_Summary.pdf. [Accessed: Dec. 06, 2025].

[10] Global Solar Atlas (GSA) 2.0, "Global Horizontal Irradiation Map," World Bank / ESMAP / Solargis, 2019. [Online]. Available: http://globalsolaratlas.info. [Accessed: Dec. 06, 2025].

[11] P. Labouret and J.-P. Braun, Solar Cells: The Basics of Photovoltaic Energy. Paris, France: Dunod, 2004.

[12] M. Azoui et al., "Sizing and optimization models for photovoltaic pumping system using CM motor," AMSE, pp. 55–66, 2003.

[13] A. Borni, "Study and optimization of a multi-hybrid system for electric energy conversion," Ph.D. dissertation, University of Ghardaïa, Ghardaïa, Algeria, 2015.

[14] M. Capderoux, Atlas solaire de l'Algérie: Modèles théoriques et expérimentaux, vol. 1. Algiers, Algeria: Office des publications Universitaires, 1987.

[15] A. Gougui, A. Djafour, N. Khelfaoui, and H. Boutelli, "Empirical models' validation to estimate global solar irradiance on a horizontal plane in Ouargla, Algeria," AIP Conference Proceedings, vol. 1968, pp. 1–16, May 2018.

[16] M. R. Yaïche and S. M. A. Bekkouche, "Estimation of global solar radiation in Algeria for different sky conditions," Revue des Energies Renouvelables, vol. 13, pp. 683–695, Dec. 2010.

[17] A. Gougui, "Study and experimentation of a hybrid photovoltaic/hydrogen system for integration into the electrical system," Ph.D. dissertation, Univ. of Ouargla, Ouargla, Algeria, 2021.

[18] A. Ghassemi, R. Foster, and A. Cota, Solar Energy: Renewable Energy and the Environment , Energy and the Environment Series, New Mexico State University, 2009, pp. 11–12.

[19] M. Thomas, "Characterization of photovoltaic solar panels under real installation conditions and depending on different technologies," Ph.D. dissertation, Univ. Paris-Sud, Paris, France, 2014.

[20] A. El Ouederni, "Evaluation of the solar resource in the Gulf of Tunis – Application to the feasibility of a mini parabolic solar concentrator," Ph.D. dissertation, École Nationale de Monastir, Monastir, Tunisia, 2016.

[21] M. L. Louazene, "Techno-economic study of a photovoltaic pumping system at the Ouargla site," Master's thesis, University of Batna, Batna, Algeria, 2008.

[22] B. Y. H. Liu and R. C. Jordan, "Daily insulation on surfaces tilted towards the equator," Trans. ASHRAE, vol. 53, pp. 526–541, 1962.

[23] H. Ghellai and M. Bouhdjar, "Évaluation de l'irradiation solaire globale sur une surface inclinée," Revue des Énergies Renouvelables, vol. 16, no. 2, pp. 331–342, 2013.

[24] Kada, "Modélisation multispectrale des images satellitaires - Application: Quantification du bilan d'énergie Sol-Atmosphère," Ph.D. dissertation, Univ. U.S.T.O, 2016–2017.

[25] C. S. Solanki, Solar Photovoltaics: Fundamentals, Technologies and Applications, 3rd ed. India: Eastern Economy Edition, 2015.

[26] A. Moummi, N. Hamani, N. Moummi, and Z. Mokhtari, "Estimation du rayonnement solaire par deux approches semi-empiriques dans le site de Biskra," in 8ème Séminaire International sur la Physique Energétique, Algérie, Nov. 2006, pp. 1–6.

[27] A. Louche, G. Peri, and M. Iqbal, "An analysis of Linke Turbidity Factor," Solar Energy, vol. 37, no. 6, pp. 393–396, 1986.

[28] I. Rougab, O. Barambones, M. Y. Silaa, and A. Cheknane, "Design, Implementation and Comparative Analysis of Three Models for Estimation of Solar Radiation Components on a Horizontal Surface," Symmetry, vol. 16, no. 1, art. 71, Jan. 2024.

[29] A. M. M. H. and A. G. F. Yettou, "Etude comparative de deux modèles de calcul du rayonnement solaire par ciel clair en Algérie," Revue des Energies Renouvelables, vol. 12, no. 2, pp. 331–346, 2009.

[30] H.-J. Bullinger, Technology Guide: Principles - Applications - Trends. Springer, 2009, pp. 1–556.

[31] D. Benatiallah, A. Benatiallah, K. Bouchouicha, M. Hamouda, and B. Nasri, "An empirical model for estimating solar radiation in the Algerian Sahara," AIP Conf. Proc., vol. 1968, pp. 1–11, May 2018.

[32] M. Ghodbane and B. Boumeddane, "Estimating solar radiation according to semi-empirical approach of PERRIN DE BRICHAMBAUT: application on several areas with different climate in Algeria," Int. J. Energetica, vol. 1, pp. 20–29, Dec. 2016.

[33] B. Y. H. Liu and R. C. Jordan, "The interrelationship and characteristic distribution of direct, diffuse and total solar radiation," Sol. Energy, vol. 4, no. 3, pp. 1–19, 1960.

[34] A. Bensaha, F. Benkouider, and S. M. A. Bekkouche, "Estimation du rayonnement solaire en ciel clair par des modèles empiriques: Application au site de Ghardaïa, Algérie," in Proc. 1st Int. Seminar on the Apport of the Simulation in Technological Innovation, pp. 1–5, Nov. 2016.

[35] M. R. Yaïche and S. M. A. Bekkouche, "Estimation du rayonnement solaire global en Algérie pour différents types de ciel," Revue des Energies Renouvelables, vol. 13, pp. 683–695, Dec. 2010.

[36] M. Hamdani, Étude et effet de l'orientation de deux pièces d'un habitat en pierre situé à Ghardaïa, Ph.D. dissertation, Univ. de Ghardaïa, Ghardaïa, Algeria, 2011.

[37] A. Bouramdane, M. L. Louazen, and A. Benmir, "Forecasting global incline solar radiation through empirical models on desert areas," in Proc. 4th Int. Conf. Technol. Adv. Electr. Eng. (ICTAEE'23), May 23–24, 2023, pp. 1–8.

[38] S. M. A. Bekkouche, Modélisation du comportement thermique de quelques dispositifs solaires, Ph.D. dissertation, Univ. de Tlemcen, Tlemcen, Algeria, May 2009.

[39] C. Cedric, Optimisation énergétique de l'étage d'adaptation électronique dédié à la conversion photovoltaïque, Ph.D. dissertation, Univ. Paul Sabatier - Toulouse III, Toulouse, France, 2008.

[40] M. Bencherif, Modélisation de système énergétique photovoltaïques et éoliens intégration dans un système hybride basse tension, Ph.D. dissertation, Univ. Abou-Bakr Belkaid, Tlemcen, Algeria, 2009.

[41] M. Koussa, A. Malek, M. Haddadi, and A. Yettou, "Apport énergétique de la poursuite solaire sur deux axes par rapport aux systèmes fixes, application aux capteurs plans," Revue des Énergies Renouvelables, vol. 10, no. 4, pp. 515–537, 2007.

[42] A. Djafour, "Étude d'un système de production d'hydrogène solaire," Ph.D. dissertation, Univ. Masdi Merbah, Ouargla, Algeria, 2013.

[43] T. Arrif, "Étude et simulation de la poursuite solaire à deux axes dans les systèmes à concentration," presented at the 2nd Int. Seminar on New and Renewable Energies, 2012.

[44] O. Sotehi, "Étude et analyse de l'influence de l'écart de température (absorbeur – vitre) sur l'efficacité d'un capteur solaire," Mémoire de Magister, Université Mentouri Constantine, 2007.

[45] H. Duzen and H. Aydin, "Sunshine-based estimation of global solar radiation on horizontal surface at Lake Van region (Turkey)," Energy Conversion and Management, vol. 58, pp. 35–46, June 2012.

[46] M. Koussa, A. Malek, and M. Haddadi, "Statistical comparison of monthly mean hourly and daily diffuse and global solar irradiation models and a Simulink program development for various Algerian climates," Energy Conversion and Management, vol. 50, pp. 1227–1235, May 2009.

[47] I. Oulimar, K. Bouchouicha, N. Bailek, and M. Bellaoui, "Statistical study of global solar radiation in the Algerian desert: a case study of Adrar town," Theoretical and Applied Climatology, vol. 155, pp. 3493–3504, Jan. 2024.

[48] M. M. Khan and M. J. Ahmad, "Estimation of global solar radiation using clear sky radiation in Yemen," Journal of Engineering Science and Technology Review, vol. 5, pp. 12–19, Aug. 2012.

[49] H. Li, X. Bu, Z. Long, L. Zhao, and W. Ma, "Calculating the diffuse solar radiation in regions without solar radiation measurements," Energy, vol. 44, pp. 611–615, Aug. 2012.

[50] T. E. Boukelia, M. S. Mecibah, and I. E. Meriche, "General models for estimation of the monthly mean daily diffuse solar radiation (Case study: Algeria)," Energy Conversion and Management, vol. 81, pp. 211–219, May 2014.

[51] A. Bouramdane, M. L. Louazene, and A. Benmir, "Forecasting global inclined solar radiation through empirical models on desert areas," in Proc. 4th Int. Conf. Technol. Adv. Electr. Eng. (ICTAEE'23), May 23–24, 2023, pp. 1–8.

[52] A. Bouramdane, M. L. Louazene, A. Benmir, and M. Ramdani, "Experimental and estimated study of global inclined solar radiation through LIU & JORDAN model applied in OUAD-NECHOU area," in Proc. Algerian Conf. Mechanics Sol. Energy (ACMSE-2023), Ouargla Univ., Ouargla, Algeria, Jun. 7–8, 2023, pp. 1–6.

[53] M. A. Husain, M. W. Ahmad, F. I. Bakhsh, S. Padmanaban, and H. Malik, Eds., Photovoltaic Systems Technology, 2024.

[54] S. J. Fonash, Solar Cell Device Physics, 2nd ed. Oxford, U.K.: Elsevier, 2010.

[55] J. Czochralski, "Ein neues Verfahren zur Messung der Kristallisationsgeschwindigkeit der Metalle," Z. Für Phys. Chem., vol. 92U, no. 1, pp. 219–221, Nov. 1918.

[56] D. M. Chapin, C. S. Fuller, and G. L. Pearson, "A new silicon p-n junction photocell for converting solar radiation into electrical power," J. Appl. Phys., vol. 25, no. 5, pp. 676–677, May 1954.

[57] S. Loff, "Vanguard Satellite, 1958," NASA, 2015.

[58] M. Yamaguchi, F. Dimroth, J. F. Geisz, and N. J. Ekins-Daukes, "Multi-junction solar cells paving the way for super high-efficiency," J. Appl. Phys., vol. 129, no. 24, p. 240901, Jun. 2021.

[59] A. M. Oni, A. S. M. Mohsin, M. M. Rahman, and M. B. H. Bhuian, "A comprehensive evaluation of solar cell technologies, associated loss mechanisms, and efficiency enhancement strategies for photovoltaic cells," Energy Reports, vol. 11, pp. 3345–3366, 2024.

[60] V. M. Andreev, A. McEvoy, T. Markvart, and L. Castañer, "GaAs and high-efficiency space cells," in Practical Handbook of Photovoltaics, 2nd ed. Cambridge, MA, USA: Academic Press, 2012, pp. 399–416.

[61] Breve História da Energia Solar, Nov. 30, 2021.

[62] S. Bernardes, R. A. M. Lameirinhas, J. P. N. Torres, and C. A. F. Fernandes, "Characterization and design of photovoltaic solar cells that absorb ultraviolet, visible and infrared light," Nanomaterials, vol. 11, p. 78, 2021.

[63] National Renewable Energy Laboratory, "Best Research-Cell Efficiency Chart," National Renewable Energy Laboratory, Nov. 17, 2021.

[64] C. B. Isabela, R. A. Marques Lameirinhas, J. P. N. Torres, and C. A. Ferreira Fernandes, "Comparative study of the copper indium gallium selenide (CIGS) solar cell with other solar technologies," Sustain. Energy Fuels, vol. 5, pp. 2273–2283, 2021.

[65] S. A. Alves dos Santos, J. P. N. Torres, C. A. Ferreira Fernandes, and R. A. Marques Lameirinhas, "The impact of aging of solar cells on the performance of photovoltaic panels," Energy Convers. Manag. X, vol. 10, p. 100082, 2021.

[66] R. Raimundo, R. A. Lameirinhas, C. A. F. Fernandes, and J. P. N. Torres, "Comparative analysis of organic and inorganic solar cells," in Proc. 2021 Telecoms Conf. (Conf. TELE), Leiria, Portugal, Feb. 11–12, 2021, pp. 1–6.

[67] M. H. Chaudhery, "Engineered nanomaterials for energy applications," in Handbook of Nanomaterials for Industrial Applications. Amsterdam, The Netherlands: Elsevier, 2018, pp. 751–767. ISBN 978-0-12-813351-4.

[68] A. da Silva Ravasco, J. P. N. Torres, and R. A. Marques Lameirinhas, "Wearable photovoltaic applications as energy sources for everyday devices," Am. J. Eng. Appl. Sci., vol. 14, pp. 337–350, 2021.

[69] Y. C. Wang, T. T. Wu, and Y. L. Chueh, "A critical review on flexible Cu(In,Ga)Se_2 (CIGS) solar cells," Mater. Chem. Phys., vol. 243, pp. 329–344, 2019.

[70] Flisom, "Description of products," Nov. 27, 2021.

[71] Fraunhofer Institute for Solar Energy Systems, Photovoltaics Report, Nov. 27, 2021.

[72] T. Alves, J. P. N. Torres, R. A. Marques Lameirinhas, and C. A. F. Fernandes, "Different techniques to mitigate partial shading in photovoltaic panels," Energies, vol. 14, p. 3863, 2021.

[73] I. Melo, J. P. N. Torres, C. A. Ferreira Fernandes, and R. A. Marques Lameirinhas, "Sustainability economic study of the islands of the Azores archipelago using photovoltaic panels, wind energy and storage system," Renewables, vol. 7, p. 4, 2020.

[74] B. Durão, J. P. N. Torres, C. A. F. Fernandes, and R. A. M. Lameirinhas, "Socio-economic assessment of renewable energy at Instituto Superior Técnico," Sustainability, vol. 12, p. 1923, 2020.

[75] S. K. Panda and S. K. Nayak, "Fundamentals of photovoltaic modules and their applications," Energy Reports, vol. 5, pp. 1081–1095, 2019.

[76] S. J. Fonash, Solar Cell Device Physics, 2nd ed. Boston, MA, USA: Academic Press, 2010.

[77] A. S. Al-Ezzi and M. N. M. Ansari, "Photovoltaic solar cells: A review," Applied System Innovation, vol. 6, no. 1, pp. 1–17, 2022.

[78] A. M. Oni, A. S. M. Mohsin, M. M. Rahman, and M. B. H. Bhuian, "A comprehensive evaluation of solar cell technologies, associated loss mechanisms, and efficiency enhancement strategies for photovoltaic cells," Energy Reports, vol. 11, pp. 3345–3366, 2024.

[79] Fraunhofer Institute for Solar Energy Systems, Photovoltaics Report, Nov. 27, 2021.

[80] R. A. M. Lameirinhas, J. P. N. Torres, and J. P. de M. Cunha, "A photovoltaic technology review: History, fundamentals and applications," Energies, vol. 15, p. 1823, 2022.

[81] A. Ben Hassen, C. Chkir, and M. Bourguiga, "Review of photovoltaic cell generations: materials, structures and performance," Solar Energy Materials and Solar Cells, vol. 276, p. 112130, Mar. 2024.

[82] M. A. Green and A. Ho-Baillie, "Nanostructured solar cells," Nat. Rev. Mater., *vol. 2, art.* 17009, pp. 1–14, 2017.

[83] N. Rathore, N. L. Panwar, F. Yettou, and A. Gama, "A comprehensive review on different types of solar photovoltaic cells and their applications*,"* Int. J. Ambient Energy, 2019.

[84] J. Zhao, A. Wang, and M. A. Green, "19.8% efficient 'honeycomb' textured multicrystalline and 24.4% monocrystalline silicon solar cells," Appl. Phys. Lett., vol. 73, no. 14, pp. 1991–1993, 1998.

[85] Circuit Globe, "Photovoltaic or solar cell," accessed Apr. 27, 2020.

[86] T. Zimmer, "Photovoltaic cell types," accessed Oct. 15, 2019.

[87] A. S. Al-Ezzi and M. N. M. Ansari, "Photovoltaic solar cells: A review," Energies, vol. 14, no. 22, art. 7596, Nov. 2021.

[88] L. A. Dobrzanski, A. Drygala, M. Giedroc, and M. Macek, "Monocrystalline silicon solar cells applied in photovoltaic system," J. Achiev. Mater. Manuf. *Eng.*, vol. 53, no. 1, pp. 1–12, 2012.

[89] A. Tascioglu, O. Taskin, and A. Vardar, "A power case study for monocrystalline and polycrystalline solar panels in Bursa City, Turkey," 2016.

[90] A. Sendy, "Pros and cons of monocrystalline vs polycrystalline solar panels," 2017.

[91] J. Zhao, A. Wang, M. A. Green, et al., "19.8% efficient 'honeycomb' textured multicrystalline and 24.4% monocrystalline silicon solar cells," Appl. Phys. Lett., vol. 73, pp. 1991–1993, 1998.

[92] Indiamart, "Tata 250-Watt Polycrystalline Solar Panel," Nov. 2019.

[93] E. van Kerschaver and G. Beaucarne, "Back-contact solar cells: a review," Prog. Photovoltaics Res. Appl., vol. 14, pp. 107–123, 2006.

[94] J. Zhao, A. Wang, and M. A. Green, "24.5% efficiency silicon PERT cells on MCZ substrates and 24.7% efficiency PERL cells on FZ substrates," Prog. Photovolt. Res. Appl., vol. 7, no. 6, pp. 471–474, 1999.

[95] R. M. Swanson, "Approaching the 29% limit efficiency of silicon solar cells," in Proc. 31st IEEE Photovoltaic Specialists Conf., 2005, pp. 889–894.

[96] M. Boutchich, J. Alvarez, D. Diouf, et al., "Amorphous silicon diamond-based heterojunctions with high rectification ratio," J. Non- Cryst. Solids, vol. 358, pp. 2110–2113, 2012.

[97] M. Gul, Y. Kotak, and T. Muneer, "Review on recent trend of solar photovoltaic technology," Energy Exploration & Exploitation, vol. 34, no. 1, pp. 1–42, 2016.

[98] C.-J. Yang, "Transparent conducting aluminium doped zinc oxide for silicon quantum dot solar cell devices in third generation photovoltaics," Ph.D. dissertation, Univ. of New South Wales, Sydney, Australia, 2015.

[99] J. Britt and C. Ferekides, "Thin-film CdS/CdTe solar cell with 15.8% efficiency," Appl. Phys. Lett., vol. 62, no. 22, pp. 2851–2852, 1993.

[100] National Renewable Energy Laboratory (NREL), "Best Research-Cell Efficiency Chart," Photovoltaic Research, NREL, Golden, CO, USA, Nov. 17, 2021.

[101] A. De Vos, J. Parrott, P. Baruch, and P. Landsberg, "Bandgap effects in thin-film heterojunction solar cells," in Proc. 12th Eur. Photovoltaic Solar Energy Conf., Amsterdam, The Netherlands, 1994, pp. 1315–1318.

[102] D. I. M. Dharmada, P. A. Bingham, O. K. Echendu, H. I. Salim, T. Drriffeel, R. Dharmadasa, G. U. Sumanasekera, R. R. Dharmasena, M. B. Dergacheva, K. A. Mit, K. A. Urazov, L. Bowen, M. Walls, and A. Abba, "Fabrication of CdS/CdTe-based thin film solar cells using an electrochemical technique," Coatings, vol. 4, no. 3, pp. 380–415, 2014.

[103] K. Ong, R. Agileswari, B. Maniscalo, P. Arnou, C. Kumar, J. Bowers, and M. Marsadek, "Review on substrate and molybdenum back contact in CIGS thin film solar cell," Int. J. Photoenergy, vol. 2018, 2018.

[104] J. Ramanujam and U. P. Singh, "Copper indium gallium selenide based solar cells – review," Energy Environ. Sci., vol. 9, no. 11, pp. 1306–1319, 2017.

[105] M. Powalla, S. Paetel, D. Hariskos, R. Wuerz, F. Kessler, P. Lechner, W. Wischmann, and T. M. Friedlmeier, "Advances in cost-efficient thin-film photovoltaics based on Cu(In,Ga)Se2," Engineering, vol. 3, no. 4, pp. 445–551, 2017.

[106] European Institute for Energy Research, "Dye-sensitized vs. thin film solar cells," Jun. 30, 2006.

[107] K. E. Sarah, U. Roland, and E. O. Ephraim, "A review of solar photovoltaic technologies," Int. J. Eng. Res. Technol. (IJERT), vol. 9, no. 7, pp. 741–749, 2020.

[108] J. Pastuszak and P. Węgierek, "Photovoltaic cell generations and current research directions for their development," Materials, vol. 15, no. 16, p. 5542, 2022.

[109] P. Peumans, A. Yakimov, and S. R. Forrest, "Small molecular weight organic thin-film photodetectors and solar cells," J. Appl. Phys., vol. 93, pp. 3693–3723, 2003.

[110] A. Luque and S. Hegedus, Eds., Handbook of Photovoltaic Science and Engineering, 2nd ed. Chichester, UK: John Wiley & Sons, 2011, pp. 4–36.

[111] C. Wu, K. Wang, M. Batmunkh, A. S. Bati, D. Yang, Y. Jiang, Y. Hou, J. G. Shapter, and S. Priya, "Multifunctional nanostructured materials for next generation photovoltaics," Nano Energy, vol. 70, p. 104480, 2020.

[112] S. Almosni, A. Delamarre, Z. Jehl, D. Suchet, L. Cojocaru, M. Giteau, B. Behaghel, A. Julian, C. Ibrahim, L. Tatry, et al., "Material challenges for solar cells in the twenty-first century: Directions in emerging technologies," Sci. Technol. Adv. Mater., vol. 19, pp. 336–369, 2018.

[113] M. V. Dambhare, B. Butey, and S. V. Moharil, "Solar photovoltaic technology: A review of different types of solar cells and its future trends," J. Phys. Conf. Ser., vol. 1913, p. 012053, 2021.

[114] F. M. A. Fazal and S. Rubaiee, "Progress of PV cell technology: Feasibility of building materials, cost, performance, and stability," Sol. Energy, vol. 258, pp. 203–219, 2023.

[115] H. Wu and Y. Hou, "Recent development of grid-connected PV systems in China," Energy Procedia, vol. 12, pp. 462–470, 2011.

[116] A. K. Akhmedov, A. K. Abduev, E. K. Murliev, V. V. Belyaev, and A. S. Asvarov, "Transparent conducting amorphous IZO thin films: An approach to improve the transparent electrode quality," Materials, vol. 16, no. 3740, 2023.

[117] A. Machín and F. Márquez, "Advancements in photovoltaic cell materials: Silicon, organic, and perovskite solar cells," Materials, vol. 17, no. 5, p. 1165, 2024.

[118] A. C. Lazaroiu, M. G. Osman, C.-V. Strejoiu, and G. Lazaroiu, "A comprehensive overview of photovoltaic technologies and their efficiency for climate neutrality," Sustainability, vol. 15, no. 23, art. 16297, Nov. 2023.

[119] A. S. Al-Ezzi and M. N. M. Ansari, "Photovoltaic solar cells: A review," Appl. Syst. Innov., vol. 5, no. 4, art. 67, pp. 1–17, Jul. 2022.

[120] A. Shah, P. Torres, R. Tscharner, N. Wyrsch, and H. Keppner, "Photovoltaic technology: The case for thin-film solar cells," Science, vol. 285, no. 5428, pp. 692–698, Jul. 1999.

[121] National Renewable Energy Laboratory, "Best Research-Cell Efficiency Chart," Photovoltaic Research, National Renewable Energy Laboratory, Feb. 13, 2022.

[122] Solar Cell Central, "Solar Cell & Panel Basics," Solar Cell Central, Aug. 30, 2023.

[123] E. Skoplaki and J. A. Palyvos, "On the temperature dependence of photovoltaic module electrical performance: A review of efficiency/power correlations," Sol. Energy, vol. 83, pp. 614–624, 2009.

[124] W. A. Herez, H. Jaber, H. E. Hage, T. Lemenand, M. Ramadan, and M. Khaled, "A review on the classifications and applications of solar photovoltaic technology," AIMS Energy, vol. 11, no. 6, pp. 1102–1130, Nov. 2023.

[125] D. Martin-Abood, T. Dudis, and T. Wagner, "Solar photovoltaic considerations for operational and warfighter support capabilities," HDIAC Journal of Homeland Defense & Security, vol. 7, no. 1, pp. 5–13, Jun. 2020.

[126] I. Paraskevopoulos and E. Tsekleves, "Simulation of photovoltaics for defence applications—power generation assessment and investigation of the available integration areas of photovoltaic devices on a virtual infantryman," in Proc. 2nd Int. Conf. Simulation and Modeling Methodologies, Technologies and Applications (SIMULTECH), Jul. 2012, pp. 384–396.

[127] M. Frączek, K. Górski, and L. Wolaniuk, "Possibilities of powering military equipment based on renewable energy sources," Applied Sciences, vol. 12, no. 2, p. 843, Jan. 2022.

[128] https://www.google.com/earth

[129] C. Kalu, I. A. Ezenugu, and A. M. Umoren, "Comparative study of performance of three different photovoltaic technologies," Materials and Software Engineering, vol. 2, no. 1, pp. 19–29, 2019.

[130] A. Allouhi et al., "Grid-connected PV systems installed on institutional buildings: Technology comparison, energy analysis and economic performance," Energy and Buildings, vol. 130, pp. 188–201, Oct. 2016.

[131] A. Al-Otaibi, A. Al-Qattan, F. Fairouz, and A. Al-Mulla, "Performance evaluation of photovoltaic systems on Kuwaiti schools' rooftop," Energy Conversion and Management, vol. 95, pp. 110–119, May 2015.

[132] A. B. Stambouli, Z. Khiat, S. Flazi, and Y. Kitamura, "A review on the renewable energy development in Algeria: Current perspective, energy scenario and sustainability issues," Renewable and Sustainable Energy Reviews, vol. 16, no. 7, pp. 4445–4460, Sep. 2012.

[133] S. Bentouba, M. Bourouis, N. Zioui, A. Pirashanthan, and D. Velauthapillai, "Performance assessment of a 20 MW photovoltaic power plant in a hot climate using real data and simulation tools," Energy Reports, vol. 7, pp. 7297–7314, Nov. 2021.

[134] M. E. H. Dahmoun et al., "Performance evaluation and analysis of grid-tied large-scale PV plant in Algeria," Energy for Sustainable Development, vol. 61, pp. 181–195, Apr. 2021.

[135] S. B. S. Kumar and K. Sudhakar, "Performance evaluation of 10 MW grid connected solar photovoltaic power plant in India," Energy Reports, vol. 1, no. 2, pp. 184–192, Nov. 2015.

[136] S. Touili, A. Alami Merrouni, Y. El Hassouani, and A. I. Amrani, "Performance analysis of large-scale grid-connected PV plants in the MENA region," International Journal of Engineering Research in Africa, vol. 42, pp. 139–148, Apr. 2019.

[137] G. C. Lazaroiu, M. Longo, M. Roscia, and M. Pagano, "Comparative analysis of fixed and sun-tracking low-power PV systems considering energy consumption," Energy Conversion and Management, vol. 92, pp. 143–148, Mar. 2015.

[138] W. Nsengiyumva, S. Chen, L. Hu, and X. Chen, "Recent advancements and challenges in solar tracking systems (STS): A review," Renewable and Sustainable Energy Reviews, vol. 81, pp. 250–279, Jan. 2018.

[139] C.-H. Wu, H.-C. Wang, and H.-Y. Chang, "Dual-axis solar tracker with satellite compass and inclinometer for automatic positioning and tracking," Energy for Sustainable Development, vol. 66, pp. 308–318, Feb. 2022.

[140] L. Zaghba et al., "Intelligent MPPT control of stationary and dual-axis tracking grid-connected photovoltaic system," Scientific Digital Library, vol. 1, pp. 199–205, 2018.

[141] M. Cubukcu and H. Gumus, "Performance analysis of a grid-connected photovoltaic plant in eastern Turkey," Sustainable Energy Technologies and Assessments, vol. 39, p. 100724, Jun. 2020.

[142] M. Pirzadi and A. A. Ghadimi, "Performance evaluation of first Iranian large-scale photovoltaic power plant," Journal of Electrical Engineering, vol. 51, no. 1, pp. 19–30, Jun. 2020.

[143] D. J. Veerendra Kumar, L. Deville, K. A. Ritter III, J. R. F. Ferdowsi, R. Gottumukkala, and T. L. Chambers, "Performance evaluation of 1.1 MW grid-connected solar photovoltaic power plant in Louisiana," Energy, vol. 15, no. 9, p. 3420, May 2020.

[144] I. Bendaas, K. Bouchouicha, S. Semaoui, A. Razagui, S. Bouchakour, and S. Boulahchiche, "Performance evaluation of large-scale photovoltaic power plant in Saharan climate of Algeria based on real data," Energy for Sustainable Development, vol. 76, p. 101293, Oct. 2023.

[145] I. Jamil, H. Lucheng, S. Habib, M. Aurangzeb, and E. M. Ahmed, "Performance ratio analysis based on energy production for large-scale solar plant," IEEE Access, vol. 10, pp. 5715–5735, Jan. 2022.

[146] A. Fezzani, M. Khennane, A. Borni, S. Mekhilef, and A. Bensaha, "Energy efficiency of multi-technology PV modules under arid climate: Experimental assessment of energy yield and performance indices," Sustainability, vol. 14, no. 3, art. 1771, Feb. 2022.

[147] N. Benbouza, M. M. S. Moghalles, A. N. El Ayad, and B. Amel, "Optimization of the solar radiation received by photovoltaic panels using solar tracking systems: Study case in south of Algeria," presented at the 5th Int. AEGEAN Symposium on Innovation Technologies and Engineering, Izmir, Turkey, Feb. 2022.

[148] M. Mehdi, N. Ammari, A. Alami Merrouni, H. El Gallassi, M. Dahmani, and A. Ghennioui, "An experimental comparative analysis of different PV technologies performance including the influence of hot-arid climatic parameters: Toward a realistic yield assessment for desert locations," Renewable Energy, vol. 205, pp. 695–716, Mar. 2023.

[149] L. H. Hicham, L. Boughamrane, and D. Izbaim, "Performance of different silicon PV technologies installed in Laâyoune – Morocco," Applied Journal of Environmental Engineering Scien*ce*, vol. 6, no. 2, pp. 160–172, Jul. 2020.

[150] A. Bouramdane, M. L. Louazene, and A. Benmir, "Comparative experimental performance study of four fixed photovoltaic subfields under Saharan climate: A case study in Oued-Nechou, Ghardaïa," Int. J. Intelligent Systems Applications in Engineering, May 2024.

[151] M. L. Louazene, A. Bouramdane, and A. Benmir, "Optimizing photovoltaic efficiency in isolated areas: A comparative study of fixed and single-axis tracking systems under real climatic conditions," J. of Information Systems Engineering and Management, vol. 10, no. 4, 2025.

[152] E. Karami, M. Rafi, A. Ridah, B. Hartiti, and P. Thevenin, "Analysis of measured and simulated performance data of different PV modules of silicon in Casablanca," in Proc. 2nd Int. Conf. on Smart Applications and Data Analysis for Smart Sites, Feb. 27–28, 2018.

[153] L. Zaghba, M. Khennane, S. Mekhilef, A. Fezzani, and A. Borni, "Experimental outdoor performance assessment and energy efficiency of 11.28 kWp grid-tied PV systems with sun tracker installed in Saharan climate: A case study in Ghardaia, Algeria," Solar Energy, vol. 243, pp. 174–192, Sep. 2022.

[154] A. Ameur, A. Sekkat, K. Loudiyi, and M. Aggour, "Performance evaluation of different photovoltaic technologies in the region of Ifrane, Morocco," Energy for Sustainable Development, vol. 52, pp. 96–103, Oct. 2019.

[155] A. Z. Hafez, J. H. Shazly, and M. B. Eteiba, "Comparative evaluation of optimal energy efficiency designs for solar tracking systems," in Proc. 3rd Int. Conf. on Advances in Applied Science and Environmental Engineering, Apr. 2015, pp. 134–141.

[156] L. A. Hussein, O. Ayadi, and M. Fathi, "Performance comparison for sun-tracking mechanism photovoltaic (PV) and concentrated photovoltaic (CPV) solar panels with fixed system PV panels in Jordan," presented at the 12th Int. Renewable Engineering Conf., IEEE, Amman, Jordan, Apr. 2021.

[157] A. Elkholy, F. H. Fahmy, A. A. Abou El-Ela, A. E. S. A. Nafeh, and S. R. Spea, "Experimental evaluation of 8 kW grid-connected photovoltaic system in Egypt," Journal of Electrical Systems and Information Technology, vol. 3, no. 2, pp. 217–229, Sep. 2016.

[158] R. Dabou, F. Bouchafaa, A. H. Arab, A. Bouraiou, M. D. Draou, A. Neçaibia, and M. Mostefaoui, "Monitoring and performance analysis of grid-connected photovoltaic under different climatic conditions in south Algeria," Energy Conversion and Management, vol. 130, no. 2, pp. 200–206, Dec. 2016.

[159] I. S. Panagea, I. K. Tsanis, and A. G. Koutroulis, "Climate change impact on photovoltaic energy output: The case of Greece," Climate Change and the Future of Sustainability, vol. 11, no. 2, pp. 85–106, 2016.

[160] C. Schwingshackl, M. Petitta, J. E. Wagner, G. Belluardo, D. Moser, M. Castelli, and A. Tetzlaff, "Wind effect on PV module temperature: Analysis of different techniques for an accurate estimation," Energy Procedia, vol. 40, pp. 77–86, 2013.

[161] E. Kaplani and S. Kaplanis, "Thermal modelling and experimental assessment of the dependence of PV module temperature on wind velocity and direction, module orientation and inclination," Solar Energy, vol. 107, pp. 443–460, Sep. 2014.

[162] H. Zainuddin, S. Shaari, A. M. Omar, Z. M. Zain, J. Soumin, and Z. Surat, "Preliminary investigations on the effect of humidity on the reception of visible solar radiation and the effect of humidity and wind speed on PV module output," presented in AIP Conf. Proc., Jul. 2010, pp. 55–58.

[163] E. Karami, M. Rafi, A. Haibaoui, A. Ridah, B. Hartiti, and P. Thevenin, "Performance analysis and comparison of different photovoltaic modules technologies under different climatic conditions in Casablanca," Journal of Fundamentals of Renewable Energy and Applications, vol. 7, no. 3, pp. 1–6, 2017.

[164] M. K. Al-Ghezi, R. T. Ahmed, and M. T. Chaichan, "The influence of temperature and irradiance on performance of the photovoltaic panel in the middle of Iraq*,"* International Journal of Renewable Energy Development, vol. 11, no. 2, pp. 501–513, 2022.

[165] B. Du, E. Hu, and M. Kolhe, "Performance analysis of water-cooled concentrated photovoltaic (CPV) system," Renewable and Sustainable Energy Reviews, vol. 16, no. 9, pp. 6732–6736, Dec. 2012.

[166] M. R. Gomaa, H. M. Fahmy, and M. M. Elsobki, "Experimental assessment of active and passive cooling techniques for enhancing photovoltaic performance," Sustainable Energy Technologies and Assessments, vol. 40, p. 100768, Aug. 2020.

ANNEXES

- Single-line diagram of the PV Power Plant

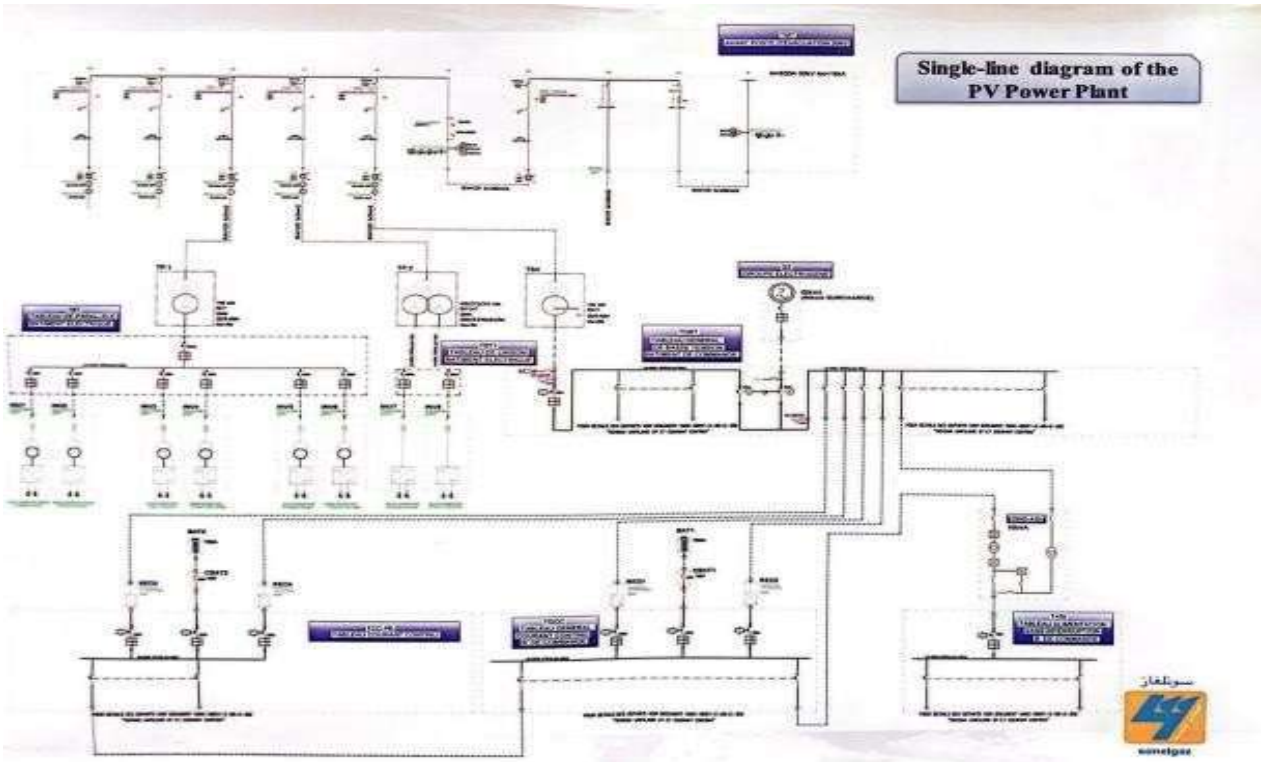

- Details of the Photovoltaic Power Plant Subfields: Configuration, Structure, and Output Capacity

#	Type	Structure	PV Panel Power (W_p)	Nbre of Strings	Nbre of Panels/String	String DC Voltage (V)	DC Power Output (kW_p)
1	C-Si	Trackers	250	21	20	590.6	105
2	mC-Si		235	21	20	580.8	98.7
3	Cd-Te	Fixed	80	105	12	582	100.8
4	a-Si		103	54	18	547.2	100.1
5	C-Si		250	21	20	590.6	105
6	mC-Si		235	21	20	580.8	98.7
7	C-Si		250	51	20	590.6	255
8	mC-Si		235	55	20	580.8	258.5
						Total	≈ 1100

- Annual Performance of the PV Power Plant: Power Generation, Natural Gas Savings, and CO_2 Emissions Reduction (2015–March 2023)

Power Generation, Natural Gas Saving and CO_2 Emissions Reduction

Year	2015	2016	2017	2018	2019	2020	2021	2022	To March 2023	Cumul
Power Generation (GWh)	2.05	1.58	1.97	1.90	1.88	1.85	1.83	1.83	0.38	15.27
Natural Gas Saving (10^3 m^3)	701.76	540.81	674.03	652.60	645.02	633.97	628.15	625.63	129.26	5 231.23
CO_2 emissions reduction (tons)	535.44	412.64	514.28	497.94	492.15	483.72	479.28	477.35	98.63	3 991.43

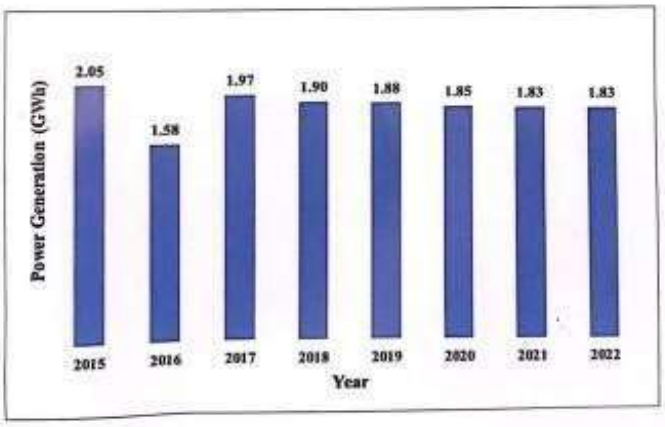

ملخص

تلعب تقنيات الخلايا الضوئية (الفوتوفولطية) دورًا أساسيًا في مجال الطاقة المتجددة من خلال تحويل ضوء الشمس مباشرة إلى كهرباء، مما يتيح إنتاج طاقة فعال وقابل للتوسع وصديق للبيئة. وبناءً على هذا الأساس، تقدم هذه الرسالة البحثية تحققًا تجريبيًا باستخدام بيانات أداء حقيقية لتقدير التدفق الكلي للإشعاع الشمسي على سطح مائل بزاوية 30°، استنادًا إلى ثلاثة نماذج شبه تجريبية: النموذج المعروف لبيرين دي بريشامبو، إلى جانب نماذج لوي وجوردن وكابديرو، وكلاهما يتضمن عوامل تصحيح مرتبطة بالعكارة الجوية. يتم تقييم دقة كل نموذج من خلال مقارنة القيم المقدرة مع بيانات الإشعاع الشمسي التي تم تسجيلها كل أربع دقائق خلال أربعة أيام تمثيلية في عام 2016، وهي 1 يناير، 1 مايو، 1 يوليو، و1 أكتوبر، والتي تمثل فصولًا مختلفة من السنة. تم جمع القياسات باستخدام جهاز بيرانومتر مثبت على سطح غرفة التحكم بمحطة الخلايا الشمسية. تُقيَّم أداء النماذج باستخدام مؤشرات إحصائية مثل الخطأ المطلق، متوسط الخطأ المطلق (واط/متر مربع)، الجذر التربيعي لمتوسط الخطأ التربيعي (واط/متر مربع)، معامل الرَّتباط، ومتوسط الخطأ النسبي المئوي (%). الهدف الأساسي هو تحديد النموذج الأكثر دقة في تقدير الإشعاع الشمسي المائل تحت الظروف المناخية لمنطقة وادي نشاو، وهو أمر ذو صلة بمناطق صحراوية مشابهة تفتقر إلى بيانات الأرصاد الجوية المباشرة.

بالإضافة إلى ذلك، تقدم هذه الرسالة تحليلًا تجريبيًا شاملًا وتقييمًا لأداء ثمانية حقول فرعية للفوتوفولطية تعمل تحت مناخ الصحراء في وادي نشاو بمنطقة غرداية بالجزائر. تدرس الدراسة أربعة أنظمة بزاوية ميل ثابتة (30°) تستخدم تقنيات فوتوفولطية مختلفة وهي: السيليكون أحادي البلورة(mc-Si) ، السيليكون متعدد البلورات(pc-Si) ، تيلورايد الكادميوم(CdTe) ، والسيليكون غير المتبلور(a-Si) ، إلى جانب أربعة حقول فرعية إضافية: اثنان بنظام ثابت واثنان بنظام تتبع شمسي بمحور واحد، تعتمد جميعها على تقنيات mc-Si و.pc-Si يُقسم التحليل المقارن إلى جزأين رئيسيين: (1) مقارنة الأداء بين الحقول الفرعية ذات الميل الثابت باستخدام مواد فوتوفولطية مختلفة، و(2) تقييم الأنظمة الثابتة مقابل أنظمة التتبع بمحور واحد باستخدام نفس التقنيات (mc-Si و pc-Si). تتيح هذه المقاربة المزدوجة تقييمًا مفصلًا لتأثير نوع المادة وتركيب النظام على أداء الفوتوفولطية في الظروف الصحراوية القاسية.

يرتكز التحليل على أربعة مؤشرات رئيسية للأداء: (1) أقصى قدرة خرج مباشر (DC) وإنتاج الطاقة اليومي، (2) العوامل البيئية المؤثرة على الأداء، (3) نسبة تحسين الأداء (%)، و(4) العائد اليومي للطاقة (كيلوواط ساعة/يوم).

الهدف العام هو تحديد التكوين الفوتوفولطي الذي يوفر أفضل أداء شامل ويناسب أكثر النشر في المناطق الصحراوية مثل وادي نشاو، خاصة في المناطق التي تفتقر إلى بنية تحتية شاملة لمراقبة الأرصاد الجوية.

الكلمات المفتاحية : تقنيات الخلايا الضوئية (الفوتوفولطية)، الطاقة الشمسية، النماذج شبه التجريبية، تصحيح العكارة، مؤشرات الأداء الإحصائية، AE، MAE، RMSE، CC، MAPE، أنظمة الخلايا الضوئية ذات الميل الثابت، أنظمة التتبع الشمسي بمحور واحد، توليد الطاقة، العائد الطاقي اليومي، تقييم الأداء .

ABSTRACT

Photovoltaic technologies play a key role in renewable energy by directly converting sunlight into electricity, enabling efficient, scalable, and environmentally friendly power generation. Building on this foundation, this research thesis presents an experimental validation using real performance data to estimate total solar radiation flux on a surface tilted at 30°, based on three semi-empirical models: the widely adopted PERRIN DE BRICHAMBAUT model, along with the LIU & JORDEN and CAPDEROU models, both incorporating turbidity-related correction factors. The accuracy of each model is assessed by comparing estimated values with solar irradiance data recorded every four minutes on four representative days in 2016, January 1st , May 1st , July 1st , and October 1st , covering different seasons. Measurements were collected using a pyranometer mounted on the control room rooftop of the photovoltaic station. Model performance is evaluated using statistical indicators, including Absolute Error (AE), Mean Absolute Error (MAE, W/m²),

RMSE(W/m²),(CC), and MAPE (%). The primary goal is to determine which model provides the highest accuracy in estimating inclined solar radiation under the climatic conditions of the OUED-NEACHOU region, which is relevant to similar Saharan areas lacking direct meteorological data. In addition, this research thesis presents a comprehensive experimental analysis and performance evaluation of eight photovoltaic (PV) subfields operating under the Saharan climate of OUED-NEACHOU in the Ghardaïa region of Algeria. The study investigates four fixed-tilt systems (30° tilt) utilizing different PV technologies mc-Si, pc-Si, CdTe, and a-Si alongside four additional subfields: two fixed and two single-axis tracking systems, each based on mc-Si and pc-Si technologies.

The comparative analysis is structured into two main components: (1) performance comparison among the four fixed-tilt subfields using different PV materials, and (2) evaluation of fixed versus single-axis tracking systems employing the same technologies (mc-Si and pc-Si). This dual approach enables a detailed assessment of the impact of both material type and mounting configuration on PV performance in harsh desert conditions. The analysis relies on four key performance indicators: (I) Maximum DC Output Power and Daily Power Generation, (II) Environmental Factors Affecting Performance, (III) Performance Improvement Percentage (%), and (IV) Daily Energy Yield (kWh/day).The overarching goal is to determine the PV configuration that delivers the best overall performance and is most suitable for deployment in desert regions such as OUED-NEACHOU, particularly in areas lacking comprehensive meteorological monitoring infrastructure.

Keywords : Photovoltaic technologies , Solar energy , Semi-empirical models , Turbidity correction , Statistical performance indicators , (AE) , (MAE) , (RMSE) , (CC) , (MAPE) , Fixed-tilt photovoltaic systems , Single-axis tracking systems , Power generation ,Daily energy yield , Performance evaluation

RÉSUMÉ

Les technologies photovoltaïques jouent un rôle clé dans les énergies renouvelables en convertissant directement la lumière solaire en électricité, permettant ainsi une production d'énergie efficace, évolutive et respectueuse de l'environnement. S'appuyant sur ce principe, cette thèse de recherche présente une validation expérimentale utilisant des données de performance réelles pour estimer le flux total de rayonnement solaire sur une surface inclinée à 30°, basée sur trois modèles semi-empiriques : le modèle largement adopté de PERRIN DE BRICHAMBAUT, ainsi que les modèles de LIU & JORDEN et CAPDEROU, tous deux intégrant des facteurs de correction liés à la turbidité. La précision de chaque modèle est évaluée en comparant les valeurs estimées avec les données d'irradiance solaire enregistrées toutes les quatre minutes sur quatre jours représentatifs de l'année 2016 1er janvier, 1er mai, 1er juillet et 1er octobre couvrant différentes saisons. Les mesures ont été recueillies à l'aide d'un pyranomètre installé sur le toit de la salle de contrôle de la station photovoltaïque. La performance des modèles est évaluée à l'aide d'indicateurs statistiques incluant l'erreur absolue (EA), l'erreur absolue moyenne (EAM, W/m²), la racine de l'erreur quadratique moyenne (RMSE, W/m²), le coefficient de

corrélation (CC) et l'erreur moyenne absolue en pourcentage (EMAP, %). L'objectif principal est de déterminer quel modèle fournit la meilleure précision pour estimer le rayonnement solaire incliné dans les conditions climatiques de la région d'OUED-NEACHOU, ce qui est pertinent pour des zones sahariennes similaires dépourvues de données météorologiques directes.

De plus, cette thèse présente une analyse expérimentale complète et une évaluation des performances de huit sous-champs photovoltaïques (PV) fonctionnant sous le climat saharien d'OUED-NEACHOU, dans la région de Ghardaïa en Algérie. L'étude porte sur quatre systèmes à inclinaison fixe (30°) utilisant différentes technologies PV : mc-Si, pc-Si, CdTe et a-Si, ainsi que sur quatre sous-champs supplémentaires : deux fixes et deux systèmes à suivi solaire à un axe, chacun basé sur les technologies mc-Si et pc-Si. L'analyse comparative est structurée en deux volets principaux : (1) comparaison des performances entre les quatre sous-champs à inclinaison fixe utilisant différents matériaux PV, et (2) évaluation des systèmes fixes versus les systèmes à suivi solaire à un axe utilisant les mêmes technologies (mc-Si et pc-Si). Cette double approche permet une évaluation détaillée de l'impact à la fois du type de matériau et de la configuration d'installation sur les performances PV dans des conditions désertiques extrêmes. L'analyse repose sur quatre indicateurs clés de performance : (I) puissance maximale en courant continu (DC) et production quotidienne d'énergie, (II) facteurs environnementaux influençant la performance, (III) pourcentage d'amélioration de la performance (%), et (IV) rendement énergétique journalier (kWh/jour).

L'objectif global est de déterminer la configuration PV qui offre la meilleure performance globale et convient le mieux à une implantation dans des régions désertiques telles qu'OUED-NEACHOU, notamment dans les zones où l'infrastructure de surveillance météorologique est limitée ou inexistante.

Mots-clés : Technologies photovoltaïques , Énergie solaire , Modèles semi-empiriques ,Correction de turbidité , Indicateurs statistiques de performance , (AE) , (MAE) , (RMSE) , (CC) , (MAPE) , Systèmes photovoltaïques à inclinaison fixe , Systèmes à suivi solaire à un axe Production d'énergie , Rendement énergétique quotidien , Évaluation de la performance .